DISS. ETH NO. 27877

NEW ELECTRON SPIN RESONANCE EXPERIMENTS WITH TAILORED WAVEFORM EXCITATION

A dissertation submitted to attain the degree of

DOCTOR OF SCIENCES of ETH ZURICH
(Dr. sc. ETH Zurich)

presented by

NINO ANDREA WILI
MSc ETH

born in Bern on 8 July 1993
citizen of Hitzkirch LU and Altwis LU in Switzerland,
and from Germany

accepted on the recommendation of

Prof. Dr. Gunnar Jeschke, examiner
Prof. Dr. Matthias Ernst, co-examiner
Prof. Dr. Thomas Prisner, co-examiner

2021

Typeset in LaTeX, figures generated with MATLAB (The MathWorks) and Inkscape.

Mirä Familiä

ABSTRACT

Electron spin resonance (ESR) is a powerful tool to investigate paramagnetic chemical systems, such as radicals, transition metal complexes, and metalloenzymes. It can provide information about the geometric and electronic structure by determining the coupling between different spins. Hyperfine couplings between electron and nuclear spins provide electron-nuclear distances and local spin densities, while weak electron-electron dipolar couplings can be used for distance measurements between said electrons. Stronger electron-electron interactions on the same or close by metal centres can inform about intricate details of the complicated electronic structure.

Until recently, pulsed ESR methods relied on monochromatic and constant-amplitude pulses. This changed with the commercial availability of fast arbitrary waveform generators (AWG), which allow pulse shaping in the microwave region. This work explores possibilities on how to make use of the new, unprecedented electron spin control.

Chapter 2 introduces Chirp Echo Epr SpectroscopY (CHEESY)-detected NMR. This sequence combines hole burning pulses with broadband chirp echoes to detect hyperfine couplings between the electron spin and surrounding nuclei. It is related to electron double resonance (ELDOR)-detected NMR, but gives an additional multiplex advantage, since all nuclear frequencies can be detected in a single shot. The method is extended to a two-dimensional version by adding an additional selective inversion pulse, which allows for acquisition of hyperfine-sublevel correlation (HYSCORE)-type spectra. This improves resolution and facilitates assignment.

Chapter 3 describes the observation of antiholes (i. e. signal enhancements) in ELDOR-detected NMR (EDNMR) spectra of an exchange coupled Cu(II)-porphyrin dimer. An algorithm is introduced that can simulate EDNMR spectra of arbitrary spin systems. Together with field-correlated ultra-wide band EDNMR spectra, this allowed the determination of the zero-field splitting in the $S = 1$ manifold of the two coupled unpaired electrons. Additionally, in a Cu(II)-porphyrin dimer with negligible exchange coupling, the EDNMR resolution was good enough to distinguish ^{63}Cu and ^{65}Cu isotopes and to resolve the nuclear quadrupole coupling.

Chapter 4 introduces dressed spin resonance with phase-modulation as a means of measuring distances between narrow-line radicals, such as trityls. A spinlock sequence is used to decouple the electron spin from the surrounding

nuclear spins, dramatically increasing its relaxation times. Short bursts of sinusoidal phase modulation (PM) periods, where the PM frequency matches the spinlock Rabi frequency, are used to manipulate the electron spins in the spinlocked frame, i.e. during microwave irradiation. Conceptual and technical problems regarding the rotating frame relaxation times and the limited microwave strength are discussed.

Chapter 5 introduces a general framework to understand pulsed dynamic nuclear polarisation (DNP) sequences with arbitrary phase- and amplitude modulation in static samples. The concept of generalised adiabatic sweeps through the resonance conditions by slow parameter variations is introduced as a means to increase robustness and effectiveness of modulated pulsed DNP sequences. All theoretical considerations and semi-numerical results are underpinned with experimental data acquired at low field and frequencies ($0.35\,\text{T}/9.5\,\text{GHz}/15\,\text{MHz}$) with a sample of OX063 trityl in a standard solvent used for DNP (glycerol-d_8:D_2O:H_2O, 6:3:1 by volume) at 80 K.

ZUSAMMENFASSUNG

Die Elektronenspinresonanz (engl. electron spin resonance, ESR) ist eine nützliche Methode zur Untersuchung paramagnetischer chemischer Systeme, wie z.B. Radikale, Übergangsmetallkomplexe und Metalloenzyme. Sie kann Informationen über die geometrische und elektronische Struktur liefern, indem mit ihr Wechselwirkungen (sog. Kopplungen) zwischen verschiedenen Spins gemessen werden. Elektron-Kern Distanzen und lokale Spindichten können aus Hyperfeinkopplungen abgeleitet werden, und schwache dipolare Kopplungen zwischen ungepaarten Elektronen geben Auskunft über Elektron-Elektron Wechselwirkungen. Starke Elektron-Elektron Interaktionen auf dem selben oder auf naheliegenden Metallzentren hängen von subtilen Details der elektronischen Struktur ab.

Bis vor einigen Jahren wurden in der Puls ESR Spektroskopie nur monochromatische Pulse mit konstanter Amplitude verwendet. Dies änderte sich mit der kommerziellen Verfügbarkeit von schnellen Arbiträr-Funktionsgeneratoren (engl. Arbitrary Waveform Generator, AWG), die es erlauben, beliebig geformte Pulse im Mikrowellenbereich zu generieren. Diese Arbeit erforscht die Möglichkeiten, die sich aus dieser vorher nie dagewesenen Kontrolle über Elektronenspins ergeben.

Kapitel 2 führt die Zirpenecho ESR-detektierte Kernspinresonanz ein (engl. Chirp Echo Epr SpectroscopY (CHEESY)-detected NMR). Diese Sequenz kombiniert Lochbrennpulse mit breitbandigen Zirpenechos und kann zur Messung von Hyperfeinkopplungen zwischen Elektronenspins und naheliegenden Kernspins verwendet werden. Sie ist mit der Elektronendoppelresonanz-detektierten Kernspinresonanz (engl. ELDOR-detected NMR, EDNMR) verwandt, verfügt aber über einen Multiplexvorteil, weil alle Kernfrequenzen gleichzeitig detektiert werden können. Die Methode wird in dieser Arbeit zu einer zweidimensionalen Version erweitert, indem ein zusätzlicher, selektiver Inversionspuls verwendet wird. Dieser erlaubt es, sog. Hyperfeinsublevelkorrelationsspektren (engl. HYSCORE) zu messen. Das verbessert die Auflösung und erleichtert die Signalzuweisung.

Kapitel 3 beschreibt die Beobachtung von Antilöchern (also Signalverstärkungen) in der Elektronendoppelresonanz-detektierten Kernspinresonanz, angewendet auf Austausch-gekoppelte Cu(II)-Porphyrindimere. Ein Algorithmus wird vorgestellt, der EDNMR Spektren von beliebigen Spinsystemen simulieren kann. Zusammen mit Feld-korrelierten Ultrabreitband (engl.

ultra-wide band, UWB) EDNMR Spektren erlaubt dies die Bestimmung der Nullfeldaufspaltung (engl. Zero-field splitting) in der $S = 1$ Mannigfaltigkeit der zwei gekoppelten ungepaarten Elektronen. Zusätzlich wird gezeigt, dass die EDNMR Auflösung gut genug ist, um die ^{63}Cu und ^{65}Cu Isotope in einem Cu(II)-Porphyrindimer mit schwacher Austauschkopplung zu unterscheiden, und um die Kernquadrupolkopplung des Kupfers zu bestimmen.

Kapitel 4 führt die phasenmodulierte "bekleidete" (engl. dressed) Spinresonanz zur Distanzmessung zwischen Radikalen mit schmalen Linien ein, wie z.B. Tritylen. Eine auf einer Spinsperre (engl. spinlock) basierende Sequenz wird verwendet, um den Elektronenspin von den Kernspins in der Umgebung zu entkoppeln, was die Relaxationszeiten dramatisch verlängert. Kurze, sinusförmige Phasenmodulationsimpulse, bei denen die Phasenmodulationsfrequenz mit der Rabifrequenz des Pulses übereinstimmt, werden verwendet, um die Elektronenspins im bekleideten Koordinatensystem zu kontrollieren, also während der Mikrowelleneinstrahlung. Konzeptionelle und technische Probleme bezüglich der Relaxationszeiten im rotierenden Koordinatensystem sowie der limitierten Mikrowellenleistung werden diskutiert.

Kapitel 5 führt eine allgemeine Beschreibung zum Verständnis gepulster dynamischer Kernpolarisationssequenzen (engl. dynamic nuclear polarisation, DNP) mit beliebiger Phasen- und Amplitudenmodulation in statischen Proben ein. Das Konzept verallgemeinerter adiabatischer Feger (engl. sweep) durch eine Resonanzbedingung mit Hilfe langsamer Veränderung der Parameter wir eingeführt. Dies kann die Robustheit und Effektivität der modulierten DNP Sequenzen verbessern. Alle theoretischen Überlegungen und semi-numerischen Resultate werden mit experimentellen Daten untermauert, die bei tiefen Felder und Frequenzen (0.35 T/9.5 GHz/15 MHz) mit einer OX063 Tritylprobe in einem Standardlösungsmittel für DNP (Glycerol-d$_8$:D$_2$O:H$_2$O, 6:3:1 Vol.) gemessen wurden.

ZÄMÄFASSIG

D Elektronäspinresonanz (ESR) isch es mächtigs Wärchzüg, wo mä cha bruchä für paramagnetischi chemischi System zungersuächä, z.B. Radikau, Übergangsmetaukomplex und Metalloenzym. Si cha informationä lifärä über die geometrischi und elektronischi Struktur, idäm mä d Kopplig zwüschä vrschidänä Spins bestimmt. Us Hyperfinkoppligä zwüschä Elektronä- und Chärnspins chamä Elektron-Chärndistanzä und lokali Spindichtinä ableitä, und schwachi Elektron-Elektron Koppligä chamä bruchä für Distanzmässigä zwüschä unpaartä Elektronä. Starchi Elektron-Elektron Koppligä ufem gliichä oder nächä Metauzenträ hangä vo dä kompliziärtä Details vor elektronischä Struktur ab.

Bis vor churzem het mä ir Puls ESR numä monochromatischi Püls mit konstanter sterchi brucht. Ds het sech gändert, wo schnäui AWGs (ängl. arbitrary waveform generator) kommerziell erhäutlech si wordä, wos erloubä, beliäbig gshapeti Pulsä im Mikrowäuäberiich z generiärä. Diä Arbeit hiä erforscht d Möglechkeitä wo sech drus ergäbä, das mä iz ä Kontrollä über Elektronäspins het, wo früächer nid müglech isch gsi.

Kapitu 2 füährt di Chirp Echo EPR-dedektiärti NMR (ängl. CHEESY-detected NMR) ii. Diä Sequänz kombinärt Lochbrönnpüls mit breidbandigä Chirp Echos, u cha brucht wärdä für d Detektion vo Hyperfinkoppligä zwüschä Elektronäspins und Chärnspins ir Umgäbig. Si isch vrwandt mit dr ELDOR-detektiärtä NMR (EDNMR), biätät aber ä Multiplexvorteil, wüu aui Chärnfrequänzä gliichzytig chöi dedektiärt wärdä. D Methodä wird zunärä zwöidimensionalä Version erwiteret, idäm mä ä zuäsätzlechä, selektivä Inversionspuls zuäfüägt. Ds ermüglecht d Ufnahm vo HYSCORE-artigä Spekträ, was d Uflösig vrbesseret u z Assignment vreifacht.

Kapitu 3 beschribt d Beobachtig vo Antilöcher (auso Signauvrsterchigä) in EDNMR spekträ vo ustuschkopplätä Cu(II)-porphyrindimer. Än Algorithmus wird iigfüährt, wo EDNMR Spekträ vo beliäbigä Spinsystem cha simuliärä. Zämä mit Fäudkorreliärtä ultrabreitband (ängl. ultra-wide band, UWB) EDNMR spekträ erloubt ds, das mä d Nullfäudufspautig (ängl. zero-field splitting, ZFS) im $S = 1$ Subsystem vo dä zwöi kopplätä unpaartä Elektronä cha bestimmä. Zuäsätzlech isch es im nä Dimer mit schwacher Ustuschwächsuwirkig möglech gsi, ^{63}Cu und ^{65}Cu Isotop z ungerschiedä, und d Quadrupolkopplig vom Chupfer ufzlösä.

Kapitu 4 füährt Dressed Spin Resonanz mit phasämodulation ii aus ä Möglechkeit für Distanzmässigä zwüschä Radikau mit schmalä Liniä, z.B. Trityl. Ä Spinlock Sequänz wird brucht, um dr Elektronäspin vo dä umgäbendä Chärnspins z enkopplä. Ds vrlengeret d Relaxationszytä dramatisch. Churzi Impulse vo sinusförmiger Phasämodulation, wo d Modulationsfrequänz dr Rabifrequänz vom Spinlock entspricht, cha brucht wärdä, für d Elektronäspins im glocktä Frame z kontrolliärä, auso während dr Mikrowäuäiistrahlig. Konzeptionelli und technischi Problem bezüglech dä Relaxationszytä im rotating Frame und dr limitärtä Mikrowäuäpower wärdä o diskutiert.

Kapitu 5 beschribt es augemeins Framework fürds Vrständnis vo pulste dynamische Chärnpolarisationssequänzä (ängl. dynamic nuclear polarisation, DNP) mit beliäbiger Phasä- und Amplitudämodulation in statischä Probä. Ds Konzept vo vraugemeineretä adiabatischä Sweeps mit Hiuf vo langsamä Vränderigä vo dä Sequänzparameter wird iigfüährt. Ds vrbesseret d Robustheit und Effektivität vo dä moduliertä DNP Sequänzä. Aui theoretischä Überlegigä und di semi-numerischä Resultat wärdä experimentell ungermuuret, und zwar bi töifem Fäud u töifä Frequänzä (0.35 T/9.5 GHz/15 MHz), mitärä Prob vo OX063 Trityl im nä Standardlösigsmittu für DNP (Glycerol-d$_8$:D$_2$O:H$_2$O, 6:3:1 Vol.).

CONTENTS

LIST OF FIGURES

NOTATION

AM	Amplitude modulation
AWG	Arbitrary waveform generator
CE	Cross effect
CHEESY	Chirp-echo EPR spectroscopy
DEER	Double electron-electron resonance
DNP	Dynamic nuclear polarisation
DQC	Double-quantum coherence
EDNMR	ELDOR-detected NMR
ELDOR	Electron double resonance
ENDOR	Electron-nuclear double resonance
EPR	Electron paramagnetic resonance
ESEEM	Electron spin echo envelope modulation
ESR	Electron spin resonance
FID	Free induction decay
FM	Frequency modulation
FT	Fourier transform
HTA	High turning angle
HYSCORE	Hyperfine sublevel correlation
IFT	Interaction frame transformation
MW	microwave
NMR	Nuclear magnetic resonance
OE	Overhauser effect
PDS	Pulsed dipolar spectroscopy
PM	Phase modulation
RF	Radio-frequency
RIDME	Relaxation-induced dipolar modulation enhancement

SE   Solid effect
TWT   Travelling wave tube
UWB   Ultra-wide band
ZFS   Zero-field splitting

FREQUENTLY USED SYMBOLS

Note: For mathematical derivations, all frequencies are given in angular frequencies, denoted with an "ω". Experimental data and determined constants on the other hand, are given in linear frequency units $\nu = \omega/2\pi$.

$\hat{\mathcal{H}}$	Hamiltonian
$\vec{\mu}_{\mathrm{e}}$	Electron magnetic moment
μ_{B}	Bohr magneton
μ_{n}	Nuclear magneton
h	Planck constant
$\hbar$	Reduced Planck constant, $h/2\pi$
μ_0	Vacuum permeability
k_{B}	Boltzmann constant
g	g-value
g_{e}	g-value of the free electron
g_{n}	g-value of a nuclear spin
g	g-matrix
γ_{e}	Gyromagnetic ratio of the electron
γ_{n}	Gyromagnetic ratio of a nucleus
ω_S	Electron Zeeman frequency
ω_{mw}	Microwave frequency
ω_1	Electron Rabi-/nutation frequency
Ω_S	Electron offset
ω_I	Nuclear Zeeman frequency
ω_{rf}	Radio-frequency
ω_0	Resonance frequency
$\vec{B}$	Magnetic field (more precise: magnetic induction)
B_0	External, strong magnetic field along z
S, m_S	Electron spin quantum number and corresponding z-projection
$\vec{\hat{S}}$	Electron spin angular momentum operator
I, m_I	Nuclear spin quantum number and corresponding z-projection
$\vec{\hat{I}}$	Nuclear spin angular momentum operator

$\mathbf{D}_{\mathrm{ZFS}}$	Zero-field splitting tensor
D, E	Axial and rhombic zero-field splitting constants
$\mathbf{D}$	Dipole-dipole interaction matrix
ω_{dd}	Dipolar frequency
d	Dipole-dipole coupling constant
r	Distance
$\mathbf{A}$	Hyperfine coupling interaction matrix
a_{iso}	Isotropic hyperfine coupling constant
$\mathbf{T}$	Anisotropic hyperfine coupling tensor
A and B	Secular and pseudosecular hyperfine coupling constant
$\mathbf{P}$	Quadrupole coupling tensor
$|\Psi\rangle$	Total wave function
$|\psi_n\rangle$	Eigenfunction of $\hat{\mathcal{H}}$
$\hat{\rho}$	Density operator
$\hat{\sigma}$	Reduced density operator
$\hat{U}$	Propagator
T_1	Longitudinal relaxation time
$T_{1,\mathrm{e}}$	Longitudinal relaxation time of the electron
$T_{1,\mathrm{n}}$	Longitudinal relaxation time of a nucleus
T_2	Transverse relaxation time
T_{m}	Phase memory time

PREFACE

Nowadays, everything has to be a "story". Every paper has to contain one main message, side notes usually get lost. At conferences and meetings, every presentation should have a single take-home message. After all, there are several talks before and after, and there is only so much coffee can do.

It makes sense to communicate effectively. There is no point in giving a talk, or writing a book, if nobody remembers what you wanted to say. However, in science[1], storytelling can give a completely skewed view on how things actually developed, and what the motives were of the people involved. Additionally, it requires the author to know what is important. This is not always the case, especially in science.

Conducting science is mostly rather messy. There is nothing scientific in the generation of scientific ideas. It's luck, inspiration, conversations, curiosity, wrong analogies that turn out to have some truth to them after all. And lots and lots and lots of serendipity. This part of science is a deeply *creative* process. With no rules, and no right and wrong.

What we colloquially call "science", is what comes afterwards. Careful analysis, painful dissection of arguments, slow and labour-intensive data gathering, reproduction of results, *etc.* However, there is no scientific way of telling *what should be investigated in the first place*. A point that the metrics-focused "new public management" just completely ignores.

This thesis contains most of the work conducted during 4.5 years of a PhD. Some of the chapters in this thesis seem rather disconnected from others. That is because we are used to thinking in terms of a *purpose*. We *walk*, because we want to *get somewhere*, we have a predefined aim. This work is more an act or *roaming* and *exploration.*

It's unlikely but not impossible that research in this thesis will help to save the world. It could be used to investigate and design catalysts and materials that help with CO_2 reduction in the atmosphere. Or they might help to investigate and treat neuro-degenerative diseases such as Alzheimer's or Parkinson's. There are definitely some scientists whos genuine purpose is

---

1 unfortunately, just as much in history.

to solve these problems, and there is no question if this is a "valid" motivation. But it was not *my* motivation.

I was simply *curious*. I am completely amazed by the fact that we can use something as complicated and abstract like an electron spin, something that we cannot see, feel, or experience directly, to learn more about nature. How atoms and molecules are arranged, and how they behave. This work contains relatively abstract and complicated maths, describing electronic and nuclear spins as a set of quantised states that somehow interact with each other and with external magnetic fields. But then you also "see" that these rather wild and abstruse descriptions make sense! I see signals acquired by our electronics, and these signals behave just as expected[2]. And although humanity has been working on magnetic resonance for over 75 years, we still find ways to communicate more effectively with our little spies, the spins. We get more information out, we get the information faster and faster, and we need less and less material to do so.

From that perspective, this thesis is completely coherent (pun intended). I explored connected regions in uncharted territory with a new tool for observations, namely a fast arbitrary waveform generator (AWG). This electronic instrument allows for unprecedented control of our communication with electron spins.

You cannot plan to discover something, but you can still wander around. And it makes sense for a society to have some people wandering around. It makes sense even under the common neo-liberal narrative. And it makes sense even if they do not find the land of milk and honey.

So let me take you take you to the land of ice, magnetic fields, noise, and pulsed microwaves...

---

[2] sometimes

INTRODUCTION

Wett nid wosch dass d miuch suur wird, de lasch sä gschider idr chuä.

If you don't want the milk to spoil, you'd better leave it in the cow. (Translation mine).

— Herr Fluehmann (Büne Huber)

1.1 GENERAL INTRODUCTION

Today, chemistry and its related disciplines, like biochemistry, molecular biology, chemical physics etc., rely heavily on analytical tools. This is an obvious necessity, because the central entity — atoms and molecules — cannot be observed directly with the human senses. Chemical thinking and discussions always surround representations of molecules, and it is a central pillar of science that the hypotheses generated in this way have to be tested at some point. Usually, this means that the chemical entities that we represent on a chalkboard have to be *observed*. Without the means to do so, directly or indirectly, chemistry stays alchemy. Historically, there were many clever ways of indirectly deducing chemical structures by running many different reactions. Modern chemistry, on the other hand, is characterized by a plethora of methods to "directly" observe structures[1].

It is beyond the scope of this work to give a comprehensive overview of methods for structure determination. Important in the context of this work is the fact that nuclear magnetic resonance (NMR), one of the most important analytical techniques in modern chemistry, often fails in the presence of unpaired electrons. These systems are somewhat unusual, but they are also associated with increased reactivity, which makes them interesting for chemists. Fortunately, electron spin resonance (ESR) was developed over the last nearly eight decades, exactly for the study of compounds with unpaired electrons.

---

1 The quotes are meant for philosophical purists

1.1.1 *A very short primer on ESR*

Electron spin resonance makes use of a peculiar property of electrons, their *spin.* This is a purely quantum mechanical phenomenon, although it bares some physical similarities with "actual" rotations. Together with the charge of the electron, the spin lets it behave like a small bar magnet, a *magnetic dipole.* In the presence of an external magnetic field the magnetic moments of all the unpaired electrons in a sample arrange parallel to said field[2]. Electromagnetic irradiation of the right frequency, the *resonance frequency*, can be used to excite the spins, meaning that they are then not aligned with the external field any more. The resonance frequency is proportional to the strength of the magnetic field. In practice, magnetic field strengths are used that correspond to resonance frequencies in the microwave region.

Once the electron spins are not aligned with the external field, they start to rotate around it. The technical term for this is *precession*. The rotating magnetic moments generate a signal that can be measured in a spectrometer.

If all unpaired electrons gave the same signal, ESR would be a curiosity, not an analytical tool. It turns out that the exact resonance frequency of each electron depends on its local environment, i. e. the chemical structure around it. The unpaired electron interacts with other electrons and with the nuclear spins. These interactions give us *chemical information.*

This thesis is less concerned with *what chemical information* we can get and how we can make use of it, but more with *how* we can get it in the first place.

1.1.2 *ESR vs. EPR*

The terms electron spin resonance (ESR) and electron paramagnetic resonance (EPR) are used interchangeably. The latter is slightly more accurate because the spin and the orbital angular momentum of electrons are mixed in general. Both terms are used interchangeably in this work.

1.1.3 *Applications of EPR spectroscopy*

As mentioned before, ESR can be used to study systems with unpaired electrons. This subsection shall give a very brief overview.

---

2 This is not entirely correct, but still illustrative

RADICALS   Radicals, i.e. organic compounds with unpaired electrons, are usually encountered as *intermediates* in some chemical reactions. They can sometimes be observed directly, or they can be trapped, and the longer lived adducts can be investigated. Knowing the structure of intermediates is a prerequisite to understanding the *mechanism* of a chemical reaction. Some stable radicals can be used as spin labels, *vide infra*.

PARAMAGNETIC METAL COMPLEXES   Transition metal complexes can have one or more unpaired electrons. EPR can be used to determine the spin state of these compounds and the nature and arrangement of the ligands. These complexes are abundant in inorganic chemistry, but also in the active sites of many enzymes. The investigation of paramagnetic transition metal catalysts is among the most important applications of EPR.

PHOTO-EXCITED STATES   Light irradiation can excite some diamagnetic systems into states with a net spin, usually into triplet states for a short amount of time. EPR can then be used to investigate these transient species.

DEFECT SITES   Defect sites in crystalline systems can be paramagnetic as well. The most important member of this class is probably the nitrogen-vacancy (NV)-centre in diamond. The spin state of this defect can be initialized and read out optically, allowing for single-spin sensitivity.

SPIN LABELLING   Most matter is diamagnetic. But many systems, especially biomacromolecules, can be *spin labelled*. For this, one or more stable radicals, usually nitroxides, are attached to it. EPR can give information about the rotational mobility of the label. Additionally, distances and distance distributions between two labels can be determined in the range of about 2–8 nm. This is useful for structural biology, especially in cases where X-ray crystallography, NMR and cryo-EM cannot provide all necessary information.

1.2   THEORY

This section introduces important terms and concepts needed to understand the results in this work. It is all "textbook knowledge", that can be found, for example, in [1, 2]. A basic understanding of quantum mechanics and magnetic resonance is assumed. Symbols and natural constants are described in Table 2. Some parts are repeated in individual chapters, because first, repetition legitimises, and second, the chapters can then be read isolated from the rest of the thesis.

1.2.1   EPR Spin Hamiltonian

In general, the Hamiltonian, the possible states, and the energies of a molecular system depend on all positions, momenta and all spin degrees of freedom of all electrons and all nuclei. While maybe desirable, it is completely unfeasible to discuss magnetic resonance experiments directly with the full, relativistic form of the Schrödinger equation, i.e. the Dirac equation. Instead, we usually use a spin Hamiltonian [1, 3].

If a multiplet, usually the ground state, is sufficiently separated from the other multiplets, for magnetic resonance experiments, we can only look at the states within this multiplet. We can set up a phenomenological Hamiltonian that contains different terms with different powers of the external magnetic field and the magnetic moments of the particles. In principle, one can then fit the polynomial parameters to the true energies. We call this the *spin* Hamiltonian, because apart from these parameters, it only depends on the spin coordinates of the system. The number of states is then finite and can be calculated from the spin quantum numbers of the electrons and nuclei.

Unfortunately, the literature is of mixed rigour when looking at how the spin Hamiltonian parameters relate to first principles. However, it is noted here that all parameters listed below *can*, in principle, be derived and calculated from first principles, at least to second order in the fields and magnetic moments. Of course, actually calculating the parameters numerically is inevitably only possible with many approximations for most systems [4].

Note that the assumption of a "sufficiently separated multiplet" is fulfilled for all systems investigated in this work, but it *can* break down. For example, in the case of heavy elements with very strong spin-orbit coupling, or in transition metal complexes with orbitally degenerate or nearly-degenerate states.

The terms in the spin Hamiltonian can be classified into spin-field and spin-spin interactions, where the spins are either electron spins or nuclear spins:

$$\hat{\mathcal{H}}_0 = \hat{\mathcal{H}}_{\mathrm{EZ}} + \hat{\mathcal{H}}_{\mathrm{ZFS}} + \hat{\mathcal{H}}_{\mathrm{EE}} + \hat{\mathcal{H}}_{\mathrm{HF}} + \hat{\mathcal{H}}_{\mathrm{NZ}} + \hat{\mathcal{H}}_{\mathrm{NQI}} + \hat{\mathcal{H}}_{\mathrm{NN}} \qquad . \quad (1.1)$$

All of these terms are discussed in the following. Note that all Hamiltonians are expressed in angular frequency units throughout this work.

1.2.1.1 Electron Zeeman interaction $\hat{\mathcal{H}}_{\mathrm{EZ}}$

The electron Zeeman term $\hat{\mathcal{H}}_{\mathrm{EZ}}$ describes the interaction of the electron magnetic moment

$$\vec{\mu}_{\mathrm{e}} = -\frac{\mu_{\mathrm{B}}\mathbf{g}}{\hbar}\vec{S} \qquad , \qquad (1.2)$$

with an external magnetic field $\vec{B}$. It is given by

$$\hat{\mathcal{H}}_{\mathrm{EZ}} = \frac{\mu_{\mathrm{B}}}{\hbar}\vec{B}^{\mathrm{T}}\mathbf{g}\hat{\vec{S}} \qquad . \qquad (1.3)$$

The interaction is parametrised by the $\mathbf{g}$-matrix [5]. Briefly speaking, the g-factor differs from the free electron value g_{e} due to spin-orbit coupling in excited states. The deviation from g_{e} is smaller in organic radicals compared to transition metal complexes. In general, $\mathbf{g}$ is anisotropic, and it reflects the local symmetry of the site where the electron is "situated". For example, the $\mathbf{g}$-matrix in axially symmetric Cu(II) complexes exhibits axial symmetry as well.

The quantity

$$\gamma_{\mathrm{e}} = -\frac{\mu_{\mathrm{B}}g_{\mathrm{e}}}{\hbar} \qquad (1.4)$$

is called the *gyromagnetic ratio*, and amounts to about $\gamma_{\mathrm{e}}/2\pi \approx -28\,\mathrm{GHz\,T^{-1}}$. For a field with strength B_0 along z and an isotropic g-factor, we can then also write

$$\hat{\mathcal{H}}_{\mathrm{EZ}} = -\gamma_{\mathrm{e}}B_0\hat{S}_z = \omega_S\hat{S}_z \qquad . \qquad (1.5)$$

1.2.1.2 Zero-field splitting $\hat{\mathcal{H}}_{\mathrm{ZFS}}$

If several unpaired electrons are strongly coupled, there exist several manifolds with different spin quantum number S. For example, two strongly coupled electrons can be described by a singlet ($S = 0$) and three triplet ($S = 1$) states. Another example is Mn(II), with five unpaired electrons. In this case,

the $S = 5/2$ manifold is the only one that has to be considered to discuss EPR spectra. The six m_S levels of this manifold are split up even in zero field, due to spin-orbit and spin-spin (dipolar) interactions. Together, the splitting can be described by [6]

$$\hat{\mathcal{H}}_{\mathrm{ZFS}} = \vec{\hat{S}}^{\mathrm{T}} \mathbf{D}_{\mathrm{ZFS}} \vec{\hat{S}} \qquad . \tag{1.6}$$

The zero-field splitting tensor $\mathbf{D}$ is usually parametrised in its principal axis frame as

$$\mathbf{D}_{\mathrm{ZFS}} = \begin{pmatrix} D_x & & \\ & D_y & \\ & & D_z \end{pmatrix} = \begin{pmatrix} -\frac{1}{3}D + E & & \\ & -\frac{1}{3}D - E & \\ & & \frac{2}{3}D \end{pmatrix} \tag{1.7}$$

The axes are defined such that $|D_x| \leq |D_y| \leq |D_z|$, which implies $|E| \leq |D/3|$.

The zero-field splitting is formally analogous to the nuclear quadrupole interaction. For half-integer spin quantum numbers, so-called *Kramers* systems, there is always a *central transition* ($m_S = -1/2 \rightarrow m_S = 1/2$), which is not affected by the ZFS to first order.

The magnitude of the ZFS can exceed the one of the electron Zeeman interaction. In the case of low symmetry and integer spin quantum number (*non-Kramers*), it is possible that the lowest frequency EPR transition is still much larger than the available microwave frequency. These systems are *effectively EPR-silent*, although they can be investigated by specialised high-frequency EPR spectrometers. In the case of large ZFS and half-integer spin, one can often use an *effective g*-value, describing the two lowest lying levels as a $S' = 1/2$ system. In this case, the absolute values of D and E cannot be determined, only the ratio D/E can be extracted.

1.2.1.3   *Electron-electron interaction $\hat{\mathcal{H}}_{\mathrm{EE}}$*

Two weakly interacting electron spins are best described in an uncoupled representation. There are two mechanisms of electron-electron interaction, the Heisenberg exchange interaction, or *J*-coupling, $\hat{\mathcal{H}}_{\mathrm{J}}$ and the through-space dipole-dipole coupling $\hat{\mathcal{H}}_{\mathrm{dd}}$,

$$\hat{\mathcal{H}}_{\mathrm{EE}} = \hat{\mathcal{H}}_{\mathrm{J}} + \hat{\mathcal{H}}_{\mathrm{dd}} \qquad . \tag{1.8}$$

The exchange interaction is essentially due to orbital overlap, in general it can be written as

$$\hat{\mathcal{H}}_{\mathrm{J}} = \vec{\hat{S}}_1^{\mathrm{T}} \mathbf{J} \vec{\hat{S}}_2 \qquad , \tag{1.9}$$

although very often only the isotropic part is considered. In this case, the tensor $\mathbf{J}$ can be replaced by a single scalar coupling constant J.

The electron-electron dipole-dipole coupling can be derived from the classical interaction of two magnetic dipoles, and is given by

$$\hat{\mathcal{H}}_{dd} = \frac{1}{r^3} \frac{\mu_0}{4\pi\hbar} g_1 g_2 \mu_B^2 \left[\vec{\hat{S}}_1^T \vec{\hat{S}}_2 - \frac{3}{r^2} \left(\vec{\hat{S}}_1^T \vec{r} \right) \left(\vec{\hat{S}}_2^T \vec{r} \right) \right] \qquad , \qquad (1.10)$$

where r is the distance between the electrons.

At high fields and with moderate g-anisotropy, we can assume parallel magnetic moments, and rewrite the dipolar interaction as

$$\hat{\mathcal{H}}_{dd} = \vec{\hat{S}}_1^T \mathbf{D} \vec{\hat{S}}_2 = \omega_{dd} \left(\hat{S}_{1z}\hat{S}_{2z} - \frac{1}{2} \left(\hat{S}_{1x}\hat{S}_{2x} + \hat{S}_{1y}\hat{S}_{2y} \right) \right) \qquad , \qquad (1.11)$$

with

$$\mathbf{D} = \begin{pmatrix} -\frac{1}{2}\omega_{dd} & & \\ & -\frac{1}{2}\omega_{dd} & \\ & & \omega_{dd} \end{pmatrix} \qquad (1.12)$$

and

$$\omega_{dd} = \frac{\mu_0}{4\pi} \frac{\mu_B^2 g_1 g_2}{\hbar} \frac{1}{r_{12}^3} \left(1 - 3\cos^2\theta \right) \qquad . \qquad (1.13)$$

The angle θ describes the angle between the external magnetic field and the inter-electron vector. The orientation-independent factor in this coupling constant, sometimes termed d, amounts to

$$d = \frac{1}{2\pi} \frac{\mu_0}{4\pi} \frac{\mu_B^2 g^2}{\hbar} \frac{1}{r^3} \qquad . \qquad (1.14)$$

which is $\approx 52.04\,\text{MHz}$ for $r = 1\,\text{nm}$ and $g = g_e$.

The dipole-dipole coupling is the decisive interaction that enables spin-based distance measurements.

1.2.1.4   *Hyperfine coupling $\hat{\mathcal{H}}_{HF}$*

The interaction between electron spins and nuclear spins is collected in the term [7]

$$\hat{\mathcal{H}}_{HF} = \vec{\hat{S}}^T \mathbf{A} \vec{\hat{I}} \qquad , \qquad (1.15)$$

with the hyperfine interaction matrix $\mathbf{A}$. The coupling is ultimately always due to the dipole-dipole coupling [4], but since there can also be a finite spin-density at the position of the nucleus, we can separate the contributions into an isotropic and an anisotropic part

$$\mathbf{A} = a_{\text{iso}}\mathbb{1} + \mathbf{T} \qquad . \tag{1.16}$$

The isotropic part a_{iso} is often called the Fermi-contact term. It is proportional to the spin density at the nucleus.

Often, the hyperfine coupling is much smaller than the electron Zeeman interaction, but of a similar magnitude as the nuclear Zeeman interaction. In this case, the high-field approximation can be used with respect to the electron spin. What remains is often written as

$$\hat{\mathcal{H}}'_{\text{HF}} = A\hat{S}_z\hat{I}_z + B\hat{S}_z\hat{I}_{x'} \qquad , \tag{1.17}$$

with $A = A_{zz}$ and $B = \sqrt{A_{zx}^2 + A_{zy}^2}$. The A and B terms are called *secular* and *pseudo-secular* hyperfine coupling, respectively. In the point-dipole approximation, we can write

$$T = \frac{\mu_0}{4\pi\hbar}g_e\mu_B g_n\mu_n r_{\text{eN}}^{-3} \tag{1.18}$$

$$A = a_{\text{iso}} + T(3\cos(\theta)^2 - 1) \tag{1.19}$$

$$B = 3T\cos(\theta)\sin(\theta) \qquad . \tag{1.20}$$

It is worth noting that the pseudo-secular B-term has no isotropic contribution, i.e. it vanishes under fast tumbling. Additionally, it is zero along the principal axes of the dipolar frame, i.e. if $\theta = 0, \pi$ or $\theta = \pm\pi/2$.

1.2.1.5 *Nuclear Zeeman interaction* $\hat{\mathcal{H}}_{\text{NZ}}$

Analogous to the electron Zeeman interaction, this term describes the interaction of the nuclear magnetic moments with the external magnetic field

$$\hat{\mathcal{H}}_{\text{NZ}} = -\frac{\mu_n g_n}{\hbar}\vec{B}^{\text{T}}\vec{\hat{I}} \qquad . \tag{1.21}$$

(Note the sign convention, which is opposite to the electron case).

The nuclear g_n-value is a constant that depends only on the isotope. As is well-known from NMR, in principle, the chemical environment slightly changes the resonance frequency. A phenomenon known as *chemical shift*. This effect is usually too small to be resolved in EPR experiments.

Similar to the electron Zeeman interaction, we can also define a nuclear gyromagnetic ratio

$$\gamma_{\mathrm{n}} = \frac{\mu_{\mathrm{n}} g_{\mathrm{n}}}{\hbar} \qquad , \qquad (1.22)$$

and again assuming a field B_0 along z

$$\hat{\mathcal{H}}_{\mathrm{NZ}} = -\gamma_{\mathrm{n}} B_0 \hat{I}_z = \omega_I \hat{I}_z \qquad . \qquad (1.23)$$

1.2.1.6   Nuclear quadrupole interaction $\hat{\mathcal{H}}_{\mathrm{NQI}}$

Partially adapted from [8]. The nuclear quadrupole coupling describes the interaction between the electric nuclear quadrupole moment with the electric field gradient at the position of the nucleus [9]. Only nuclei with a spin quantum number $I \geq 1$ exhibit such a nuclear quadrupole moment[3]. Although it is a purely electrostatic interaction, it shows up in the spin Hamiltonian as an interaction of the nuclear magnetic moment with itself. Roughly speaking, this can be understood because the electric field gradient acting on the electric quadrupole moment of the nucleus leads to a torque, which acts on the nuclear angular momentum.

Mathematically, the nuclear quadrupole interaction is described by the term

$$\hat{\mathcal{H}}_{\mathrm{NQI}} = \vec{I}\mathbf{P}\vec{I} \qquad , \qquad (1.24)$$

with the nuclear quadrupole tensor

$$\mathbf{P} = \begin{pmatrix} P_x & 0 & 0 \\ 0 & P_y & 0 \\ 0 & 0 & P_z \end{pmatrix} = \begin{pmatrix} K(-1+\eta) & 0 & 0 \\ 0 & K(-1-\eta) & 0 \\ 0 & 0 & 2K \end{pmatrix} \qquad , \quad (1.25)$$

with

$$K = \frac{e^2 q Q/h}{4I(2I-1)} \qquad . \qquad (1.26)$$

The term $e^2 q Q/h$ is also known as the quadrupole coupling constant and is related to the electric field gradient at the position of the nucleus ($eq = V_{zz} = \partial^2 V/\partial z^2$). The nuclear quadrupole moment enters via the term eQ. The asymmetry parameter is given by $\eta = (V_{xx} - V_{yy})/V_{zz}$.

---

3 Note that nuclei also have excited states. For example, the ground state of ^{57}Fe is $I = 1/2$, but there are excited states with higher spin quantum numbers. The nuclear quadrupole interaction in these excited states is what can be observed with Mössbauer spectroscopy

1.2.1.7 *Nuclear-nuclear couplings* $\hat{\mathcal{H}}_{NN}$

Analogous to electron-electron exchange and dipolar couplings, there are also nuclear-nuclear exchange and dipolar couplings. Exchange couplings are isotropic, and between common nuclei they are usually much less than 1 kHz. The nuclear-nuclear dipolar coupling is formally the same as the electron-electron dipolar coupling, but the gyromagnetic ratios in the coupling constant should be replaced by the gyromagnetic ratios of the involved nuclei i and j,

$$\hat{\mathcal{H}}_{NN}^{(i,j)} = \omega_{dd}^{(i,j)} \left(\hat{I}_{iz}\hat{I}_{jz} - \frac{1}{2} \left(\hat{I}_{ix}\hat{I}_{jx} + \hat{I}_{iy}\hat{I}_{jy} \right) \right) \tag{1.27}$$

with

$$\omega_{dd}^{(i,j)} = \frac{\mu_0}{4\pi} \frac{\mu_n^2 g_{n,i} g_{n,j}}{\hbar} \frac{1}{r_{ij}^3} \left(1 - 3\cos_{ij}^2 \theta \right) \qquad . \tag{1.28}$$

The coupling between two protons at a distance of 1 Å is about 120 kHz. Because it is so small, it is usually neglected in the discussion of EPR experiments. However, it is the driver of nuclear spin diffusion. A phenomenon which is central to dynamic nuclear polarisation, and also usually the limiting factor in pulsed EPR-based distance measurements.

1.2.2 *Spin dynamics*

1.2.2.1 *Schrödinger equation*

Quantum mechanical systems obey the time-dependent Schrödinger equation

$$\frac{\mathrm{d}}{\mathrm{d}t} |\Psi\rangle = -i\hat{\mathcal{H}} |\Psi\rangle \qquad , \tag{1.29}$$

with the *wave function*, or *state* $|\Psi\rangle$. The eigenfunctions $|\psi_n\rangle$ and eigenvalues E_n of $\hat{\mathcal{H}}$ can be found with the time-independent Schrödinger equation

$$\hat{\mathcal{H}} |\psi_n\rangle = E_n |\psi_n\rangle \qquad . \tag{1.30}$$

The $|\psi_n\rangle$ form a convenient basis to describe an arbitrary state. i. e.

$$|\Psi\rangle = \sum_{n=1}^{N} c_n |\psi_n\rangle \qquad . \tag{1.31}$$

Because $\hat{\mathcal{H}}$ is Hermitian, eigenfunctions of different energies are orthogonal. Eigenfunctions of the same energy (degenerate) can always be chosen in such a way that they are mutually orthogonal.

1.2.2.2 *Expectation values and the density operator*

Expectation values of measurements can be expressed as expectation values of operators

$$\langle \hat{A} \rangle = \langle \Psi | \hat{A} | \Psi \rangle = \sum_{ij} c_i^* c_j \underbrace{\langle \psi_i | \hat{A} | \psi_j \rangle}_{A_{ij}} \quad , \tag{1.32}$$

where we assumed $\langle \Psi | \Psi \rangle = 1$. As seen from Equation (1.32), all information about expectation values is contained in the products $c_i^* c_j$. This motivates the definition of a *density operator*

$$\hat{\rho} = | \Psi \rangle \langle \Psi | = \sum_{ij} c_i c_j^* | \psi_i \rangle \langle \psi_j | \quad . \tag{1.33}$$

If we consider a single spin, or a *pure state*, the density operator contains the same information as the wave function, with the expectation value equal to

$$\langle \hat{A} \rangle = \sum_{ij} \underbrace{c_i^* c_j}_{\rho_{ji}} \underbrace{\langle \psi_i | \hat{A} | \psi_j \rangle}_{A_{ij}}$$

$$= \sum_{j} \left(\hat{\rho} \hat{A} \right)_{jj} = Tr \left\{ \hat{\rho} \hat{A} \right\} = Tr \left\{ \hat{A} \hat{\rho} \right\} \quad . \tag{1.34}$$

Note that the adjoint operation matters in the case of quadrature detection, which generates a complex observable, although artificially. The diagonal elements of $\hat{\rho}$ are given by $c_i c_i^* = |c_i|^2$, and correspond to the probability of finding the system in state i and are termed *populations*. The off-diagonal elements $c_{ij} = c_i c_j^*$ can only be non-zero if the system is in a coherent superposition of states. Thus, these elements in the density operator are called *coherences*.

The majority of magnetic resonance experiments is conducted on an *ensemble* of spins, not on single ones. Such ensembles cannot be described by a single wave function, but with a set of wave functions with corresponding probabilities. The same system can still be described by a single density operator

$$\hat{\rho} = \sum_{k} P_k | \psi_k \rangle \langle \psi_k | = \sum_{ij} \overline{c_i c_j^*} | \psi_i \rangle \langle \psi_j | \quad , \tag{1.35}$$

where the overbar represents an ensemble average.

1.2.2.3 *Liouville-von Neumann equation*

The equation of motion of the density operator can easily be derived from Equation (1.29)

$$\frac{\mathrm{d}}{\mathrm{d}t}\hat{\rho} = \frac{\mathrm{d}}{\mathrm{d}t}\left(|\Psi\rangle\langle\Psi|\right) = \left(\frac{\mathrm{d}}{\mathrm{d}t}|\Psi\rangle\right)\langle\Psi| + |\Psi\rangle\left(\frac{\mathrm{d}}{\mathrm{d}t}\langle\Psi|\right)$$

$$= -i\hat{\mathcal{H}}\underbrace{|\Psi\rangle\langle\Psi|}_{\hat{\rho}} + \underbrace{|\Psi\rangle\langle\Psi|}_{\hat{\rho}}i\hat{\mathcal{H}}^{\dagger} =$$

$$\frac{\mathrm{d}}{\mathrm{d}t}\hat{\rho} = -i\left[\hat{\mathcal{H}},\hat{\rho}\right] \qquad , \tag{1.36}$$

and is known as the *Liouville-von Neumann* equation.

A convenient property of the density operator formalism with respect to magnetic resonance is that both the Hamiltonians and the states (i. e. the density operator) can be expressed in terms of angular momentum operators. For a spin-1/2 system in an external magnetic field B_0 along z, we can write

$$\hat{\mathcal{H}} = -\gamma B_0 \hat{S}_z = \omega_0 \hat{S}_z \tag{1.37}$$

$$\hat{\rho} = c_{\mathbb{1}}\mathbb{1} + c_x\hat{S}_x + c_y\hat{S}_y + c_z\hat{S}_z \qquad , \tag{1.38}$$

where the part proportional to the unit operator is often left away, leading to a reduced density operator

$$\hat{\sigma} = \rho - c_{\mathbb{1}}\mathbb{1} \qquad . \tag{1.39}$$

The distinction between $\hat{\rho}$ and $\hat{\sigma}$ should be kept in mind. When in doubt if the part proportional to unity is important, $\hat{\rho}$ should be used. If we look at the equation of motion for our spin-1/2 system, we get

$$\frac{\mathrm{d}}{\mathrm{d}t}\hat{\sigma} = -i\left[\hat{\mathcal{H}},\hat{\sigma}\right]$$

$$\frac{\mathrm{d}}{\mathrm{d}t}\left(c_x\hat{S}_x + c_y\hat{S}_y + c_z\hat{S}_z\right) = -i\left[\omega_0\hat{S}_z, c_x\hat{S}_x + c_y\hat{S}_y + c_z\hat{S}_z\right] \qquad . \tag{1.40}$$

The angular momentum operators, by definition, fulfil the commutation rules

$$\left[\hat{S}_x, \hat{S}_y\right] = i\hat{S}_z$$

$$\left[\hat{S}_y, \hat{S}_z\right] = i\hat{S}_x$$

$$\left[\hat{S}_z, \hat{S}_x\right] = i\hat{S}_y \qquad . \tag{1.41}$$

Applied to Equation (1.40), we arrive at a set of equations in the coefficients

$$\frac{\mathrm{d}}{\mathrm{d}t}\begin{pmatrix} c_x \\ c_y \\ c_z \end{pmatrix} = \begin{pmatrix} 0 & \omega_0 & 0 \\ -\omega_0 & 0 & 0 \\ 0 & 0 & 0 \end{pmatrix}\begin{pmatrix} c_x \\ c_y \\ c_z \end{pmatrix}. \tag{1.42}$$

Since the magnetisation is proportional to the angular momentum, i.e.

$$\vec{M} \propto \gamma \vec{S} \quad , \tag{1.43}$$

Equation (1.42) is fully equivalent to the classical Bloch equations [10] (without relaxation). The latter, however, can only be used in case of an uncoupled spin-1/2, while the Liouville-von Neumann equation can describe arbitrary spin systems.

For a time-independent Hamiltonian $\hat{\mathcal{H}}$, the solution to Equation (1.36) is given by

$$\hat{\rho}(t) = \exp\left(-i\hat{\mathcal{H}}t\right)\hat{\rho}(0)\exp\left(i\hat{\mathcal{H}}t\right) \quad , \tag{1.44}$$

where we identify the *propagator*

$$\hat{U} = \exp\left(-i\hat{\mathcal{H}}t\right) \quad . \tag{1.45}$$

1.2.2.4 *Product operator formalism*

If an experiment can be described as a series of time-steps with time-independent Hamiltonians, Equation (1.44) can be applied repeatedly to analyze the spin dynamics. Even in the case of continuously time-dependent Hamiltonians, *time-slicing* with very short time steps can be used for numerical simulations. For analytical computations, it is good to know that Equation (1.44) can be solved relatively easily for systems with one or more spin 1/2, because there is only a finite set of spin operators. One can remember a set of rules, which are collectively known as the *product operator formalism* [11]. In short, the transformation

$$\hat{C} = \exp\left(-i\hat{B}\beta\right)\hat{A}\exp\left(i\hat{B}\beta\right) \tag{1.46}$$

is represented as

$$\hat{A} \xrightarrow{\beta\hat{B}} \hat{C} \tag{1.47}$$

and the solution is given by

$$
\hat{C} = \begin{cases} \hat{A} & \text{if } \left[\hat{A}, \hat{B}\right] = 0 \\ \cos\beta \cdot \hat{A} + \sin\beta \cdot i \left[\hat{A}, \hat{B}\right] & \text{else} \end{cases} \quad . \quad (1.48)
$$

These rules have very simple graphical representations. They can be visualised as rotations in three-dimensional subspaces spanned by the operators $\hat{A}$, $\hat{B}$, and $\hat{C}$.

1.2.2.5 *Equilibrium density operator*

In thermal equilibrium, the density operator is given by

$$
\hat{\rho}_{\text{eq}} = \frac{\exp\left(-\hbar\hat{\mathcal{H}}/k_{\text{B}}T\right)}{Z} \quad , \quad (1.49)
$$

where Z is the partition function

$$
Z = Tr\left\{\exp\left(-\hbar\hat{\mathcal{H}}/k_{\text{B}}T\right)\right\} \quad . \quad (1.50)
$$

At high temperatures, i. e. if the largest difference between two energy levels is much smaller than $k_{\text{B}}T$, we can approximate the exponential by a Taylor series truncated after the linear term

$$
\begin{aligned}
\hat{\rho}_{\text{eq}} &\approx \frac{\mathbb{1} - \hbar\hat{\mathcal{H}}/k_{\text{B}}T}{Tr\left\{\mathbb{1} - \hbar\hat{\mathcal{H}}/k_{\text{B}}T\right\}} \\
&\approx \frac{\mathbb{1}}{Tr\left\{\mathbb{1}\right\}} - \frac{\hbar\hat{\mathcal{H}}}{k_{\text{B}}T \cdot Tr\left\{\mathbb{1}\right\}} \quad .
\end{aligned} \quad (1.51)
$$

Again, the part proportional to unity is usually left away, and we work with

$$
\hat{\sigma}_{\text{eq}} \approx \frac{-\hbar}{k_{\text{B}}T \cdot Tr\left\{\mathbb{1}\right\}} \hat{\mathcal{H}} \quad . \quad (1.52)
$$

Since there are many more proportionality constants that would need to be taken in account when discussing actual signal intensities, all constants are often left away as well. And since the Zeeman interaction with the static field along z usually dominates, one often simply uses

$$
\hat{\sigma}_{\text{eq}} \approx \hat{S}_z \quad . \quad (1.53)
$$

Sometimes, an explicit minus sign is used for the electron spin, because the energies of the $|m_S = \pm 1/2\rangle$ levels are reversed compared to e. g. protons.

1.2.2.6 *Interaction frame transformation*

One of the most important concepts in modern magnetic resonance is the interaction frame transformation (IFT). In some textbooks on quantum mechanics, this is also called the *Dirac* picture. Essentially, an IFT can be used to remove the explicit time evolution of certain terms in the Hamiltonian. These terms are usually large, and their influence more or less trivial, but evolution under these terms "masks" the effect of other, smaller terms in the Hamiltonian.

In general, we can split a Hamiltonian quite arbitrarily into two parts,

$$\hat{\mathcal{H}} = \hat{\mathcal{H}}_0 + \hat{\mathcal{H}}_1 \qquad . \tag{1.54}$$

Often, $\hat{\mathcal{H}}_0$ is chosen to be the dominant part. Going into an interaction frame with $\hat{\mathcal{H}}_0$ means that we transform all operators according to

$$\hat{A}' = \hat{U}_0^\dagger \hat{A} \hat{U}_0 \tag{1.55}$$

$$\hat{U}_0 = \exp\left(-i\hat{\mathcal{H}}_0 t\right) \qquad . \tag{1.56}$$

Note that the term $\hat{\mathcal{H}}_0$ is unaffected, i.e.

$$\hat{\mathcal{H}}_0' = \hat{\mathcal{H}}_0 \tag{1.57}$$

$$\left[\hat{U}_0, \hat{\mathcal{H}}_0\right] = 0 \qquad . \tag{1.58}$$

One can easily find the equation of motion for the density operator in the interaction frame by applying the product rule for derivatives, and the Liouville-von Neumann equation,

$$\begin{aligned}
\frac{\mathrm{d}}{\mathrm{d}t}\hat{\rho}' &= \frac{\mathrm{d}}{\mathrm{d}t}\left(\hat{U}_0^\dagger \hat{\rho} \hat{U}_0\right) = \frac{\mathrm{d}}{\mathrm{d}t}\hat{U}_0^\dagger \left(\hat{\rho}\hat{U}_0\right) + \hat{U}_0^\dagger \left(\frac{\mathrm{d}}{\mathrm{d}t}\hat{\rho}\right)\hat{U}_0 + \left(\hat{U}_0^\dagger \hat{\rho}\right)\frac{\mathrm{d}}{\mathrm{d}t}\hat{U}_0 \\
&= i\hat{\mathcal{H}}_0 \hat{U}_0^\dagger \hat{\rho}\hat{U}_0 + \hat{U}_0^\dagger\left(-i\left[\hat{\mathcal{H}}_0 + \hat{\mathcal{H}}_1, \hat{\rho}\right]\right)\hat{U}_0 + \hat{U}_0^\dagger \hat{\rho}\cdot(-)i\hat{\mathcal{H}}_0 \hat{U}_0 \\
&= \underbrace{+i\hat{\mathcal{H}}_0 \hat{\rho}' - i\hat{\rho}'\hat{\mathcal{H}}_0}_{i[\hat{\mathcal{H}}_0,\hat{\rho}']} - i\left[\hat{\mathcal{H}}_0' + \hat{\mathcal{H}}_1', \hat{\rho}'\right]
\end{aligned}$$

$$\frac{\mathrm{d}}{\mathrm{d}t}\hat{\rho}' = -i\left[\hat{\mathcal{H}}' - \hat{\mathcal{H}}_0, \hat{\rho}'\right] = -i\left[\hat{\mathcal{H}}_1', \hat{\rho}'\right] = -i\left[\hat{\mathcal{H}}'', \hat{\rho}'\right] \qquad . \tag{1.59}$$

As visible from Equation (1.59), the dominant part $\hat{\mathcal{H}}_0$ that was used for the IFT does not appear anymore in the equation of motion. It was absorbed into the frame. In many derivations, the step from $\hat{\mathcal{H}}'$ to $\hat{\mathcal{H}}''$ is skipped, i.e. one starts with

$$\hat{\mathcal{H}} = \hat{\mathcal{H}}_0 + \hat{\mathcal{H}}_1 \qquad , \tag{1.60}$$

and after an IFT with $\hat{\mathcal{H}}_0$ ends up with

$$\tilde{\hat{\mathcal{H}}} = \hat{\mathcal{H}}_1' \qquad . \tag{1.61}$$

It is implied that the part of the Hamiltonian that was used for the IFT is subtracted from the new Hamiltonian.

It is important to remember that observables have to be transformed into the same interaction frame as well.

EXAMPLE: ROTATING FRAME AND OSCILLATING FIELD

Let us look at the example of how pulses are treated in magnetic resonance. The coils or resonators in the spectrometer generate a small oscillating magnetic field $2B_1 \cos(\omega_{\mathrm{mw}}t)$ that is perpendicular to the large static magnetic field B_0. In total, we have

$$\vec{B}(t) = \begin{pmatrix} 2B_1 \cos(\omega_{\mathrm{mw}}t) \\ 0 \\ B_0 \end{pmatrix} \qquad . \tag{1.62}$$

Assuming an isotropic g-value[4], we get a time-dependent Zeeman Hamiltonian

$$\begin{aligned} \hat{\mathcal{H}}(t) =& -2\gamma_e B_1 \cos(\omega_{\mathrm{mw}}t)\hat{S}_x - \gamma_e B_0 \hat{S}_z \\ =& 2\omega_1 \cos(\omega_{\mathrm{mw}}t)\hat{S}_x + \omega_S \hat{S}_z \qquad . \end{aligned} \tag{1.63}$$

Solving the Liouville-von Neumann equation with such a Hamiltonian is quite an involved task, although possible numerically. However, there is an alternative way to analyse the spin dynamics during pulses, using a *rotating frame*. The problem becomes easier if we rotate the frame with a frequency ω_{mw} around z. This corresponds to an IFT with $\omega_{\mathrm{mw}}\hat{S}_z$, which gives

$$\begin{aligned} \hat{\mathcal{H}}'' =& \hat{\mathcal{H}}' - \omega_{\mathrm{mw}}\hat{S}_z \\ =& 2\omega_1 \cos(\omega_{\mathrm{mw}}t)\left(\cos(\omega_{\mathrm{mw}}t)\hat{S}_x - \sin(\omega_{\mathrm{mw}}t)\hat{S}_y\right) + \underbrace{(\omega_S - \omega_{\mathrm{mw}})}_{\Omega}\hat{S}_z \\ =& \omega_1\left(\hat{S}_x + \cos(2\omega_{\mathrm{mw}}t)\hat{S}_x - \sin(2\omega_{\mathrm{mw}}t)\hat{S}_y\right) + \Omega\hat{S}_z \qquad . \end{aligned} \tag{1.64}$$

One way to look at these trigonometric manipulations is that linearly polarised radiation is the superposition of two circularly polarized waves. If one of these waves is on or close to resonance, the other one is far away (about twice

---

4 Note that the problem gets significantly more complicated for strongly anisotropic g-matrices, as these can tilt the quantization axis away from the static magnetic field.

the resonance frequency). Usually, the perpendicular field is much smaller than the static field, i. e. $B_1 \ll B_0$. In this case, we can use the *rotating wave approximation*. In other words, we simply neglect the terms oscillating with $2\omega_{\mathrm{mw}}$

$$\hat{\mathcal{H}}'' \approx \omega_1 \hat{S}_x + \Omega \hat{S}_z \qquad . \tag{1.65}$$

In the language of average Hamiltonian theory, this is the *first order average Hamiltonian*, which in general is given by

$$\overline{\hat{\mathcal{H}}}^{(1)} = \int_0^{\tau_m} \hat{\mathcal{H}}(t)\mathrm{d}t \qquad , \tag{1.66}$$

where τ_m is the periodicity of the time-dependent Hamiltonian. The second-order contribution to the average Hamiltonian is given by

$$\overline{\hat{\mathcal{H}}}^{(2)} = \frac{-i}{2\tau_\mathrm{m}} \int_0^{\tau_\mathrm{m}} \int_0^{t_2} \left[\hat{\mathcal{H}}(t_2), \hat{\mathcal{H}}(t_1)\right] \mathrm{d}t_1 \mathrm{d}t_2 \qquad , \tag{1.67}$$

In the case of linearly polarised irradiation and the rotating frame, the counter-rotating wave generates a *Bloch-Siegert shift* in second order. This can usually be neglected.

1.2.2.7 *Forbidden transitions in electron-nuclear two-spin systems*

Under high-field conditions, the Zeeman interactions of both electron spins and nuclear spins are much larger than all other interactions. In this case, the angular momentum projection quantum number m_S and m_I are good quantum numbers in an electron-nuclear two-spin system. In other words, the Hamiltonian is diagonal in the usual product basis $\{|S, m_S, I, m_I\rangle = |S, m_S\rangle \otimes |I, m_I\rangle\}$. Equivalently, it only contains terms proportional to $\hat{S}_z$ or $\hat{I}_z$. Under these conditions, electromagnetic irradiation can only induce transitions that fulfil $\Delta m_S = \pm 1, \Delta m_I = 0$ (EPR) or $\Delta m_S = 0, \Delta m_I = \pm 1$ (NMR). These are the *allowed* transitions. They are a consequence of angular momentum conservation. One can also look at the $\hat{F}_x = \hat{S}_x + \hat{I}_x$ operator, which only contains off-diagonal elements that connect levels which fulfil the above selection rules.

There are, however, situations, where these rules do not hold, namely if the high-field approximation is violated. In EPR, it is the hyperfine interaction that can be comparable to the nuclear Zeeman frequency that leads to weakly or strongly allowed forbidden transitions. This case, shortly mentioned in Section 1.2.1.4, will now be discussed in detail. These forbidden transitions

are essential for many effects and sequences in EPR, *vide infra*. We limit ourselves to a system of $S = 1/2$ and $I = 1/2$, although we note that the quadrupole interaction can also play an important role. Again, we assume an isotropic g-factor

$$\hat{\mathcal{H}} = \omega_S \hat{S}_z + \omega_I \hat{I}_z + \vec{\hat{S}}^{\mathrm{T}} \mathbf{A} \vec{\hat{I}} \quad . \tag{1.68}$$

The electron Zeeman frequency ω_S is usually much larger than all other terms. The nuclear Zeeman frequency ω_I, however, can be on the same order of magnitude than the hyperfine coupling terms. We now go to a rotating frame with $\omega_{\mathrm{mw}} \hat{S}_z$ and neglect all time-dependent terms (high-field approximation for the electron spin). This leads to

$$\hat{\mathcal{H}}' = \Omega_S \hat{S}_z + \omega_I \hat{I}_z + \hat{S}_z \left(A_{zz} \hat{I}_z + A_{zx} \hat{I}_x + A_{zy} \hat{I}_y \right) \quad , \tag{1.69}$$

with $\Omega_S = \omega_S - \omega_{\mathrm{mw}}$. In the absence of radio-frequency irradiation, we can turn the nuclear coordinate system such that $A_{zy'} = 0$. This simplifies the notation a bit

$$\hat{\mathcal{H}}' = \Omega_S \hat{S}_z + \omega_I \hat{I}_z + \hat{S}_z \left(A \hat{I}_z + B \hat{I}_x \right) \quad , \tag{1.70}$$

as introduced in Equation (1.17). This Hamiltonian is not diagonal, but it is block-diagonal. This is best seen if it is re-written in terms of electron projection operators

$$\mathbb{1} = \hat{S}^\alpha + \hat{S}^\beta \tag{1.71}$$

$$\hat{S}_z = 1/2 \left(\hat{S}^\alpha - \hat{S}^\beta \right) \quad , \tag{1.72}$$

giving

$$\begin{aligned} \hat{\mathcal{H}}' =\, & \Omega_S \hat{S}_z \\ & + \hat{S}^\alpha \left((\omega_I/2 + A/2) \hat{I}_z + B/2 \hat{I}_x \right) \\ & + \hat{S}^\beta \left((\omega_I/2 - A/2) \hat{I}_z - B/2 \hat{I}_x \right) \quad . \end{aligned} \tag{1.73}$$

The offset term only shifts the α and β subspaces relative to each other. The two subspaces can be diagonalised separately, because the projection operators commute.

The unitary (frame) transformations which diagonalise the Hamiltonian are then given by

$$\hat{U}_\alpha = \exp \left(i \eta_\alpha \hat{S}^\alpha \hat{I}_y \right) \tag{1.74}$$

$$\hat{U}_\beta = \exp \left(-i \eta_\beta \hat{S}^\beta \hat{I}_y \right) \quad . \tag{1.75}$$

with

$$\eta_\alpha = \arctan\left(\frac{B}{2\omega_I + A}\right) \tag{1.76}$$

$$\eta_\beta = \arctan\left(\frac{B}{2\omega_I - A}\right) \tag{1.77}$$

$$\omega_\alpha = \sqrt{(\omega_I + A/2)^2 + B^2/4} \tag{1.78}$$

$$\omega_\beta = \sqrt{(\omega_I - A/2)^2 + B^2/4} \qquad . \tag{1.79}$$

The $\arctan(x/y)$ function is the four quadrant arctangent such that $-\pi \leq \arctan(x/y) \leq \pi$. The two transformations commute and we can write

$$\hat{U}_{\text{diag}} = \hat{U}_\alpha \hat{U}_\beta = \exp(i\left(\eta_\alpha \hat{S}^\alpha \hat{I}_y - \eta_\beta \hat{S}^\beta \hat{I}_y\right)) \qquad . \tag{1.80}$$

For a more intuitive formulation we can express the projection operators again in a Cartesian basis:

$$\eta_\alpha \hat{S}^\alpha \hat{I}_y - \eta_\beta \hat{S}^\beta \hat{I}_y = \eta_\alpha(\mathbb{1}/2 + \hat{S}_z)\hat{I}_y - \eta_\beta(\mathbb{1}/2 - \hat{S}_z)\hat{I}_y$$
$$= \frac{\eta_\alpha - \eta_\beta}{2}\hat{I}_y + \frac{\eta_\alpha + \eta_\beta}{2}2\hat{S}_z\hat{I}_y \qquad . \tag{1.81}$$

and if we define

$$\xi = \frac{\eta_\alpha - \eta_\beta}{2} \tag{1.82}$$

$$\eta = \frac{\eta_\alpha + \eta_\beta}{2} \qquad , \tag{1.83}$$

we get

$$\hat{U}_{\text{diag}} = \exp\left(-i\left(\xi\hat{I}_y + \eta 2\hat{S}_z\hat{I}_y\right)\right) \qquad . \tag{1.84}$$

The diagonalized Hamiltonian reads

$$\hat{\mathcal{H}}' = \hat{U}_{\text{diag}}^\dagger \hat{\mathcal{H}} \hat{U}_{\text{diag}}$$
$$= \Omega_S \hat{S}_z + \omega_+ \hat{I}_z + \omega_- \hat{S}_z\hat{I}_z \qquad , \tag{1.85}$$

with

$$\omega_+ = \frac{\omega_\alpha + \omega_\beta}{2} \tag{1.86}$$

$$\omega_- = |\omega_\alpha - \omega_\beta| \qquad . \tag{1.87}$$

The diagonalized Hamiltonian looks like a hyperfine coupled electron-nuclear spin system with nuclear frequency ω_+ and only a secular hyperfine splitting ω_-.

It is important to notice that the frame where the Hamiltonian is diagonal does not coincide with the rotating frame/lab frame of the electron/nucleus. But pulses and detection still work in the lab frame! If we want to use the diagonalized static Hamiltonian, we have to transform the operator for the pulses and detection, $\hat{S}_x$ or $\hat{S}_y$ to the same frame.

$$\hat{S}_x \xrightarrow{\;\xi \hat{I}_y + \eta 2\hat{S}_z \hat{I}_y\;} \cos(\eta)\hat{S}_x + \sin(\eta)2\hat{S}_y \hat{I}_y \tag{1.88}$$

$$\hat{S}_y \xrightarrow{\;\xi \hat{I}_y + \eta 2\hat{S}_z \hat{I}_y\;} \cos(\eta)\hat{S}_y - \sin(\eta)2\hat{S}_x \hat{I}_y \tag{1.89}$$

$$\hat{S}_z \xrightarrow{\;\xi \hat{I}_y + \eta 2\hat{S}_z \hat{I}_y\;} \hat{S}_z \qquad . \tag{1.90}$$

The $\hat{S}_x$ operator, upon transformation into the eigenframe of the Hamiltonian, contains terms of the form $\hat{S}_y \hat{I}_y$, which contains zero-quantum and double-quantum operators. These transitions flip both the electron and the nuclear spin simultaneously, and are partially allowed if $\sin(\eta) \neq 0$. In this case, there are four transitions around the electron Zeeman frequency, centered around Ω_S, split by ω_- and $2\omega_+$, and with transition moments $\cos(\eta)$ and $\sin(\eta)$, respectively.

These forbidden transitions are responsible for the electron spin echo envelope modulation (ESEEM)-effect, and the occurrence of sideholes in electron-double resonance (ELDOR)-detected NMR.

1.2.2.8   *Relaxation*

The Liouville-von Neumann equation (1.36) is completely coherent. In other words, the propagators calculated from it are unitary and do not change the norm of $\hat{\rho}$. This would e. g. mean that once a coherence is created, it would evolve infinitely long. This is not physical and not observed in reality. Fluctuating spin interactions, induced by any form of chemical dynamics (motion, rotation, vibrations, etc.) and a finite temperature of the environment drive the spin system back to equilibrium. The most used and most successful approach in magnetic resonance goes back to Redfield. A quite intricate mathematical derivation including many assumptions leads to a Master equation

$$\frac{\mathrm{d}}{\mathrm{d}t}\hat{\rho} = -i\left[\hat{\mathcal{H}}, \hat{\rho}\right] + \hat{\hat{\Gamma}}\left(\hat{\rho} - \hat{\rho}_{\mathrm{eq}}\right) \qquad , \qquad (1.91)$$

where $\hat{\hat{\Gamma}}$ is the relaxation superoperator that drives the system back to equilibrium. In the case of a spin-1/2, there is a *longitudinal relaxation time* T_1 that acts on the $\hat{S}_z$ operator and a *transverse relaxation time* T_2 that acts on $\hat{S}_{x,y}$ operators.

Unfortunately, such a description is usually inadequate to properly describe most pulse EPR experiments in frozen solution at low temperatures. The main problem is usually that it is very difficult to distinguish "true" incoherent relaxation induced by stochastic modulations of the environment, and coherent contributions due to couplings to a large number of other spins (nuclei or electrons). For example, the coherences of dilute organic radicals at low temperatures relax mainly due to so-called *nuclear spin diffusion*. This effect can be quantitatively simulated by a static Hamiltonian that includes a vast amount of nuclei around the electron spin [12]. No stochastic motion is needed. Nevertheless, the spin echo intensity does decay with time, and it looks like relaxation (albeit with functional forms different from simple exponentials). In this case, the term *dephasing* is more appropriate than *relaxation*. And the apparent transverse relaxation time is usually called the *phase memory time* in EPR.

Although general statements are impossible, typical transverse relaxation times in EPR are in the lower µs region (at about $50\,\mathrm{K}$ for organic radicals or about $10\,\mathrm{K}$ for transition metals), while longitudinal relaxation times are typically a few ms or less.

1.3 ESTABLISHED EPR PULSE SEQUENCES

A comprehensive description of common EPR pulse sequences is beyond the scope of this work. Nevertheless, the basic principles are shortly discussed here. The pulse sequences are shown in Figure 1.1.

HAHN ECHO AND ECHO-DETECTED FIELD SWEEP (EDFS)

Due to broad lines and significant dead-time, FID-detection usually does not work in EPR. Accordingly, the basic building block of many sequences is the Hahn echo, or two-pulse echo. An EPR spectrum can be acquired for a fixed echo sequence by stepping the magnetic field. Note that due to relaxation and forbidden transitions/ESEEM, this does not necessarily give the same spectrum as CW EPR.

1.3.1   *Hyperfine spectroscopy*

1.3.1.1   *ESEEM-based sequences*

2-PULSE ESEEM
By changing the inter-pulse delay τ in a two-pulse echo, and integrating the echo intensity for each point, one can obtain a so-called 2-pulse ESEEM trace. Note that the sequence is the same for the measurement of T_m. Due to forbidden transitions discussed above, the echo intensity is modulated by the nuclear frequencies ω_α, ω_β, ω_+, and ω_-. The resolution is limited, because the linewidth is determined by the electron transverse relaxation time.

3-PULSE ESEEM
The resolution of ESEEM can be increased by using a three-pulse sequence. This is a stimulated echo. The sequence $\pi/2 - \tau - \pi/2$ generates nuclear coherence due to the forbidden transitions. This coherence decays much slower than the electron coherence, leading to much better resolution. Additionally, only the nuclear frequencies ω_α and ω_β contribute. The nuclear coherence is then converted back to electron coherence by the readout sequence $\pi/2 - \tau$. A drawback of 3p-ESEEM is that there are blind-spots in the spectra that depend on the time τ and the hyperfine coupling.

HYSCORE
By adding an additional π pulse to 3p-ESEEM, one obtains the the HYSCORE sequence. The π pulse is applied during evolution of the nuclear coherences, such that coherences on the transitions oscillating with ω_α are transferred to coherences oscillating with ω_β and vice versa. A Fourier transform of both indirect dimensions allows for correlating nuclear frequencies between different electron m_S manifolds. This increases resolution, and facilitates signal assignment.

1.3.1.2   *ENDOR*

MIMS ENDOR
This is a stimulated echo sequence. The $\pi/2 - \tau - \pi/2$ block generates a state of the form $\hat{S}_z \hat{I}_z$, depending on the hyperfine coupling and the delay τ (this again leads to blindspots in the final spectra). The echo intensity is then recorded as a function of the frequency of the rf-π pulse. The intensity is decreased any time a nuclear frequency is hit.
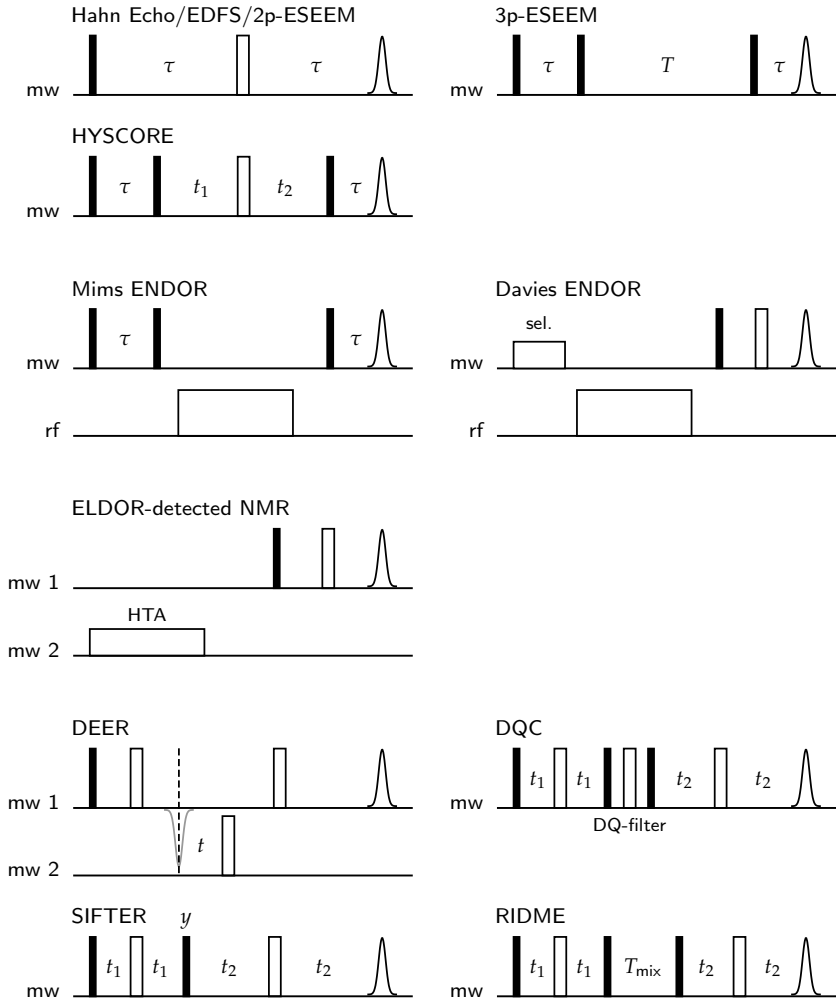
FIGURE 1.1: Common EPR pulse sequences. Short descriptions are given in the main text.

This sequence works similar to Mims ENDOR, but the nuclear polarisation generator is a simple selective π-pulse that inverts one of the hyperfine transitions of the electron. Accordingly, it does not work well for small couplings, in contrast to Mims ENDOR.

1.3.1.3 *ELDOR*

ELDOR-DETECTED NMR (EDNMR)

EDNMR makes use of two different mw frequencies. One is used to observe an echo, and another one to drive forbidden transitions with a high-turning angle (HTA) pulse. If the difference between the two frequencies matches a nuclear frequency, the echo intensity is reduced. This sequence is discussed in much more detail in Chapter 2 and Chapter 3.

1.3.2 *Dipolar spectroscopy*

DEER

Double electron-electron resonance uses two microwave frequencies as well. A refocused echo that remains unchanged is applied to the observer spins. For weakly coupled electrons, this refocuses the offsets and the dipolar coupling. An additional π pulse is applied to the pumped spins, which reintroduces the dipolar coupling. The position of this pump pulse is moved step by step to observe dipolar oscillations.

DQC

Double quantum coherence is a single-frequency technique. It consists of two echo sequences, with a double-quantum filter in the middle. The times t_1 and t_2 are swept, but $t_1 + t_2$ stays constant. Extensive phase cycling is needed for the DQ-filter.

SIFTER

The single-frequency technique for refocusing is based on a solid echo, which refocuses the dipolar coupling. Two π pulses are needed to refocus the offsets. Again, the overall sequence lengths stays constant while sweeping $t_2 - t_1$.

RIDME

Relaxation-induced dipolar modulation enhancement can be looked at as a DEER sequence where the pump pulse is replaced by a $\pi/2 - T_{\mathrm{mix}} - \pi/2$

mixing block. During the mixing time, longitudinal relaxation leads to spin-flips, which changes the resonance frequency of the observed spins.

1.4 ARBITRARY WAVEFORM GENERATORS (AWG)

Until roughly a decade ago, EPR was limited to monochromatic and mostly constant-amplitude pulses. With the available microwave power and resonators, electron nutation frequencies of about $\omega_1/2\pi \approx 30\text{--}100$ MHz can be achieved. The excitation bandwidth of rectangular pulses is on the same order. Advances in digital technology, mainly the commercial availability of fast AWGs, now allow *pulse shaping* in the microwave region [13–16]. The amplitudes and phases of the pulses can now be chosen with a time resolution of about 100 ps, corresponding to a sampling rate of 10 GS/s. The excitation bandwidth can be increased tremendously by using *frequency-swept* pulses, also called *chirps* [17–19]. On the other hand, pulses can also be tailored to have well-defined frequency-excitation profiles [20, 21].

For practical purposes, there is nearly an infinite number of possibilities of waveforms to choose from. With this great freedom come many complications. *How* should one use the AWG best? And how can we understand the electron-nuclear and electron-electron spin dynamics during arbitrary pulses? This work gives some answers for cases previously not considered in the EPR literature, especially in Chapter 4 and Chapter 5.

Part I

HOLE BURNING

2

CHIRP ECHO FOURIER TRANSFORM EPR-DETECTED NMR

Scientific articles are love letters to the future.
— Zen Faulkes

SUMMARY

A new ultra-wide band (UWB) pulse EPR method is introduced for observing all nuclear frequencies of a paramagnetic centre in a single shot. It is based on burning spectral holes with a high turning angle (HTA) pulse that excites forbidden transitions and subsequent detection of the hole pattern by a chirp echo. We term this method Chirp Echo Epr SpectroscopY (CHEESY)-detected NMR. The approach is a revival of FT EPR-detected NMR. It yields similar spectra and the same type of information as electron-electron double resonance (ELDOR)-detected NMR, but with a multiplex advantage. We apply CHEESY-detected NMR in Q-band to nitroxides and correlate the hyperfine spectrum to the EPR spectrum by varying the frequency of the HTA pulse. Furthermore, a selective π pulse before the HTA pulse allows for detecting hyperfine sublevel correlations between transitions of one nucleus and for elucidating the coupling regime, the same information as revealed by the HYSCORE experiment. This is demonstrated on hexaaquamanganese(II). We expect that CHEESY-detected NMR is generally applicable to disordered systems and that our results further motivate the development of EPR spectrometers capable of coherent UWB excitation and detection, especially at higher fields and frequencies.

The supplementary information can be found online under the given DOI as well. Raw data including the human-readable pulse program used in our home-written software (based on MATLAB) and also the commented scripts used for processing and plotting are deposited at `http://dx.doi.org/10.17632/ykyybhp5yk.2`.

The results obtained with the copper complex and the Ti(III) catalyst were not a part of the original article. The part on titanium was published as [23] ("Gold Open Access"):

Ashuiev, A., Allouche, F., Wili, N., Searles, K., Klose, D., Copéret, C. & Jeschke, G. Molecular and supported Ti(iii)-alkyls: efficient ethylene polymerization driven by the π-character of metal-carbon bonds and back donation from a singly occupied molecular orbital. *Chem. Sci.* **12**, 780. doi:`10.1039/d0sc04436a` (2021)

2.1 INTRODUCTION

Hyperfine couplings and nuclear frequencies can give detailed and valuable information about the local structure of paramagnetic centres. Sometimes these couplings can be resolved in the CW EPR spectra. If this is not the case, several different pulse EPR methods are available. The most prominent ones are ESEEM (electron spin echo envelope modulation), ENDOR (electron nuclear double resonance) and ELDOR-detected NMR (electron-electron double resonance-detected NMR, or EDNMR) [1].

EDNMR is used to measure the nuclear frequencies of paramagnetic centres employing microwave irradiation only. It was introduced more than two decades ago by Schosseler et al. [24]. This experiment is particularly useful at high fields and frequencies [25] and has recently gained popularity [26–28]. It relies on driving forbidden transitions by a very selective high turning angle (HTA) pulse whose large nominal turning angle compensates for the low transition moment. The two levels of a forbidden transition are shared with two allowed transitions that differ by the nuclear frequencies of the hyperfine doublet from the frequency of the allowed transition. Hence, a polarisation change on the forbidden transition decreases the polarisation of these two allowed transitions and thus their signal. The hole pattern created by the HTA pulse is measured stepwise in the frequency domain by changing the frequency difference between HTA pulse and observer sequence. This has the advantage that the holes are detected on resonance, which alleviates the dead-time problem, such that broad features can be detected. Compared to ENDOR, the resolution is usually worse, but there is no need for long radio-frequency (rf) irradiation, which prevents the application of ENDOR to centres with fast longitudinal relaxation of the electron spin. Compared to ESEEM, the resolution of EDNMR is also lower, but larger couplings are detectable and sensitivity enhancement by strongly driving the forbidden transitions is easier and more transparent than pulse matching [29].

Conceptually easier and also historically older than EDNMR is the idea of Fourier transform (FT) EPR-deteced NMR [30], where the hole pattern is detected by recording an FID and a subsequent Fourier transform. The forbidden transition labelled EPR (FORTE) experiment enhances sensitivity of FT EPR-detected NMR by burning the hole with a HTA pulse and correlates the hole pattern to the EPR spectrum in a second dimension [31]. EDNMR and FT EPR-detected NMR give similar spectra and information, as they both rely on detecting a hole pattern created by a HTA pulse. However, at a given magnetic field, the spectra are different because the orientation selection affects them differently. In EDNMR, orientation selection is governed by the detection sequence, in FT EPR-detected NMR, it is governed by the HTA pulse. FT EPR-detected NMR has not become popular as it does not work well for large couplings and broad holes, because of the limited excitation bandwidth and severe dead time.

Both of these limitations can be overcome by the use of chirp echoes, where the frequency is swept through the spectrum during the pulse [32]. The chirp echo acquisition can be viewed as a broadband "polarisation readout", which gives the complete hole pattern in one shot. In analogy to FT-NMR, this

gives the direct dimension for free. The dead time problem could also be solved by a normal Hahn echo, but the bandwidth of rectangular pulses is very limited compared to chirp pulses and is insufficient for large hyperfine couplings. Several possible additional, indirect dimensions can be imagined, the most obvious one being the EPR spectrum itself. That way, the FT EPR-detected NMR spectrum can be correlated to the EPR spectrum, which gives additional information about the relative orientations of g-tensor and hyperfine coupling tensor [25].

Earlier work on the use of chirp echoes in hyperfine spectroscopy focused on ESEEM sequences [33]. In the case of single crystals, EPR spectra broader than 800 MHz in the direct dimension and nuclear frequencies up to 200 MHz in the indirect dimension could be detected. This is impossible with rectangular pulses. However, the ESEEM experiment suffers from short transverse relaxation times typical for systems with medium to large couplings, and from transverse interference effects [34]. In our hands, it did not yield satisfying spectra for disordered systems, most likely due to destructive interference from closely spaced nuclear frequencies with different phases. The problems associated with short transverse relaxation times and transverse interference are not expected for hole burning experiments.

In this work, we demonstrate the use of chirp echoes to detect the complete FT EPR-detected NMR spectrum of a nitroxide radical and the correlation to the EPR spectrum by changing the frequency of the HTA pulse step by step. The same correlation experiment is also performed on the manganese hexaquacomplex, but there the additional information is limited because of the mainly isotropic g-value and hyperfine coupling. A hyperfine sublevel correlation (HYSCORE)-type correlation experiment is introduced that is based on a polarisation transfer step by a π-pulse on an allowed transition before the HTA pulse.

2.2 THEORY

2.2.1 *General principle of side hole burning*

Polarisation transfer experiments can be illustrated and discussed rather generally with the three-level system shown in Figure 2.1. The states are denoted by $|i\rangle$, the corresponding population before a pulse is applied as $p_{i,0}$ and the population after the pulse as p_i.
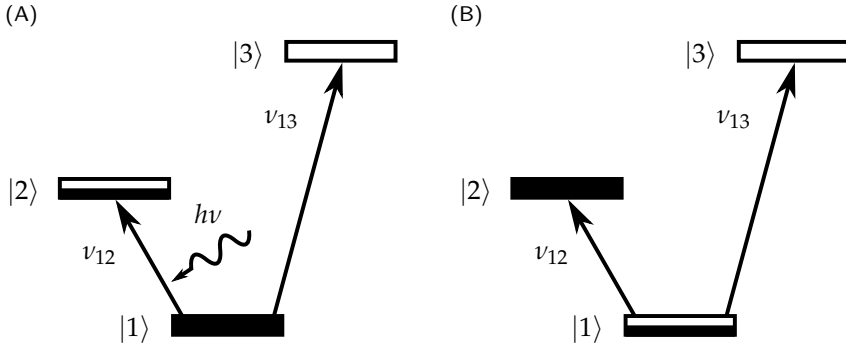
FIGURE 2.1: Polarisation transfer in systems with connected levels. (A) Before a hole burning pulse is applied. (B) After a hole burning pulse is applied. Any change of the polarisation of the transition $|1\rangle \to |2\rangle$ also leads to a change in polarisation of the transition $|1\rangle \to |3\rangle$. This manifests as a change in spectral intensity at an offset of $\Delta\nu = \nu_{13} - \nu_{12}$. If the spectral intensity decreases, as shown in this illustration, it is denoted hole burning. If the population of level $|2\rangle$ before the pulse is lower than the population of level $|1\rangle$, the polarisation of the transition $|1\rangle \to |3\rangle$ increases, resulting in a polarisation enhancement.

In order to discuss EDNMR, we make the correspondence of observing the decreased intensity of the allowed transition $|1\rangle \to |3\rangle$ after having applied a hole burning pulse to the forbidden transition $|1\rangle \to |2\rangle$. However, the concept of hole burning is much more general. For example, in systems with zero-field splittings, a hole burning pulse is expected to increase the polarisation of connected transitions (see Chapter 3). We will make no assumptions about the transition moments in the following general discussion and treat the special case of hyperfine spectroscopy in the next section. We look at spectral intensity changes of the transition $|1\rangle \to |3\rangle$. We can define a relative depth

$$d_{\text{hole}} := \frac{(p_1 - p_{1,0}) - (p_3 - p_{3,0})}{2(p_{3,0} - p_{1,0})} \qquad . \tag{2.1}$$

Without any perturbation, this hole depth parameter takes the value $d_{\text{hole}} = 0$. If the transition $|1\rangle \to |3\rangle$ is saturated, then $p_1 = p_3 = (p_{2,0} + p_{3,0})/2$ and $d_{\text{hole}} = 1/2$. Finally, if the transition $|1\rangle \to |3\rangle$ is inverted, then $p_3 = p_{1,0}$ and $p_1 = p_{3,0}$ which leads to $d_{\text{hole}} = 1$. $d_{\text{hole}} < 0$ corresponds to polarisation enhancement.

If we assume that a (hole burning) pulse is applied to transition $|1\rangle \to |2\rangle$, then level $|3\rangle$ is untouched. Still, the intensity of the observed transition

$|1\rangle \to |3\rangle$ at an offset of $\Delta\nu = \nu_{13} - \nu_{12}$ with respect to the hole burning pulse changes. Since $p_3 = p_{3,0}$, it follows that

$$d_{\text{hole}} = \frac{p_1 - p_{1,0}}{2(p_{3,0} - p_{1,0})} = \frac{p_1 - p_{1,0}}{-2(\Delta_0 p_{13})} \qquad , \qquad (2.2)$$

with the initial polarisation $\Delta_0 p_{13} = p_{1,0} - p_{3,0}$ on transition $|1\rangle \to |3\rangle$.

For a given microwave strength B_1 we can define a nominal flip angle for the hole burning pulse [31].

$$\beta_0 = \frac{g_e \mu_B}{\hbar} B_1 \cdot t_p = \omega_1 \cdot t_p \qquad , \qquad (2.3)$$

with the electron g-factor g_e, the Bohr magneton μ_B, the reduced Planck constant $\hbar$, the pulse length t_p and $\omega_1 = g_e \mu_B B_1 / \hbar$. Since different transitions can have different transition moments μ, it is sensible to define an effective flip angle per transition $|i\rangle \to |j\rangle$

$$\beta_{ij} = \mu_{ij} \beta_0 \qquad . \qquad (2.4)$$

If $|i\rangle \to |j\rangle$ is a forbidden transition, μ_{ij} is very small, and a high nominal turning angle is needed to achieve a significant change in populations.

We can now express p_1 and d_{hole} as a function of the effective flip angle of the hole burning pulse

$$
\begin{aligned}
p_1 \qquad &= \frac{1}{2} \left[p_{1,0} \cdot (1 + \cos\beta_{12}) + p_{2,0} \cdot (1 - \cos\beta_{12}) \right] \\
p_1 - p_{1,0} \qquad &= \frac{1}{2} \left[p_{1,0} \cdot (\cos\beta_{12} - 1) + p_{2,0} \cdot (1 - \cos\beta_{12}) \right] \\
&= -\frac{\Delta_0 p_{12}}{2} \left[1 - \cos(\mu_{12}\, \beta_0) \right] \qquad , \qquad (2.5)
\end{aligned}
$$

which yields

$$d_{\text{hole}} = \frac{\Delta_0 p_{12}}{4\Delta_0 p_{13}} \left[1 - \cos(\mu_{12}\, \beta_0) \right] \qquad . \qquad (2.6)$$

We can identify the inversion factor

$$f_{\text{inv}} = \frac{1}{2} \left[1 - \cos(\mu_{12}\, \beta_0) \right] \qquad , \qquad (2.7)$$

which is 0 before hole burning, 1/2 for saturation , corresponding to an effective flip angle of $\pi/2$, and 1 for inversion. This simplified expression

neglects relaxation. In the presence of significant relaxation, f_{inv} has to be computed numerically. We finally have

$$d_{\text{hole}} = \frac{f_{\text{inv}}}{2} \frac{\Delta_0 p_{12}}{\Delta_0 p_{13}} \quad . \tag{2.8}$$

In the following, we will discuss the specific case of hyperfine spectroscopy.

2.2.2 *Hole burning in hyperfine spectroscopy*

Hole burning experiments that investigate nuclei coupled to unpaired electrons, can most easily be illustrated with an electron-nuclear two-spin system coupled by an anisotropic hyperfine interaction [1]. Such a system shows four EPR transitions, two allowed and two forbidden ones, with transition probabilities I_a and I_f. The effective flip angles for these transition are given by

$$\beta_{a,f} = \mu_{a,f}\,\beta_0 = \sqrt{I_{a,f}}\,\beta_0 \quad . \tag{2.9}$$

The transition moments $\mu_{a,f}$ are related to the relative magnitudes of the nuclear Zeeman frequency ω_I and the hyperfine coupling constants $A = A_{zz}$ and $B = \sqrt{A_{zx}^2 + A_{zy}}$ [1]. The forbidden transitions are most intense at the exact cancellation condition $A/2 = \omega_I$.

Figure 2.2 (A) shows the energy level diagram of this system. We can now connect this specific case to the general picture described in the previous section. Let us use the following correspondence:

$$|\beta\beta\rangle \leftrightarrow |1\rangle$$
$$|\alpha\alpha\rangle \leftrightarrow |2\rangle$$
$$|\alpha\beta\rangle \leftrightarrow |3\rangle \quad .$$

The hole burning pulse then acts on a forbidden double-quantum transition. The hole depth of the allowed transition $(|1\rangle \rightarrow |3\rangle \,\hat{=}\, |\beta\beta\rangle \rightarrow |\alpha\beta\rangle)$ in this case is given by

$$d_{\text{hole}} = \frac{f_{\text{inv}}}{2} \frac{\Delta_0 p_{12}}{\Delta_0 p_{13}} = \frac{1 - \cos(\mu_f\,\beta_0)}{4} \quad . \tag{2.10}$$
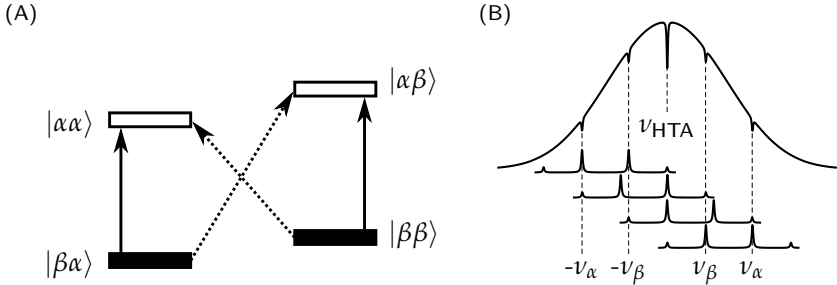
(A)

(B)

FIGURE 2.2: (A) Energy level diagram for an electron nuclear two-spin system. The solid and dashed arrows represent formally allowed and forbidden transitions, respectively. Note that driving a forbidden transition lowers the polarisation of the allowed transitions and vice versa. (B) Illustration of the effect of a HTA pulse on an inhomogeneously broadened line made up of several spin packets with a Gaussian distribution of resonance offsets. The side holes which appear additionally to the central hole encode the nuclear frequencies ν_α and ν_β.

if we assume that the levels within one electron spin manifold are equally populated. The maximal hole depth is $1/2$, which corresponds to saturation. Such a deep hole would need an effective flip angle of π on the forbidden transition, which often cannot be achieved in practice, because the transition moment is usually too small. The cases of exciting the other forbidden transition or observing on the other allowed transition are analogous.

In an inhomogeneously broadened system, such as a powder or frozen solution, the description becomes more complicated. Figure 2.2 (B) shows a simulation of an inhomogeneously broadened line consisting of 500 spin packets with a Gaussian distribution of resonance offsets. A HTA pulse applied at ν_{HTA} can hit any of the four possible transitions of a spin packet, depending on the offset frequency. By looking at the energy level diagram in Figure 2.2 (A) it becomes clear that any perturbation of an allowed transition lowers the polarisation of the forbidden transitions but does not affect the other allowed transition. On the other hand, driving a forbidden transition lowers the polarisation on the corresponding allowed transitions but leaves the polarisation of the other forbidden transition unperturbed. This leads to the hole pattern shown in Figure 2.2 (B). The positions of the side holes relative to ν_{HTA} give the nuclear frequencies.

2.2.3   *Detecting the hole pattern*

The pulse sequences and detection schemes discussed in this article are shown in Figure 2.3. It is clear that one can obtain the nuclear frequencies by detecting the hole pattern described in the previous section. The most popular approach for doing this is ELDOR-detected NMR. In the established approach, one uses a fixed detection frequency ν_{DET} in the centre of the resonator and rather narrow-band pulses for echo- or FID-integral detection. The frequency ν_{HTA} of the hole burning pulse is then stepped discretely (see Figure 2.3 (B)). Every time a side hole is on resonance with ν_{DET}, the echo or FID intensity is decreased. In FT-EPR detected NMR, the complete hole pattern created by a single HTA pulse is detected in a single shot by exciting the whole EPR line and by subsequent Fourier transform of the echo Figure 2.3 (C). The difference of the spectra with and without hole burning pulse is calculated. Two problems are associated with the FT approach in pulse EPR. First, the dead time is usually so long that broad features are lost completely. Second, the available pulse power is usually not enough to excite the whole spectrum. Both problems are overcome by the use of chirp echo detection. The chirp pulses provide the necessary bandwidth and the echo scheme circumvents dead time problems. Note that chirp echoes can be used to detect *any* change in polarisation, not only the ones associated with hyperfine spectroscopy. They could also be used, for example, to detect spectral spin diffusion after hole burning. We refer to this detection method as chirp echo EPR spectroscopy (CHEESY), and to the particular case of hyperfine spectroscopy via forbidden transitions as CHEESY-detected NMR.

In CHEESY-detected NMR, quantification of hole depths is affected by the width of the resonator mode and, potentially, by longitudinal interference during the chirp pulse [32], which can redistribute polarisation between connected transitions before conversion to detectable coherence. For electron spin $S = 1/2$, the latter effect is significant only if forbidden transitions with a large transition moment exist, since two allowed EPR transitions cannot share a level in this case. The former effect applies to EDNMR as well, since the width of the resonator mode causes variation of the nominal flip angle of frequency-swept HTA pulses. This effect can be corrected if the resonator mode profile is experimentally known.
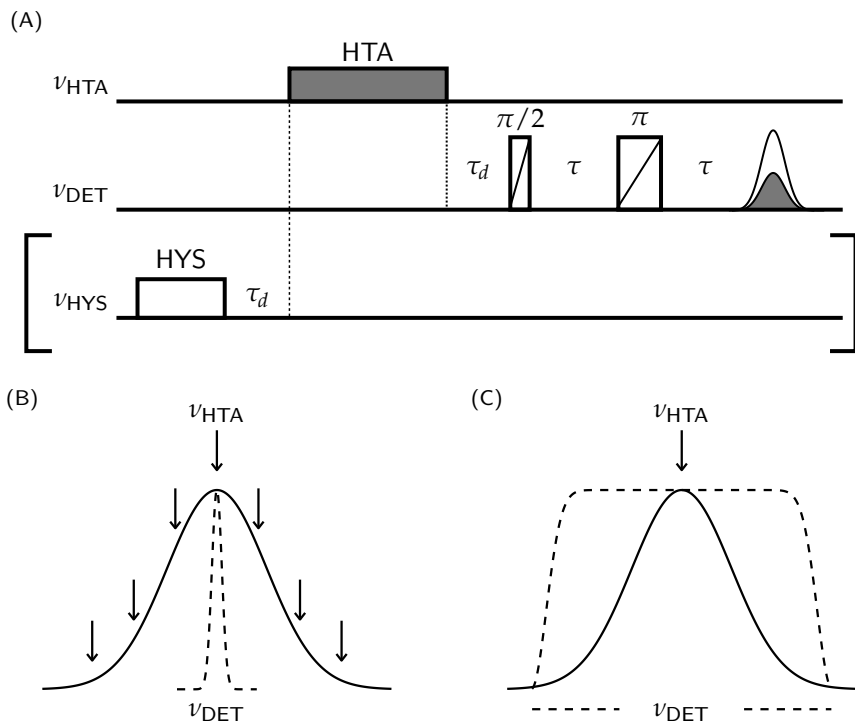
FIGURE 2.3: (A) Pulse sequence for EDNMR. In chirp echo FT EPR-detected NMR (CHEESY-detected NMR), chirp pulses with pulse lengths $t_{\pi/2} = 2t_\pi$ are used for detection. A selective π pulse, which we term HYS pulse, can be inserted to correlate transitions and determine the coupling regime, similar to HYSCORE (see below). (B) Detection scheme in ELDOR-detected NMR. The frequency of the selective detection sequence is held constant, while the frequency of the HTA pulse is swept stepwise. (C) Detection scheme in (Chirp Echo) FT-EPR detected NMR. The complete hole pattern of a single HTA pulse can be detected by a single chirp echo.

FIGURE 2.4: Series of experimental chirp echo FT EPR nitroxide spectra with a hole burned at different positions indicated with the gray lines. The deep side holes arise from weakly coupled protons.

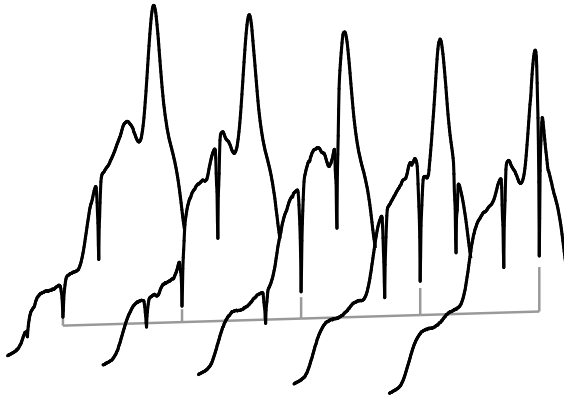### 2.2.4   *Going to higher dimensions*

2.2.4.1   *EPR-correlated hyperfine spectroscopy*

The approach presented here offers a multiplex advantage because the complete hole pattern can be acquired in a single shot. The hole pattern is basically obtained for free. This facilitates the introduction of additional dimensions to the experiment. The easiest extension is the correlation of the hole pattern to the EPR spectrum. The detection sequence and the magnetic field are held constant while the frequency of the hole burning pulse is stepped through the EPR spectrum. At each position, the obtained echo is Fourier transformed, subtracted from a reference spectrum without any hole, and shifted such that the frequency of the central hole is zero. A series of experimental spectra with holes burned at different frequencies is shown in Figure 2.4.

This approach can give valuable information about the different components of hyperfine and g-tensors and their relative orientation. Examples of conventionally obtained EPR-correlated EDNMR spectra of a nitroxide in W-band are found in [25] and [26].

2.2.4.2 *HYSCORE-type correlations*

The HYSCORE experiment is widely used because, first, it correlates peaks from the same nucleus and second, it distinguishes weakly and strongly coupled spins. Together with enhanced separation of peaks inherent to all 2D experiments, this greatly facilitates signal assignment. Nevertheless, the sensitivity is rather low in the case of low transition moments of the forbidden transitions and of distributed spectroscopic parameters, such as the hyperfine coupling. Additionally, HYSCORE suffers from blind spots, and several 2D spectra might thus be needed, which can drastically increase the measurement time.

The EDNMR experiment has been extended to a second dimension by triple-resonance approaches that employ either a second HTA pulse at a different frequency [35] or an additional radio-frequency pulse [36]. The latter experiment is alike to the TRIPLE experiment employing two radio-frequency pulses, whereas the former experiment also encodes TRIPLE-type correlation information, albeit in a somewhat more complicated way. For many applications, it is of interest to obtain HYSCORE-type information on nuclear frequencies of the same nucleus. This is possible in an EDNMR setting by applying a selective π pulse (which we denote as HYS pulse in the context of this work) before the HTA pulse. This pulse significantly changes polarisation on only the allowed transitions and thus saturates the connected forbidden transitions. A subsequent HTA pulse thus does not create side holes on the other allowed transition that shares levels with the saturated forbidden transitions. In the general description (Figure 2.1), this would correspond to a saturation of the transition $|1\rangle \rightarrow |2\rangle$ before the hole burning pulse by driving an additional transition connected to level $|2\rangle$, such that $\Delta p_{12} = 0$ and the hole depth of the side hole becomes

$$d_{\text{hole}} = \frac{f_{\text{inv}}}{2} \frac{\Delta_0 p_{12}}{\Delta_0 p_{13}} = 0 \qquad , \qquad (2.11)$$

irrespective of the flip angle of the hole burning pulse.

The situation becomes again more complicated for disordered systems. The possible polarisation transfer steps in an inhomogeneously broadened line are illustrated in Figure 2.5. Shown are the spin packets contributing to the hole pattern if the hole burning pulse is applied at ν_{HTA}. Note that the intensity of the forbidden transitions is chosen rather high for illustration purposes. The black lines show the spectrum without any hole burning, the red lines show the spectrum after the HTA pulse (the lines are perfectly inverted
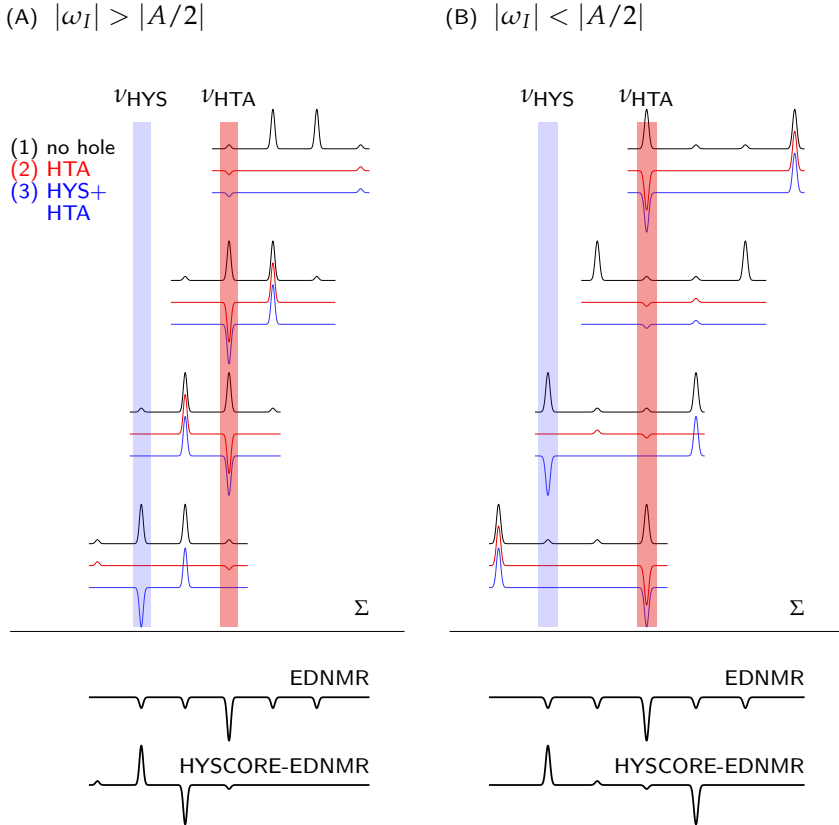
FIGURE 2.5: Illustration of the principle behind HYSCORE-EDNMR. Shown are all spin packets affected by the HTA pulse. (1) Black: before the HTA pulse, (2) red: after the HTA pulse, (3) blue: after the HYS pulse and a subsequent HTA pulse. A simple EDNMR spectrum (the sum of all red spectra minus the sum of all black spectra) does not yield any information about the coupling regime and the correlation of peaks. Applying a HYS pulse before the HTA pulse gives exactly this information (HYSCORE-EDNMR: the sum of all red spectra minus the sum of all blue spectra). A more detailed explanation is given in the main text.

for illustration purposes, which is not possible for allowed and forbidden transitions simultaneously). The blue spectra result after applying the HYS pulse at ν_{HYS} first and then the HTA pulse. It is assumed that this HYS pulse only affects allowed transitions. All the spectra are constructed with the idea that pulses on forbidden transitions saturate the allowed transitions and vice versa. The EDNMR spectra shown at the bottom are obtained by taking the difference between the red and the black spectra (with and without HTA pulse), and summing over the spin packets. It is apparent that the EDNMR spectra of weakly coupled nuclei, shown in Figure 2.5 (A), are indistinguishable from strongly coupled nuclei shown in Figure 2.5 (B) (there might be cases where they are not, e.g. when burning holes at the edges of the EPR spectrum). The HYSCORE-EDNMR spectra are obtained by taking the difference between the red and the blue spectra and summing up over the spin packets. One can think about these spectra as a measure of how much deeper the holes get by applying the HYS pulse. Obviously, the hole where the HYS pulse is applied becomes deeper, but more importantly, there are holes which become less deep if the HYS pulse is applied. The HYS pulse saturates the two connected forbidden transitions, and a subsequent HTA pulse does not have any influence. In the weak coupling case in Figure 2.5 (A), the negative peak appears on the side of the central hole where the HYS pulse was applied, whereas in the strong coupling case in Figure 2.5 (A), the negative peak appears on the opposite side of the central hole.

Note that the use of this additional π-pulse is completely independent of the use of chirp echoes for detection. It can just as well be used with the conventional EDNMR approach.

2.3   MATERIALS AND METHODS

2.3.1   Sample preparation

2.3.1.1   Nitroxides

The nitroxide model compounds are shown in Figure 2.6. Their synthesis is described in a recent article [37]. Compound **1** was used at a concentration of 217 μM. Compound **2** was used at a concentration of 100 μM. Both compounds were dissolved in deuterated o-terphenyl (dOTP).
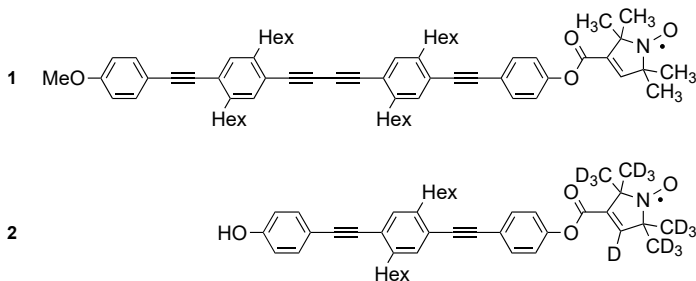
FIGURE 2.6: Structures of the nitroxide compounds used for holeburning experiments.

2.3.1.2 *Hexaquamanganese (II)*

The complex was prepared following the procedure in [38] ($MnCl_2$ from Merck). The final concentration was 2.3 mM in a 1:1 (v/v) mixture of ddH_2O:MeOH. 12 μl of the solution were transferred into a 1.6 mm EPR tube and shock frozen in liquid nitrogen before inserting it into the spectrometer.

2.3.2 *EPR spectroscopy*

2.3.2.1 *Spectrometer*

All measurements were performed on a home-built Q-band spectrometer equipped with a Keysight M8190A AWG operating at 8 GS/s and an ADC with a sampling frequency of 2 GHz (SP Devices ADQ412) [39]. Pulses were amplified by a traveling wave tube (TWT) amplifier with 150 W nominal output power. Our recently developed Q-band loop-gap resonators were used to fully exploit the broadband capabilities of the spectrometer [40].

2.3.2.2 *Measurement setup*

Measurements were set up in the following way: 1) Setting the temperature. 2) Maximizing the echo by adjusting the coupler position of the resonator. 3) Measuring an echo-detected field-swept EPR spectrum. 4) Characterizing the magnitude response of the resonator by means of frequency-swept nutation experiments at full power on the maximum of the spectrum. This was used for a resonator compensation of the chirp pulses [17]. 5) Measurement of the non-linearity of the excitation chain at the centre of the resonator by means

of power-dependent nutation experiments [17]. 6) A quick estimate of T_1 and T_m values was obtained by inversion recovery and spin-echo experiments and visual inspection of the traces. 7) Chirp echoes following the Kunz scheme [41] (in the magnetic resonance spectroscopy literature, it is usually known under Boehlen-Bodenhausen scheme [42]) were set up by choosing an appropriate frequency range and pulse length first, depending on the spectral width and the phase memory time. Subsequently the pulse amplitudes were optimized by visually inspecting the Fourier transforms of the echoes. It was found to be helpful to look at the whole spectrum rather than only the integral of the echo (which gives the spectral intensity at zero frequency only).

The choice of an appropriate length and amplitude of the HTA pulse is delicate, not trivial, and depends on what one wants to observe [26]. In this work, different settings were tried and usually evaluated by visual inspection.

More experimental details about temperature, shot repetition time, total measurement time etc. can be found in the SI of [22][1].

2.3.3   *CHEESY-detected NMR and HYSCORE-type correlations*

In order to record a 1D CHEESY-detected NMR spectrum, the chirp echo spectrum was measured once with and once without a HTA pulse before the chirp echo. The CHEESY-detected NMR spectrum is then obtained by taking the difference of the two. Note that this can lead to artifacts if some external condition changes between the two spectra. Because of this, we acquire the two echo traces in a single experiment immediately after each other. The frequency axis is chosen relative to the frequency of the HTA pulse. In the case of the EPR-correlated 2D spectra, no reference spectrum without hole burning pulse is required, because the reference spectrum can be constructed by a maximum projection of all chirp echo EPR spectra. This is only possible if the magnetic field is held constant and the frequency of the HTA pulse is swept. For very broad EPR spectra, it is necessary to change the magnetic field and leave the frequency of the HTA pulse constant. In this case, a reference spectrum is needed at each field position.

The HYSCORE-type correlations are obtained by observing the influence of the HYS pulse on the hole pattern. Two chirp echo spectra are measured, one with both the HYS pulse and the HTA pulse and one only with the HTA pulse, and the difference between the latter and the former spectrum is plotted.

---

1 At least at the time of writing, this is the direct PDF link: `https://ars.els-cdn.com/content/image/1-s2.0-S1090780718300466-mmc1.pdf`

2.3.4 *Data processing*

Chirp echoes after digital down conversion were symmetrically cut around the maximum to the appropriate length, apodised by a Chebyshev window, zero-filled symmetrically and Fourier transformed after cyclic permutation. The EPR-correlated CHEESY-detected NMR spectra were shifted such that the frequency of the HTA pulse corresponds to zero frequency for each trace, which simplifies the interpretation. The 2D spectra were processed with a Gaussian filter in order to improve the visibility of smaller peaks. This is necessary mainly because of the different signal-to-noise levels over the spectrum inherent in an approach that measures holes. The filter is not necessary when inspecting the single traces rather than a contour plot. The exact processing can be inferred from the MATLAB scripts deposited on Mendeley Data.

2.4   RESULTS AND DISCUSSION

2.4.1   *CHEESY-detected NMR*

A comparison between conventional EDNMR and CHEESY-detected NMR applied to compound **1** is shown in Fig. 2.7. Both spectra (C) and (D) were recorded with the same HTA pulse length and power. The measurement time was also the same for both (about 90 minutes). Note that such a comparison is not direct, since the two spectra differ subtly. In the conventional EDNMR approach, the detection frequency is held constant, while the frequency of the HTA pulse is swept. Orientation selection [43] is thus determined by the observer echo sequence and relates to the allowed observer transitions. In the chirp echo approach, the observer transitions are detected during free evolution and thus not broadened beyond their natural line width. Orientation selection is governed by the HTA pulse that is usually more selective than the observer echo in conventional EDNMR. Furthermore, the orientation selection now corresponds to the forbidden transitions. The spectra give similar information, but it is impossible to obtain exactly the same spectrum with the two approaches. The quality of the CHEESY-detected NMR spectrum is better in terms of both signal-to-noise ratio and resolution. For a fairer comparison, the conventional EDNMR spectrum was inverse Fourier transformed, multiplied by a Chebyshev window and transformed back (shown in red), which is equivalent to the filtering inherent in the FT approach. Even after filtering, the signal-to-noise ratio of the chirp echo detected approach is 2-3 times higher. Besides the sensitivity gain, the chirp echo approach shows some clear, practically relevant advantages. 1) In CHEESY-detected NMR, the detection resolution is independent of the exact settings in the detection sequence and only affected by the observation window, which has to be long enough. 2) There is no need for setting the step size of the frequency difference between observer and HTA pulses. In principle, in Figure 2.7 (C), bigger frequency steps could have been chosen for the observed peak widths, but there might be many examples where one does not know the peak width beforehand, especially if the signal-to-noise ratio is low. In CHEESY-detected NMR, this step size does not exist at all in the 1D case. 3) In the conventional approach, the HTA pulse length is often optimized by a nutation experiment [26], where the HTA pulse is applied to a peak in the EDNMR spectrum. This works very well - if the peak position is already known. In the CHEESY approach, one can observe the influence of the HTA pulse on the hole spectrum rather

than only parts of it. In this way, the experimentalist does not need to know beforehand where the peaks are in order to optimize the HTA pulse.
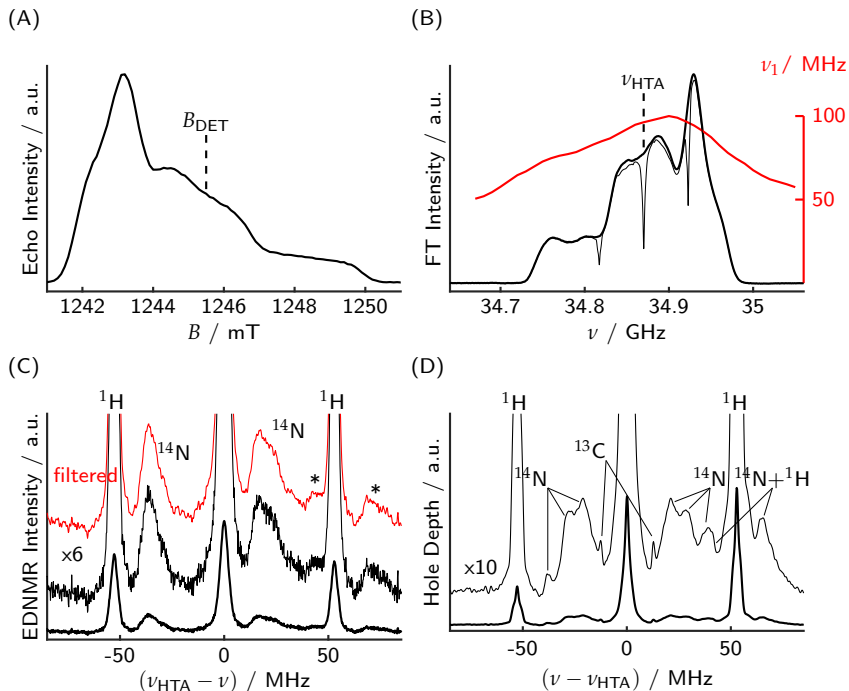

FIGURE 2.7: Comparison between conventional EDNMR and CHEESY-detected NMR. (A) Echo detected field sweep spectrum of compound **1**. The dashed line indicates the field position used for the conventional EDNMR. (B) CHEESY spectrum obtained by Fourier transformation of a chirp echo without an HTA pulse applied (thick black line) and with a HTA pulse applied at the indicated position (thin black line). The experimentally measured resonator profile is indicated in red. (C) Conventionally recorded EDNMR spectrum. The red line on top shows a spectrum to which equivalent filtering was applied as to the CHEESY spectrum. Asterisks denote either ^{14}N DQ transitions or ^{14}N+^{1}H combination frequencies. (D) CHEESY-detected NMR spectrum obtained by taking the difference between the spectra shown in (B). The frequency axis is relative to the frequency of the HTA pulse. The peak positions in (C) and (D) are different because the orientation selection in EDNMR is different than in CHEESY-detected NMR. Nevertheless, a difference in signal-to-noise is visible. In (D) the two ^{14}N single-quantum transitions (lower frequencies) are resolved (see [44]), while the double-quantum transition overlaps with the ^{1}H peak and the ^{14}N+^{1}H combination peak.

2.4.2   *EPR-correlated hyperfine spectroscopy*

Correlating the hyperfine spectrum in Figure 2.7 (D) to the EPR spectrum is straightforward. The whole detection sequence as well as the magnetic field is held constant, and only the position of the HTA pulse is swept step by step, giving the indirect dimension. Altough an EPR spectrum is detected in the direct dimension, the information in FT EPR-detected NMR and CHEESY-detected NMR is the hole pattern, and thus the nuclear frequencies. It is sensible to shift the nuclear spectrum such that the zero frequency corresponds to the position of the HTA pulse for each point of the indirect dimension. The EPR dimension then corresponds to the sweep of the HTA pulse frequency. The resulting EPR-correlated CHEESY-detected NMR spectrum for compound **1** is shown in Figure 2.8. The spectrum shows a strong central hole and two intense peaks arising from weakly coupled protons. The g-tensor and nitrogen hyperfine tensor are nearly collinear. Thus, at the g_{zz} position (the low-frequency edge) of the EPR spectrum, the correlation pattern shows a nitrogen hyperfine coupling of about 95 MHz. The resolution is not sufficient to easily discern in the correlation pattern the additional splitting of these nitrogen peaks, which is approximately twice the nuclear Zeeman frequency with additional splitting induced by the nuclear quadrupole interaction. At the high-frequency edge of the spectrum, the hyperfine coupling is smaller (around 11.5 MHz) and the spectrum becomes rather crowded. The shape of the spectrum is indicative of the relative orientation of the hyperfine coupling tensor with respect to the g-tensor. Additional lines indicate the presence of combination peaks, where both the spin state of the nitrogen as well as a weakly coupled proton change. These combination peaks become more intense if stronger HTA pulses are used (see SI of [22]). In the 2D version, these combination peaks look like a copy of the nitrogen peaks, but shifted by the Zeeman frequency of the protons in both dimensions. Such combination frequencies were also observed in [26] and more pronounced in Q-band in [38]. Their presence is the reason why it took rather long to acquire the 2D spectrum. In order to avoid that strong combination peaks obscure the spectrum we could work only with moderate nominal flip angles of the HTA pulse, resulting in shallow nitrogen holes.

In order to obtain a spectrum with better resolved nitrogen peaks and less intense proton and proton combination peaks, we also obtained an EPR-correlated CHEESY-detected NMR spectrum of the partially deuterated compound **2**, see Figure 2.9. Because no combination peaks obscure the spectrum, the nominal flip angle of the HTA pulse could be increased by

FIGURE 2.8: Experimental EPR-correlated CHEESY-detected NMR spectrum of compound **1**. The contour lines show isohypses from 0.01 to 0.06 of the complete 2D spectrum, including the central hole. Reference spectrum on top. Measurement time 16.25 h, 61 points along the indirect dimension (5 MHz steps), 217 μM, 4 μs Gauss pulse with $\nu_1 \approx 5$ MHz at the centre of the resonator. 200/100 ns chirp echo with $\Delta f = 400$ MHz. Integration window of 3 μs.
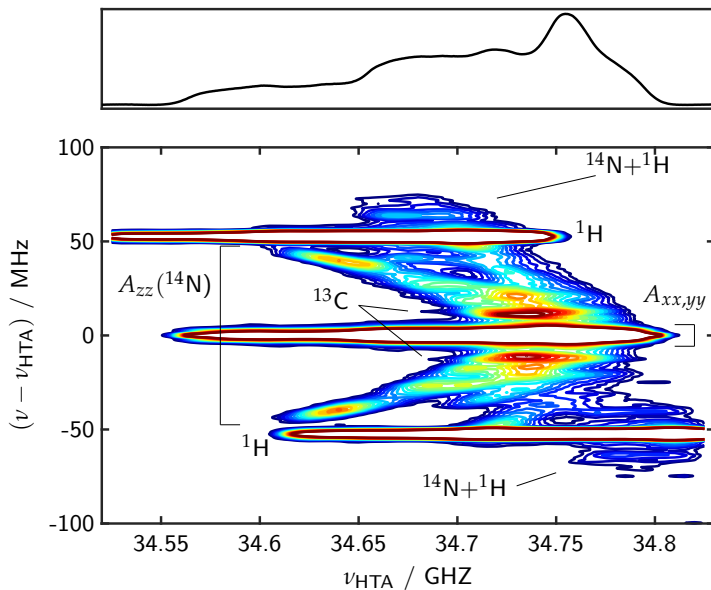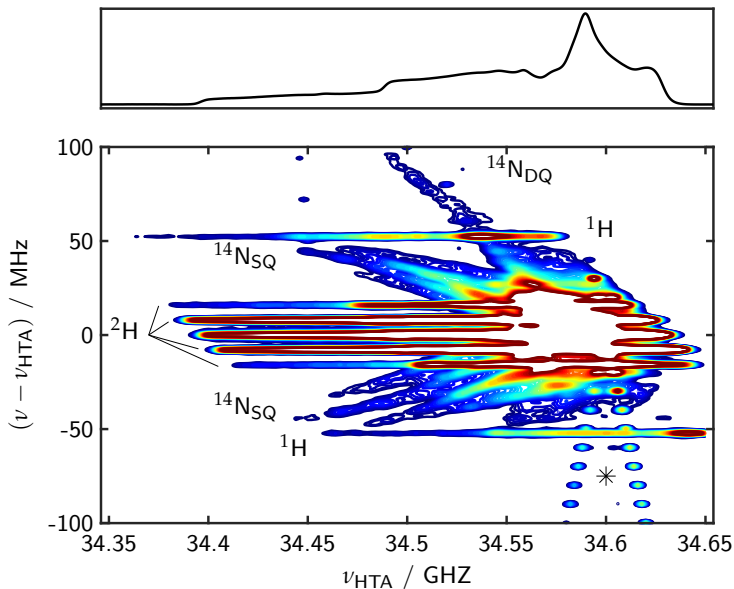
FIGURE 2.9: Experimental CHEESY-detected NMR spectrum of compound **2**. The contour lines show isohypses from 0.007 to 0.045 of the complete 2D spectrum, including the central hole. Reference spectrum on top. Measurement time 15.1 h, 150 points along the indirect dimension (2 MHz steps), 100 μM, 20 μs Gauss pulse with $\nu_1 \approx 3.5$ MHz at the centre of the resonator. 200/100 ns chirp echo with $\Delta f = 400$ MHz. Integration window of 3 μs.

increasing its length. The nitrogen peaks at the low-frequency edge of the EPR spectrum are much better resolved, and due to the long HTA pulse compared to Figure 2.8 one can also see the nitrogen double-quantum peak. On the other hand, the deuteration leads to strong single-quantum and double-quantum peaks arising from the weakly coupled deuterons. Artifacts important in the context of CHEESY detection are marked with an asterisk. We strongly suspect that they arise from spurious frequencies caused by the frequency mixing before the detection. They are most likely always present, but only strong enough if any of the holes lies on the maximum of the nitroxide EPR-spectrum. We investigated this hypothesis with a sample of γ-irradiated quartz glass (see SI of [22]). Such artefacts can be recognized by shifting the local oscillator frequency, since they do depend on it while the real peaks do not.

Another interesting system for EDNMR studies, especially in Q-band, are Mn(II) complexes [38]. The EPR-correlated CHEESY-detected NMR spectrum of hexaquamanganese(II) is shown in Figure 2.10. First of all, it is notable that with our resonator, it is possible to detect EDNMR peaks in the conventional way over a range of more than 600 MHz. A comprehensive explanation of the origin and position of all the basic frequency and combination peaks in this spectrum can be found in a recent article [38]. Due to the fact that both the g- and A-tensor are isotropic, correlation of the nuclear frequencies to the EPR spectrum does not reveal additional information. By illustrating the bandwidth that can be achieved, this 2D spectrum shows the current limitations of our new approach. The excitation- and detection bandwidth is still not enough to detect the whole EPR spectrum of the manganese complex. Note that the signal-to-noise ratio is not the same over the whole spectrum. Side holes that lie on the narrow central ($m_S = -1/2 \leftrightarrow +1/2$) transitions can be detected with much higher sensitivity than those lying on the satellite transitions. This is why the spectrum seems to depend strongly on the position of the HTA pulse. The spectrum on the right is not a projection, but a slice through the diagonal (although in this case the difference is minor). This slice corresponds to the conventionally recorded EDNMR spectrum (for a direct comparison see the SI of [22]). This indicates that EDNMR with a long integration window does not need selective observation pulses for high resolution.
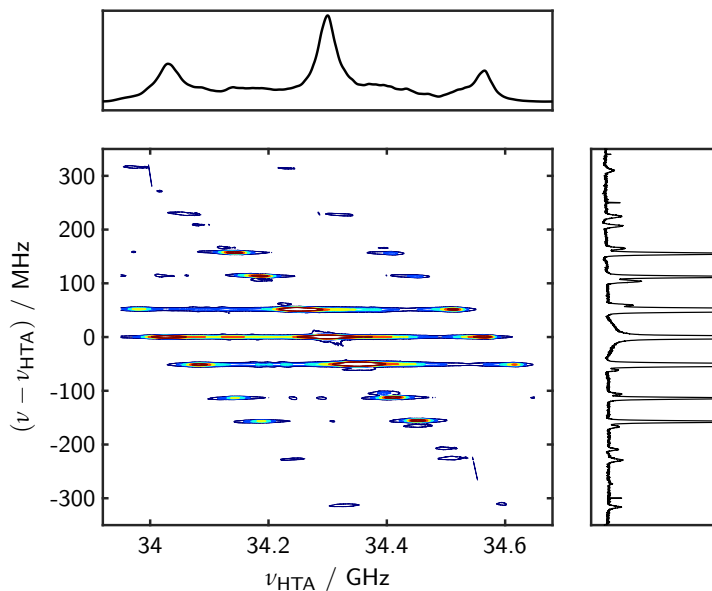
FIGURE 2.10: Experimental EPR-correlated CHEESY-detected NMR spectrum of $[Mn(H_2O)_6]^{2+}$. The contour lines show isohypses from 0.028 to 0.19 of the complete 2D spectrum, including the central hole. Reference spectrum on top. Measurement time 14.5 h, 3500 points along the indirect dimension (0.2 MHz steps), 2.3 mM, 1 μs Gauss pulse with $\nu_1 \approx 5$ MHz at the centre of the resonator. 200/100 ns chirp echo with $\Delta f = 0.8$ GHz. Integration window of 1 μs. On the right is a slice through the diagonal, which corresponds to the conventional spectrum with observation of the central maximum. Note that the x-axis is the frequency of the HTA pulse, and thus maps the position of forbidden transitions in the spectrum.

2.4.3 *HYSCORE-type correlations*

The isolated lines of the hexaquamanganese complex make it a nice model system to illustrate the correlation experiment introduced above. Fig. 2.11 shows a 1D CHEESY-detected NMR spectrum on top and two selected correlation traces on bottom, with the HYS pulse applied at the indicated positions. The reduced intensity of the connected holes clearly indicate which pairs of peaks belong to the same nucleus and also the strong coupling regime.
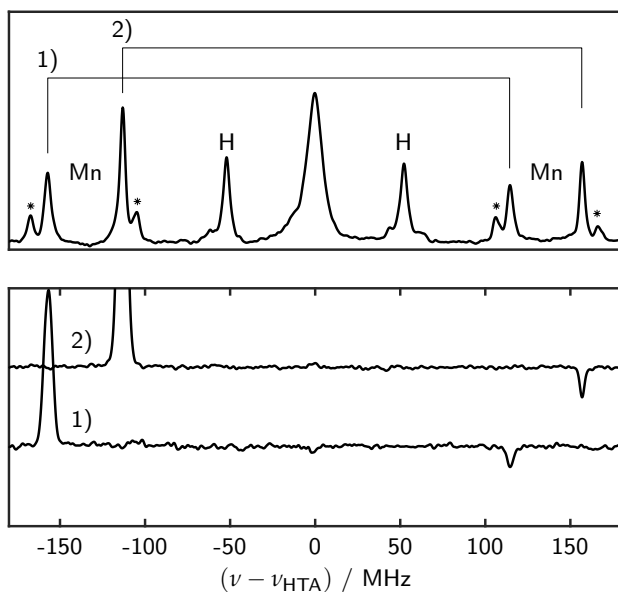
FIGURE 2.11: Top: CHEESY-detected NMR spectrum of $[Mn(H_2O)_6]^{2+}$. Bottom: Difference in hole intensities with and without the HYS pulse before the HTA pulse. The HYS pulse was applied to the peaks at -157.2 and -113.2 MHz, respectively. The corresponding negative peaks on the other side of the central hole clearly indicate, which peaks correspond to the same nucleus and that $|A|/2 > |\omega_I|$. Asterisks indicate Mn-^{1}H combination peaks.

2.5   CONCLUSION AND OUTLOOK

The CHEESY-detected NMR experiment makes use of recently developed ultra-wide band (UWB) detection in EPR. It is easy to set up if coherent arbitrary waveform excitation with sufficient bandwidth and a detection arm with sufficient bandwidth are available. It yields a true multiplex advantage over the similar conventional EDNMR. Even if it is impossible to excite the complete EPR spectrum, this approach is still useful, since it is sufficient to excite and detect the side holes.

The obtained hyperfine spectrum can be correlated to the EPR spectrum. In this work, this was achieved by sweeping the frequency of the hole burning pulse, but one could also step the magnetic field. In this case, a reference spectrum has to be recorded at each field position.

By applying a selective π pulse (termed HYS pulse) before the HTA pulse, peaks in the hole pattern can be correlated that belong to the same nucleus in different electron spin manifolds. This can help to disentangle a crowded spectrum and gives information about the coupling regime of different nuclei. We showed selected correlation traces for hexaquamanganese(II), a sample where peaks are resolved already in the 1D spectrum. In the case of broader and overlapping peaks, it can be necessary to record a full 2D spectrum, *vide infra*. In general, the HYS pulse also creates side holes, but they will have the same sign as the hole at the frequency of this pulse, while the change in intensity of the correlated holes has the opposite sign. In the case of weak holes, one might gain sensitivity in this experiment by gradually changing the power of the HYS pulse. This generates a nutation curve, which is anti-correlated to the intensity change of the side hole.

All presented spectra were recorded in Q-band ($\approx$35 GHz). The resolution of the spectra could be enhanced dramatically by performing the measurements in W-band ($\approx$95 GHz), where the nuclear Zeeman frequencies are larger and better separated. We are not aware of any spectrometer that is capable of coherent UWB detection in W-band to date (2018). So far, only incoherent setups are published [45]. At higher fields, the forbidden transitions of weakly coupled nuclei become weaker, but to a certain extent this can be compensated by using an appropriate HTA pulse. Such compensation is more transparent, more versatile, and easier to set up than power matching in ESEEM and HYSCORE experiments [29, 46, 47]. The forbidden transitions of strongly coupled nuclei ($|A/2| > \omega_I$) even become stronger at higher fields. Although spectra showing g-anisotropy become broader, it is important to note that the chirp pulses do not need to cover the complete EPR spectrum; it is

sufficient to cover the nuclear frequencies. For large hyperfine couplings the width of the NMR spectrum increases only moderately in W-band compared to Q-band. In conclusion, our findings strongly motivate the implementation of coherent UWB detection in W-band.

2.6   ADDITIONAL DATA: 2D CHEESY AND CHEMICAL APPLICATIONS

In the following, we show some additional data that illustrate the usefulness of CHEESY-detected NMR. Figure 2.12 shows a full, two-dimensional CHEESY spectrum of $[Cu(DETA)Im(H_2O)_2]$ (DETA = Diethylenetriamine = 2,2'-Iminodi(ethylamine), Im = Imidazole). The x-axis shows the direct dimension, i. e. the Fourier transform of the directly sampled echo signal, while the y-axis shows the difference between the HTA pulse, and the HYS pulse, i. e. the selective inversion. For each frequency of the HYS pulse, a 1D CHEESY spectrum is acquired. Once with the selective inversion, and once without, but both with the HTA pulse. The difference of the two is calculated for each frequency of the HYS pulse, and the resulting two-dimensional spectrum is plotted. On top, the usual one-dimensional CHEESY-detected NMR spectrum is plotted. The spectrum is was acquired at the magnetic field corresponding to the maximum of the echo-detected field sweep. Clearly, it would be very difficult to confidently assign the one-dimensional spectrum (A_r indicates the coupling to the remote nitrogen in the imidazole ligand). For the small couplings, only shoulders, and nearly no real peaks are visible. However, in the two-dimensional spectrum, the couplings and nuclear Zeeman frequencies can easily be read out. The right quadrant only shows weakly coupled nuclei. Single-quantum (SQ) and double quantum (DQ) transitions are visible at once and twice the nuclear Zeeman frequency. The SQ are broadened along the diagonal because of additional nuclear quadrupole interaction, which has no first order contribution to the DQ transitions. The directly bound nitrogen nuclei are strongly coupled, and accordingly are only visible in the left quadrant. Again, there is a contribution from the nuclear quadrupole interaction. A complete assignment of all four strongly coupled nitrogens is beyond the scope of this work. Very likely orientation selection strongly affects these peaks.

Last but not least, we shortly mention a chemical application of the method. More details can be found in [23]. In brief, a Ti(III) catalyst, namely $[Ti(nacnac)(CH_2tBu)_2]$ (**1**), was shown to polymerise ethylene. The proposed mechanism predicted that one of the neopentyl ligands should be lost to make space for binding of ethylene and the growing polymer chain. To

test this hypothesis, the α-carbons of the neopentyl ligands were labelled with ^{13}C (giving **1***), see Figure 2.13 (top). The corresponding signal in a hyperfine spectrum should then be reduced upon polymerisation, as less ^{13}C is directly bound to Ti. Unfortunately, neither HYSCORE nor ENDOR yielded clear spectra where the ^{13}C peaks could be assigned, and their reduction measured. However, a 2D CHEESY spectrum clearly showed a peak along the anti-diagonal corresponding to ^{13}C that was absent in the unlabelled compound (data not shown here). The couplings of both the nitrogen nuclei as well as the ^{13}C were in reasonable agreement with DFT calculations. The experimental 1D CHEESY-spectra and theoretical predictions of the polymerisation experiment are shown in Figure 2.13 (bottom). The spectra before and after polymerisation are shown in black and red, respectively. The positions of ^{13}C SQ peaks, as well as a ^{13}C+^{14}N combination peak are indicated by stick spectra. The reduced intensity at these positions is highlighted in light blue. Note that the exact ^{14}N couplings are slightly different in the DFT prediction. However, their intensity does not change at all in the experimental spectrum, indicating that the NacNac ligand is unaffected during the polymerisation reaction. The spectrum was simulated with an algorithm that will be introduced in Chapter 3. Nitrogen hyperfine
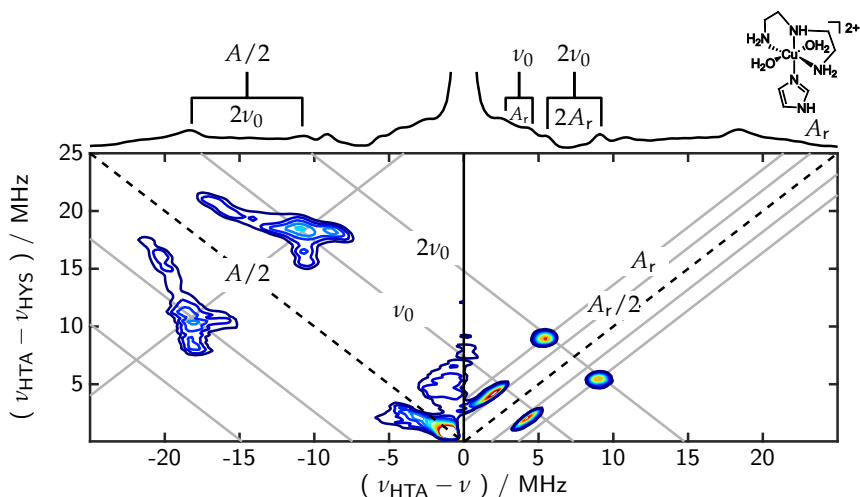

FIGURE 2.12: 2D CHEESY-detected NMR of Cu-DETA-Im. The structure is shown at the top right. The 1D CHEESY-detected NMR spectrum on top. Right quadrant: weakly coupled nuclei, left quadrant: strongly coupled nuclei. Hyperfine couplings and nuclear Zeeman frequencies are indicated in the figure.
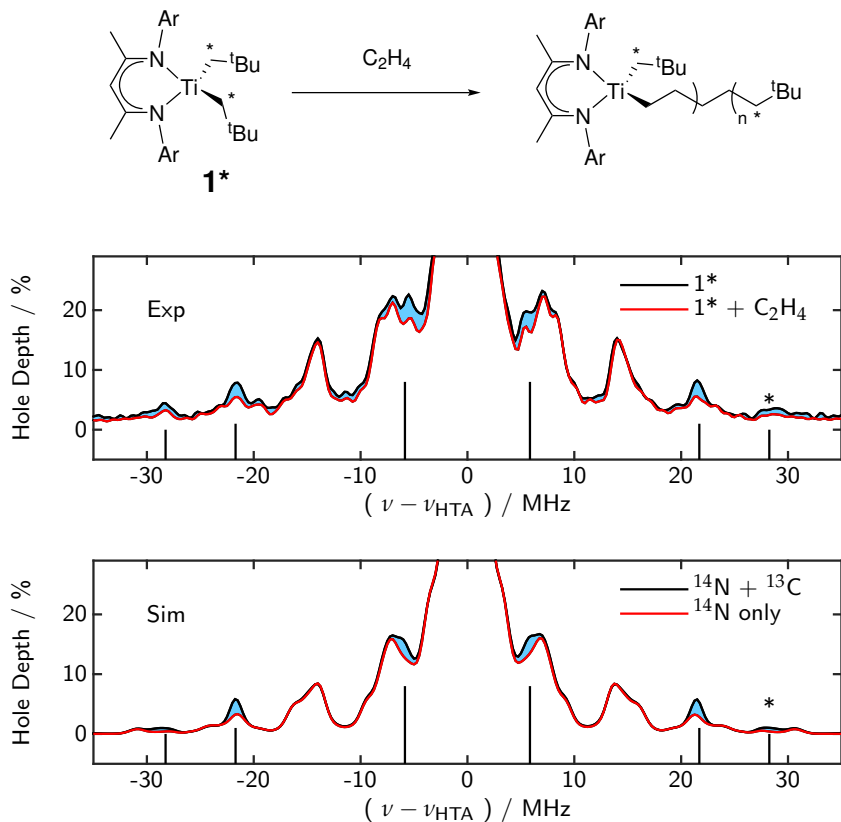
FIGURE 2.13: Detection of a ligand loss during ethylene polymerisation with CHEESY-detected NMR. Top: reaction scheme. Bottom: Experimental and simulated spectra of the complex with and without ^{13}C.

and quadrupole couplings were calculated by DFT. The ^{13}C peaks were slightly adjusted from the DFT calculations to fit the experimental spectra.

In conclusion, CHEESY-detected NMR of the ^{13}C-labelled catalyst strongly supports the proposed mechanism, that includes back donation from the singly occupied molecular orbital (SOMO) on Ti to the metal-carbon π-bond.

ELDOR-DETECTED NMR OF CU(II)-PORPHYRIN DIMERS

Heute ist Bildung Vorbereitung auf den Kampf um Ressourcen. Wenn man Bildung so auffasst, entspringen dem Bildungssystem gute und schlechte Überwältiger, aber nicht […] reflektierte, kreative Menschen.

Today, education is the preparation for the fight for resources. If you understand education in this way, then our system creates good and bad overwhelmers, and not […] reflected and creative human beings. (Translation mine).

— Michael Hampe

SUMMARY

The pulse EPR method ELDOR-detected NMR (EDNMR) is applied to two Cu(II)-porphyrin dimers that are suitable building blocks for molecular wires. One of the dimers is *meso-meso* singly linked, the other one is β,*meso*,β-fused. We show experimentally and theoretically that EDNMR spectra contain information about the electron-electron couplings. The spectra of the singly linked dimer are consistent with a perpendicular arrangement of the porphyrin planes and negligible exchange coupling. In addition, the resolution is good enough to distinguish ^{63}Cu and ^{65}Cu in frozen glassy solution and to resolve a metal-ion nuclear quadrupole coupling of 32 MHz. In the case of the fused dimer, we observe so far unreported signal enhancements, or anti-holes, in the EDNMR spectra. These are readily explained in a generalized framework based on [Cox *et al., Journal of Magnetic Resonance*, 2017, **280**, 63-78], if an effective spin of $S = 1$ is assumed, in accordance with SQUID measurements. The positions of the anti-holes encode a zero-field splitting with $|D| = 240$ MHz, which is about twice as large as expected from the point-dipole approximation. These findings demonstrate the previously unrecognized applicability and versatility of the EDNMR technique in the quantitative study of complex paramagnetic compounds.

3.1 INTRODUCTION

Electron-electron double resonance (ELDOR)-detected NMR (EDNMR) is a pulse EPR technique that was introduced by Schosseler *et al.* in 1994 [24]. It is intended for the measurement of hyperfine couplings to nuclei in the vicinity of unpaired electrons and works best for moderately sized couplings that are not resolved in EPR spectra, but may also be hard to access by electron spin echo envelope modulation (ESEEM) or electron nuclear double resonance (ENDOR) techniques. For weakly coupled, low-γ nuclei (*e.g.* ^{14}N), EDNMR is most useful at high fields and high frequencies, *e.g.* at W-band

frequencies ($\approx$95 GHz) [25], and became popular only relatively recently [26, 28, 48]. It proved to be an invaluable tool, for example, in the study of the oxygen-evolving complex of photosystem II [49] and the spectroscopic investigation of ATP turnover in ABC exporters [50]. EDNMR was also applied to investigate Mn(II) complexes inside cells [51]. Only in a few cases was the technique applied at Q-band frequencies ($\approx$35 GHz) [38, 52, 53].

In contrast to their widespread use for ligand nuclei, hyperfine techniques have only in a few cases been applied to gain information about the central ions of metal complexes [52, 54–60]. Only the last two studies cited here made use of EDNMR, although it might be more sensitive than ENDOR if the lines are mainly inhomogeneously broadened - which is often the case for metal hyperfine couplings.

Several groups have introduced modifications and extensions in order to increase the information content of EDNMR spectra. An additional microwave (mw) or radio-frequency (rf) source is employed in the triple resonance techniques 2D-EDNMR [35] and THYCOS [61], respectively, that correlate hyperfine couplings of several nuclei coupled to the same paramagnetic centre. Alternatively, the nuclear frequency spectrum can be correlated to the EPR spectrum in order to gain information about the relative orientation of the tensors [25]. With arbitrary waveform generator (AWG)-controlled spectrometers, it is possible to detect the complete hole pattern in one shot by the use of chirp pulses [22]. In this context, it was also shown that it is possible to obtain hyperfine sublevel correlation (HYSCORE)-type information with hole burning experiments. The latter experiment can also be performed in a classical EDNMR fashion without chirp pulses.

In this study we highlight, on the example of two Cu(II)-porphyrin dimers, that even the basic form of EDNMR can provide more information than generally appreciated, in particular, on metal-ion nuclear quadrupole and on electron-electron couplings.

Porphyrins are suitable components for molecular wires that mediate long distance charge transport, because of their large delocalized π-systems, small HOMO-LUMO gaps, rigid frameworks, and small reorganisation energies [62–66]. The edge-fused porphyrin tapes, pioneered by Osuka and coworkers [67–69], exhibit particularly strong electronic coupling, leading to highly conductive molecular wires [70]. Here we report an EDNMR investigation of two copper porphyrin dimers: the edge-fused dimer $\boldsymbol{f}$-**CuP2** and the *meso-meso* singly linked dimer **CuP2**; see chemical structures in Figure 3.1. The dimers $\boldsymbol{f}$-**CuP2** and **CuP2** are very similar to copper porphyrin dimers reported previously [68, 71], except that the compounds investigated here have bulky
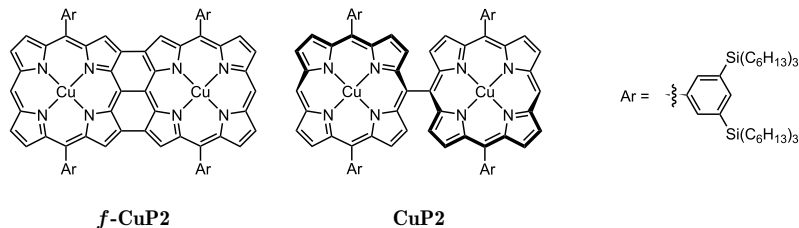
FIGURE 3.1: Chemical structures of the Cu(II)-porphyrin dimers investigated in this study.

3,5-bis(trihexylsilyl)phenyl substituents to provide high solubility and prevent aggregation [72]. Previous crystallographic studies [68, 71] have shown that the Cu-Cu distance in both of these dimers is in the range of 8.3-8.4 Å, and that the planes of the two porphyrin units are almost perpendicular in **CuP2**, whereas they are coplanar in **ƒ-CuP2**. DFT studies of **CuP2** revealed that the rigidity is much higher compared to ethyne or butadiyne-linked structures [73]. The twisted conformation of **CuP2** prevents orbital overlap between the π-systems of the porphyrin units [66]. In a different study it was demonstrated that copper(II)-porphyrin dimers, similar to **ƒ-CuP2** and **CuP2**, exhibit anti-ferromagnetic coupling between the metal centres [74]. Variable-temperature magnetic susceptibility measurements in the range 2-300 K on the fused dimer revealed that the value of χT drops sharply at temperatures below 20 K, and a Bleaney-Bowers fit to these data gave a J value of 1.43 cm^{-1} (for $\hat{\mathcal{H}} = 2J\vec{\hat{S}}_1\vec{\hat{S}}_2$). Recently, it was also shown that a doubly fused Cu(II)-porphyrin dimer exhibits electrocatalytic porperties for hydrogen evolution [75].

Here we demonstrate that the EDNMR spectra of **CuP2** are consistent with a small exchange coupling between the Cu(II) centres and a perpendicular orientation of the porphyrin planes. The strong orientation selection of the experiment leads to a striking resolution of the copper hyperfine peaks and makes it possible to resolve the isotopes ^{63}Cu and ^{65}Cu at natural abundance in glassy frozen solution. Additionally, we determine the copper quadrupole coupling in a similar way as previously shown for nitroxides [44]. A recently proposed fast simulation algorithm [26] quantitatively reproduces the experiment in spectral regions where only copper signals contribute to the spectrum. In the case of a relatively strong exchange coupling in **ƒ-CuP2** (79 GHz for $J\vec{\hat{S}}_1\vec{\hat{S}}_2$, corresponding to 1.32 cm^{-1} for $2J\vec{\hat{S}}_1\vec{\hat{S}}_2$), we observe anti-holes or signal enhancements in the EDNMR spectra. These anti-holes are
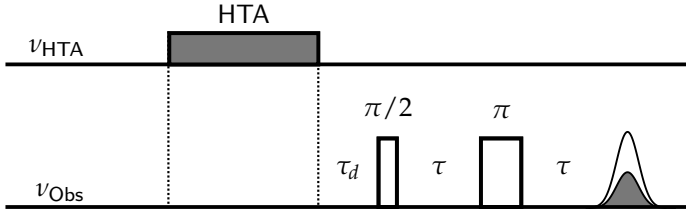
FIGURE 3.2: Pulse sequence for EDNMR. Usually, a long and weak high turning angle pulse burns a hole at ν_{HTA}. A spin echo (or alternatively, an FID) is detected at ν_{Obs}. The latter frequency is kept fixed in the centre of the resonator, while ν_{HTA} is swept. If $\nu_{\mathrm{HTA}} - \nu_{\mathrm{Obs}}$ matches the difference between two allowed or weakly allowed transitions sharing a level, the echo intensity changes.

in line with our previous general description of polarisation changes in hole burning [22] and their correlation to the EPR spectrum can be simulated with a generalized algorithm that can treat arbitrary spin systems. The correlation confirms the expected orientation of the dipolar coupling tensor with respect to the **g**- and **A**-tensors of the Cu(II)-porphyrin subsystems. In addition, the magnitude of the dipolar coupling is found to be significantly larger than expected from a simple point-dipole approximation, contradicting previous interpretations of the CW EPR spectra of similar Cu(II)-porphyrin dimers [74, 75]. Since the information content of the expriment goes beyond the nuclear frequencies, the *NMR* in ELDOR-detected NMR can be misleading.

3.2   THEORY

3.2.1   *Description of ELDOR-detected NMR and ELDOR-detected hole burning*

The pulse sequence for EDNMR is shown in Figure 3.2. The hole burned at $\nu_{\mathrm{HTA}} = \nu_{\mathrm{Obs}}$ is referred to as the central hole. This central hole obscures side holes at low frequencies. If a transition irradiated by the hole burning pulse shares a level with another transition that is either fully or weakly allowed, the polarisation of the latter transition is changed and a side hole (or side anti-hole) is created. Anisotropic hyperfine couplings of the same order of magnitude as the nuclear Zeeman frequency lead to weakly allowed electron-nuclear transitions that correspond to side holes offset by the nuclear frequencies. By changing the frequency of the HTA pulse in a stepwise fashion, one can obtain the spectrum of the side holes if the variable echo intensity is plotted against
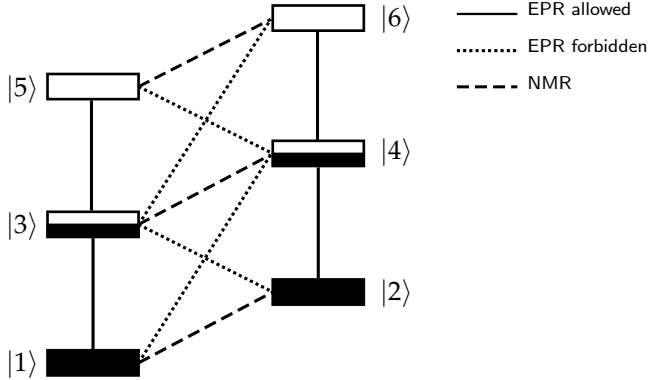
FIGURE 3.3: Energy level diagram of a system where allowed transitions share a common level. The subsystem $\{|1\rangle, |2\rangle, |3\rangle, |4\rangle\}$ is typically discussed in the context of EDNMR. Connected allowed transitions, *e.g.* $(|1\rangle \rightarrow |3\rangle)$ and $(|3\rangle \rightarrow |5\rangle)$ are usually ignored.

$\nu_{\mathrm{HTA}} - \nu_{\mathrm{Obs}}$. This experiment is usually applied for the detection of nuclear frequencies, hence the name ED*NMR*. The standard description of EDNMR uses a two-spin system consisting of one electron and one nucleus [26, 28], usually also of spin-1/2. This four-level system corresponds to the subsystem $\{|1\rangle, |2\rangle, |3\rangle, |4\rangle\}$ in Figure 3.3. If the HTA pulse drives, for example, the transition $(|1\rangle \rightarrow |4\rangle)$, which is formally forbidden, then the polarisation, and thus the signal, of the formally allowed transitions $(|1\rangle \rightarrow |3\rangle)$ and $(|2\rangle \rightarrow |4\rangle)$ is also decreased. This results in the mentioned side holes offset by the NMR frequencies. In an inhomogeneously broadened EPR line, any of the allowed or forbidden EPR transitions in the mentioned subsystem can be driven by the HTA pulse. In this case, the peak intensity (*i.e.*, the hole depth h) is described as

$$h = 1 - I_{\mathrm{a}} \cos \left(\beta_0 \sqrt{I_{\mathrm{f}}} \right) - I_{\mathrm{f}} \cos \left(\beta_0 \sqrt{I_{\mathrm{a}}} \right) \quad , \qquad (3.1)$$

where I_{a} and I_{f} are the transition probabilities of the allowed and forbidden transitions, respectively, and β_0 is the nominal flip angle. This description is suitable to explain the basic phenomenon of EDNMR as well as some quantitative aspects, but it is restricted to systems with a single electron spin with spin-1/2. The same description is applied to some high-spin systems, such as Mn^{2+} $(S = 5/2)$, by considering only the central $(|-1/2\rangle \rightarrow |1/2\rangle)$ transition and treating it as a fictitious spin-1/2. However, this approximation does not generally hold for high-spin systems or systems of several moderately

coupled electron spins. If several unpaired electrons are present in a system, there are always allowed transitions that share a common level. An example for such a system is shown in Figure 3.3. Some of the three-level subsystems relevant for hole burning [22] behave like those in a usual electron-nuclear two-spin system (as discussed before), but the complete level system cannot be reduced only to subsystems of this kind. For example, the inversion of the allowed transition ($|1\rangle \rightarrow |3\rangle$) will lead to an enhancement of transition ($|3\rangle \rightarrow |5\rangle$), which is also allowed. Additionally, inverting the forbidden transition ($|1\rangle \rightarrow |4\rangle$) will decrease the polarisation of ($|1\rangle \rightarrow |3\rangle$) and ($|2\rangle \rightarrow |4\rangle$), but it will *increase* the polarisation of ($|4\rangle \rightarrow |6\rangle$). Clearly, the current understanding of EDNMR is insufficient to describe such systems. In a general description, all transitions could be observed, all transitions could be pumped, and all levels are potentially connected.

In the case of several unpaired electrons, the side holes and anti-holes will also contain information about the electron-electron coupling, or, if this coupling is very large, about the zero-field splitting. In these cases, we simply denote the method as ELDOR instead of ELDOR-detected NMR.

ELDOR was used before for the quantification of electron spectral diffusion [76]. However, in this context, no anti-holes were observed, and the high concentration (10–40 mM) that was used makes electron spectral diffusion a bulk property, whereas we focus on interactions of isolated systems. Note that the pulse sequence is the same, but the parameters for the hole burning pulse are vastly different. Measurements of electron spectral diffusion are carried out with HTA pulses of about 100 ms, EDNMR normally uses pulses of about 5–50 µs, and some of the spectra shown in this work were even acquired with pulses as short as 50 ns.

Interestingly, the signal enhancement by inversion pulses on connected transitions that correspond to the anti-holes has already been used as a means of sensitivity enhancement in NMR [77] and EPR [78, 79]. However, to the best of our knowledge, this kind of signal enhancement has not been used to date as a spectroscopic tool.

3.2.2 *Simulation Algorithm*

The simulation algorithm used in this work is based on earlier work by Cox *et al* [26]. Before we discuss our extensions, we need to recapitulate the important steps and comment on the validity of the approximations.

1. Generate the Hamiltonian $\hat{\mathcal{H}}_0$ for a particular orientation.

2. Diagonalize $\hat{\mathcal{H}}_0$ to get the energy levels and transition frequencies.

3. Calculate transition probabilities between the eigenstates of the system.

4. Introduce orientation selection by weighting the transitions according to a Gaussian function centreed at the detection frequency.

5. Calculate the inversion efficiency of each transition by assuming selective excitation by the HTA pulse and using a Bloch picture.

6. Check which transitions share a common level and calculate the intensity change of the observed transitions due to the polarisation transfer induced by the HTA pulse.

7. Build the spectrum by adding up all possible peaks and orientations.

The approach is valid as long as the excitation is transition-selective within each three-level subsystem and spectral diffusion processes are negligible. It is orders of magnitudes faster than a full quantum-mechanical calculation of spin dynamics employing the Liouville-von Neumann equation. While EDNMR spectra including some ^{63,65}Cu signals have been interpreted before taking into account off-resonance effects and relaxation, [35, 80] we will show here that the above algorithm can quantitatively reproduce our experimental EDNMR spectra.

In addition to the spin system, one needs to provide the program with the length and amplitude of the HTA pulse, t_{HTA} and ν_1, the phase memory time of the electron spins, T_{m}, and the quality factor of the resonator, Q_{res}. These parameters can be determined experimentally.

The published implementation of Cox *et al.* cannot be used to simulate arbitrary spin systems, because it makes implicit assumptions about the structure of the Hamiltonian, namely the m_S sub-blocks. Signal enhancements are not possible. In the general case, m_S is not necessarily a good quantum number. Additionally, the published version only considers ($m_S = -1/2 \rightarrow m_S = 1/2$) transitions, which do not exist at all in the case of $\boldsymbol{f}$-**CuP2**. Therefore, we extended the published algorithm to an electron-nuclear spin system that may contain more than one unpaired electron. A more detailed description is given in the ESI of [8][1], (see section S.5) and the code is available online.

3.2.3 *Description of the spin system*

The structures of the compounds investigated in this work are shown in Figure 3.1. While there are many nuclei with nuclear spin $I > 0$, we focus on

---

1 Direct PDF link: `https://www.rsc.org/suppdata/c9/cp/c9cp01760g/c9cp01760g1.pdf`

the copper nuclei and the unpaired electrons, which contribute the dominating interactions [81].

The Hamiltonian that describes a system of two electrons $S_1 = S_2 = 1/2$ and two nuclei $I_1 = I_2 = 3/2$, with zero hyperfine coupling between S_1 and I_2 as well as between S_2 and I_1, reads in *linear frequency* units[2]

$$\hat{H} = \sum_{i=1}^{2} \left(\frac{\mu_B}{h} \vec{B}_0 \mathbf{g}_i \vec{S}_i - \frac{\gamma_n}{2\pi} \vec{B}_0 \vec{I}_i + \vec{S}_i \mathbf{A}_i \vec{I}_i + \vec{I}_i \mathbf{P}_i \vec{I}_i \right) + \vec{S}_1 \mathbf{d} \vec{S}_2 + J \vec{S}_1 \vec{S}_2 \quad . \quad (3.2)$$

The first term describes the electron Zeeman interaction, where μ_B is the Bohr magneton, h the Planck constant, $\vec{B}_0$ the external static magnetic field and $\mathbf{g}$ the electron g-tensor. The second term describes the nuclear Zeeman interaction, where γ_n is the gyromagnetic ratio of the respective nucleus. $\mathbf{A}_i$ denotes the hyperfine coupling between electron i and nucleus i. The last term in parentheses is the nuclear quadrupole interaction, which is given in its principal axis system by [9]

$$\mathbf{P} = \begin{pmatrix} P_x & 0 & 0 \\ 0 & P_y & 0 \\ 0 & 0 & P_z \end{pmatrix} = \begin{pmatrix} K(-1+\eta) & 0 & 0 \\ 0 & K(-1-\eta) & 0 \\ 0 & 0 & 2K \end{pmatrix} \quad (3.3)$$

with

$$K = \frac{e^2 qQ/h}{4I(2I-1)} \quad . \quad (3.4)$$

The term e^2qQ/h is also known as the quadrupole coupling constant (`Sys.Q` in *EasySpin* [82]) and is related to the electric field gradient at the position of the nucleus ($eq = V_{zz} = \partial^2 V/\partial z^2$). The nuclear quadrupole moment enters via the term eQ. The asymmetry parameter is given by $\eta = (V_{xx} - V_{yy})/V_{zz}$. The tensor $\mathbf{d}$ contains the symmetric electron-electron coupling. If the only contribution to $\mathbf{d}$ is the dipole-dipole coupling, and the point-dipole approximation is valid, then this interaction is given in its principal axis system by

$$\mathbf{d} = \frac{\mu_0}{4\pi h} \frac{g_1 g_2 \mu_B^2}{r_{12}^3} \begin{pmatrix} 1 & 0 & 0 \\ 0 & 1 & 0 \\ 0 & 0 & -2 \end{pmatrix} \quad . \quad (3.5)$$

The constant μ_0 is the vacuum permeability and r_{12} the distance between the unpaired electrons. For $r_{12} = 1$ nm, the prefactor amounts to $\frac{\mu_0}{4\pi h} \frac{g_1 g_2 \mu_B^2}{r_{12}^3} =$

---

2 Experimental spectra are more easily interpreted in linear frequencies, but mathematical derivations are easier in angular frequency units.

52.041 MHz. The term $J\vec{\hat{S}}_1\vec{\hat{S}}_2$ describes the isotropic exchange coupling between the electron spins. Note that several other conventions exist in the literature. In this convention, J describes the energetic singlet-triplet separation, and a positive J describes an anti-ferromagnetic coupling with the singlet state at lower energy than the triplet state.

3.2.3.1   *Limit of large exchange coupling*

If the exchange coupling J is large, a system with several electron spins is best described in a coupled representation. For simplicity, we focus here on a system with two electron spins. Extension to a system with more than two unpaired electrons is straightforward. For two electron spins, the energy levels are split into a singlet and a triplet state (separated by J for $J\vec{\hat{S}}_1\vec{\hat{S}}_2$). The singlet is EPR-silent, and the triplet state can be described by an effective spin 1 [83]. The effective hyperfine coupling in the triplet manifold is halved compared to the uncoupled case (see also section 3.3.5 *vide infra*), but the effective electron spin couples to any nucleus that has non-zero hyperfine coupling with one of the electron spins in the uncoupled representation, in the present case to both copper nuclei. The dipolar coupling in the uncoupled basis manifests itself as a zero-field splitting (ZFS) in the coupled basis with the Hamiltonian

$$\hat{\mathcal{H}}_{\mathrm{ZFS}} = \vec{\hat{S}}\mathbf{D}\vec{\hat{S}} \tag{3.6}$$

$$\mathbf{D} = \begin{pmatrix} D_x & 0 & 0 \\ 0 & D_y & 0 \\ 0 & 0 & D_z \end{pmatrix} = \begin{pmatrix} -D/3+E & 0 & 0 \\ 0 & -D/3\text{--}E & 0 \\ 0 & 0 & 2D/3 \end{pmatrix} \tag{3.7}$$

$$D = 3/2D_z \quad E = (D_x - D_y)/2 \quad . \tag{3.8}$$

Further contributions to the ZFS may arise from spin-orbit coupling. If the dipole-dipole coupling is the only contribution to the ZFS and the point-dipole approximation is valid, then $E = 0$ and

$$D = -\frac{3}{2} \cdot \frac{\mu_0}{4\pi h} \frac{g_1 g_2 \mu_B^2}{r_{12}^3} \quad . \tag{3.9}$$

3.2.3.2   *Orientations of interaction tensors*

All interaction tensors above are given in their respective principal axis frames. In addition, the orientations between the tensors need to be known.
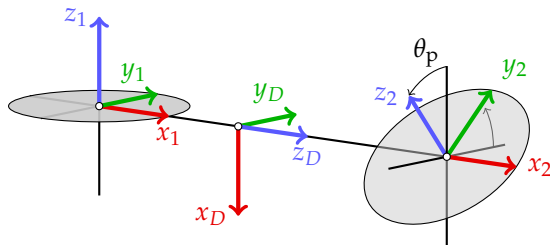
FIGURE 3.4: Illustration of the relative orientations of the different interaction tensors and the porphyrin planes. The subscripts 1, 2, and D stand for the **g**-tensors on porphyrin 1 and 2, and the dipolar/ZFS tensor, respectively. Gray discs illustrate the porphyrin planes which are twisted by an angle θ_p with respect to each other. More details are given in the main text.

In principle, the orientation of each tensor is characterized by three Euler angles, but we make a set of reasonable simplifying assumptions for the copper porphyrin dimers investigated in this work. First, because of the C_4 pseudosymmetry of the individual copper centres, we assume that the **g**, **P** and **A**-tensors on the same porphyrin unit are collinear and axial, and that the unique axis of each of these tensors is parallel to the normal vector of the corresponding porphyrin plane. Second, we can choose the x-axes of the two **g**-tensors to be collinear without loss of generality, since for axial tensors the $x-$axes can be chosen in any direction perpendicular to the unique z-axis. This leaves one free parameter for the relative orientation of the two porphyrin units, namely the angle θ_p between the two z-axes of the **g**-tensors, see Figure 3.4.

Taking into account the assumptions above, we can immediately fix the orientation of the unique axis of the dipolar tensor denoted as z_D in Figure 3.4, along the x-axes of the other tensors. For the ZFS tensor, this is a good approximation if the dipolar component dominates. The situation would be considerably more complicated if rhombic tensors were involved.

3.3 RESULTS AND DISCUSSION

The synthesis of **CuP2** and **f-CuP2** is described in the ESI of [8] (see section S.1). The samples were dissolved in toluene to give a final concentration of about 1 mM. We verified that the rather high concentration does not affect the EDNMR measurements by checking representative spectra at a
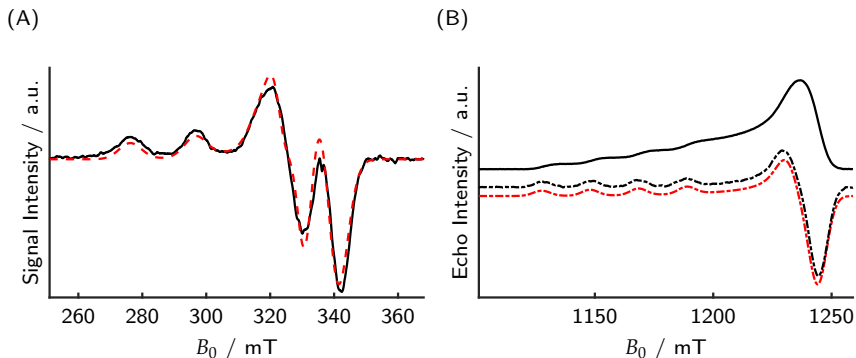
(A)   (B)

FIGURE 3.5: Field-swept EPR spectra of **CuP2**. (A) Experimental (solid black) and simulated (dashed red) X-band CW EPR spectrum. Recorded at 20 K. (B) Experimental Q-band echo-detected field-swept spectrum (solid black), smoothed numerical derivative (dashed black) and corresponding simulation (dashed red). Recorded at 15 K. Parameters: One electron $S = 1/2$, one copper $I = 3/2$ (both isotopologues). $g = [2.048, 2.19]$, $A_{\mathrm{Cu}} = [-80, -613]$ MHz.

concentration of 0.2 mM (see the ESI of [8], section S.10). For both samples, 40 μL of solution was transferred to a 3 mm (outer diameter) quartz tube. A 3 mm Q-band resonator with large bandwidth ($Q_{\mathrm{res}} \approx 110$) was used for the EDNMR measurements. Further details on the EPR spectrometers are presented in the ESI of [8] (see section S.2). A detailed description of the parameters and where to find the raw data is given for each figure at the end of the ESI of [8] (see section S.15).

Note that the results for the copper hyperfine and quadrupole couplings are specified for the slightly more abundant isotope ^{63}Cu. The parameters were scaled according to the natural constants (gyromagnetic ratio and quadrupole moment of the nucleus) of ^{65}Cu to calculate the spectra of isotopologues. Isotope effects beyond this scaling were neglected. Natural isotope abundance was assumed.

3.3.1 *CuP2: small exchange coupling*

The X-band continuous wave (CW) spectrum and the Q-band echo-detected field sweep (EDFS) spectra of **CuP2** are shown in Figure 3.5. The spectra are typical for axially symmetric Cu(II) compounds. The nitrogen hyperfine couplings are not resolved. For simulating the spectra, we only included a single copper nucleus. No further hyperfine couplings or electron-electron

couplings were included. Nevertheless, a rather good estimate of the g-values and of $A_{\parallel,\mathrm{Cu}}$ (≈ 610 MHz) can be obtained. By including more parameters in the simulation, such as the nitrogen couplings and the exchange coupling, the fit could most likely be improved [81]. However, the rather featureless character of the spectrum makes it difficult to assign quantitatively and confidently precise values to the different interactions, as all of these additional parameters only contribute to field-dependent line broadening in the present case. Note that similar, butadiyne-linked, compounds [81], exhibit an exchange coupling of about 50 MHz. But if the two porphyrin planes of **CuP2** are perpendicular to each other, consistent with X-ray and DFT studies of similar compounds, the exchange coupling is expected to be close to zero. In this case, it is also reasonable to model the EDNMR spectra (*vide infra*) by only considering a single, isolated copper site.

Q-band EDNMR spectra obtained at the low-field edge of the spectrum are shown in Figure 3.6. The high resolution and information content of these spectra was surprising. In order to simulate the spectra quantitatively, it was necessary to include both copper isotopes (^{63}Cu/^{65}Cu, nat. abund. $\approx 70/30\%$, $\gamma_{63}/\gamma_{65} = 0.934$) and also a substantial quadrupole coupling of $e^2qQ/h = 32 \pm 7$ MHz. The uncertainty is an estimate based on the linewidth of the peaks. The standard deviation σ of a Gaussian is related to the full width at half maximum Γ by $\sigma = \Gamma/(2\sqrt{2\ln 2}) \approx \Gamma/2.3548$, and for these spectra $\Gamma \approx 15$ MHz. The quadrupole tensor was assumed to be axial, but because of the rather low resolution in the high-field region, the fitting is not very sensitive to the asymmetry parameter η. The quadrupole coupling of the metal centre is of considerable interest, as it gives information about the coordination environment. Since it depends on total electron density, particularly the charge distribution, rather than on spin density, we expect that computation with quantum chemical approaches is more reliable than that of metal hyperfine couplings. While quadrupole interactions of copper have been determined before, the approach used in the literature relied on second order shifts in the EPR spectra [84] usually of single crystals. [85, 86] In the latter case, also ENDOR was used. [87]

The approach used here to determine the quadrupole coupling is analogous to that employed for nitroxides at W-band, where the coupling can be determined by analyzing a series of spectra at the high-field edge of the EPR spectrum [44]. An energy level diagram for our particular situation is shown in the ESI of [8] (see section S.7.1). Note that the spectra are asymmetric with respect to zero offset because the detection is selective with respect to the copper hyperfine components. In this particular case, there are no peaks
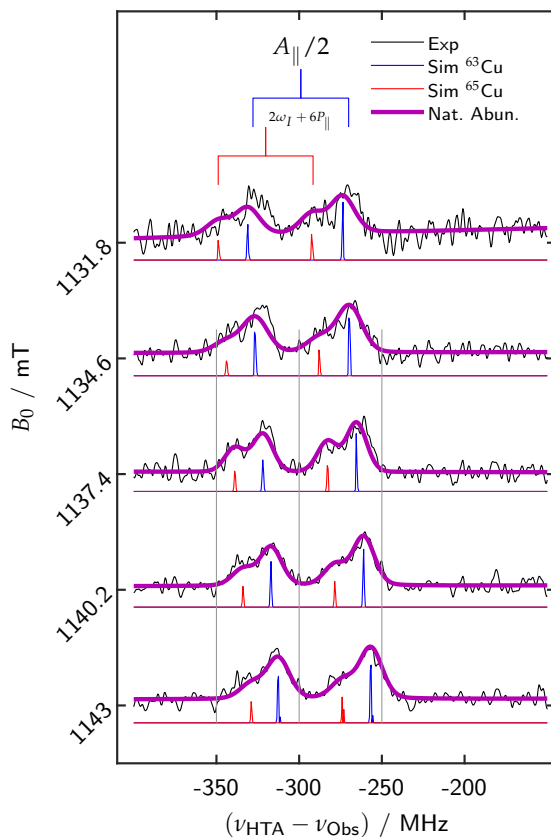
FIGURE 3.6: EDNMR spectra of **CuP2** at the low-field edge of the EPR spectrum together with the corresponding simulations that neglect electron-electron couplings. The stick spectra are the direct output of the simulation. The absolute intensities and linewidths were then fitted to the experimental spectra. Natural isotope abundance was assumed. The splitting induced by the quadrupole interaction of the copper nucleus is substantial. Parameters: One electron $S = 1/2$, one copper $I = 3/2$ (both isotopologues). $g = [2.048, 2.19]$, $A_{\mathrm{Cu}} = [-80, -613]$ MHz. $e^2qQ/h = 32$ MHz, $\eta = 0$, $\nu_{\mathrm{Obs}} = 35.5$ GHz, $\nu_1 \approx 2.2$ MHz (resonator centre), $t_{\mathrm{HTA}} = 20\,\mu\text{s}$, $T_{\mathrm{m}} = 1.5\,\mu\text{s}$, $Q_{\mathrm{res}} = 112$. The hole depth for all spectra is between one and two percent.

at positive offsets at all, because there are no forbidden transitions at higher frequencies than the observed allowed transitions. The surprising resolution of the two copper isotopes is a result of the large and strongly anisotropic hyperfine coupling combined with the strong orientation selection of EDNMR.

EDNMR spectra acquired at various field positions spanning the whole EPR spectrum are shown in Figure 3.7. A slightly shorter and softer HTA pulse was used because the effective nutation frequency is larger for EDNMR peaks at smaller resonator offsets. The strong correlation of the **g**-tensor to the **A**-tensor is clearly visible from the strong shift of the copper peaks when changing the field position.

In regions where the copper peaks are isolated, the agreement between experiment and simulation is quantitative. If the copper peaks overlap with the proton and nitrogen peaks or with the central hole (shown in gray and scaled down for clarity), the agreement is worse. The main discrepancy is actually a slight asymmetry of the overall intensity between the right-hand side (RHS) and the left-hand side (LHS) of the spectrum. Note that we fitted the linewidth in the simulated spectra (excluding the gray part of the spectra) and found that it is correlated with the field position. The resolution decreases by going from the low-field to the high-field edge. We tentatively assigned this to the different effective microwave powers at higher offsets and increased spectral diffusion at the maximum of the EPR spectrum. Additionally, the neglected electron-electron coupling could influence the observed linewidth. Note that the model we used here, *i.e.* only a single electron and a single copper nucleus, fits the EDNMR data better than the CW data, especially those recorded at X-band frequencies. This is due to the reduced number of parameters that influence the copper EDNMR peaks. The nitrogen nuclei and the exchange coupling have nearly no influence on these EDNMR peaks, in contrast to their significant influence on the EPR spectrum.

Again, the spectra are asymmetric with respect to the central hole because the detection selects specific hyperfine components of the EPR spectrum. This is illustrated in Figure 3.8 (A), where we show only the left-hand side of the EDNMR spectrum for simplicity. The contributions of the different Cu-hyperfine components to the EPR or EDNMR spectrum at a particular field position are indicated. In this case, the $m_I = +3/2$ component is not observed at all. Note that the different hyperfine components that are selected by the observer sequence have also different orientations with respect to the external magnetic field (see top right panel). In principle, the orientation selection is slightly different for the different isotopes, but this difference is
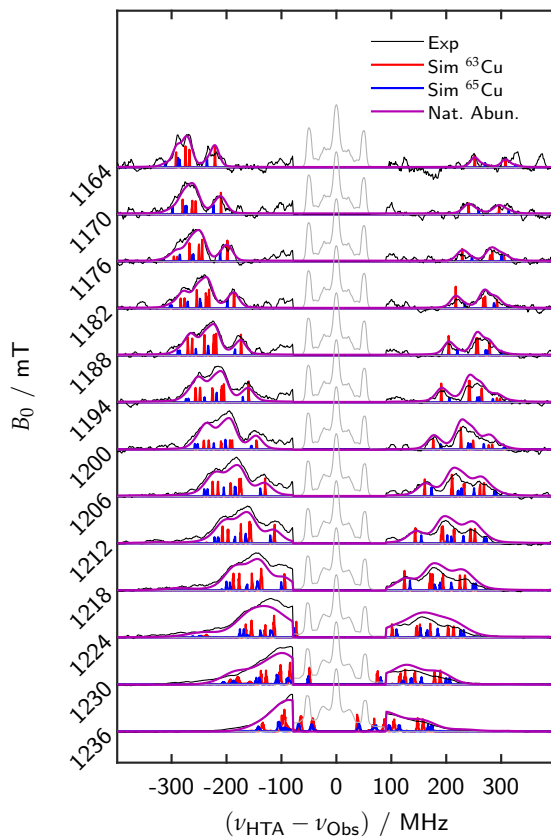
FIGURE 3.7: EDNMR spectra of **CuP2** acquired at various field positions spanning the whole EPR spectrum. The central hole and peaks due to nitrogens and protons are grayed out and scaled down. This part was not used to fit the linewidths and absolute intensities of the spectra. Parameters: same as in Figure 3.6, but with $t_{\text{HTA}} = 10\,\mu\text{s}$ and $\nu_1 \approx 1$ MHz. The hole depth of the copper peaks increases from around one percent at 1164 mT to about five percent at 1236 mT. The fitted linewidth increases accordingly from about 18 MHz to nearly 50 MHz. The spectrum at 1164 mT shows a feature at >300 MHz that we consider an artifact arising from the low signal-to-noise ratio at this field.

(A)

(B)
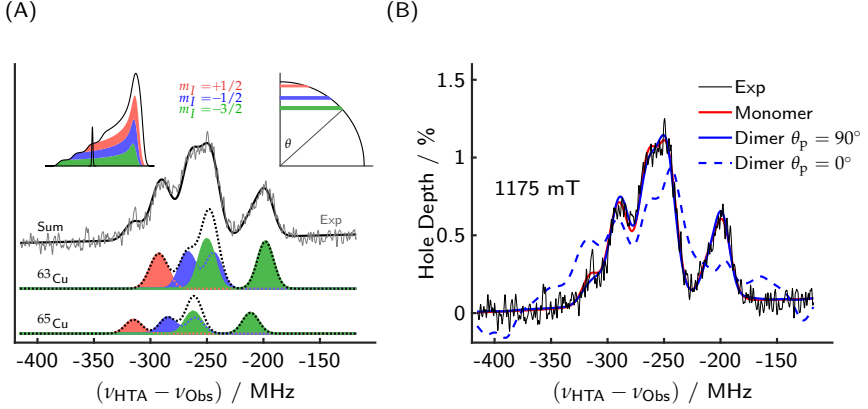
FIGURE 3.8: (A) Orientation selection in the EDNMR spectra of **CuP2**. ν_{obs}=35.5 GHz, B_0=1175 mT. The contributions of the different Cu-hyperfine components to the total EDNMR spectrum are shown. Top left inset: Contributions to the EPR spectrum. Top right inset: Observed orientations corresponding to the Gaussian in the top left panel. θ refers to the angle between the external magnetic field and the unique axis of the **g**-tensor. (B) Influence of the electron-electron coupling and relative porphyrin plane orientation on the ED-NMR spectra of **CuP2**. The same parameters as in Figure 3.7 were used for the simulation, but the blue spectra were simulated for a dimer including $J = 50$ MHz and $d = 85$ MHz.

very small here. The splitting induced by the nuclear quadrupole coupling and the nuclear Zeeman interaction depends on m_I. Therefore, the contribution of the $m_I = +1/2$ component (in red) to the EDNMR spectrum does not show any resolved splitting. The nuclear Zeeman interaction and the nuclear quadrupole interaction nearly cancel each other in this particular case.

We also simulated some of the spectra assuming two copper sites and including a dipolar coupling of $\frac{\mu_0}{4\pi h} \frac{g_1 g_2 \mu_B^2}{r_{12}^3} = 85$ MHz and an exchange coupling with a somewhat arbitrary but illustrative value of $J = 50$ MHz. For a perpendicular orientation of the porphyrin planes, *i.e.* $\theta_p = 90°$, no significant difference was found compared to a monomer simulation, see Figure 3.8 (B). On the other hand, if the porphyrin planes are assumed to be parallel ($\theta_p = 0°$), the simulated EDNMR spectra look very different. In case of a non-parallel arrangement, the two copper centres have different effective g-values, and the perturbation by the electron-electron coupling is reduced compared to a parallel arrangement. In summary, the effect of the electron-
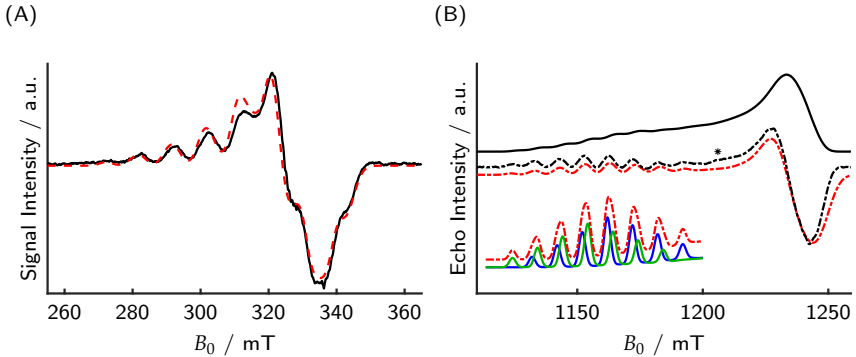
FIGURE 3.9: Field swept EPR spectra of *f*-**CuP2**. (A) Experimental (solid black) and simulated (dashed red) X-band CW EPR spectra. Recorded at 20 K. (B) Experimental Q-band echo-detected field swept spectrum (solid black), numerical derivative (dashed black) and simulation (dashed red). Recorded at 15 K. Parameters: $S = 1$, two copper nuclei. $g = [2.048, 2.19]$, $A_{\mathrm{Cu}} = [-40, -306]$ MHz (for both nuclei). $D = -240$ MHz, and the full **D**-tensor is rotated $90°$ around the y-axis with respect to the **g**- and **A**-tensors. The inset shows a simulation with only one isotope and reduced linewidth to illustrate the eight-line pattern which arises from two septets that are split by the ZFS (the blue and green lines are due to EPR transitions with different lower m_S values). We can currently not assign the feature marked with an asterisk (only visible in the numerical derivative), but the position does not match with the splitting of the other low-field peaks.

electron couplings on the EDNMR spectra is strongly dependent on the other interactions present in the system. In the case of **CuP2**, the effect is marginal, which is in line with X-ray crystallography studies and DFT calculations demonstrating a perpendicular orientation and high rigidity of the two porphyrin planes.

3.3.2 *f*-**CuP2**: large exchange coupling

The X-band continuous wave (CW) spectrum and the Q-band EDFS spectrum of *f*-**CuP2** are shown in Figure 3.9. They clearly differ from the spectra of **CuP2**, with several additional splittings appearing. Nevertheless, the Q-band spectrum still indicates an axial **g**-tensor. In this case, both copper centres were included in the simulation and an effective spin-1 was assumed. This is justified if the exchange coupling constant J is much bigger than both the

hyperfine coupling and the electron Zeeman anisotropy, or more precisely, if there is no significant singlet-triplet mixing. Agreement of the EPR spectrum with a simulated spectrum assuming the absence of singlet-triplet mixing poses a lower bound on the exchange coupling. This will be discussed below. The g- and A-values were assumed to be the same as for the **CuP2** compound (apart from the fact that A has to be halved if the system is treated as a triplet). This is justified by the same local structure of the copper centres up to the third coordination sphere. The normal vectors of the two porphyrin planes were assumed to be parallel, implying $\theta_\mathrm{p} = 0$.

A ZFS with $|D| =$240 MHz had to be included in the simulation to obtain a satisfactory agreement with the experimental data. This value is about a factor of two higher than the expectation based on the dipole-dipole approximation (Equation (3.9)), which would be around 130 MHz for a distance of 8.4 Å. Note that the unique axis of the **D**-tensor is assumed to be collinear with the x-axes of the **g**-tensors, see Figure 3.4.

Interestingly, because the ZFS splitting is roughly the same as the copper hyperfine splitting, one obtains an eight-line pattern along the parallel direction, clearly visible in the simulated Q-band spectrum and the inset. This is in contrast to the seven-line pattern expected if the ZFS is either much smaller or much larger than the hyperfine coupling. It is hard to claim the magnitude and orientation of the ZFS tensor from the field-swept spectra alone, since the signal-to-noise ratio of the low-field peaks is not sufficient in either case. However, we will provide additional support for the ZFS parameters by analysis of the field-correlated ELDOR spectra below.

In principle, one can gain additional information about the dipolar coupling and the relative orientation of the two copper centres by investigating the intensity and shape of the half-field transition [88]. In the present case, the sample concentration we had available (1 mM) was only sufficient to just about distinguish the half-field transition from the noise. A reliable quantification was not possible (see the ESI of [8], section S.8.1). This is consistent with the observation by Ikeue *et al.* [74].

The field-correlated ELDOR spectrum of *f*-**CuP2** is shown in Figure 3.10.

Two features are striking compared to **CuP2**. First, the resolution is much worse, and second, there are clear signal enhancements (or anti-holes) visible (blue areas). Because we assign positive intensity to EDNMR side holes in agreement with previous work, the anti-holes correspond to negative intensities. In the spectrum shown in Figure 3.10 (A), the poor resolution could be ascribed to the settings used. The hole burning pulse was relatively short and strong, compared to the usual settings of EDNMR, where one

generally uses long and soft pulses. Interestingly, softer and longer pulses did not lead to a better resolution (see the ESI of [8], section S.8.2). The poor resolution is thus intrinsic to the spin system at hand, where the large exchange coupling leads to many side holes close to each other as verified by simulations (see the ESI of [8], section S.12, for simulated single-orientation spectra, which are surprisingly complicated). Note that, in this case, the hole burning pulse predominantly excites allowed or only weakly disallowed transitions, in stark contrast to the usual EDNMR situation, where the side holes correspond to rather strongly disallowed transitions.

The positive part of the spectrum (red ridges) corresponds to side holes that increase in offset when going from higher to lower fields. These ridges roughly indicate the effective copper hyperfine coupling at a given field, similar to what is seen in the EDNMR spectra of **CuP2**. We find both 'single quantum' ridges, corresponding to an offset around 300 MHz ($\approx A_{\mathrm{Cu}}/2$) near the low-field edge and 'double quantum' ridges, corresponding to an offset around 600 MHz ($\approx A_{\mathrm{Cu}}$). In between these hole ridges, one can see signal enhancements or anti-holes (blue), which are due to the moderate ZFS and the exchange coupling. The strong anti-holes at positive and negative offsets around 1240 mT are due to the ZFS, which, for these orientations, is much larger than the hyperfine coupling.

The simulation program that we developed on the basis of the algorithm of Cox *et al.* [26] was used to generate spectra for a multitude of possible spin Hamiltonian parameters, see Figure 3.10 (C)–(F). The comparison between the experimental spectrum and the simulated spectra led to the conclusions that 1) There must be a significant exchange coupling (>15 GHz). For lower exchange couplings, the splittings in the CW spectrum do not fit the experimental ones. 2) The ZFS is about $|D| = 240$ MHz, which is approximately twice as much as expected from the point-dipole approximation. If one assumes a smaller ZFS, again the splittings in the CW spectra do not match. On top of this, the strong anti-holes at the high-field edge in the 2D correlation plots are shifted to smaller offsets (see Figure 3.10 (E)–(F) at around 1150 mT). Note that changing the sign of the ZFS does not change the outcome of the simulations. However, if the ZFS is dominated by the dipole-dipole contribution, as we assume here, its sign is known. Note that it is difficult to predict the appearance of the field-correlated ELDOR spectra of f-**CuP2** in an intuitive way, because the ZFS and the hyperfine couplings are in the same range. For the interested reader, we also simulated simpler model systems, and displayed the spectrum in Figure 3.10 (B) in terms of the individual EPR transitions, see the ESI of [8], section S.11.

The agreement between experimental data and simulation obtained for our best parameter set is not as good as in the case of **CuP2**, but it is at the very least semi-quantitative. The main features are very well reproduced. The lower bound of the exchange coupling can be estimated with certainty, especially if the field-correlated ELDOR spectra and the CW spectra are inspected together. While the uncertainty in the ZFS is rather high (around 20 MHz, judged only by visual inspection of a range of simulations), it is still clear that the ZFS is much larger than estimated from the point-dipole approximation. This is not unexpected, since the large exchange coupling (*vide infra*) indicates significant spin density in the π-system in between the copper atoms. In all cases, we assumed that $E = 0$, and we did not obtain better fitting simulations by including a non-zero E.

We would like to emphasize that using CW EPR alone can lead to wrong conclusions regarding the spin Hamiltonian parameters. Ikeue *et al.* [74] measured the exchange coupling of a very similar fused dimer by variable-temperature magnetometry, but they ignored the ZFS/dipolar coupling, stating that it is not resolved in the EPR spectrum. Accordingly, their fit gave very different g-values for the fused and the singly-linked dimer. Our ELDOR spectra contradict this interpretation. Khusnutdinova *et al.* [75] investigated a fused dimer that was fused only at two points instead of three (the *meso*-position of one porphyrin was coupled to a β-position of the other porphyrin and *vice versa*, and the two porphyrin moieties were slightly shifted with respect to each other). They did not consider any dipolar electron-electron coupling and obtained a very different and rhombic **g**-tensor and approximately halved copper hyperfine constants. They also observed the shoulder at the high-field edge of the X-band CW spectrum, but did not reproduce it in their simulation (Khusnutdinova *et al.* [75], Fig. 1(a) therein). We expect that similar problems will arise in other multi-nuclear complexes. ELDOR can give valuable information in these cases, where many parameters have to be fitted to a single spectrum and several local minima are possible.

3.3.3   Comparison of **CuP2** and **f-CuP2**

Here we highlight the differences in the field-correlated ELDOR spectra of **CuP2** and **f-CuP2**. Figure 3.11 shows the two spectra as filled contour plots side by side. 1) As mentioned above, the resolution is much better in the case of **CuP2** compared to **f-CuP2**. A contour plot is not the optimal representation for showing the high resolution for **CuP2** (Figure 3.11 (A)). This can be judged from Figure 3.6. 2) The ELDOR spectra of **f-CuP2**
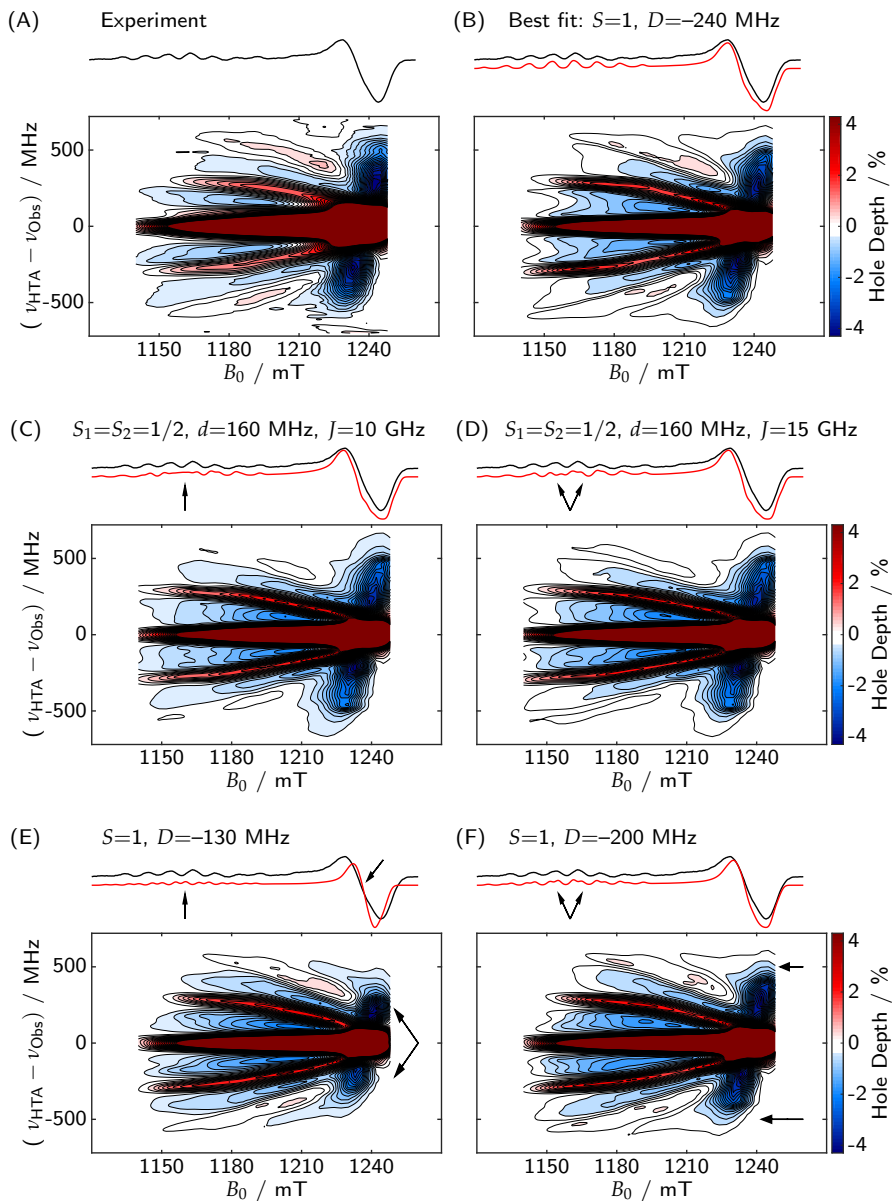
FIGURE 3.10: Caption on next page.

FIGURE 3.10: (Previous page.) Field-correlated ELDOR spectra of f-**CuP2**. (A) Experimental 2D spectrum, with the first derivative of the echo-detected field-swept spectrum displayed on top. (C)–(F) Simulated 2D spectra. Experimental (black) and simulated (red) echo-detected field-swept spectra displayed on top (numerical derivative). The arrows highlight deviations from the experimental data. Parameters: g, Q, and A-values the same as for **CuP2**. In the case of $S = 1$, the hyperfine coupling constants were halved, but both copper nuclei were equivalent. $\nu_{\text{Obs}} = 35.5$ GHz, $\nu_1 \approx 20$ MHz (resonator centre), $t_{\text{HTA}} = 50$ ns, $T_{\text{m}} = 1.5\,\mu$s, $Q_{\text{res}} = 110$.

show anti-holes, while the **CuP2** spectra only show holes. This is due to the difference in electron spin state ($S = 1$ *vs.* $S = 1/2$). 3) The side holes arising from the Cu-hyperfine coupling are more pronounced in the case of f-**CuP2**, although the nominal flip angle of the hole burning pulse was smaller. For example, we could observe clear double-quantum peaks in the case of f-**CuP2** (seen around ± 600 MHz at the low-field edge), while we could not detect any double quantum peaks at all in the case of **CuP2**. This is due to the $S = 1$ spin state of f-**CuP2**: In the strong coupling regime, the transition moments for the forbidden transitions in the $S = 1/2$ case go towards zero if $|A| \gg |\nu_I|$, because the quantisation axes of the nuclear spin in the two different electron spin manifolds are approximately (anti-)parallel to each other. The same is not true in the $S = 1$ case, because there is no hyperfine contribution in the $M_S = 0$ manifold. This means that even if $|A| \gg |\nu_I|$, the quantisation axes of the $M_S = \pm 1$ and the $M_S = 0$ manifold are not parallel and therefore the transition moments of the forbidden transitions do not vanish. A detailed discussion can be found in the ESI of [8] (section S.13). In addition to these considerations, the effective electron spin in f-**CuP2** couples to two equivalent nuclei, which makes the holes more intense.

3.3.4 *SQUID magnetometry*

So far, all arguments regarding the exchange coupling of f-**CuP2** were given on the basis of EPR data, but only a lower bound of roughly 15 GHz (or 0.5 cm^{-1}) could be inferred that way. Additionally, we conducted SQUID magnetometry measurements of f-**CuP2** and a corresponding Cu(II) monomer (see the ESI of [8] for the structure). The data for the temperature-dependent susceptibility per mole Cu shown in Figure 3.12 clearly show a maximum at about 2.4 K in the case of f-**CuP2**, which indicates an anti-ferromagnetic coupling of 79 GHz (for JS_1S_2, corresponding to 1.32 cm^{-1} for $2JS_1S_2$).

(A) **CuP2**, $\nu_1 \approx 2.2$ MHz, $t_{HTA} = 20\,\mu s$ (B) **f-CuP2**, $\nu_1 \approx 20$ MHz, $t_{HTA} = 50\,ns$

FIGURE 3.11: Comparison of the field-correlated ELDOR spectra of **CuP2** (A) and **f-CuP2** (B). The data underlying (A) are the same as in Figure 3.7. The asterisk indicates a field-independent spurious frequency which leads to a small and very sharp peak that is not visible in (B) because a larger step size was used.

FIGURE 3.12: Magnetic susceptibilities per mole Cu of **f-CuP2** (red) and the corresponding monomer (black). The experimentally measured points are shown together with the *EasySpin* simulation using the function `curry`. The maximum at around 2.4 K for **f-CuP2** indicates an anti-ferromagnetic coupling of 79 GHz (for JS_1S_2, corresponding to $1.32\,cm^{-1}$ for $2JS_1S_2$).

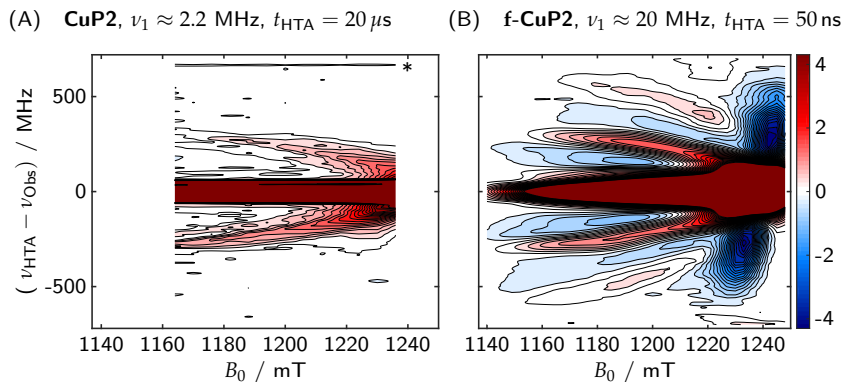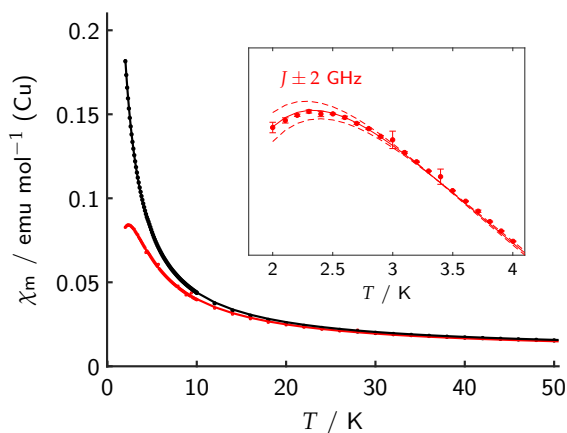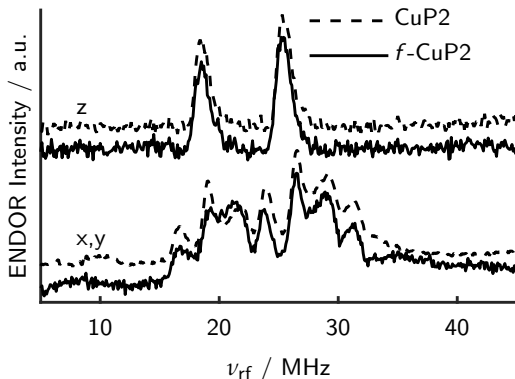FIGURE 3.13: Q-band ENDOR spectra of **CuP2** and ***f*-CuP2** obtained at two different field positions corresponding to different orientations of the **g**-tensor. The signals are due to strongly coupled ^{14}N nuclei. A naive interpretation of the spectra could lead to the assumption that the exchange couplings of the two compounds do not significantly differ. However, the ENDOR spectra are theoretically expected to be the same in the weak and strong exchange coupling limits.

This is consistent with the measurements of Ikeue *et al.* [74]. The magnetisation observed by SQUID is also consistent with thermal excitation of the triplet state at the temperatures of our EPR measurements. For a more accurate determination of J, lower temperatures would be needed. A detailed description of the SQUID measurements is given in the ESI of [8] (see section S.4).

3.3.5   *A comment on ENDOR of **CuP2** and **f-CuP2***

It is a well known fact that, in the case of a system with large exchange coupling, the apparent hyperfine coupling is halved [83, 89]. Interestingly, this does not lead to different ENDOR spectra, as the spectra displayed in Figure 3.13 clearly show.

This was surprising to us at first and led us to the wrong assumption that the exchange coupling of ***f*-CuP2** is of the order of a few hundred MHz at the most. On closer inspection, we found that the ENDOR spectra indeed do not change when going from the uncoupled to the strongly coupled case. In fact, this is straightforward to see, if one notes that ENDOR transitions inside the $|\alpha\alpha\rangle$ (T_1 substate) and $|\beta\beta\rangle$ (T_{-1} substate) manifolds of the electron

spins are untouched by the exchange coupling, which mixes only the $|\alpha\beta\rangle$ with the $|\beta\alpha\rangle$ state. Since, in the weak and strong exchange limits, ENDOR transitions are always within one M_S manifold, ENDOR spectra for the $|\alpha\alpha\rangle$ and $|\beta\beta\rangle$ electron spin states must be the same in the two limiting cases. In the strong exchange limit, the T_0 triplet substate should, in principle, give rise to peaks at nuclear frequencies without hyperfine couplings (nuclear Zeeman and nuclear quadrupole), but for strongly hyperfine-coupled nuclei, the peaks in the other triplet substates will be much more intense due to hyperfine enhancement. A more detailed discussion is presented in the ESI of [8] (see section S.14).

3.4   CONCLUSION AND OUTLOOK

We applied ELDOR-detected hole burning experiments to two Cu(II)-porphyrin dimers and interpreted the results with a generalisation of the algorithm introduced by Cox *et al.* [26] In the case of the singly-linked dimer with small exchange coupling and perpendicular orientation of the porphyrin planes, the EDNMR description is fully adequate and the experiment could resolve the two isotopes of copper as well as the nuclear quadrupole coupling constant in frozen solution. The simulation algorithm quantitatively reproduces these highly resolved experimental spectra. In the case of the fused dimer with large anti-ferromagnetic exchange coupling, anti-holes were observed in the ELDOR experiment. These anti-holes are due to allowed transitions that share a level. They are also well reproduced by simulations with the extended algorithm. From these experiments alone, a lower bound for the exchange coupling of about 15 GHz could be derived. SQUID measurements confirmed the presence of a significant exchange coupling of 79 GHz (singlet-triplet separation) at a distance of about 8.4 Å between the copper ions, in line with Ikeue *et al.* [74] The EPR data also revealed a previously neglected dipolar coupling, which manifests as a ZFS in this strongly exchange-coupled system. The determined dipolar coupling is about twice as large as that expected based on a point-dipole approximation.

Both findings, the large exchange and the large dipolar coupling, point to substantial spin delocalisation and are thus consistent with an interaction of the copper d-orbitals with the delocalised π-system. The detailed experimental data presented here could serve as a starting point for in-depth quantum-chemical studies of the spin distribution in the fused system.

Our findings suggest that ELDOR experiments are even more useful than generally assumed: they can reveal more than "just" hyperfine and nuclear

quadrupole couplings. By applying the extended simulation algorithm, a detailed understanding of systems with strong exchange and dipolar couplings can be achieved. Careful optimisation of experimental parameters is needed, as much information comes from the connections between allowed transitions, *i.e.* much shorter pulses should be used compared to the usual setup of EDNMR.

Nevertheless, the interactions have to be accessible inside the resonator bandwidth, which might prevent the elucidation of very large ZFS or dipole-dipole couplings. This is where non-resonant setups, such as HiPER [90] could have a dramatic advantage, provided they are combined with ultra-wideband frequency generation. While the bandwidth has to be large, the power does not need to be.

Surprisingly, anti-holes have not been reported before in EDNMR studies on Mn(II), although the polarisation enhancement of the central transition by inversion of satellite transitions [78] is based on the same effect. We can only speculate on the cause. For large ZFS and, accordingly, substantial second-order broadening, the anti-holes may be so strongly broadened that they go unnoticed or are considered baseline artefacts. In addition, they are less prominent compared to the nuclear-frequency holes if the flip angle of the hole-burning pulse is very high. Here we worked with lower nominal flip angles and shorter hole-burning pulses to enhance the anti-holes.

The emergence of anti-holes in exchange-coupled systems with rather large dipolar couplings also implies that ELDOR-detected NMR or related sequences with additional pulses might be useful to study biradicals with moderately strong dipole-dipole and exchange couplings that are commonly employed in dynamic nuclear polarisation (DNP) experiments and are difficult to characterise only via their CW EPR spectra [91].

Part II

SPINLOCKS FOR DISTANCE MEASUREMENTS

4

DISTANCE MEASUREMENT BETWEEN TRITYL RADICALS BY PULSE DRESSED ELECTRON PARAMAGNETIC RESONANCE WITH PHASE MODULATION

Repetition legitimizes.

— Adam Neely

SUMMARY

Distance measurement in the nanometre range is among the most important applications of pulse electron paramagnetic resonance today, especially in biological applications. The longest distance that can be measured by all presently used pulse sequences is determined by the phase memory time T_{m} of the observed spins. Here we show that one can measure the dipolar coupling *during* strong microwave irradiation by using an appropriate frequency- or phase-modulation scheme, i. e. by applying pulse sequences in the nutating frame. This decouples the electron spins from the surrounding nuclear spins and thus leads to significantly longer relaxation times of the microwave-*dressed* spins (i. e. the rotating frame relaxation times $T_{1\rho}$ and $T_{2\rho}$) compared to T_{m}. The electron-electron dipolar coupling is not decoupled as long as both spins are excited, which can be implemented for trityl radicals at Q-band frequencies ($35\,\mathrm{GHz}$, $1.2\,\mathrm{T}$). We show results for two bis-trityl rulers with inter-electron distances of about $4.1\,\mathrm{nm}$ and $5.3\,\mathrm{nm}$ and discuss technical challenges and possible next steps.

4.1 INTRODUCTION

Pulsed dipolar electron paramagnetic resonance (EPR) spectroscopy emerged as a powerful tool to measure distance distributions between electron spins in the nanometer range [93]. This information is particularly useful when studying molecules and molecule assemblies that are intrinsically disordered or partially disordered or otherwise hard to crystallize and difficult to study with NMR or cryo-EM alone, e. g. certain membrane proteins [94] or protein-RNA complexes [95]. The distance information is encoded in the magnetic dipole-dipole coupling between the electron spins, which depends on the inverse cubed distance, r^{-3}. A plethora of different techniques have been introduced, most notably double electron electron resonance (DEER) [96, 97], double quantum coherence (DQC) [98], the single frequency technique for refocusing (SIFTER) [99], and relaxation induced dipolar modulation enhancement (RIDME) [100, 101]. The limiting factor for all these pulse sequences is the electron phase memory time T_{m}, which determines the maximum dipolar evolution time and thus the longest distance that can be measured. In many cases, the phase memory time can be prolonged by deuterating the solvent, or even the whole protein [102–104]. However, such an approach is costly

and is rarely feasible, e. g. it is very difficult for membrane proteins in a lipid bilayer and impossible for in-cell work.

In recent years, several groups tried to use dynamical decoupling sequences based on multiple refocusing pulses (also known as Carr-Purcell sequences) in order to prolong the coherence times [105, 106]. Although shaped pulses significantly improved the fidelity of EPR experiments, pulse frequency band overlap and non-uniform inversion are still a problem in these sequences and can lead to artefacts, which may be corrected if traces with sufficient signal-to-noise and only moderately decaying background can be acquired [20]. Nevertheless, the improvements in T_{m} so far are on the order of a factor of 2, which only marginally (though sometimes decisively) improves the longest attainable distance.

Recently, a sequence based on spin-diffusion, which would be limited by T_1 rather than T_{m}, was proposed [107]. This proposal is still waiting for experimental verification.

Here we propose a sequence where the longest dipolar evolution time is, in principle, limited by the rotating frame relaxation time $T_{2\rho}$, which is often much longer than T_{m} (for a discussion of $T_{2\rho}$ vs. the more familiar $T_{1\rho}$, *vide infra*). The complete dipolar evolution takes place *during* strong microwave irradiation. This decouples the electron spins from the surrounding nuclei [108] while the electron-electron coupling is still active. The spin manipulation during the strong microwave irradiation is achieved by short intervals of sinusoidal phase modulation. The frequency of this modulation needs to match the Rabi or nutation frequency of the spin-locking irradiation.

The latter approach was discovered more than once in the history of magnetic resonance. It traces back to investigations of Redfield on "rotary saturation" [109]. Hoult introduced the related idea of longitudinal field modulation for nutation frequency selective pulses to MRI [110]. Grzesiek and Bax picked up Hoult's idea, but used a phase modulation scheme instead and applied it to homonuclear mixing in solution state NMR [111]. They termed the technique "Audio-frequency NMR in a nutating frame", because their phase modulation (PM) frequency is in the audible range, and the pulse sequences effectively take place in a frame that nutates with the Rabi frequency of the spin-lock. Independently, Jeschke used longitudinal field modulation during a spin-lock for pulse EPR [112] and used the term "dressed EPR", because the spins are dressed by the microwave field during the spin-lock. This term is borrowed from quantum optics [113]. The idea of dressed EPR originated in artefacts in hyperfine-decoupled electron-nuclear double resonance (ENDOR) spectra, which appear if the radio-frequency coil is not

aligned perfectly perpendicular to the static field [108]. Much later, it was also realized that field modulation should also prolong Rabi oscillations in the presence of inhomogeneous microwave fields [114]. Recently, the quantum information processing community picked up the idea of dressing electron spins in order to prolong coherence times [115–117]. During the writing of this manuscript, Chen and Tycko came up with the idea of phase-modulation during a spin-lock independently again, and used it for slice selection during off-resonance spin-locks in solid-state, DNP-enhanced MRI [118].

Here we combine the ideas of applying pulse sequences on dressed spins [111, 112] with the one of prolonging coherence times as a means of improving distance distribution resolution or prolonging distance range in pulsed dipolar EPR spectroscopy. To test the method, we used two bis-trityl rulers in which two trityl radicals are connected by a rather stiff linker. Linker length and residual flexibility are known [119, 120]. The chosen trityl radical is structurally closely related to the Finland trityl radical and has similar EPR spectroscopic properties [121]. The narrow EPR spectrum of the used trityl radical makes it particularly amenable to single-frequency techniques for measurements of the dipole-dipole coupling [122] in a regime that is analogous to the one of homonuclear NMR experiments. Note that the sequence presented in this work relies on the narrow spectrum of the trityl radicals. We do not expect it to work with the much more commonly used nitroxide radicals.

The article is organized as follows: First, we review mathematically, in the language of the magnetic resonance community, what happens to all the interactions in the spin Hamiltonian if we apply a strong microwave field. In order to do this, we will introduce a nutating frame description. Then we explain how an appropriate phase modulation scheme leads to "pulses" in the nutating frame. In the results section we show the synthesis of the bis-trityl rulers and present the application of a dressed spin echo experiment to such rulers to measure the dipolar coupling between two trityl radicals.

4.2 THEORY

We use the following convention for operators: No prime refers to the laboratory frame and one prime to the electron-spin rotating frame, i. e. the interaction frame with the Zeeman Hamiltonian of the electrons. Two primes refer to the nutating frame, which is obtained with an additional interaction frame transformation with the pulse Hamiltonian. We will usually only denote the Hamiltonian with primes, and not all operators. If we mention axes in the

text, we will explicitly use the primes, but we will omit them in mathematical formulas.

4.2.1 *Averaging of interactions by strong continuous microwave irradiation*

In order to understand the observations in this work, we need to study the influence of strong microwave irradiation on the different interactions present in the spin system. The spin Hamiltonian of a system with two coupled electrons ($S = 1/2$) in a bath of nuclei is given in the electron-spin rotating frame by

$$\hat{\mathcal{H}}' = \hat{\mathcal{H}}'_{\text{mw}} + \hat{\mathcal{H}}'_{\text{offset}} + \hat{\mathcal{H}}'_{\text{e-e}} + \hat{\mathcal{H}}'_{\text{e-n}} + \hat{\mathcal{H}}'_{\text{nuc}} \quad . \tag{4.1}$$

The first term is the microwave Hamiltonian, which is given in the same frame by

$$\hat{\mathcal{H}}'_{\text{mw}} = \omega_1 \left(\hat{S}_{1,x} + \hat{S}_{2,x} \right) \text{ with } \omega_1 = -\gamma_{\text{e}} B_1 \quad . \tag{4.2}$$

The Rabi or nutation frequency is denoted by ω_1, which depends on the microwave amplitude B_1 and the gyromagnetic ratio of the electron, γ_{e}. We assume a constant microwave phase and neglect the influence of the microwaves on the nuclear spins. In the following, we will apply an interaction frame transformation (IFT) with $\hat{\mathcal{H}}'_{\text{mw}}$ to all other terms and use first-order average Hamiltonian theory to gain physical insight. The new frame is referred to as the nutating frame. The nutating frame Hamiltonian is based on spin operators for dressed electron spins and bare nuclear spins. For mathematical details please consult the SI of [92].

If we choose the nutating frame frequency ω_{PM} equal to the Rabi frequency, $\omega_{\text{PM}} = \omega_1$, the irradiation term is completely absorbed into the frame. In a real experiment with an ensemble of spins, ω_1 will be distributed due to microwave inhomogeneities, thus we will always have a remaining contribution of

$$\hat{\mathcal{H}}''_{\text{mw}} = \Omega_{\text{d}} \left(\hat{S}_{1,x} + \hat{S}_{2,x} \right) \text{ with } \Omega_{\text{d}} = (\omega_1 - \omega_{\text{PM}}) \quad . \tag{4.3}$$

The dressed spin offset Ω_{d} will be distributed over the sample, but as a molecule is by orders of magnitude smaller than the microwave wavelength, Ω_{d} will be the same for all electron spins within one molecule.

As usual, the influence of a small g-anisotropy and of an inhomogeneous static magnetic field B_0 is captured in offset terms in the rotating frame

$$\hat{\mathcal{H}}'_{\text{offset}} = \Omega_{S,1} \hat{S}_{1z} + \Omega_{S,2} \hat{S}_{2z} \quad . \tag{4.4}$$

We neglect any tilt of the electron spin quantisation axis due to strong g-anisotropy, which is a good approximation for trityl and other organic radicals. The first-order average Hamiltonian after an IAT with $\hat{\mathcal{H}}'_{\mathrm{mw}}$ vanishes, i. e.

$$\hat{\mathcal{H}}''_{\mathrm{offset}} = 0 \quad . \tag{4.5}$$

In pulse EPR, the spectral width is often much larger than the Rabi frequency. In this case, the first order approximation will be poor. It is, however, not a poor approximation for trityl radicals with our setup. For simplicity, we will mostly neglect the effect of resonance offsets $\Omega_{S,1}$ and $\Omega_{S,2}$.

The most important term in the context of distance measurements is the electron-electron coupling Hamiltonian, which contains dipolar and exchange (J) contributions

$$\begin{aligned}
\hat{\mathcal{H}}'_{\mathrm{e\text{-}e}} &= \hat{\mathcal{H}}'_{\mathrm{e\text{-}e,dip}} + \hat{\mathcal{H}}'_{\mathrm{e\text{-}e,J}} \\
\hat{\mathcal{H}}'_{\mathrm{e\text{-}e,dip}} &= \omega_{\mathrm{dd}} \left(\hat{S}_{1z}\hat{S}_{2z} - \frac{1}{2}\left(\hat{S}_{1x}\hat{S}_{2x} + \hat{S}_{1y}\hat{S}_{2y} \right) \right) \\
\omega_{\mathrm{dd}} &= \frac{\mu_0}{4\pi} \frac{\mu_{\mathrm{B}}^2 g_1 g_2}{\hbar} \frac{1}{r_{12}^3} \left(1 - 3\cos^2\theta \right) \\
\hat{\mathcal{H}}'_{\mathrm{e\text{-}e,J}} &= J\left(\vec{\hat{S}}_1 \cdot \vec{\hat{S}}_2 \right) \quad ,
\end{aligned} \tag{4.6}$$

where μ_0 is the vacuum permeability, μ_{B} the Bohr magneton, g_1 and g_2 are the g-factors of the two electron spins, and θ is the angle between the external magnetic field and the interspin vector with length r_{12}. The exchange contribution is often, but not always negligible in pulse EPR based distance measurements. The prefactor of the dipolar coupling contains the distance information and is given by

$$d = \frac{1}{2\pi} \frac{\mu_0}{4\pi} \frac{\mu_{\mathrm{B}}^2 g^2}{\hbar} \frac{1}{r^3} \quad . \tag{4.7}$$

This amounts to $52.04\,\mathrm{MHz}$ for $r = 1\,\mathrm{nm}$. After transformation to the nutating frame, we obtain

$$\begin{aligned}
\hat{\mathcal{H}}''_{\mathrm{e\text{-}e,dip}} &= -\frac{1}{2} \cdot \omega_{\mathrm{dd}} \left(\hat{S}_{1x}\hat{S}_{2x} - \frac{1}{2}\left(\hat{S}_{1z}\hat{S}_{2z} + \hat{S}_{1y}\hat{S}_{2y} \right) \right) \\
\hat{\mathcal{H}}''_{\mathrm{e\text{-}e,J}} &= \hat{\mathcal{H}}'_{\mathrm{e\text{-}e,J}} = J\left(\vec{\hat{S}}_1 \cdot \vec{\hat{S}}_2 \right) \quad .
\end{aligned} \tag{4.8}$$

The electron-electron dipolar coupling is not averaged to zero, but only scaled by a factor of -1/2. It is also tilted such that the unique axis of the coupling

Hamiltonian points along the spin-lock axis ($z' \rightarrow x'' = x'$, in the NMR literature, often a tilted frame is used). In other words, the two dressed spins are still dipole-dipole coupled with half the original coupling strength and with inverted sign of the interaction. This result is well-known in solid-state NMR [123], where it is used to generate "magic echoes". The isotropic J-coupling is unaffected if both spins are irradiated. Note however that the difference of the resonance frequencies of the two dressed spins is much smaller than the one of the bare spins, as remarked upon already by Grzesiek and Bax [111]. The difference in relative magnitude of the exchange coupling and resonance frequency difference can lead to a different manifestation of the exchange coupling in the spectra. If, both, the dressed spin offsets as well as the spin states of the two spins are the same, exchange coupling has no influence on the evolution. This is analogous to the situation of magnetically equivalent nuclei in liquid state NMR. This different averaging of dipolar and exchange contributions might be exploited experimentally to distinguish the two contributions.

The term $\hat{\mathcal{H}}'_{\text{e-n}}$ contains all electron-nucleus (hyperfine) couplings. If the Rabi frequency of the irradiation is much larger than all hyperfine couplings and nuclear Zeeman frequencies, this term also averages to zero in the nutating frame, i.e.

$$\hat{\mathcal{H}}''_{\text{e-n}} = 0 \quad , \tag{4.9}$$

an effect referred to as hyperfine decoupling [108]. Terms that do not contain an electron spin operator are assumed to be unaffected by the microwave irradiation,

$$\hat{\mathcal{H}}_{\text{nuc}} = \hat{\mathcal{H}}'_{\text{nuc}} = \hat{\mathcal{H}}''_{\text{nuc}} \quad . \tag{4.10}$$

Equation (4.9) and Equation (4.10) might appear to be irrelevant to distance measurements between electrons, but they are not. The terms $\hat{\mathcal{H}}_{\text{e-n}}$ and $\hat{\mathcal{H}}_{\text{nuc}}$ do not commute if nuclear-nuclear flip-flop terms are present, even if the hyperfine coupling $\hat{\mathcal{H}}_{\text{e-n}}$ is purely secular (no electron spin echo envelope modulation effect). For example, for the flip-flop terms in $\hat{\mathcal{H}}_{\text{nuc}}$, $\left[\hat{S}_z \hat{I}_{iz}, \hat{I}_i^+ \hat{I}_j^- \right] \neq 0$. A simple spin echo sequence on the electron spins thus does *not* completely refocus the hyperfine coupling - the result is a dephasing of the electron spins, sometimes loosely referred to as "relaxation". In principle, this dephasing stems from coherent evolution, but since the nuclear spin bath is usually very large, it is computationally very expensive to simulate a real system. Accordingly, most theoretical studies treat the internuclear couplings phenomenologically using effective flip rates [124][1]. The situation

---

1 Timeline break: In the meantime, fully coherent simulations using cluster-correlation expansion were shown to reproduce experimental results very well [12].

during microwave irradiation of an electron-nuclear spin system has many parallels with heteronuclear decoupling in solid-state NMR [125], where one distinguishes between the "real" transverse relaxation time due to incoherent dynamics, T_2, and the effective relaxation time that is measured with a spin echo, T_2' and has large coherent contributions. Of course, in EPR, the coupling strengths and Rabi frequencies are several orders of magnitude higher than in NMR.

In EPR measurements of organic radicals at sufficiently low temperatures, usually at 50 K and below, the hyperfine and nuclear-nuclear couplings dominate the dephasing [126]. In this case, averaging the hyperfine coupling to zero should drastically increase the dephasing time, because $\hat{\mathcal{H}}_{\mathrm{nuc}}$ commutes with all remaining terms containing electron spin operators. At the same time, according to Equation (4.8), the effective dipolar coupling is scaled by a factor -1/2. If the gain in dephasing time is larger than a factor of two, it should - in principle - be possible to measure longer dipolar dephasing traces and thus longer distances. As we shall see later, the effective scaling factor may be even more favourable (-3/4), as the flip-flop terms in the electron-electron dipolar Hamiltonian may be truncated for bare spins but can be significant for dressed spins.

The immediate next question is then how one can measure the dipolar coupling during a spin-lock pulse. We propose to use a phase-modulation scheme that we discuss in the next section.

4.2.2   *Pulse dressed spin resonance with phase-modulated pulses*

The basic theory of dressed spin resonance is already described in [111] and [112] but we describe it here again for completeness and consistency.

For simplicity and illustration, we first look at an isolated electron (spin 1/2) in a static magnetic field B_0 along the laboratory-frame z-axis. If we irradiate this system with a linearly polarized electromagnetic field with frequency ω_{mw} and amplitude $2B_1$, the Hamiltonian in angular frequency units is given by

$$\hat{\mathcal{H}} = \omega_0 \hat{S}_z + 2\omega_1 \cos\left(\omega_{\mathrm{mw}} t + \phi_{\mathrm{mw}}(t)\right) \hat{S}_x \qquad , \qquad (4.11)$$

with $\omega_0 = -\gamma B_0$. We include an arbitrary phase $\phi_{\mathrm{mw}}(t)$, which we will use later to generate dressed spin PM pulse sequences. As usual, we now go into a rotating frame with frequency ω_{mw}. If we neglect the time-dependent terms (rotating wave approximation, RWA), we obtain

$$\hat{\mathcal{H}}' = \Omega_S \hat{S}_z + \omega_1 \left(\cos\left(\phi_{\mathrm{mw}}(t)\right) \hat{S}_x + \sin\left(\phi_{\mathrm{mw}}(t)\right) \hat{S}_y\right) \qquad , \qquad (4.12)$$

with the offset $\Omega_S = (\omega_0 - \omega_{\mathrm{mw}})$, which is also used in Equation (4.4). The main effect of the time-dependent terms is a Bloch-Siegert shift, i. e. just a small correction of Ω_S. We can choose the PM as

$$\phi_{\mathrm{mw}}(t) = \phi_0 + a_{\mathrm{PM}} \cos\left(\omega_{\mathrm{PM}} t + \phi_{\mathrm{PM}}\right) \qquad , \qquad (4.13)$$

with a modulation amplitude a_{PM}, a modulation frequency ω_{PM} and a modulation phase ϕ_{PM}. The phase ϕ_0 is what one would conventionally call the phase of the microwave pulse applied to the bare spins, i. e. $[0, \pi/2, \pi, 3\pi/2]$ for $[x, y, -x, -y]$. Likewise, ϕ_{PM} is the phase of the PM pulse that is applied to the dressed spins. We use $\phi_0 = 0$ for the following discussion. For small modulation amplitudes, $a_{\mathrm{PM}} \ll 1$, we can use the approximations $\cos\left(\phi_{\mathrm{mw}}\right) \approx 1$ and $\sin\left(\phi_{\mathrm{mw}}\right) \approx \phi_{\mathrm{mw}}$ and obtain a truncated rotating-frame Hamiltonian

$$\hat{\mathcal{H}}' \approx \Omega_S \hat{S}_z + \omega_1 \hat{S}_x + \omega_1 a_{\mathrm{PM}} \cos\left(\omega_{\mathrm{PM}} t + \phi_{\mathrm{PM}}\right) \hat{S}_y \qquad . \qquad (4.14)$$

For a hard pulse, i. e. $\omega_1 \gg \Omega_S$, we can now apply a second interaction frame transformation with $\omega_{\mathrm{PM}} \hat{S}_{x'}$, use the RWA again, and obtain the dressed rotating frame Hamiltonian

$$\hat{\mathcal{H}}'' = \Omega_{\mathrm{d}} \hat{S}_x + \frac{\omega_1 a_{\mathrm{PM}}}{2} \left(\cos\left(\phi_{\mathrm{PM}}\right) \hat{S}_y + \sin\left(\phi_{\mathrm{PM}}\right) \hat{S}_z\right) \qquad , \qquad (4.15)$$

with the dressed spin offset $\Omega_{\mathrm{d}} = (\omega_1 - \omega_{\mathrm{PM}})$, already introduced in Equation (4.3), and a dressed spin nutation (Rabi) frequency of $\omega_1 a_{\mathrm{PM}}/2$. Again, the RWA implies that we neglect a Bloch-Siegert shift, now for the dressed spins, which would introduce a correction to Ω_{d}. The whole situation is analogous to the rotating frame Hamiltonian in Equation (4.12), but with an exchange of axes.

Some words of caution: First, in EPR unlike in NMR, the hard pulse limit will often not be fulfilled. In a first step, one can use an interaction frame transformation with the whole effective nutation field, $\Omega_S \hat{S}_z + \omega_1 \hat{S}_x$. For the sake of intuitive clarity, we will not do this for the qualitative discussion. Second, one can easily choose a large a_{PM}, such that the RWA leading from Equation (4.14) to Equation (4.15) is seriously invalid. This was recognized already in [111], and studied separately in [115]. In our study, imperfection of the RWA is visible in nutation curves, but the final results do not seem to be affected. The problem might be alleviated by using an appropriate frequency or amplitude modulation in order to generate a circularly polarized field in the rotating frame.

There are two alternatives to the phase-modulation schemes. One could equivalently formulate the dressed spin resonance as a frequency-modulation.

Phase- and frequency modulation are physically equivalent, but we prefer the phase-modulation because the description of frequency-modulation involves a time-dependent offset/detuning and thus a "wobbling" frame, which makes it harder to keep track of relative phases of coherences. Instead of any microwave/radio-frequency modulation, one could also use a modulation of the magnetic field along the laboratory frame z direction [112]. Depending on the setup, the relative phase of the modulation can be locked to the phase of the driving field or not. If an arbitrary waveform generator setup is available, phase modulation may be preferable, as it does not require modulation coils and a radiofrequency amplifier and makes synchronisation of bare-spin and dressed-spin pulses much easier. However, the amplitude of the phase pulses depends on the Rabi frequency itself in the case of phase modulation. By using an external oscillating field, this dependence would vanish.

4.2.3   *Pulse sequence*

The pulse sequence used to measure the dipolar coupling in this work is the dressed-spin primary echo sequence shown in Figure 4.1. It can be readily understood with results from the previous sections. For dipolar measurements, one chooses $\tau_1 = \tau_2$ and constant T_{SL}. The first $\pi/2$ pulse generates electron coherence. Since we deal with trityl radicals, the excitation can be nearly uniform on our setup. The spins are then locked with a spin-lock pulse that is 90 degrees phase shifted with respect to the first pulse. Let us assume that the spin-lock and the coherences are along x'. For free dressed-spin evolution, i. e. in the absence of phase modulation, we can assume the following Hamiltonian during the spin-lock in the nutating frame:

$$
\begin{aligned}
\hat{\mathcal{H}}'' = {} & \Omega_{\mathrm{d}} \left(\hat{S}_{1x} + \hat{S}_{2x} \right) \\
& - \frac{\omega_{\mathrm{dd}}}{2} \left(\hat{S}_{1x} \hat{S}_{2x} - \frac{1}{2} \left(\hat{S}_{1z} \hat{S}_{2z} + \hat{S}_{1y} \hat{S}_{2y} \right) \right) \quad ,
\end{aligned}
\tag{4.16}
$$

where we recall that $\Omega_{\mathrm{d}} = (\omega_1 - \omega_{\mathrm{PM}})$. Note that ω_1 is inhomogeneous over the sample, but is the same within each pair of spins.

The Hamiltonian in Equation (4.16) is analogous to the one in the rotating frame, but to a very good approximation the offsets are the same for both dressed electron spins. Additionally, all hyperfine couplings vanish. The phase modulation pulses act on the dressed spins in the nutating frame. We can thus generate a *dressed spin echo* by a phase-pulse sequence $\pi/2 - t - \pi - t$. A third $\pi/2$ pulse is needed that rotates any refocused dressed-spin coherence back to the $x'' = x'$ axis. The magnetization resulting from this backrotation
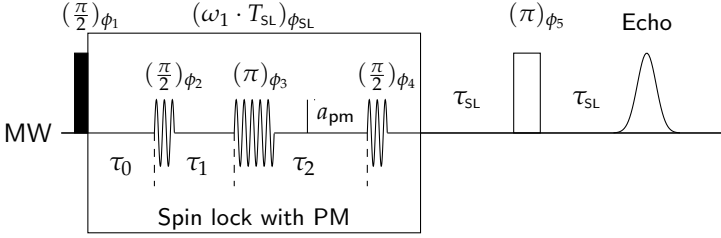
FIGURE 4.1: Pulse sequence used to measure the dipolar coupling during a spin-lock. Note that $|\phi_{\mathrm{SL}} - \phi_1| = \pi/2$. The phases ϕ_{2-4} correspond to ϕ_{PM} in Equation (4.13), while $\phi_{\mathrm{SL}} = \phi_0$ in the same equation. Details for the inner working of the sequence are given in the main text.

is locked again, until it is detected by the remaining $\tau - \pi - \tau-$ echo sequence. A very similar sequence was already demonstrated with z-modulation pulses in [112], albeit not for dipole-dipole coupled electron spins.

The dressed-spin echo is needed to refocus microwave field inhomogeneities (i. e. a distribution of ω_1 and thus also Ω_{d}). The dipolar part of the Hamiltonian is unaffected by the PM-π pulse, because this pulse inverts both spin operators at the same time. With effects of the other terms being refocused, it is sufficient to only keep the dipolar part during the periods τ_1 and τ_2:

$$\tilde{\hat{\mathcal{H}}}'' = -\frac{\omega_{\mathrm{dd}}}{2}\left(\hat{S}_{1x}\hat{S}_{2x} - \frac{1}{2}\left(\hat{S}_{1z}\hat{S}_{2z} + \hat{S}_{1y}\hat{S}_{2y}\right)\right) \qquad . \qquad (4.17)$$

At the start of the period τ_1, after the first phase pulse, the system is in the state $\hat{\sigma}'' = \hat{S}_{1z} + \hat{S}_{1z}$ (or along y'', depending on the phase ϕ_2). For $\tau_1 = \tau_2$, this evolves according to

$$\hat{\sigma}'' \xrightarrow{\tilde{\hat{\mathcal{H}}}'' \cdot 2\tau_1} \cos\left(\frac{3}{4}\omega_{\mathrm{dd}}\tau_1\right)\left(\hat{S}_{1z} + \hat{S}_{1z}\right)$$
$$+ \sin\left(\frac{3}{4}\omega_{\mathrm{dd}}\tau_1\right)\left(2\hat{S}_{1x}\hat{S}_{1y} + 2\hat{S}_{1y}\hat{S}_{1x}\right) \qquad . \qquad (4.18)$$

The z'' terms are then flipped to $x'' = x'$, are transferred to bare-spin coherence at the end of the microwave pulse and are then detected by the echo. The other terms do not contribute to the detected signal. The factor of $3/4$ has two contributions. A factor of $(-)1/2$ is due to the spin-lock and the partial averaging of the dipolar coupling, see Equation (4.8). A factor of $3/2$ is due to the strong coupling regime in the dressed frame, because the dressed electron spins are equivalent. This scaling by a factor of $3/2$ for trityl

biradicals has been observed before at short distances with established single-frequency techniques [127], where it results from the dipole-dipole coupling being much larger than the mean difference of the resonance frequencies of two trityl radicals. In conclusion, we expect that for dressed spins echo intensity oscillates with 3/4 of the dipolar coupling, which for a fixed or narrowly distributed distance will manifest in a Pake pattern because the measurements are conducted in frozen solution.

The timing τ_{SL} of the read-out echo does, in principle, affect the resulting dipolar spectrum, because it acts as filter with the signal intensity scaling with $\cos\omega_{\text{dd}}\tau_{\text{SL}}$. However, for short interpulse delays and long distances, such filtering should be negligible. If necessary, a SIFTER-type readout sequence could be used, which refocuses both the offsets and the dipolar couplings.

It is noteworthy that, in principle, a normal two-pulse echo on the bare spins with non-selective pulses would be sufficient to measure the dipolar coupling. In practice, this approach is usually much inferior to the DQC and SIFTER sequences, because the phase memory time is of the same order of magnitude as the dipolar oscillations, echo decay is not monoexponential and contains other contributions, and dead-time is significant. The combination of these complications makes it very difficult to separate the dipolar oscillation. Under the spin-lock, the relaxation is sufficiently slowed down, such that the dipolar evolution is clearly distinguishable, and the dead time in a PM-pulse sequence is nearly zero. If the dead time becomes too large for the relevant dipolar oscillations, one could, in principle, apply the known dead-time free single-frequency pulse sequences DQC and SIFTER also as a phase-pulse sequence in the nutating frame.

4.2.4   *Expected limitations*

The derivation of the modulation formula in Equation (4.18) depends on the condition that ω_1 is much bigger than all other frequencies present in the system. Especially for the bare-spin resonance offsets, this approximation is not fulfilled very well. In principle, one could account for the different offsets analytically, but this is rather tedious and does not provide much additional insight. We will present numerical simulations in the result section to illustrate the deviations.

4.3 MATERIALS AND METHODS

All measurements were performed on a home-built Q-band spectrometer equipped with a Keysight M8190A arbitrary waveform generator operating at 8 GS/s and an ADC with a sampling frequency of 2 GHz (SP Devices ADQ412) [128]. The highly flexible software made it straightforward to implement the pulse sequences with PM pulses, in contrast to commercial analogues. Microwave pulses were amplified with a travelling wave tube (TWT) amplifier with 150 W nominal output power (Applied Systems Engineering). A home-built Q-band loop-gap resonator for 1.6 mm tubes was used [40]. Note that the long spin-lock pulses with full power can be dangerous for the receiver, since much of the power is reflected by the overcoupled resonator. We did not take any special measures beyond the receiver protection switch [19]. However, we are planning to install an additional limiter or a slow switch that could take more power. Since the spin-lock pulses are rather long, a slow switch could be used for most of the time , while the fast switch could be used for the transient times of the pulses to still provide the small dead time.

As model compounds, we used bis-trityl rulers with electron-electron distances of about 4.1 nm and 5.3 nm. The synthesis is discussed in Section 4.4.1. The bis-trityl rulers were dissolved in *ortho*-terphenyl (OTP) or its perdeuterated analogue dOTP providing solutions of different concentrations. More details are given in each figure and the SI of [92].

Measurements were conducted at 50 K using a liquid helium flow cryostat. We did not systematically test the optimal temperature for each measurement. However, it is likely that higher temperatures would allow for shorter shot repetition times without dramatically changing the dephasing times.

Frequency-domain spectra were measured with chirp echoes and subsequent Fourier transform instead of field sweeps [32]. Chirp pulses covered a range of 300 MHz symmetrically around the centre of the spectrum. The powder spectrum was simulated with the *EasySpin* library [82].

The two-pulse dephasing time T_m was measured with a sequence $\pi/2 - \tau - \pi - \tau-$ echo with $t_\pi = 2t_{\pi/2}$. Different pulse lengths were used to check whether instantaneous diffusion contributes to coherence loss. Similar to previous findings by [127], it was found that flip angles of $\pi/2$ or $3\pi/2$ for the second pulse gave higher echo intensities than an angle of π. More details are given in the SI of [92].

The rotating frame relaxation time $T_{1\rho}$ was measured with the sequence in Figure 4.1 in the absence of any phase-modulation pulses and variable T_{SL} and with $\tau_{SL} =$ 200 ns. Interestingly, $T_{1\rho}$ is significantly different when

measured with a simple spin-locked echo with the sequence $\pi/2 - \tau -$ lock $-\tau-$ echo. More details are given in the results section and the SI of [92].

The rotating frame relaxation time $T_{2\rho}$ for the mono-trityl was measured with the sequence in Figure 4.1 including the phase-modulation pulses and fixed T_{SL} and with $\tau_{SL} =$200 ns. In the case of the bis-trityls, it is impossible to measure $T_{2\rho}$ independent of the dipolar coupling. Where applicable, we mention the decay rate of the "intramolecular background" for comparison.

All decay rates were obtained by fitting a stretched exponential of the functional form

$$f(t) = \exp\left(-(t/T)^{\xi/3}\right) \tag{4.19}$$

to the relaxation curves, where $t = 2\tau$ and $T = T_m$ for the two-pulse echo decay, $t = 2\tau_1$ and $T = T_{2\rho}$ for dressed echo decays, and $t = T_{SL}$ and $T = T_{1\rho}$ for the longitudinal rotating frame relaxation time.

The Rabi frequency ω_1 was measured with a nutation experiment $t_{nut} - T - \pi/2 - \tau - \pi - \tau-$ echo. As a control, we performed a dressed-spin resonance experiment with the sequence in Figure 4.4, but only one PM pulse with low amplitude and variable frequency. This also yields the ω_1 spectrum (see the SI of [92]). A similar experiment with z-modulation was demonstrated in [112].

When the Rabi spectrum is known, one can set the value of the PM frequency ω_{PM}. One then needs to choose a value for the modulation amplitude a_{PM} and set up the PM pulse lengths. This can be achieved with a PM nutation experiment. Again, one uses the basic sequence in Figure 4.1, with one pulse only with now fixed ω_{PM}. One then observes the echo intensity as a function of the PM pulse length. That way the optimal PM pulse length can be determined. When choosing $a_{PM} = 0.3$, we observed only slight Bloch-Siegert shift related oscillations in the PM pulse nutation traces while achieving a PM π-pulse length of $40 - 42$ ns.

The dressed echo can not be detected directly, because τ_1 and τ_2 are both indirect variables. Only the actual echo at the end of the microwave pulse sequence is digitized continuously. In order to optimize indirect detection, we checked that the last PM pulse in Figure 4.1 is applied at the correct position. We observed that the position seems to be nearly perfectly predictable by setting $\tau_2 = \tau_1 + t_{\pi/2}$, where $t_{\pi/2}$ refers to the length of the PM-$\pi/2$-pulse. We observed crossing dressed-spin echoes when changing interpulse delays in the PM pulse sequence, similar to what is known in microwave multi-pulse sequences in pulse EPR. Interestingly, the position of some unwanted echoes depends on the choice of τ_0. Nevertheless, all these unwanted echoes can be suppressed by phase cycling the initial phases ϕ_{PM} of the PM pulses, ϕ_{2-4}.

A step-by-step guide to setting up the sequence is provided in the SI of [92].

4.4 RESULTS

4.4.1 *Synthesis*

The synthesis of bis-trityl rulers **1** and **2** is presented in Figure 4.2. They were assembled from the rodlike building blocks **6** equipped with amino groups at both ends and trityl acid chloride **8**. The latter was prepared from the corresponding trityl acid **7** (also named mono-trityl) using a procedure that has been described for the corresponding conversion of the structurally related Finland trityl radical [129]. To achieve a complete conversion of the building blocks **6**, trityl acid chloride **8** was used in excess. Leftover trityl acid chloride **8** is hydrolysed upon workup and the resulting trityl acid **7** is easily removed by filtration through silica gel. The building blocks **6** were obtained through a sequence of alkynyl-aryl coupling reactions [130–132] and a final oxidative alkyne dimerization. Oxidative alkyne dimerization is a very efficient way to obtain rod-like spacers with the same functional groups at both ends. Although this gives a butadiyne moiety, the spacer is still rather stiff and therefore the spin-spin distance sufficiently well-defined [119, 120].

4.4.2 *Relaxation of mono-trityl 7*

As a reference, we measured the spectrum and the relaxation properties of the mono-trityl **7** in dOTP, see Figure 4.3. As visible in panel (B), $T_{1\rho}$ is orders of magnitude larger than T_{m}. Unfortunately, our TWT prevents us from using spin-lock pulses of more than $40\,\mu s$, meaning that uncertainty in $T_{1\rho}$ is rather large. Nevertheless, fitting a single stretched exponential to each curve yields values of T_{m}=2.9 μs and $T_{1\rho} \approx 930\,\mu s$. As mentioned above, the distance measurements based on dressed spin echoes are limited by the transverse rotating frame relaxation time $T_{2\rho}$ rather than the longitudinal one $T_{1\rho}$. The blue curve in panel (B) shows the dressed echo decay, indicating that $T_{\mathrm{m}} < T_{2\rho} \ll T_{1\rho}$, with a fitted value of $T_{2\rho}$=13.1 μs.

The large difference between $T_{1\rho}$ and $T_{2\rho}$ was rather surprising to us. We are not aware of any example in the literature where $T_{2\rho}$ is discussed in-depth in the context of EPR, although there are several discussion in NMR and MRI [133]. It remains unclear what the limiting contribution to $T_{2\rho}$ is. In analogy to solid-state NMR, residual coupling terms of the hyperfine interactions certainly contribute. An additional contribution would be the
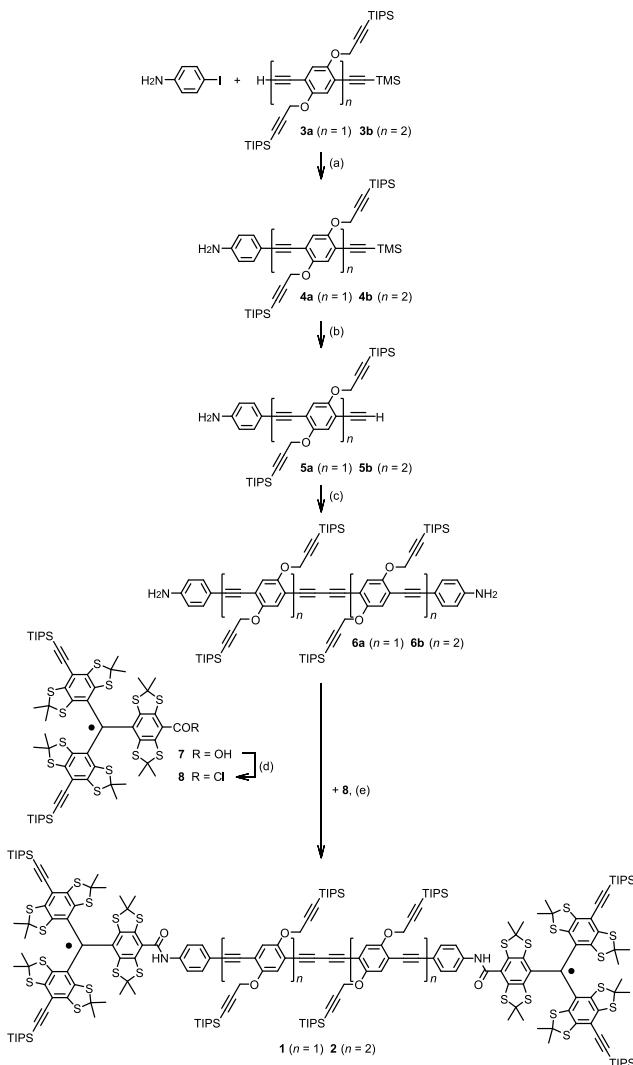
FIGURE 4.2: Synthesis of the bis-trityl rulers **1** and **2**. For $n = 1$: (a) PdCl$_2$(PPh$_3$)$_2$, CuI, piperidine, THF, rt, 25 h, 84%; [132] (b) K$_2$CO$_3$, MeOH, CH$_2$Cl$_2$, rt, 14.5 h, 96%; (c) PdCl$_2$(PPh$_3$)$_2$, CuI, piperidine, THF, air, rt, 16 h, 36%; (d) SOCl$_2$, CHCl$_3$, 50 °C, 90 min, not isolated; (e) ^{i}Pr$_2$NEt, CHCl$_3$, rt, 17 h, 40%. For $n = 2$: (a) PdCl$_2$(PPh$_3$)$_2$, CuI, piperidine, THF, rt, 46 h, 86%; (b) K$_2$CO$_3$, MeOH, CH$_2$Cl$_2$, rt, 14.5 h, 96%; (c) PdCl$_2$(PPh$_3$)$_2$, CuI, piperidine, THF, air, rt, 15.5 h, 65%; (d) SOCl$_2$, CHCl$_3$, 50 °C, 90 min, not isolated; (e) ^{i}Pr$_2$NEt, CHCl$_3$, rt, 19 h, 64%. For further details see the SI of [92] part B. THF = tetrahydrofuran, TIPS = triisopropylsilyl, TMS = trimethylsilyl, rt = room temperature.

remaining intermolecular dipolar couplings, but then we would expect a strong dependence on the concentration, which we did not observe. Another factor that will definitely contribute is the noise of the driving field [117]. The noise (phase and amplitude) of the TWT during spin lock will not be refocused by the dressed echo. It is hard to quantify this contribution, since we do not have high-power amplifiers with different noise figures. In the future, we might investigate the influence of artificially added driving noise on $T_{2\rho}$.

The large difference between $T_{1\rho}$ and $T_{2\rho}$ is unfortunate, because our proposed sequence will be limited by the latter. Nevertheless, one might come up with a sequence that will be limited by the former, longer relaxation time, and thus we measured $T_{1\rho}$ also for the bis-trityl rulers.
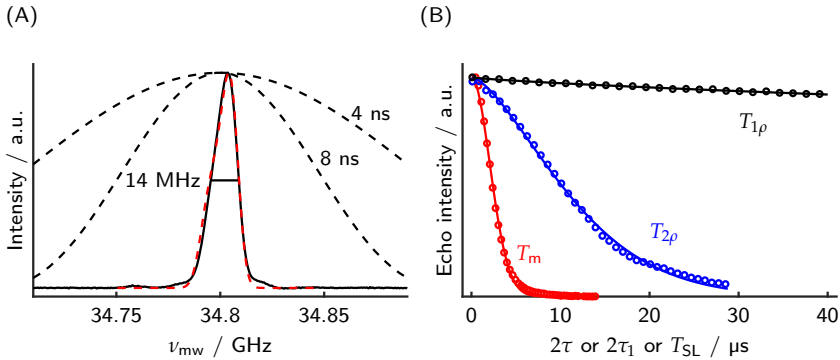

FIGURE 4.3: Measurements on mono-trityl **7**. (A) EPR spectrum. The excitation profiles of the rectangular pulses used are indicated. They are sufficiently strong to excite the whole EPR line. The red dashed lines indicate a simulation based on the g-values given in [121] and an Gaussian broadening of 8 MHz FWHM. (B) Corresponding echo decay curves. Experimental points in circles (not all points shown for clarity), and best fit in solid lines. The fitted values are T_{m}=2.9 μs ($\xi = 5.9$), $T_{2\rho}$=13.1 μs ($\xi = 4.6$) and $T_{1\rho}$=930 μs ($\xi = 2.4$).

4.4.3   *Bis-trityl 1, r ≈ 4.1 nm*

The results for bis-trityl **1** are shown in Figure 4.4. The chirp echo FT-EPR spectrum is shown in panel (A). The spectrum consists of a slightly asymmetric line with an FWHM of 16 MHz. The theoretical excitation profile

of a 4 ns and an 8 ns microwave pulse are overlaid, showing that the whole spectrum can be excited almost uniformly with rectangular pulses.

The relaxation measurements for T_m and $T_{1\rho}$ are displayed in panel (B), and they show the same trends as in the case of the mono-trityl. Note that the T_m measurement displayed was done with 100 ns/200 ns pulses. Otherwise, the dipolar oscillations are already strongly visible in the two-pulse echo decay. It is immediately clear that the rotating frame relaxation time $T_{1\rho}$ is much longer than the phase-memory time, $T_{1\rho} \gg T_m$. The phase memory time is about 3.3 µs, while after 40 µs of spin-lock, the echo intensity is still more than 90 % of its maximal value. A naive fit with a stretched exponential yields $T_{1\rho} \approx 560$ µs.

The modulation of the dressed-spin echo is displayed in panel (C). Clear oscillations are visible in the primary data. Since we do not currently have a model for the background, we fitted a stretched exponential to the data. This background is very similar to the $T_{2\rho}$ measurement of the mono-trityl (14.3 µs *vs.* 13.1 µs decay constant), which also means that it decays much faster than $T_{1\rho}$. Note that not only intermolecular dipolar couplings from remote spins contribute to the background. Transverse relaxation of dressed spins with time constant $T_{2\rho}$ also contributes because we do not perform a constant time experiment. Regarding modulation depth we would have expected it to be unity, which is clearly not seen in our experiments. We suspect that imperfections in the dressed spin π-pulse lead to an unmodulated background, which cannot be removed by phase-cycling. The phenomenon is similar to reduced instantaneous diffusion for a Hahn echo if the flip angle of the π-pulse is reduced.

After background correction by division and a Fourier transform, we obtain the spectrum in Figure 4.4 (D). The spectrum is a nice Pake pattern with the characteristic singularities at one and two times the dressed-spin dipolar frequency. The singularities appear at the expected positions. The splitting parameter d can be calculated from the expected distance of 4.1 nm, but it is scaled by a factor of 3/4 as discussed above.

4.4.4   *Bis-trityl 2, r ≈ 5.3 nm*

The analogous data of bis-trityl **2** are displayed separately in Figure 4.5. The chirp echo FT EPR spectrum looks essentially the same as for bis-trityl **1**, with the same slight asymmetry and an FWHM of 16 MHz.

The two-pulse microwave echo decay is slightly faster for bis-trityl **2** (2.9 µs vs. 3.3 µs). Again, it is difficult to really quantify a decoherence time that is
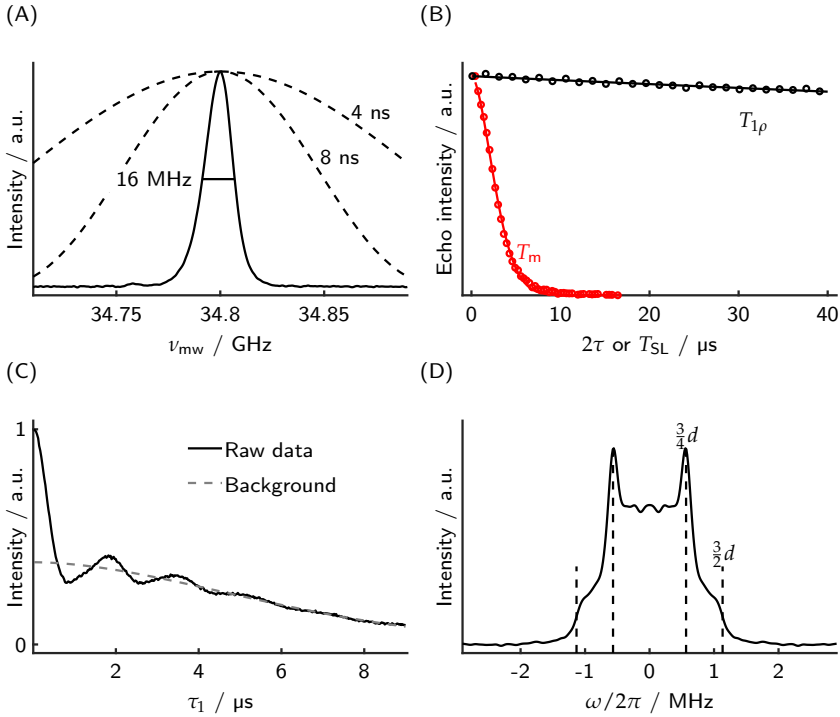
FIGURE 4.4: Measurements on bis-trityl **1**. (A) EPR spectrum. (B) Comparison of the decay of a microwave two-pulse echo (red, bare-spin decoherence) with the decay of the spin-locked echo as a function of T_{SL} (black, dressed-spin polarization decay). Experimental points in circles (not all points shown for clarity), and best fit in solid lines. The fitted values are T_{m}=3.3 μs ($\xi = 5.3$), and $T_{1\rho}$= 560 μs ($\xi = 2.9$) (C) Dressed-spin echo evolution as a function of $\tau_1 = \tau_2$. The dipolar oscillations are clearly visible. A stretched exponential background with $T_{2\rho}$=14.3 μs ($\xi = 5.4$) is shown in gray. (D) Dipolar spectrum obtained by a Fourier transform of (C) after background division. The positions of the expected singularities based on the distance of the electrons are indicated by dashed lines. Note that there are small artefact peaks outside the plotting range at ±8 MHz which we suspect to be a sampling artefact.
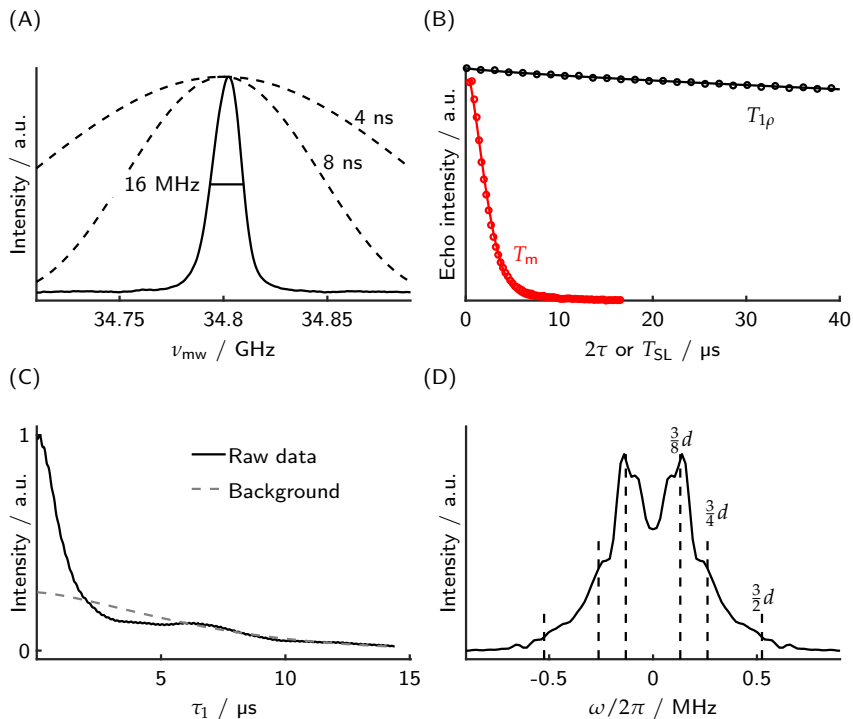
FIGURE 4.5: (Measurements on bis-trityl **2**. (A) EPR spectrum. (B) Bare-spin decoherence (two-pulse echo decay, red) and dressed-spin polarization decay (spin-locked echo decay, black). Experimental points in circles (not all points shown for clarity), and best fit in solid lines. The fitted values are T_{m} =2.6 μs ($\xi = 4.9$), and $T_{1\rho} \approx$730 μs ($\xi = 2.4$) (C) PM echo evolution as a function of $\tau_1 = \tau_2$. A stretched exponential background with $T_{2\rho}$ =14.5 μs ($\xi = 4.4$) is shown in gray. The dipolar oscillations are damped and the background obscures the oscillations at long dipolar evolution times. (D) Dipolar spectrum obtained by a Fourier transform of (C) after background division. In addition to the singularities expected from our basic theoretical treatment strong singularities at $3/8d$ are apparent. These features are explained in the main text.

not influenced by residual echo envelope contributions from intramolecular electron-electron coupling. Even with $100\,\mathrm{ns}/200\,\mathrm{ns}$ pulses the excitation profile of the π-pulse is still larger than the dipolar coupling and some dipolar contribution to the echo envelope function is expected. The signal decay of dressed spin polarization under the spin lock($T_{1\rho}=730\,\mathrm{\mu s}$) is again much slower, and comparable to the case of bis-trityl **1**. Unfortunately, the dipolar oscillations in panel (C) are not as clear as in the case of shorter distances. Also, the background is already rather fast compared to the dipolar frequencies ($14.5\,\mathrm{\mu s}$ decay constant). In the dipolar spectrum, panel (D), it becomes clear that this case is more complicated, because additional singularities appear at around $3/8 \cdot d$. These features must result from the breakdown of some approximation that we have made in our theoretical description. Most likely they are due to the finite strength of the spin-lock compared to the inhomogeneous spectral width. For two spins with different bare-spin resonance offsets, both the direction and magnitude of the effective field in the rotating frame differs. Accordingly, the two dressed spins have different resonance frequencies and quantization axes. Unless the dipole-dipole coupling is much larger than the frequency difference, it is significantly perturbed. In order to give a more quantitative explanation, we will show simplified numerical simulations in the following.

4.4.5 *Numerical Simulations*

In order to understand the deviation of our experimental results from the theoretical expectation based on first-order average Hamiltonian theory (especially in the case of bis-trityl **2**), we performed simplified numerical simulations. In principle, one could simulate the complete sequence, including the time-dependent phase during the phase-pulses. We chose a simplified route: We start with both spins along z' and then calculate the expectation value of $\hat{S}_z = \hat{S}_{1z} + \hat{S}_{1z}$ during the spin lock using the Hamiltonian

$$
\begin{aligned}
\hat{\mathcal{H}}' =\,&\Omega_1\hat{S}_{1z} + \Omega_2\hat{S}_{2z} \\
&+ \omega_{\mathrm{dd}}(r,\theta)\left(\hat{S}_{1z}\hat{S}_{2z} - \frac{1}{2}\left(\hat{S}_{1x}\hat{S}_{2x} + \hat{S}_{1y}\hat{S}_{2y}\right)\right) \\
&+ 2\pi \cdot \nu_1(t)\left(\hat{S}_{1x} + \hat{S}_{2x}\right) \qquad .
\end{aligned}
\tag{4.20}
$$

In order to refocus the nutation of the spins around the effective field, we invert the phase of the irradiation in the middle of the spin-lock, such that

$$\nu_1(t) = \begin{cases} \nu_1(0), & \text{for } 0 \le t < \tau_1 \\ -\nu_1(0), & \text{for } \tau_1 \le t < 2\tau_1 \end{cases} . \tag{4.21}$$

This emulates the effect of the dressed refocusing (phase) pulse. With this choice, the evolution consists of two periods with time-independent Hamiltonians, which is straight-forward to calculate on a computer.

In our implementation, which is available online, the parameters Ω_1, Ω_2, r, and θ are drawn in Monte-Carlo fashion from their respective distributions (Gaussian for the first three, $P(\theta) = \sin(\theta)$ with $0 \le \theta \le \pi/2$ for the latter). Statistical independence of the parameters is assumed. It is not unlikely that this assumption is at least partially wrong, since the respective orientation of the trityl moieties is restricted by the rigid linker. Although we have implemented simulations with a distance distribution, we do not consider such cases here but rather assume fixed values of r. Additionally, all the simulations shown here assume on-resonance irradiation in the sense that the mean values of Ω_1 and Ω_2 are 0.

Some illustrative simulations are shown in Figure 4.6. For each parameter set, we display the numerical simulation in time and frequency domain as solid lines and show the analytical dipolar powder pattern (scaled by 3/4) as dashed lines on top. In panel (A), we show simulations assuming infinitely narrow EPR lines. In this case, the numerical and analytical results are the same. Panel (B) shows a simulation were we assume a FWHM of 16 MHz for both offset distributions (denoted by Γ_Ω). For the case of $r = 5.3$ nm, the simulation qualitatively reproduces the experimental results for bis-trityl **2**, especially regarding the singularities in the dipolar spectra. For $r = 4.1$ nm, the experimental results actually look better than the simulation if one regards the additional singularities at $3/8 \cdot d$ as an artefact. In this case, simulations with $\Gamma_\Omega = 8$ MHz are actually closer to the experimental results (see panel (C)). This might suggest that the difference in offsets of bis-trityl **1** is smaller than the EPR spectrum might suggest. Either hyperfine and dipolar couplings significantly contribute to the linewidth of the EPR spectrum, or the offsets are not completely uncorrelated in reality. In order to guide future developments, we also simulated traces assuming $\Gamma_\Omega = 8$, but with significantly larger microwave strengths of ν_1=200 MHz and 400 MHz, see panel (D). Compared to panels (B) and (C), these simulations already show much better defined dipolar spectra. In conclusion, the simulations confirm that at least some of the artefacts in the experimental results are due to

the finite size of the electron spin nutation frequency. The contribution of the artefacts becomes larger for larger offset differences and smaller dipolar couplings.

4.4.6   *Conclusions and outlook*

We showed that it is possible to measure the dipolar coupling between trityl radicals during a spin-lock by using short intervals of phase-modulations, i.e. by a *dressed*-spin echo generated with PM pulses. The relaxation during the spin lock is much slower compared to a simple two-pulse echo decay. The phenomena can be conceptually understood by describing the spin-lock in a nutating frame and using average Hamiltonian theory. For an electron-electron distance of ≈ 4.1 nm, the experimental spectra agree very well with the theoretical expectations that assume a microwave Rabi frequency much larger than all other interactions in the system. For a distance of ≈ 5.3 nm, additional singularities appear in the dipolar spectrum. While the spin dynamics underlying these additional contributions can be understood by numerical simulations, they might seriously complicate data analysis in terms of distance distributions and have to be addressed in the future, if the sequence should be used in application work. Additionally, we showed a profound difference between the longitudinal and transverse rotating frame relaxation times, $T_{1\rho}$ and $T_{2\rho}$. In our case, the latter is much smaller than the former and unfortunately limits the distance measurements by the sequence introduced here. Preliminary results with the OX063 trityl and its partially deuterated analogue OX71 in different solvent compositions (not shown) revealed that even bare-spin relaxation at low temperatures and low concentrations is complicated to understand, let alone dressed-spin relaxation with characteristic times $T_{2\rho}$ and $T_{1\rho}$. We are planning to investigate this in more detail and to compare the different relaxation times also at different temperatures. Note that in dOTP, the T_m values of the slow relaxing component of nitroxides (the relaxation of nitroxides in dOTP can be described by a sum of two stretched exponentials) can still be bigger than the $T_{2\rho}$ times measured here for trityl radicals [91].

Since there are still significant artefacts present in the dipolar spectra when measuring longer distances, we refrained from a systematic analysis of signal-to-noise ratio and a comparison with existing pulse sequences.

Nevertheless, we are confident that the presented obstacles can be overcome. First, it might very well be possible to come up with a dressed pulse sequence that measures the dipolar coupling with an observation time limited by $T_{1\rho}$
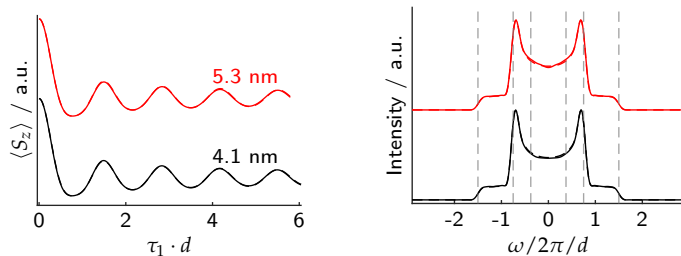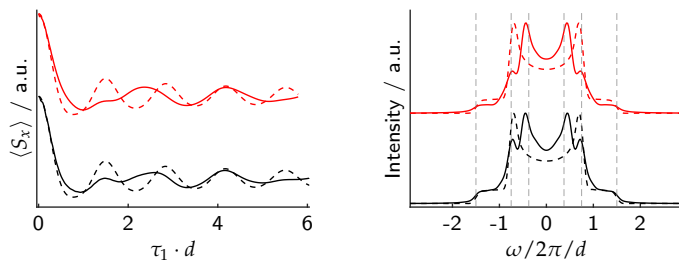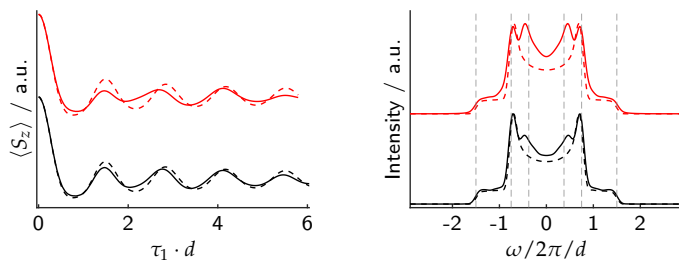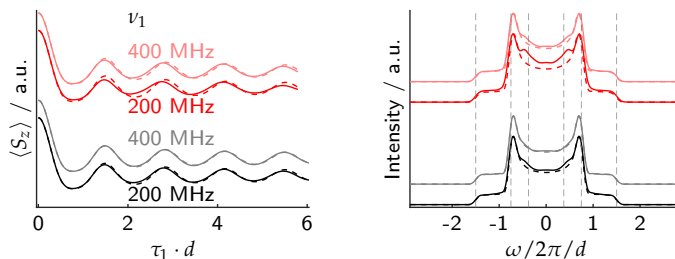
(A) $\Gamma_\Omega = 0$ MHz, $\nu_1 = 100$ MHz

(B) $\Gamma_\Omega = 16$ MHz, $\nu_1 = 100$ MHz

(C) $\Gamma_\Omega = 8$ MHz, $\nu_1 = 100$ MHz

(D) $\Gamma_\Omega = 8$ MHz

FIGURE 4.6: Caption on next page.

FIGURE 4.6: (Previous page.) Numerical simulations with different dipolar couplings, offset distributions, and Rabi frequencies. Time and frequency axes are scaled by the dipolar coupling to facilitate comparison. Dashed lines represent the analytical Pake pattern (with the frequency scaled by 3/4). (A) No offsets at all, 100 MHz Rabi frequency. The numerical simulation of the spin-lock completely matches the analytical expectation. (B) Gaussian offset distribution with FWHM of 16 MHz, 100 MHz Rabi frequency. The numerical simulations deviate from the analytical expectation. In the frequency domain, "artefacts" appear at lower frequencies, around $3/8 \cdot \nu_\perp$. (C) Same as (B), but with reduced offset FWHM of only 8 MHz. The intensity of the artefacts is reduced compared to larger offset distributions. (D) same as (C), but with increased Rabi frequencies. The intensity of the artefacts is again reduced compared to smaller Rabi frequencies.

instead of $T_{2\rho}$. This appears feasible because, unlike the sum of dressed spin polarizations of the two spins, their difference is affected by dipolar coupling. This fact is used in cross-polarization in solid-state NMR and oscillatory behavior of magnetization transfer in the rotating frame has been studied in the context of heteronuclear correlation spectroscopy [134]. Second, the ratio of Rabi frequency to offsets could be reduced by going to a lower field. While in principle we could have done the experiments at X-band frequencies, our TWT in this range can only generate pulses of up to 15 μs. The Rabi frequencies generated by our setup are already rather high ($\approx$ 100 MHz compared to $\approx$50 MHz in most commercial setups), but several groups around the world are working on micro resonators [135–138], which generally give higher conversion factors and could be used to generate higher Rabi frequencies. If these difficulties can be overcome, pulse dressed electron paramagnetic resonance could significantly expand the measurable distance range, at least for trityl radicals.

4.5 ADDITIONAL HYPOTHESIS: $T_{1\rho}$ VS. $T_{2\rho}$

During the writing of this thesis, a new hypothesis emerged why $T_{1\rho} \gg T_{2\rho}$. It might be due to second-order cross terms between the electron offsets and the secular hyperfine coupling. For this, we can look at a simple electron-nuclear system under a spin lock with secular couplings only, this is given by

$$\hat{\mathcal{H}}' = \Omega_S \hat{S}_z + A \hat{S}_z \hat{I}_z + \omega_1 \hat{S}_x \qquad . \tag{4.22}$$

We neglected the nuclear Zeeman interaction, because it commutes with all other terms in this Hamiltonian and has no effect on the electron spin. An IFT with $\omega_1 \hat{S}_x$ leads to

$$\hat{\mathcal{H}}'' = \Omega_S \left(c\hat{S}_z + s\hat{S}_y \right) + A\hat{I}_z \left(c\hat{S}_z + s\hat{S}_y \right) \tag{4.23}$$
$$c = \cos(\omega_1 t)$$
$$s = \sin(\omega_1 t) \qquad .$$

$$(4.24)$$

As mentioned before, the first order average Hamiltonian is zero, i. e.

$$\hat{\mathcal{H}}^{(1)} = 0 \qquad . \tag{4.25}$$

However, the second-order contribution does not vanish. It is given by

$$\hat{\mathcal{H}}^{(2)} = \frac{-i}{2\tau_c} \int\limits_0^{\tau_c} \int\limits_0^{t_2} \left[\hat{\mathcal{H}}''(t_2), \hat{\mathcal{H}}''(t_1) \right] \mathrm{d}t_1 \mathrm{d}t_2 \qquad , \tag{4.26}$$

with $\tau_c = 2\pi/\omega_1$. After a significant amount of algebra, we arrive at

$$\hat{\mathcal{H}}^{(2)} = \frac{1}{2\omega_1} \left(\left(\Omega_S^2 + (A/4)^2 \right) \hat{S}_x + \Omega_S \cdot A \cdot 2\hat{I}_z \hat{S}_x \right) \qquad . \tag{4.27}$$

The term proportional to $\hat{S}_x$ should not contribute to any losses in the spin-locked echo experiment. It just looks like an additional spin-lock field, which should be refocused. On the other hand, the second term, proportional to $2\hat{I}_z \hat{S}_x$ *does* contribute to dephasing of any electron magnetisation orthogonal to the spin lock axis. Electron spins along the spin lock axis are unaffected.

Numerical simulations of a simple electron-nuclear system are shown in Figure 4.7. These simulations confirm the algebraic derivations. The simulations only show a very simple system. One could look at the dephasing of a system with many nuclei, and again a Gaussian distribution of offsets, and see if this reproduces the experimental time scales. Additionally, this hypothesis predicts that the dephasing is proportional to $\frac{1}{\omega_1}$. This should be tested experimentally in the range where it is possible. One remaining question is, if these higher order terms are fully refocused in the dressed echo, or if nuclear-nuclear couplings lead to incomplete refocusing, similar to the case of the normal electron spin echo in a nuclear spin bath.

If it is indeed due to this second order effect, it should be possible to design sequences which suppress this dephasing pathway up to third order.
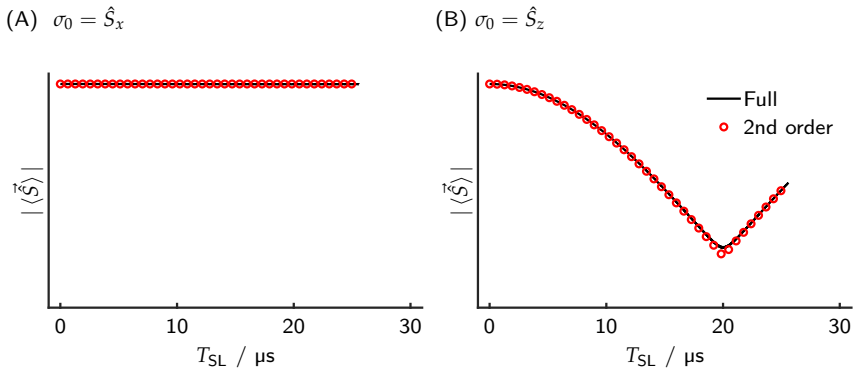
FIGURE 4.7: Second-order effect on $T_{1\rho}$ and $T_{2\rho}$. Full numerical simulations of an electron-nuclear two-spin system (black) and calculations with the second order average Hamiltonian (red circles). The $y-$axis shows the norm of the expectation value of the the electron magnetisation. In this way, effects due to full refocusing of the nutation phase do not have to be considered. Clearly, the second order effective Hamiltonian describes the dynamics very well. Parameters: $\Omega_S/2\pi$=5 MHz, $A/2\pi$=0.5 MHz, $\omega_1/2\pi$=100 MHz.

Part III

PULSED DYNAMIC NUCLEAR
POLARISATION

5

UNDERSTANDING PHASE- AND AMPLITUDE MODULATED PULSED DYNAMIC NUCLEAR POLARISATION IN STATIC SOLIDS

Repetition legitimizes.

— Adam Neely

SUMMARY

We introduce a theoretical approach based on average Hamiltonian and operator-based Floquet theory to describe pulsed dynamic nuclear polarisation (DNP) with arbitrary periodic phase- and amplitude modulation in static solids. We focus on DNP mechanisms involving a single electron spin. The formalism is based on an interaction frame transformation of the electron spin only, which can be calculated analytically in some cases, and numerically in general. The ability to predict resonance conditions and *relative* polarisation enhancements is exemplified with a low-power XiX sequence and a high-power sequence termed broadband amplitude modulated signal enhanced (BASE) DNP. Experimental results are obtained with OX063 trityl radicals in DNP juice at X-band frequencies (9.5 GHz/15 MHz/0.35 T). We show how periodically modulated pulsed DNP sequences can be turned into adiabatic transfer sequences by slowly changing any of the sequence parameters from one modulation period to the next. An adiabatic version of BASE shows an improved bandwidth by a factor of about three with respect to NOVEL and ramped-amplitude NOVEL, with comparable maximal polarisation enhancements of about 360. The theoretical approach allows for rapid exploration of different sequences and can be used to design pulsed DNP sequences that are tailored to the experimental constraints.

5.1   INTRODUCTION

Dynamic nuclear polarisation (DNP) is a powerful tool to increase the sensitivity of nuclear magnetic resonance (NMR) by transferring the much higher spin polarisation of electron spins to nuclear spins. Several different DNP mechanisms are known, most notably the Overhauser effect (OE), the solid effect (SE), the cross effect (CE) and thermal mixing (TM) [139]. The established approaches in chemical and biological research use continuous-wave (CW) microwave (mw) irradiation of the electron spin, mostly because of the limited power and pulse shaping hardware at the frequencies needed to combine DNP with high-field NMR.

The most widespread approach, DNP-enhanced magic angle spinning (MAS)-NMR, uses bis-nitroxides as polarising agents dispersed in a glassy matrix, and gyrotrons to generate the necessary microwave powers at hundreds of GHz [140]. Under these circumstances, the CE dominates, further enhanced by MAS and related level anti-crossings due to modulated anisotropic interactions [141, 142].

However, DNP is also used under different conditions. Dissolution DNP is conducted with static samples at very low temperatures, with magnetic fields where the thermal electron spin polarisation approaches unity [143]. Triplet-DNP makes use of the non-Boltzmann polarisation of photo-excited triplet states. Accordingly, no high fields are required to reach nuclear polarisations approaching unity [144]. DNP can also be used in combination with nitrogen-vacancy (NV)-centres in diamond [145].

In recent years, there was increased interest in developing pulsed DNP sequences [146]. It is usually argued that these might potentially lead to enhancements with a more favourable field dependence compared to CW methods. Examples include nuclear orientation via spin locking (NOVEL) [147–149], ramped-amplitude (RA)-NOVEL [150], off-resonance NOVEL [151],

the integrated solid effect (ISE) [152], also in its frequency swept variant (FS-ISE) [153], the adiabatic solid effect (ASE) [154], nuclear rotating frame (NRF)-DNP [155], the dressed spin solid effect (DSSE) [156], time-optimised pulsed (TOP)-DNP [157], and PulsePol [158], a sequence based on hard $\pi/2$ and π pulses with particular phases and strategically timed delays.

The naming is unfortunately not very descriptive, which makes it difficult to grasp the similarities and differences, even for otherwise experienced researchers in solid-state NMR and EPR. The SE, off-resonance NOVEL and NOVEL make use of the same generalised resonance condition, where the electron effective field matches the nuclear Zeeman frequency. RA-NOVEL, ASE and ISE are variations that use adiabatic sweeps to increase the robustness for broader lines and microwave inhomogeneities. NRF- and DSSE-DNP use a combination of microwave and radio-frequency irradiation. Only PulsePol and TOP-DNP are modulated sequences with basic units that are repeated periodically. The modulation frequency is then a part of the resonance condition, similar to the plethora of sequences in MAS NMR. In the latter case, the modulation frequency interferes with the MAS frequency, while in DNP, it is the nuclear Zeeman frequency, or the nuclear effective frequency that interferes with the modulation.

Although we will discuss a new DNP sequence, namely broadband amplitude-modulated signal enhanced (BASE)-DNP, it is not the main purpose of this work to introduce a particular sequence. Rather, we want to discuss how any modulated DNP sequence can be understood, and how slow variations of nearly any parameter can lead to generalised adiabatic sweeps through the resonance conditions. Consequently, while obviously important, the absolute signal enhancements are secondary for this work.

In the following, we will provide a description applicable to arbitrary periodic DNP sequences and how basically any sequence can be made adiabatic. We will then underpin the theoretical results with experimental data acquired with 5 mM Ox063 trityl in "DNP juice" (glycerol-d_8:D_2O:H_2O, 6:3:1 by volume) at 80 K at X-band frequencies (about 9.8 GHz electron Zeeman frequency, corresponding to 0.35 T and 15 MHz proton frequency).

5.2 THEORY

In this section, we describe how periodic pulse sequences lead to an electron-nuclear polarisation transfer in static solids, i.e. without MAS. We limit ourselves to a system of one electron spin and one nuclear spin, although the effective Hamiltonian could be used to describe systems with multiple nuclei

as well, as long as the repeating unit of the pulse sequence is short enough that no nuclear-nuclear transfer takes place. The limitation to one electron excludes the description of CE and TM, at least for now.

We will expand on the theoretical description used for TOP-DNP [157], which in turn followed the treatment used in operator-based Floquet theory [159]. The calculation of Fourier coefficients and some tedious book keeping of different resonance conditions and corresponding effective Hamiltonians is simplified by following [160]. First, an interaction frame transformation with respect to the microwave irradiation is used. The resulting time-dependent Hamiltonian is then expanded into Fourier coefficients. From these, an effective, time-independent Hamiltonian can be derived. Depending on the sequence and its parameters, the coefficients can be calculated analytically. If not, they can be extracted from a numerically calculated single-spin trajectory of one repeating unit of the sequence. From the coefficients, which only depend on the sequence, and not the spin system, a numerical scaling factor is calculated. Together with the hyperfine coupling, the scaling factor determines the polarisation transfer frequency.

We want to emphasize at this point that the scaling factors are *not* the same as the polarisation enhancement. The scaling factor in this paper describes the strength of the zero-quantum or double-quantum part of the coupling Hamiltonian in an effective frame. There are many other parameters than the scaling factors which influence the nuclear polarisation enhancement, such as relaxation times, electron concentration, proton concentration, nuclear spin diffusion, the chemical structure of the polarising agent, and in the case of pulsed dynamic nuclear polarisation, the repetition rate of the DNP sequence [146, 161, 162]. A simple "Gedankenexperiment" can illustrate this. In the limit of very fast electron and very slow nuclear relaxation, DNP will lead to an equilibration of polarisations, *irrespective* of the transfer efficiency (unless it is zero). Of course, outside of this idealised limit, the scaling factors should at least partially explain the relative enhancements, i. e. maximising them as much as possible is still a target of sequence design.

For large scaling factors and long enough contact times, the polarisation transfer can show transient behaviour. In these cases, it can make sense to adjust sequences in a way that decrease the scaling factor, but increase the robustness towards experimental imperfections and distributions of parameters.

One way of doing this is by generalised adiabatic sweeps through resonance conditions, which we will also discuss in detail.

5.2.1 *Derivation of the effective Hamiltonian*

We start with the Hamiltonian of an electron-nuclear two-spin system in the laboratory frame of reference in angular frequencies[1]:

$$\hat{\mathcal{H}}^{(\text{LAB})} = \omega_S \hat{S}_z + \omega_I \hat{I}_z + \vec{\hat{S}} \cdot \mathbf{A} \cdot \vec{\hat{I}} \quad , \tag{5.1}$$

where $\omega_S = -\gamma_e B_0$ and $\omega_I = -\gamma_n B_0$ are the electron and nuclear Zeeman frequencies, respectively. The gyromagnetic ratios of the electron and nucleus are denoted by γ_e and γ_n, and the external, static magnetic field with magnitude B_0 is assumed to be along the z-axis. The last term in Equation (5.1) is the hyperfine coupling with the tensor $\mathbf{A}$. We describe experiments in a substantial external field, where the electron Zeeman frequency is much larger than all other frequencies in the system. Thus, we go into a rotating frame with $\omega_{\text{mw}} \hat{S}_z$ and neglect all time-dependent terms (secular approximation). This leads to

$$\hat{\mathcal{H}}^{(\text{RF,S})} = \Omega_S \hat{S}_z + \omega_I \hat{I}_z + \hat{S}_z \left(A_{zx} \hat{I}_x + A_{zy} \hat{I}_y + A_{zz} \hat{I}_z \right) \quad , \tag{5.2}$$

with the electron offset $\Omega_S = \omega_S - \omega_{\text{mw}}$. It is customary to rotate the nuclear spin coordinates around $\hat{I}_z$ to obtain the most commonly used form of the electron-nuclear Hamiltonian

$$\hat{\mathcal{H}}_0 = \Omega_S \hat{S}_z + \omega_I \hat{I}_z + A \hat{S}_z \hat{I}_z + B \hat{S}_z \hat{I}_x \quad . \tag{5.3}$$

The term $A \hat{S}_z \hat{I}_z$ with $A = A_{zz}$ is called the secular hyperfine coupling, while $B \hat{S}_z \hat{I}_x$ with $B = \sqrt{A_{zx}^2 + A_{zy}^2}$ is called the pseudosecular hyperfine coupling. In the absence of dynamics and radio-frequency irradiation of the nucleus, it is always the latter that leads to electron-nuclear polarisation transfer. The pseudosecular coupling originates from the dipolar interaction, which is averaged in solution due to fast tumbling. There is no isotropic contribution. Additionally, $B = 0$ along the principal axes of the hyperfine tensor.

If we use microwave irradiation with frequency ω_{mw} to manipulate the electron spin, we get an additional term, already in the electron rotating frame, of the form

$$\hat{\mathcal{H}}_{\text{mw}} = \omega_1(t) \left(\cos \phi(t) \hat{S}_x + \sin \phi(t) \hat{S}_y \right) \quad . \tag{5.4}$$

---

[1] Some text books use an explicit negative sign for the nuclear frequency. We omit this, assuming that the gyromagnetic ratio can be positive or negative. For electrons and protons, ω_S and ω_I have opposite signs.

Here we neglected the counter-rotating component of linearly polarized microwaves (rotating-wave approximation). The Rabi or nutation frequency is given by $\omega_1(t) = -\gamma_e B_1(t)$, where $B_1(t)$ is the amplitude of the microwave field. Modulations of $\omega_1(t)$ are called amplitude modulation (AM). Moreover, we can use a time-dependent phase $\phi(t)$ (phase modulation (PM)). Written this way, the frequency of the microwave is hidden in the offset Ω_S in Equation (5.3). It could also be time-dependent, $\Omega_S(t)$, which corresponds to a frequency modulation (FM).

In principle, one could also use irradiation on the nuclear spins, and the extension would be straight-forward [160], but we restrict ourselves here to microwave irradiation only.

Now we should discuss the relative magnitudes of A, B, and ω_I. In principle, the hyperfine couplings can be (much) larger than the nuclear Zeeman frequency, even at rather high fields of >3 T. This situation is quite common in EPR, known as "strong coupling". Nevertheless, we want to describe DNP only, where in the end, nuclei in the bulk, far away from any electrons, are observed. In all known cases, this happens via relatively weakly coupled nuclei, where $|A|, |B| \ll |\omega_I|$. These nuclei can more or less efficiently transfer their polarisation to the bulk, in contrast to strongly coupled nuclei.

Next, we look at the influence of the microwave irradiation on the other terms in the Hamiltonian. We do this by going into an interaction frame with the microwave irradiation, including the offset.

$$U_S(t) = \hat{T} \exp\left(-i \int_0^t \Omega_S(\tau)\hat{S}_z + \hat{\mathcal{H}}_{\mathrm{mw}}(\tau)\mathrm{d}\tau\right) \tag{5.5}$$

$$\hat{\mathcal{H}}' = U_S^\dagger \left(\hat{\mathcal{H}}_0 - \Omega_S(\tau)\hat{S}_z\right) U_S \quad , \tag{5.6}$$

where $\hat{T}$ is the Dyson time-ordering operator. Note that U_S only acts on the electron spin. It represents nothing else than a time-dependent, three-dimensional rotation, that transforms the $\hat{S}_z$ operator [2]:

$$\hat{S}_z = \sum_{\chi=x,y,z} R_{\chi z}^{(S)}(t)\hat{\tilde{S}}_\chi \quad . \tag{5.7}$$

The so-called interaction frame trajectory $R_{\chi z}^{(S)}(t)$ can sometimes be calculated analytically, but it can also be calculated easily numerically with successive rotations. Our implementation uses quaternions for this task. In the case of a periodic pulse sequence with period τ_{m}, the relation $\hat{\mathcal{H}}_{\mathrm{mw}}(t) = \hat{\mathcal{H}}_{\mathrm{mw}}(t + \tau_m)$

---

2 There will be additional interaction frames, but we will not use additional tildes or primes for the operators in different interaction frames.

holds. However, this does *not* imply that the overall rotation over one period is described by the unit operator, i.e. $U_S(\tau_m) \neq \mathbb{1}$. If there is an overall rotation over one period, it can always be described by a rotation by an angle β_{eff}, about an axis which we call the "effective field". Together with the modulation frequency

$$\omega_m = \frac{2\pi}{\tau_m} \quad , \tag{5.8}$$

we can define the effective frequency as

$$\omega_{\text{eff}} = \frac{\beta_{\text{eff}}}{\tau_m} \quad . \tag{5.9}$$

Additionally, we set the boundary condition

$$|\beta_{\text{eff}}| \leq \pi \tag{5.10}$$

which is equivalent to

$$|\omega_{\text{eff}}| \leq \omega_m/2 \quad . \tag{5.11}$$

If the calculated flip angle is larger than π, one can always invert the direction of the effective field, which then leads to a smaller effective flip angle. Both the magnitude and direction of the effective field can be extracted from the quaternion or rotation matrix that describe the overall rotation.

In principle, one could express the interaction frame trajectory as a dual-mode Fourier series, i.e.

$$R_{\chi z}^{(S)}(t) = \sum_{k=-\infty}^{\infty} \sum_{\ell=-1}^{1} a_{\chi z}^{(k,\ell)} e^{ik\omega_m t} e^{i\ell\omega_{\text{eff}}t} \quad . \tag{5.12}$$

This is indeed possible [157], but it has three disadvantages. First, when evaluating the Fourier coefficients $a_{\chi z}^{(k,\ell)}$ numerically, one has to evaluate the integral

$$a_{\chi z}^{(k,\ell)} = \int_{0}^{\infty} R_{\chi z}^{(S)}(t) e^{-ik\omega_m t} e^{-i\ell\omega_{\text{eff}}t} \mathrm{d}t \tag{5.13}$$

numerically, which is neither very efficient nor very stable, Second, at the point where we evaluate resonance conditions (*vide infra*), several combinations of k and ℓ can lead to DNP transfer with different effective Hamiltonians. Third, it is not very transparent how a slight mismatch with respect to the resonance conditions affects the spin dynamics. Hence we introduce some further steps which at first seem to complicate the problem, but ultimately simplify it.

First we rotate the S-spin coordinate system such that the new z-axis is along the effective field. This is achieved with a rotation matrix $R^{(\text{flip})}$ (or the corresponding quaternion). Note that this is also a usual step in the analysis of sequences that use CW-irradiation only, such as off-resonance NOVEL. In a second step, we rotate this frame around the new z-axis, i.e. now the effective field direction, with a frequency ω_{eff}. Opposite to the usual rotating frame, this removes the time-dependency of the S-spin operators due to the effective field. In this new frame, the interaction frame trajectory is cyclic:

$$\hat{S}_z = \sum_{\chi=x,y,z} R^{(C)}_{\chi z}(t)\hat{\tilde{S}}_\chi \qquad (5.14)$$

$$R^{(C)}(t) = R^{(C)}(t+\tau_{\text{m}}) = R_z(-\omega_{\text{eff}}t) \cdot R^{(\text{flip})} \cdot R^{(S)}(t) \qquad . \qquad (5.15)$$

R_z is a rotation around the z-axis,

$$R_z(\alpha) = \begin{pmatrix} \cos\alpha & \sin\alpha & 0 \\ -\sin\alpha & \cos\alpha & 0 \\ 0 & 0 & 1 \end{pmatrix} \qquad , \qquad (5.16)$$

where α is the angle of rotation. Flipping the coordinate system does not add additional terms to the Hamiltonian, it only flips coordinates. Rotating around the effective field, however, corresponds to an interaction frame transformation with $\omega^{(S)}_{\text{eff}}\hat{S}_z$ (in the flipped frame), and thus introduces a Coriolis term of $-\omega^{(S)}_{\text{eff}}\hat{S}_z$. The effective Hamiltonian in this new frame is given by

$$\hat{\mathcal{H}}' = -\omega^{(S)}_{\text{eff}}\hat{S}_z + \omega_I \hat{I}_z + \sum_{\chi=x,y,z} R^{(C)}_{\chi z}(t)\hat{S}_\chi \cdot (A\hat{I}_z + B\hat{I}_x) \qquad , \qquad (5.17)$$

where the time-dependent rotation can now be written as a Fourier series with a single frequency

$$R^{(C)}_{\chi z}(t) = \sum_{k=-\infty}^{\infty} a^{(k)}_{\chi z} e^{ik\omega_{\text{m}}t} \qquad . \qquad (5.18)$$

At this point we have to look at the nuclear spin. It is easy to evaluate the effect of the nuclear Zeeman term, $\omega_I \hat{I}_z$, on the terms in the hyperfine coupling. Instead of going into an interaction frame with $\omega_I \hat{I}_z$, we only use the resonant part of it, with

$$k_I = \text{round}\left(\frac{\omega_I}{\omega_{\text{m}}}\right) \qquad (5.19)$$

$$\omega^{(I)}_{\text{eff}} = \omega_I - k_I\omega_{\text{m}} \qquad . \qquad (5.20)$$

In the additional interaction frame with $k_I \omega_{\mathrm{m}} \hat{I}_z$, the Hamiltonian is given by

$$\hat{\mathcal{H}}'' = -\omega_{\mathrm{eff}}^{(S)} \hat{S}_z + \omega_{\mathrm{eff}}^{(I)} \hat{I}_z$$
$$+ \sum_{\chi = x,y,z} \sum_{k=-\infty}^{\infty} a_{\chi z}^{(k)} e^{ik\omega_{\mathrm{m}}t} \hat{S}_\chi \quad \times$$
$$\left(A\hat{I}_z + \frac{B}{2} \left(e^{ik_I \omega_{\mathrm{m}}t} \hat{I}^+ + e^{-ik_I \omega_{\mathrm{m}}t} \hat{I}^- \right) \right) \qquad . \tag{5.21}$$

Note that so far, no approximations were made, we simply expressed the Hamiltonian in Equation (5.3) in a different frame, and as a Fourier series. But at this point, we will neglect all time-dependent terms. In the form above, it is easy to evaluate which terms remain time-independent, namely only terms with $k = 0$ or $k = \pm k_I$. Thus, we obtain the first order average Hamiltonian

$$\bar{\hat{\mathcal{H}}}^{(1)} = -\omega_{\mathrm{eff}}^{(S)} \hat{S}_z + \omega_{\mathrm{eff}}^{(I)} \hat{I}_z$$
$$+ A \sum_{\chi = x,y,z} a_\chi^{(0)} \hat{S}_\chi \hat{I}_z$$
$$+ \frac{B}{2} \left(a_z^{(-k_I)} \hat{S}_z \hat{I}^+ a_z^{(k_I)} \hat{S}_z \hat{I}^- \right)$$
$$+ \frac{B}{4} \left(a_-^{(-k_I)} \hat{S}^- \hat{I}^+ + a_+^{(k_I)} \hat{S}^+ \hat{I}^- \right.$$
$$\left. + a_-^{(k_I)} \hat{S}^- \hat{I}^- + a_+^{(-k_I)} \hat{S}^+ \hat{I}^+ \right) \qquad , \tag{5.22}$$

where we left away the z-subscripts of the coefficients and used the identities

$$a_x \hat{S}_x + a_y \hat{S}_y = \frac{1}{2} \left(a_+ \hat{S}^+ + a_- \hat{S}^- \right) \tag{5.23}$$
$$a_\pm = a_x \mp i a_y \quad . \tag{5.24}$$

We now discuss that most terms can be neglected. First of all we assume that for an efficient DNP sequence, one needs a substantial effective field on the electrons. Otherwise any magnetization will quickly decay. Note that this assumption is true for all published pulsed DNP sequences [3]. If we assume that $|\omega_{\mathrm{eff}}| \gg |A|, |B||$, then we can distinguish two types of resonance conditions. 1) $\omega_{\mathrm{eff}}^{(S)} = \omega_{\mathrm{eff}}^{(I)}$. Here, apart from the effective fields, only the double-quantum

---

3 In principle, one could take a sequence like NOVEL, and choose an artificial modulation period such that effective field exactly cancels. In this case, however, the non-secular terms become zero on the resonance condition by symmetry arguments. Whether this is generally true is not entirely clear.

(DQ) parts, i.e. terms in the last line of Equation (5.22), contribute. 2) $\omega_{\text{eff}}^{(S)} = -\omega_{\text{eff}}^{(I)}$, where only the zero-quantum (ZQ) parts, i.e. terms in the second to last line, matter. The term proportional to $A\hat{S}_z\hat{I}_z$ is secular with respect to the effective fields, but it shifts both levels of the ZQ subspace in the same direction, and also both levels of the DQ subspace. Thus, it does not shift the resonance condition to first order. All other terms are small off-diagonal elements compared to the difference of the diagonal elements, i.e. they are non-secular. However, if A or B terms are substantial, they can lead to second-order shifts of the energy levels in the effective frame and might thus shift the resonance condition. There are known experimental cases where this happens. For example, for solid effect DNP, the resonance condition is given by $\omega_I = \sqrt{\Omega_S^2 + \omega_1^2} \approx \Omega_S$. The same effect leads to a hole around the nuclear Zeeman frequency in ELDOR-detected NMR. However, if there is a substantial hyperfine coupling, the shift in resonance condition is so large that the coupling can be determined from the shift. These shifts are negligible for DNP, but one should take care when doing numerical simulations, because the resonance conditions can be quite narrow for the small, idealised spin systems needed for a full quantum mechanical treatment.

Neglecting the non-secular terms in Equation (5.22), we arrive at

$$
\begin{aligned}
\tilde{\tilde{\mathcal{H}}}^{(1)} = &-\omega_{\text{eff}}^{(S)}\hat{S}_z + \omega_{\text{eff}}^{(I)}\hat{I}_z \\
&+ \frac{B}{4}\left(a_-^{(-k_I)}\hat{S}^-\hat{I}^+ + a_+^{(k_I)}\hat{S}^+\hat{I}^- \right) \quad \text{if} \quad \omega_{\text{eff}}^{(S)} \approx -\omega_{\text{eff}}^{(I)}
\end{aligned}
\tag{5.25}
$$

$$
\begin{aligned}
\tilde{\tilde{\mathcal{H}}}^{(1)} = &-\omega_{\text{eff}}^{(S)}\hat{S}_z + \omega_{\text{eff}}^{(I)}\hat{I}_z \\
&+ \frac{B}{4}\left(+a_-^{(k_I)}\hat{S}^-\hat{I}^- + a_+^{(-k_I)}\hat{S}^+\hat{I}^+ \right) \quad \text{if} \quad \omega_{\text{eff}}^{(S)} \approx \omega_{\text{eff}}^{(I)}
\end{aligned}
\tag{5.26}
$$

We can now define a scaling factor that describes the efficiency of the electron-nuclear transfer independent of the actual coupling constant

$$
a_{\text{eff}} = \begin{cases} \frac{1}{2}\left(|a_-^{(-k_I)}| + |a_+^{(k_I)}| \right), & \text{if } \omega_{\text{eff}}^{(S)} \approx -\omega_{\text{eff}}^{(I)} \\ -\frac{1}{2}\left(|a_-^{(k_I)}| + |a_+^{(-k_I)}| \right), & \text{if } \omega_{\text{eff}}^{(S)} \approx \omega_{\text{eff}}^{(I)} \end{cases}
\tag{5.27}
$$

The minus sign in the second case is because a DQ Hamiltonian leads to a transfer $\hat{S}_z \to -\hat{I}_z$. Note that for symmetry reasons, and because the resulting effective Hamiltonian still has to be Hermitian, $|a_-^{(-k_I)}| = |a_+^{(k_I)}|$ and $|a_-^{(k_I)}| = |a_+^{(-k_I)}|$.

At this point it is important to note that only the part that is initially along the effective field of the electron will be transferred to the nucleus. In principle, one could also imagine an INEPT-type coherence transfer instead of polarisation transfer, but we will not discuss this further.

If the initial electron magnetisation is denoted by a three-dimensional vector $\vec{\sigma}_0$ and the direction of the electron effective field by $\vec{z}_{\text{eff}}$, then the time evolution of the nuclear polarisation can be calculated from simple product operator calculations, giving

$$P_I(t) = \vec{\sigma}_0 \cdot \vec{z}_{\text{eff}} \times \text{sign}(a_{\text{eff}}) \sin\left(\frac{B}{4}a_{\text{eff}}t\right)^2 \quad . \tag{5.28}$$

For small couplings or contact times, this can be approximated by a Taylor series, which yields

$$P_I(t) \approx \vec{\sigma}_0 \cdot \vec{z}_{\text{eff}} \times \text{sign}(a_{\text{eff}}) \frac{B^2}{16} a_{\text{eff}}^2 t^2 + \mathcal{O}(t^4) \quad . \tag{5.29}$$

Obviously, without specifying a coupling and a contact time, one cannot really predict the DNP enhancements. But we will show that the - in some sense extremely rough - parameter

$$\vec{\sigma}_0 \cdot \vec{z}_{\text{eff}} \times a_{\text{eff}} \quad , \tag{5.30}$$

evaluated on the resonance conditions, is quite a good predictor of *relative* DNP enhancement.

COMMENT ON THE CHOICE OF EFFECTIVE FIELDS

In Equation (5.19), we made a particular choice about how to define the nuclear effective field. With this, the maximum of the nuclear effective field is $\omega_{\text{m}}/2$, the same as for the electron effective field. The choice is arbitrary. But if we allow for larger effective field, it is much harder to keep track of resonance conditions, because they can occur in any of the modulation sidebands. Nevertheless, for our choice, there is one special case, when $|\omega_{\text{eff}}^{(I)}| \approx |\omega_{\text{eff}}^{(S)}| \approx |\omega_{\text{m}}|/2$. In this case, two resonance conditions are fulfilled at the same time. This is usually not a good idea, unless the scaling factor of one is close to zero.

5.2.2 *Adiabatic sweeps*

In this section, we discuss adiabatic sweeps through a resonance condition. We assume that only one resonance condition is passed during the course of

the experiment, and that the scaling factor only changes little in the vicinity of the resonance. Additionally, the electron spin should follow the effective field at all times, which corresponds to the adiabatic limit.

Let us define a "mismatch" of the effective fields

$$\Delta\omega_{\mathrm{eff}}(t) = |\omega_{\mathrm{eff}}^{(S)}(t)| - |\omega_{\mathrm{eff}}^{(I)}(t)| \qquad , \qquad (5.31)$$

which can be interpreted as the offset or z-component in the ZQ/DQ subspace of the electron-nuclear system. For adiabatic polarisation transfer, the mismatch passes through zero. For a modulated sequence, the effective fields can be changed from one modulation period to the next by changing one or more modulation parameters by a small amount. In principle, the effective fields are only defined over one cycle but if the change is small, we can assume it to be smooth to a good approximation. The time-dependent Hamiltonian in the ZQ/DQ subspace can then be written as

$$\hat{\mathcal{H}}^{\mathrm{ZQ/DQ}} = \Delta\omega_{\mathrm{eff}}(t)\hat{S}_z^{\mathrm{ZQ/DQ}} + \frac{B \cdot a_{\mathrm{eff}}}{2}\hat{S}_x^{\mathrm{ZQ/DQ}} \qquad . \qquad (5.32)$$

If $\Delta\omega_{\mathrm{eff}}(t)$ passes through zero, this corresponds to an adiabatic passage of an effective spin-$1/2$. The adiabaticity Q_{crit} at the moment of resonance is given by [163, 164]

$$Q_{\mathrm{crit}} = \frac{1}{4}\frac{(B \cdot a_{\mathrm{eff}})^2}{\frac{\mathrm{d}}{\mathrm{d}t}\Delta\omega_{\mathrm{eff}}(t)} \qquad , \qquad (5.33)$$

which can be translated to an inversion efficiency in the ZQ/DQ subspace — corresponding to the polarisation transfer efficiency — by the Landau-Zener formula

$$\langle I_z \rangle = 1 - \exp\left(-\frac{\pi}{2}Q_{\mathrm{crit}}\right) \qquad . \qquad (5.34)$$

Note that for a powder, one needs to average the transfer efficiencies, not the adiabaticities.

The transfer efficiency thus strongly depends on the hyperfine coupling, which implies that the exact sweep parameters should always be optimized experimentally. However, it is important how the mismatch behaves with respect to the sequence parameters, such that reasonable starting points can be chosen.

5.3   MATERIALS AND METHODS

5.3.1   *Numerical calculation of scaling factors*

All numerical calculations were implemented in MATLAB (Mathworks). For piece-wise constant pulse sequences, effective fields were calculated by quaternion multiplication of the individual pieces. Interaction frame trajectories of all, and effective fields of continuously modulated sequences were calculated by time-slicing. Fourier coefficients were calculated with an `fft` of $R^{(C)}(t)$. For parameter sweeps and comparison with fully numerical simulations, the parameters at the resonance conditions were optimised numerically by minimising the mismatch in effective fields. This search is not necessary for the effective Hamiltonian calculations, but for numerical simulations, as these can be very sensitive to the mismatch, depending on the coupling parameter.

The two-dimensional simulation of BASE-DNP was implemented with the simulation package SPINACH [165]. A spin system with one electron and two protons was used, with a **g**-tensor of [2.0046 2.0038 2.0030], e-n distances of r_1=4.5 Å and r_1=6.5 Å, polar angles of θ_1=0° and θ_2=90° and azimuthal angles ϕ_1=0° and ϕ_2=70°. A simple T_1/T_2 relaxation theory was used, with $T_{1,e}$=2.5 ms, $T_{2,e}$=5 µs and $T_{1,n}$=36 s, $T_{2,n}$=1 ms. Thermalisation was achieved via the Levitt-di Bari approach. A two-angle Lebedev grid with 194 orientations was used.

5.3.2   *Experimental implementation*

All experimental results were acquired on a new home-built X-band spectrometer which is based on the design described in [19]. Notable differences for the experiments described in this work were that a 1.8 GS/s digitizer (SP Devices ADQ412) was used and that the temperature of 80 K was achieved with a cryogen-free cryostat (Cryogenic Limited). Microwave pulses were generated with an arbitrary waveform generator (AWG, Keysight M8190A) and amplified with a 1 kW travelling wave tube (TWT) amplifier (Applied Systems Engineering). A standard Bruker EN4118A-MD4 ENDOR resonator was used, with an external tuning and matching circuit attached to the N-type connectors. NMR excitation and detection was achieved with a Stelar PC-NMR spectrometer. An Arduino board was used to count TWT gate triggers of the EPR spectrometer, each corresponding to one DNP contact, and subsequently to trigger the NMR detection after a particular number of DNP contacts. All signal processing was implemented in MATLAB.

A 5 mM sample of OX063 trityl radical in DNP juice (glycerol-d_8:D_2O:H_2O, 6:3:1 by volume) at 80 K was used for all experiments. In detail, 1.65 mg trityl radical (MW=1359 g mol^{-1}, 1.2 µmol) were dissolved in 24.3 µL of H_2O and 48.6 µL D_2O. Of the resulting solution, 48.6 µL were mixed with 72.9 µL of gly-d_8. 40 µL of the final solution were transferred to a 3 mm OD quartz capillary and flash frozen in liquid nitrogen before the measurements.

While the majority of results were reproduced several times, all the ones presented in this work were acquired within the same session, i. e. one cooldown of the cryostat. The sample was not moved at all between different experiments.

5.3.3 *Pulse sequences*

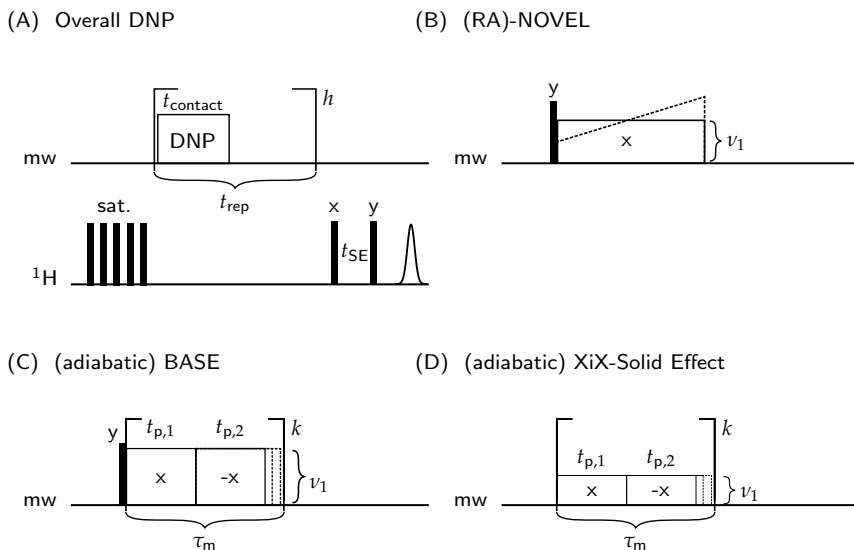The sequences used in this work are shown in Figure 5.1. The basic structure

FIGURE 5.1: Pulse sequences used in this work. (A) Basic sequence used to measure polarisation enhancement. (B) NOVEL sequence, with either constant or ramped amplitude (RA). (C) BASE sequence. (D) XiX-Solid Effect (XiX-SE).

of all DNP experiments is shown in Figure 5.1 (A). After a saturation train on the proton spins (usually eleven 100° pulses spaced by 1 ms), the respective DNP sequence was applied h times, with a total build-up time $T_{\mathrm{DNP}} = h \cdot t_{\mathrm{rep}}$. The contact time t_{contact}, during which the microwaves

are on, is generally much shorter than the repetition time t_{rep}, at most 1%, due to duty cycle limitations of the TWT. The proton spin polarisation was then read out with a solid echo sequence with 90° pulse lengths of typically 2.5 μs, and an echo delay of $t_{\text{SE}}=80$ μs. The conventional eight-step phase cycle was used (first pulse and detection: $x, x, y, y, -x, -x, -y, -y$, second pulse: $y, -y, x, -x, y, -y, x, -x$).

The reference proton spectrum was acquired with presaturation pulses, a waiting time of 180 s without microwaves, and the same solid echo. A total of 660 scans were acquired.

In the majority of cases, we report the *polarisation enhancement*, given by the ratio of the signal intensity obtained by DNP divided by the reference intensity (normalised by signal scans). For the latter, the repetition time of 180 s corresponds to $5 \cdot T_{1,\text{n}}$, i.e. the fully relaxed signal ($T_{1,\text{n}}=36$ s was determined both with a saturation recovery sequence, and by the decay of polarisation after DNP). These values can be completely different from simple on/off signal enhancements, because the DNP build-up time T_B can be much shorter than $T_{1,\text{n}}$. In fact, if $T_B < T_{1,\text{n}}$ the on/off enhancement can easily be larger than 660, i.e. the ratios of gyromagnetic ratios. The highest possible polarisation enhancement is denoted by ϵ_{max}. The sensitivity enhancement by unit time is given by $\epsilon_{\text{max}}/\sqrt{T_B}$.

Most parameter optimisations used a repetition time t_{rep} of 1 ms, and a build-up time T_{DNP} of 2 s. Build-up curves were acquired by changing the value of h, and with variable repetition times mentioned in the respective figures.

The NOVEL and RA-NOVEL sequences are shown in Figure 5.1 (B). A $\pi/2$ pulse of typically 6 ns length flips the electrons into the transverse plane. The magnetisation is then spin-locked by a long pulse, phase-shifted by 90°. For NOVEL, the spinlock strength has to match the nuclear Zeeman frequency, $\nu_1 \approx \nu_I$, while in RA-NOVEL, the nutation frequency is slowly increased from below the matching condition to above it in a linear fashion. In principle, other amplitude modulations than linear sweeps can be used.

The sequence for BASE-DNP and its adiabatic variant are shown in Figure 5.1 (C) The basic structure is similar to NOVEL, but the phase of the spin lock is periodically inverted. This is repeated k times, leading to a total contact time of $t_{\text{contact}} = k \cdot \tau_{\text{m}} = k \cdot (t_{\text{p,1}} + t_{\text{p,2}})$. Adiabatic sweeps through resonance conditions can be achieved by slowly changing $t_{\text{p,2}}$ from one modulation period to the next, i.e. in the first round, $t_{\text{p,1}}=20$ ns and $t_{\text{p,2}}=26$ ns, in the second round $t_{\text{p,1}}=20$ ns and $t_{\text{p,2}}=26.2$ ns etc.

If the first $\pi/2$ pulse is left away and the power is reduced, one arrives at the sequence shown in Figure 5.1 (D), which we term in general XiX-Solid Effect (XiX-SE). The "solid effect" part should indicate that an offset is needed to lead to polarisation transfer. Again, adiabatic sweeps through the DNP resonance condition can be achieved by sweeping $t_{p,2}$.

5.4   RESULTS

5.4.1   *Illustration of the interaction frame transformation*

In a first part, we illustrate the interaction frame transformations involved in calculating the scaling factors a_{eff}, see Figure 5.2. As an illustration, we use the example of XiX-SE with $\nu_1{=}4\,\text{MHz}$, $t_{p,1}{=}14\,\text{ns}$, $t_{p,2}{=}28\,\text{ns}$ and $\Omega_S/2\pi{=}25\,\text{MHz}$. These parameters are not representative for any good DNP sequence, they are mainly chosen because the trajectory is uncluttered.

Figure 5.2 (A) illustrates the initial interaction frame transfomration $R^{(S)}(t)$ plotted over one period τ_{m}. The blue curves denote the trajectory of the normal rotating frame operator $\hat{S}_z$. Note that $R^{(S)}(0) = \mathbb{1} \neq R^{(S)}(\tau_{\text{m}})$, i.e. the trajectory is not cyclic with τ_{m}.

The same trajectory, but in the flipped, effective (or cyclic) frame, $R^{(C)}(t)$, is depicted in Figure 5.2 (B). All the coefficients are cyclic with time τ_{m}. A Fourier transform of the respective time-dependent coefficients directly yields $a_{\chi z}^{(k)}$. The fact that the frame is flipped with respect to the normal rotating frame can be seen because $R^{(C)}(0) \neq \mathbb{1}$.

Figure 5.2 (C) shows the three-dimensional trajectory of the original $\hat{S}_z$ operator in the initial interaction frame (the three blue components in (A)). The trajectory of the first modulation period is marked in red. The end points of the subsequent five periods are shown as black dots in panel (C). The overall rotation from one period to the next can be described by an effective field shown in dark red. This can be looked at as a CW-field, which can be removed by flipping the frame such that the effective field is along z, and then going into an interaction frame with said effective field. The result of this transformation is shown in Figure 5.2 (D). The axis $z^{(C)}$ now points along $\vec{z}_{\text{eff}}$ in (C), and the effect of the overall rotation was eliminated by a counter rotation, i.e. start and end points are now the same.

(A) $R^{(S)}(t)$

(B) $R^{(C)}(t)$

(C) $R^{(S)}(t)\,|\hat{S}_z\rangle$

(D) $R^{(C)}(t)\,|\hat{S}_z\rangle$

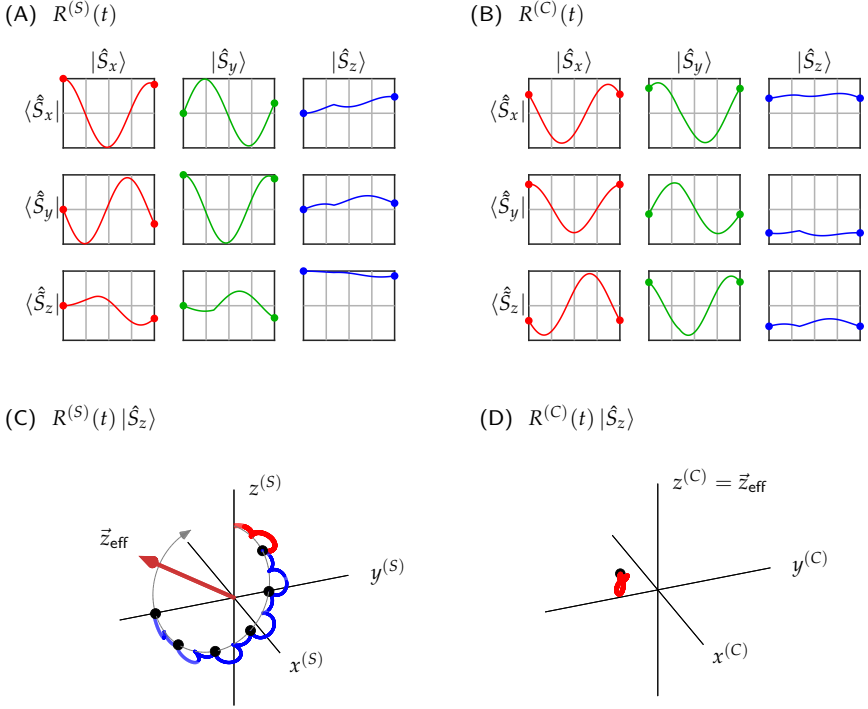FIGURE 5.2: Illustration fo the interaction frames employed in this work, on the example of XiX-SE (detail see main text). (A) Illustration of the initial interaction frame transformation $R^{(S)}(t)$ plotted over one period τ_{m}. (B) The same trajectory, but in the flipped, effective (or cyclic) frame. (C) Three-dimensional trajectory of the original $\hat{S}_z$ operator in the initial interaction frame (the three blue components in (A)). The trajectory of the first modulation period is marked in red. The end points of the subsequent five periods are shown as black dots. (D) The $\hat{S}_z$ operator in the cyclic frame. Start and end points are the same.

5.4.2 *Verification of the analytical considerations and used approximations*

In this section, we show how the formalism introduced above can be used to determine resonance conditions and verify the analytical derivations the used approximations by comparing effective Hamiltonian calculations with full numerical simulations. Typically when looking for resonance conditions, some parameters are fixed while others are swept. In the example here, we use a representative parameter set for XiX-SE, with $\nu_1=4\,\mathrm{MHz}$, $t_{\mathrm{p,1}}=6\,\mathrm{ns}$,

$t_{p,2}=12\,\text{ns}$, a nuclear Zeeman frequency $\nu_I=-14.8\,\text{MHz}$, and variable offset Ω_S.

Figure 5.3 (A) shows the absolute value of the electron effective field $\nu_{\text{eff}}^{(S)}$ as a function of the offset. For each offset, $\nu_{\text{eff}}^{(S)}$ is calculated via a quaternion multiplication of the two quaternions describing the pulses. Note the enforced inflection because $|\nu_{\text{eff}}^{(S)}| < \nu_m/2$. In this example, the nuclear effective field is simply given by the Zeeman frequency, $\nu_{\text{eff}}^{(I)} = \nu_I$, because the modulation frequency ν_m is not a function of the electron offset (and $k_I = 0$). Resonances occur at $|\nu_{\text{eff}}^{(I)}| = \nu_{\text{eff}}^{(S)}$, marked with black circles.

For each resonance condition, we show in Figure 5.3 (B) the scaling factor a_{eff} (blue), the projection of the initial density matrix ($\hat{S}_z$ in this case) onto the effective field (red) and the predicted relative DNP transfer according to Equation (5.29), neglecting the influence of B and t (purple). The grey curve shows a numerical simulation of the transfer to a single proton at 8 Å distance. The numerical transfer around the resonance conditions shows sinc-wiggles because only 30 cycles were simulated, which leads to a broadening of the resonance conditions. All curves and coefficients were normalized to the maximum.

We then tested how well the approximations made in the analytical derivations hold true, depending on the strength of the hyperfine couplings. Figure 5.3 (C) and (D) show the same calculations, once for a relatively strongly coupled proton at a distance of 3.5 Å (C), and once for a weakly coupled proton 6 Å apart from the electron spin (D). All calculations were summed over the polar angle θ. Full, exact numerical simulations are shown as black circles, effective Hamiltonian calculations using the full first order Hamiltonian in Equation (5.22) are shown in blue. These two perfectly overlap, even for the close proton, illustrating that the first order approximation is very good. Note, however, that this depends on the magnitude of the hyperfine coupling and the modulation period. Predictions based on including only the ZQ/DQ part of the effective Hamiltonian, i.e. by Equation (5.28), are shown in red. For the weakly coupled proton at 6 Å, this prediction is virtually perfect, the red line is barely visible. However, for the more strongly coupled proton at 3.5 Å, deviations from the exact simulations become visible. This indicates that the terms neglected from the first order Hamiltonian begin to interfere with the polarisation transfer. Nevertheless, the polarisation transfer is still reasonably approximated by Equation (5.28). Last but not least, the initial build-up predicted by Equation (5.29) is shown in green. As expected, this is only a good approximation for small couplings and short times.
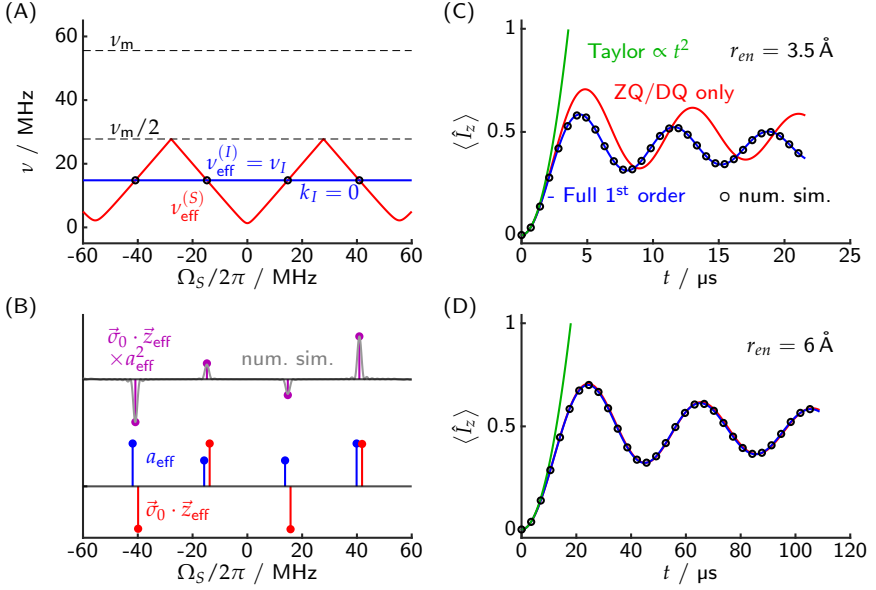
FIGURE 5.3: Resonance conditions, scaling factors, and comparison with numerical calculations, on the example of XiX-SE (details in the main text) (A) The absolute value of the effective fields $\nu_{\text{eff}}^{(S)}$ and $\nu_{\text{eff}}^{(I)}$ as a function of the offset. (B) Scaling factors a_{eff} (blue), projections (red) and the predicted relative DNP transfer (purple) at the resonance conditions. The gray curve shows a numerical simulation of the transfer. (C) and (D) Comparison of an effective Hamiltonian calculation including all terms (blue) or only the flip-flop terms (red) with a full numerical simulation (black circles), assuming a proton at 3.5 Å and 6 Å distance. The green line illustrates the initial build-up in Equation (5.29).

5.4.3   Simulated illustration of adiabatic DNP transfers

In the following, we illustrate the concept of adiabatic polarisation transfer by slowly changing of the sequence parameters from one modulation period to the next. As an example, we use adiabatic BASE, with $t_{\text{p,1}}$=20 ns, variable $t_{\text{p,2}}$ as a sweep parameter, a nuclear Zeeman frequency of ν_I=−14.853 MHz, and a range of different spin lock strengths and offsets (given in Figure 5.4 (B)). This illustrates the decreased sensitivity of adiabatic sweeps with respect to exact matching conditions. First, we calculate again both the nuclear and electron effective fields as a function of $t_{\text{p,2}}$, shown in Figure 5.4 (A). Note that in this case, the nuclear effective field *is* a function of the sweep parameter, via its dependence on the modulation frequency. The resonance

conditions for the different parameter combinations are illustrated by dashed lines.

Figure 5.4 (B) shows the nuclear polarisation dynamics as a function of time, assuming that $t_{p,2}$ is linearly swept along the dimension in (A). A proton at a distance of $5\,\text{Å}$ was assumed. The coloured lines show calculations assuming a smooth variation of mismatch and effective coupling, including the flip-flop terms only. Full numerical simulations in black below are virtually indistinguishable. One can see the transfer starts once the resonance condition is hit, and after some wiggles, ends up at a constant value. This is typical for adiabatic transfers. Straight lines and numbers at the right indicate the powder-averaged polarisation values computed from the Landau-Zener formula in Equation (5.34). The latter assumed a constant scaling factor over the adiabatic sweep. Figure 5.4 (C) shows the effective coupling coefficients as a function of $t_{p,2}$ for the different parameter sets. One can see that in this case, a_{eff} is not a exactly constant, but it only weakly and slowly changes with the sweep parameters. For the Landau-Zener calculations, the value at the resonance passing was used, as it determines critical adiabaticity.

The improved robustness of adiabatic sequences compared to their diabatic counterpart is illustrated in (D). The numerically simulated polarisation transfers for diabatic BASE, with $t_{p,2}=29\,\text{ns}$, and the respective parameter values are shown as solid lines. The adiabatic polarisation values are shown as dashed lines. For some parameter combinations, where the resonance conditions are fulfilled nearly exactly, the nuclear polarisation may transiently be higher. But for most small parameter variations, adiabatic sweeps through the resonance conditions lead to much better transfer. Note that the improvement heavily depends on the exact coupling parameters, such that these insights cannot be applied to experimental situations one to one, if the hyperfine couplings are not exactly known. Nevertheless, the improved transfers should still be observable after experimental optimisation of the sweep parameters.
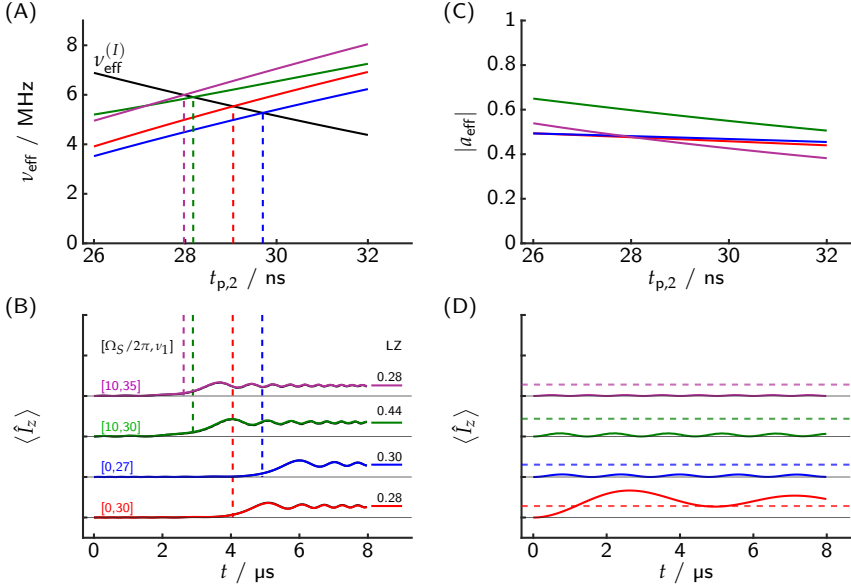
FIGURE 5.4: Adiabatic sweeps through DNP resonance conditions, on the example of adiabatic BASE. (A) Nuclear (black) and electron (coloured) effective fields for slightly different values of offset and nutation frequency values (given in (B)). Resonance conditions are marked with dashed lines. (B) Polarisation build-up during adiabatic sweep through the resonance condition by sweeping $t_{p,2}$ in a linear fashion over the range in (A). Calculations via effective ZQ/DQ Hamiltonian are shown as coloured lines. Exact simulations shown in black below are virtually indistinguishable. Powder-averaged polarisation values calculated via the Landau-Zener formalism are indicated to the right. (C) Dependence of a_{eff} on $t_{p,2}$ for the different parameter sets. The values are nearly constant during a sweep of $t_{p,2}$. (D) Comparison of the polarisation transfer with diabatic BASE ($t_{p,2}=29$ ns, solid lines) with the final values of the adiabatic transfer (dashed lines).

### 5.4.4 *Experimental results: Low power XiX-Solid Effect*

We first show experimental results for XiX-SE, because they nicely illustrate the theoretical insight discussed above. Figure 5.5 (A) shows the resonance conditions and relative enhancements obtained with XiX-SE with a fixed modulation frequency, but differenct combinations of $t_{p,1}$, $t_{p,2}$. The case of $t_{p,2} = 0$ corresponds to the usual SE. In all cases, $\nu_1=4$ MHz, $t_{contact}=8$ µs, $\tau_{rep}=1$ ms, and $T_{DNP}=2$ s. The experimental polarisation enhancements are

shown in black, while the theoretical values of $\vec{\sigma}_0 \cdot \vec{z}_{\mathrm{eff}} \times a_{\mathrm{eff}}$ are shown in red. Note that both the experimental and the theoretical values are normalized overall to the maximum of the pure SE enhancement profile. Clearly, the theory predicts well both the position and the relative intensities. The small peaks visible in the experimental data correspond to 1-electron-2-proton transitions. Their position can be predicted by doubling the nuclear Zeeman frequency (data not shown).
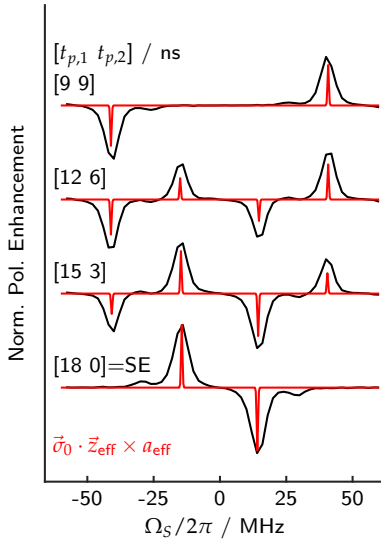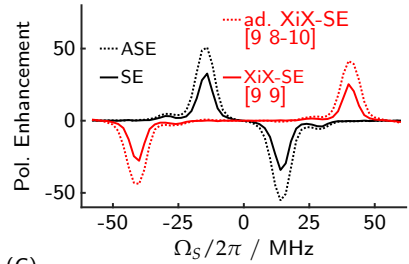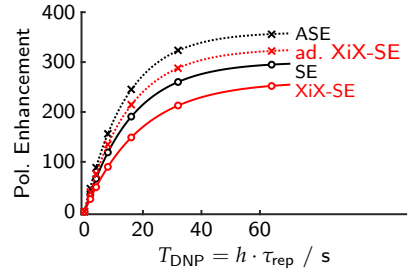

FIGURE 5.5: XiX-Solid Effect resonance conditions, adiabatic version, and build-up characteristics. (A) Experimental enhancements and theoretical scaling factors of XiX-SE as a function of electron spin offset, for different combinations of $t_{\mathrm{p},1}$ and $t_{\mathrm{p},2}$, but all with the same modulation period τ_{m}. (B) Comparison of XiX-SE and its adiabatic version (red solid and dashed lines) with the solid effect (SE) and the adiabatic solid effect (ASE). (C) Build-up curves for all sequences shown in (B).

Because the electron nutation frequency is very low, the electron effective fields and the resonance conditions are nearly completely determined by the offset and the modulation frequency alone. However, the coefficients depend on the actual interaction frame trajectory. In the case of $t_{\mathrm{p},1} = t_{\mathrm{p},2}$, the normal SE enhancement is completely suppressed, because the corresponding scaling

factor is zero by symmetry. Nevertheless, no variant of XiX-SE outperforms the SE in terms of either the scaling factor or the experimental enhancement.

One interesting way to turn the XiX-SE sequence into an adiabatic one is by slowly increasing $t_{p,2}$ from one modulation period to the next. The improved enhancement is shown (B). The adiabatic version of XiX-SE, where the second pulse is swept from 8–10 ns (red dashed line) outperforms its diabatic counterpart (red solid line) as well as the usual solid effect (black solid line). However the ASE, where the frequency of the pulse is swept by a small amount ($\approx 5\,\mathrm{MHz}$) around the SE condition, still leads to larger enhancements. The build-up behaviour of each sequence, with optimised parameters, is shown in Figure 5.5 (C). With the ASE, a polarisation enhancement of 355 can be achieved.

5.4.5 *Experimental results: High power BASE-DNP*

We now turn to the high-power sequence BASE-DNP. The experimental enhancement profile and theoretical prediction for on-resonance irradiation as a function of $t_{p,2}$ are shown in Figure 5.6 (A), for fixed $t_{p,1}=20\,\mathrm{ns}$, $t_{\mathrm{contact}}=8\,\mathrm{\mu s}$, and $\nu_1=32\,\mathrm{MHz}$, $\tau_{\mathrm{rep}}=1\,\mathrm{ms}$, $T_{\mathrm{DNP}}=2\,\mathrm{s}$. Again, the theory predicts both the positions and relative enhancements well. Note that the theoretical prediction neglected any distributions in offsets and spin lock strength. The two different resonance conditions are labelled $k_I = 0$ and $k_I = 1$ for later reference.

A full, two-dimensional sweep as a function of both $t_{p,1}$ and $t_{p,2}$ is shown in Figure 5.6 (B). In this case, $T_{\mathrm{DNP}}=1\,\mathrm{s}$ only, for time reasons. Black and white dashed lines indicate the resonance conditions. The corresponding theoretical scaling factors are shown in Figure 5.6 (C). The position, the sign, and the relative enhancements are again predicted well.

Additionally, we performed numerical simulations on a simplified spin system in SPINACH. Note that the simulated enhancements are usually much larger than the experimental ones, because there are fewer nuclei and no spin-diffusion to bulk nuclei. While our theoretical approach cannot predict anything that SPINACH can, it is much faster (because the latter treats a much more complicated system). It allows exploring resonance conditions while working on the spectrometer and serves as guidance. It also gives an orientation of how to perform adiabatic sweeps, because it can easily be avoided to hit more than one resonance condition during the sweep.
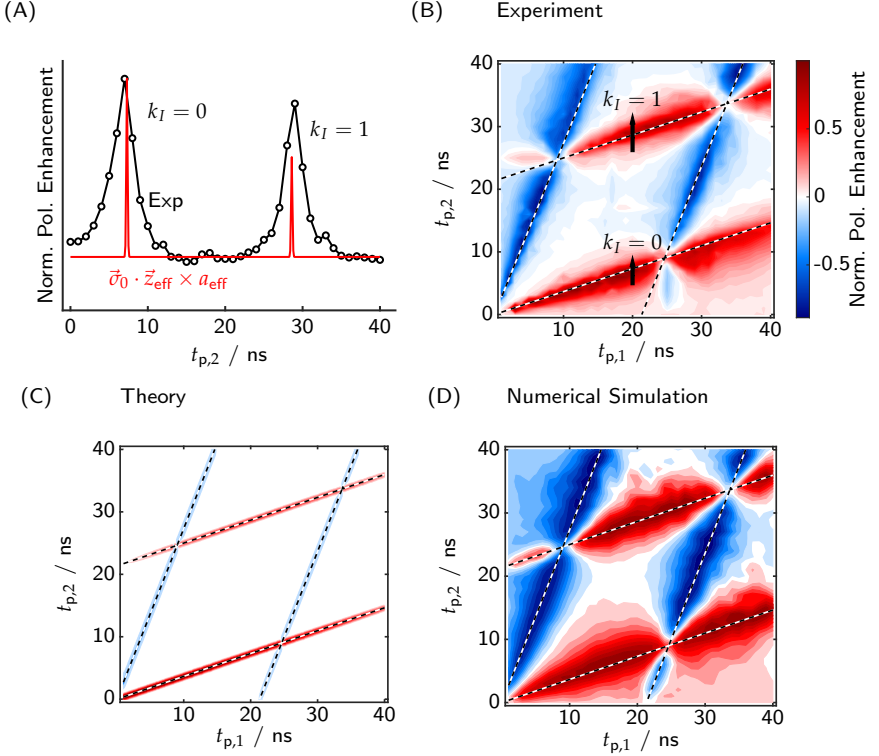
FIGURE 5.6: Experimental verification of our theoretical approach in the case of BASE DNP. (A) Experimental polarisation enhancement (black) and theoretical prediction (red) as a function of $t_{p,2}$. (B) Experimental polarisation enhancement in BASE as a function of both pulse lengths ($T_{DNP}=1\,s$). Theoretical resonance conditions shown as black and white dashed lines. The ranges for the adiabatic sweeps (*vide infra*) are shown as black arrows. (C) Theoretical values of $\vec{\sigma}_0 \cdot \vec{z}_{eff} \times a_{eff}$, (D) SPINACH simulation of a simple spin system.

In the following, we look more closely at how different parameters affect the performance of BASE and adiabatic BASE compared to NOVEL and RA-NOVEL.

The polarisation enhancement as a function of the spin lock strength ν_1 is shown in Figure 5.7 (A). The BASE parameters were $t_{p,1}=20\,ns$, $t_{contact}=8\,\mu s$, and $\nu_1=32\,MHz$, $\tau_{rep}=1\,ms$, $T_{DNP}=2\,s$. The pulse length of the second pulse, $t_{p,2}$ was fixed in the case of (diabatic) BASE (cirlces) to $7\,ns$ ($k_I = 0$) and $29\,ns$ ($k_I = 1$). For adiabatic BASE (crosses), $t_{p,2}$ was swept, $4.75 - 9.25$ ns ($k_I = 0$) or $26 - 32$ ns ($k_I = 1$). Clearly, ramping the amplitude in the

case of NOVEL leads to both higher enhancement and more robust transfer with respect to the spin lock strength. The adiabatic version of BASE is also much more efficient and robust than its diabatic counterpart. For one of the resonance conditions, the best transfer was achieved with the highest power available. A closer look at the $k_I = 0$ and $k_I = 1$ resonance conditions reveals that the position of the latter is much more robust with respect to the spin lock strength, in agreement with the experimental data (data not shown).

We then compared the offset dependence of (RA)-NOVEL and (adiabatic) BASE ($k_I = 1$ resonance condition). This is shown in Figure 5.7 (B) The magnetic field was held constant. The frequency of both the $\pi/2$ pulse (6 ns) and the spin lock was swept. The bandwidth of the $\pi/2$ pulse is large enough to have an negligible influence in this case. The amplitude of the spin lock was adjusted to the resonator profile where possible, to fulfil the matching condition at each frequency. This compensation was not possible in the case of adiabatic BASE, where the maximal available power was used. Interestingly, the RA-NOVEL hardly improves the bandwidth of the sequence compared to constant-amplitude NOVEL. We explain this by the fact that during the start of the amplitude ramp, the spin lock strength is reduced, which leads to dephasing of the electron magnetization. For BASE, it is clearly visible that the increased spin lock strength increases the bandwidth of the sequence with respect to (RA)-NOVEL by a factor of about three. The enhancement variations in the centre qualitatively follow the resonator profile. The small enhancements at larger offsets correspond to Fourier sidebands of the sequence. These sidebands are expected from an XiX-type sequence like BASE. To further confirm the adiabatic nature of the transfer in adiabatic BASE, we recorded enhancements as a function of the contact time t_{contact}, i.e. the length of the amplitude-modulated spin lock. The results are shown in Figure 5.8 (A). The BASE polarisation enhancement was again recorded with $\tau_{\text{rep}}{=}1\,\text{ms}$, $T_{\text{DNP}}{=}2\,\text{s}$, and all other parameters optimised (see above). The curves show the typical behaviour and improvement when going from a non-adiabatic to an adiabatic version of a pulse sequence, comparable to e.g. cross-polarisation. The enhancement of the diabatic versions grows rapidly, shows slightly transient behaviour, then levels off. The adiabatic versions first follow their diabatic counterparts, but their enhancement keeps on increasing when the diabatic enhancement already stagnates. The improvements are between 1.3 and 1.6. This is comparable to the experience with adiabatic cross-polarisation and RA-NOVEL [150].

As mentioned earlier, the sweep ranges of the parameters used to make a sequence adiabatic should be optimised experimentally, guided by theory.
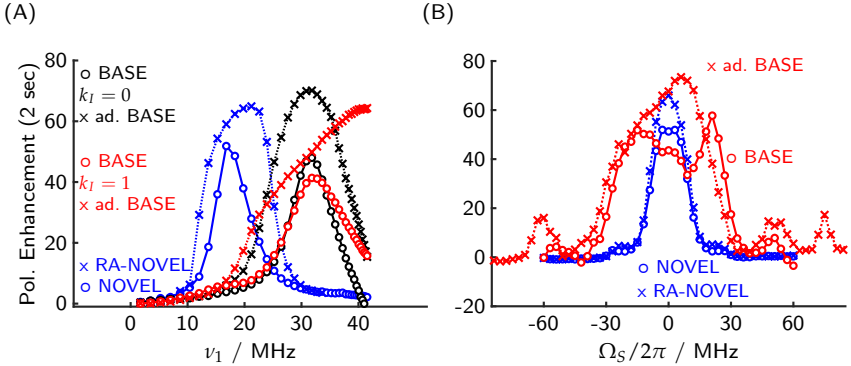
(A) (B)

FIGURE 5.7: Power and electron offset dependence of NOVEL (blue) and BASE (red and black). (A) Polarisation enhancement as a function of the spin lock strength ν_1. (B) Polarisation enhancement for NOVEL and BASE (condition $k_I = 1$) at different electron offsets. Clearly, the increased spin lock strength of BASE increases the bandwidth of the sequence with respect to (RA)-NOVEL.

Figure 5.8 (B) shows the polarisation enhancement of adiabatic BASE as a function of the sweep width of the second pulse length. The first pulse $t_{p,1}$ was set to $20\,\mathrm{ns}$ and the second one was swept from $t_{p,2}(\text{centre}) - 1/2\Delta t_{p,2}$ to $t_{p,2}(\text{centre}) + 1/2\Delta t_{p,2}$ (different for $k_I = 0$ and $k_I = 1$). Note that the maximal available power was used for condition $k_I = 1$, which is optimal for the adiabatic version, but quite far from optimal for the non-adiabatic one.
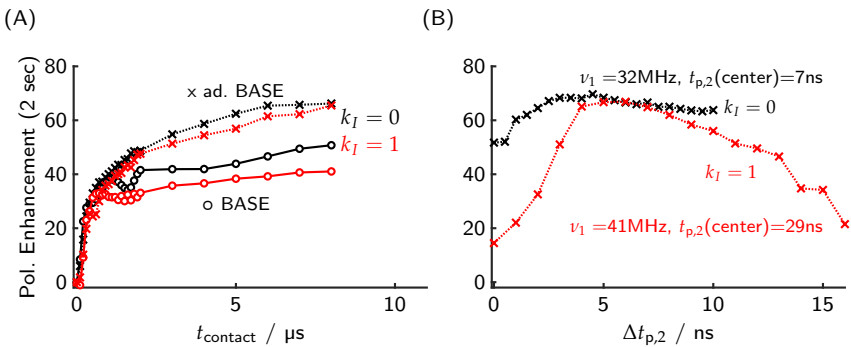
(A) (B)

FIGURE 5.8: Experimental optimisation of the BASE parameters. (A) Dependence of (adiabatic) BASE polarisation enhancement on t_{contact}. (B) Polarisation enhancement as a function of the sweep width of the second pulse length.

Last but not least, we characterised the build-up behaviour of BASE and adiabatic BASE and compared it to RA-NOVEL. All build-ups could be fitted well with exponential functions $\epsilon(t) = \epsilon_{\max}\left(1 - \exp(-T_{\mathrm{DNP}}/T_B)\right)$. We measured build-up curves for several different repetition times τ_{rep}. A summary of the fitted values is given in Figure 5.9. We show this extensive characterisation because it illustrates how different experimental parameters can influence the DNP behaviour, and how difficult in can be to optimise a sequence globally and to compare different sequences in a fair manner. Figure 5.9 (A) shows the maximal enhancement. For RA-NOVEL, we also
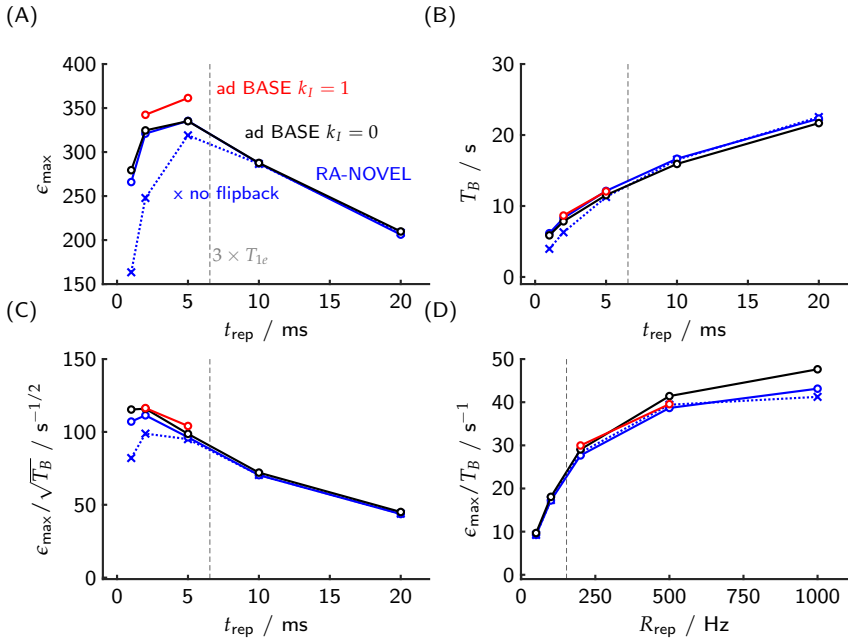

FIGURE 5.9: Build-up behaviour of RA-NOVEL without flip-back pulse, RA-NOVEL with flip-back pulse and adiabatic BASE at conditions $k_I = 0$ and $k_I = 1$, for different repetition times τ_{rep}. (A) Maximum polarisation enhancement. (B) DNP build-up times T_B. (C) Sensitivity per unit time expressed as $\epsilon_{\max}/\sqrt{T_B}$. (D) Initial polarisation build-up rates as a function of the repetition rate $R_{\mathrm{rep}} = 1/\tau_{\mathrm{rep}}$.

looked at a sequence with a flip-back pulse at the end. Clearly, flip-back pulses help to increase the maximal polarisation at repetition times comparable or lower than $T_{1,\mathrm{e}}$. As expected, they make no difference at much longer

repetition times, because the electron fully relaxes after each DNP contact. Flip-back pulses were thus also used for BASE. Adiabatic BASE and RA-NOVEL are comparable, with the full power adiabatic variant of BASE using the $k_I = 1$ having the slight edge, achieving ϵ_{max}=361. The DNP build-up times are shown in Figure 5.9 (B). Note that T_{1H}=36 s, i.e. much longer. The build-up times of all compared sequences are very similar. The flip-back pulses also lead to slightly longer build-up times.

If DNP is used as a means of reducing measurement time, the decisive factor is the sensitivity enhancement per unit time. This is given in Figure 5.9 (C), expressed as $\epsilon_{\mathrm{max}}/\sqrt{T_B}$. Note that compared to the non-enhanced proton signal, there is another factor of $\sqrt{T_{1H}}$=6 s$^{1/2}$. Again, adiabatic base is slightly better than RA-NOVEL, but the differences are marginal.

Figure 5.9 (D) shows the initial polarisation build-up rates as a function of the repetition rate $R_{\mathrm{rep}} = 1/\tau_{\mathrm{rep}}$. At low repetition rates, the electron spins are fully relaxed and the proton polarisation fully diffused before each contact. The initial build-up rate thus linearly increases with the repetition rate. At faster repetition rate though, both the incomplete electron relaxation and slow proton spin diffusion lead to a flattening of the initial build-up rate.

Overall, while the robustness of (adiabatic) BASE with respect to microwave inhomogeneity and offsets is improved compared to RA-NOVEL, the actual gain in maximal enhancement and sensitivity is only marginal, mostly because the bandwidth of RA-NOVEL is sufficient for OX063. The differences are expected to be larger for broader EPR lines.

5.4.6 *Conclusions and outlook*

We derived an effective Hamiltonian that can be used to describe periodically modulated DNP sequences in static samples. Resonance conditions and relative enhancements can be predicted by looking at only the interaction frame trajectory of the electron spin over one modulation period, and extracting the relevant Fourier coefficients. We showed that modulated DNP experiments can be turned into adiabatic sequences by slowly sweeping any modulation parameter from one modulation period to the next. In the case of XiX-SE and BASE, this was achieved by sweeping one of the two pulse lengths. In both cases, the adiabatic variants outperform their diabatic counterparts in terms of maximal polarisation enhancement. The amplitude-modulated sequence BASE, and its adiabatic variant, show improved offset compensation compared to NOVEL and RA-NOVEL, because an increased Rabi-frequency can be used. However, for the narrow-line trityl radical, the increased band-

width only leads to marginally increased maximal polarisation enhancement. We want to emphasise that the strength of the theoretical approach lies in the fact any modulated sequence can quickly be adapted for whatever experimental constraints one encounters. While for high-field MAS DNP, this usually means very little power, other areas of DNP have completely different constraints. For example, in NV-centre based DNP, the problem is mostly the narrow bandwidth of NOVEL when applied to the low-γ nucleus ^{13}C. For example, the recently introduced PulsePol used a electron Rabi frequency that is about 25 times higher than the nuclear Zeeman frequency [158].

While we only looked at piece-wise constant sequences, our semi-numerical approach works just as well for continuously modulated sequences, simply by time-slicing. One only has to take care that the time-step of the calculation is small enough such that the effective field is obtained with sufficient accuracy.

So far, we only considered static samples. When using MAS, there are several complications. As long as the modulation frequency is fast compared to the MAS frequency, the rotation is quasi-static compared to the modulation. Nevertheless, our approach gets complicated because we explicitly consider the electron offset for the interaction frame transformation. This offset would become time-dependent under MAS if the g-tensor is anisotropic, and for the quasi-static approximation, it would slowly change from one modulation period to the next. This time-dependence would be different for each crystallite orientation. An interesting situation would arise if the MAS frequency would approach the modulation frequencies, and maybe even the nuclear Zeeman frequency of low-γ nuclei at low fields.

Currently, the most effective mechanism for MAS DNP is the CE. This mechanism needs two coupled electrons, a situation we have not treated in our formalism in this work. If microwave sources with significant power and modulation capacities, as well as better resonance structures in or around the MAS rotors would become available at hundreds of GHz, a generalisation of the theory would be needed.

One aspect that gets "swept under the rug" by using effective Hamiltonians and numerically calculated interaction frame transformations is the field dependence. It is hidden in the nuclear Zeeman frequency and thus the nuclear effective field, and in the spread of the electron offsets. In order to determine the field dependence of the scaling factor of a given resonance condition, one would need to follow said condition for a set of different nuclear Zeeman frequencies and determine the scaling factors for each. If the interaction frame trajectories can be given in an analytical form, so can the Fourier coefficients and thus the scaling factors. Otherwise, only numerical

dependencies can be given. At this point, we want to point out an important detail when discussing pulsed DNP. Often, a case for pulsed DNP is made because it might allow for field-independent enhancements, arguing with the effective Hamiltonian of NOVEL. Of course, NOVEL implies that the electron nutation frequency matches the nuclear Zeeman frequency, i. e. the NOVEL scaling factor is field-independent *IF the microwave field strength grows linearly with the field*. Exactly the same is true for the Solid Effect. The SE scaling factor is field-independent *IF the microwave field strength grows linearly with the field*. In other words, pulsed DNP is not a magic potion that automatically solves all problems of CW DNP.

An important limitation with respect to design is that our approach only analyses sequences, it does not generate them. We calculate scaling factors and thus effective Hamiltonians by considering a given sequence. True *design* of a sequence would correspond to the inverse problem. Is it possible to start with an effective Hamiltonian and its dependence on experimental constraints, and generate a sequence from it?

Last but not least, we would like to highlight the possibility of this approach to be applied to electron paramagnetic resonance (EPR) pulse sequences. The fields and frequencies of most EPR spectrometers allow for the precise spin control needed, given a fast AWG is available. Efficient DNP sequences could be used in conjunction with electron-nuclear double resonance (ENDOR) experiments. On the other hand, one can also envisage modulated coherence transfer experiments similar to matched ESEEM (electron echo envelope modulation) [29]. This could allow for sensitive ESEEM-based experiments at higher fields, and thus with better resolution of nuclear Zeeman frequencies. For strongly coupled nuclei, the approach introduced here should be generalised beyond the first-order approximation.

6

OUTLOOK

This chapter is a loose set of speculations about the future of the topics addressed in this work. After addressing a few possibilities of technical advances, I will also have a quick look at EPR as a field, and at academia in general. Especially the latter contains a large portion of personal views and intuition of the author, i. e. they are not "scientific", and should be taken with a grain of salt.

6.1 TECHNICAL AND SPECTROSCOPIC ADVANCES

6.1.1 *CHEESY at higher field*

CHEESY-detected NMR was shown in this work to be a powerful method to detect hyperfine couplings, see Chapter 2. The exact sensitivity gain compared to ELDOR-detected NMR depends on the ratio of peaks to baseline in the hole burning spectrum. Additionally, the usefulness should be even higher at higher fields, where low-γ nuclei are further away from the central hole, and Zeeman resolution is generally better. Both points suggest that CHEESY at higher fields and frequencies would be a very valuable addition to the EPR toolbox. In fact, the National High Magnetic Field Laboratory in Tallahassee, Florida, is currently implementing coherent UWB detection with an AWG attached to a HiPER W-band system [90]. The main difficulty at higher frequencies is the available microwave power and the means for broadband excitation and detection. The HiPER system uses a non-resonant sample holder, such that the excitation bandwidth is limited by the microwave source and amplifier. Additionally, it increases the available sample volume and thus concentration sensitivity at the cost of significant microwave inhomogeneity. Fortunately, CHEESY does not need very high power nor good microwave homogeneity.

Nevertheless, the resolution in CHEESY is still limited by the electron phase memory time. Accordingly, it will not be the method of choice for applications where utmost resolution is needed. In the case of broad lines due to inhomogeneous broadening, however, CHEESY will surpass the sensitivity of ENDOR and ESEEM-based methods by far.

6.1.2 *Multi-centre complexes*

In Chapter 3, it was shown that field-correlated ELDOR spectra could give information about electron-electron couplings. When taking a step back, the information needed for fitting a CW spectrum of such a multi-centre complex is enormous. In general, two anisotropic **g**-tensors, **A**-tensors, and a ZFS have to be extracted, all with an arbitrary orientation. The case of Cu(II)-porphyrin is rather easy, because one can assume axial interaction matrices, and in our case the relative orientation was known from crystal structures. *Even then*, the literature shows cases where the symmetry of the problem was assigned incorrectly, and a significant ZFS was simply ignored. This was possible because CW spectra can be so difficult to interpret, and there can exist several possible solutions.

As multi-centre complexes can show very interesting catalytic behaviour and unusual electronic structures, field-correlated ELDOR spectra should be recorded for such complexes if possible. There is no guarantee that they will facilitate the assignment of interactions, but as our example showed, it can be extremely helpful and prevent misinterpretation of CW spectra.

6.1.3 *Multi-pulse distance measurements with improved relaxation properties*

Chapter 4 showed that the relaxation times of dressed, or spin-locked electron spins are prolonged compared to the bare phase memory time. However, there are still two problems. First, the transverse relaxation time in the spin-locked frame, $T_{2\rho}$, is still much shorter than $T_{1\rho}$ or T_1. Second, a simple spin-lock is inefficient in compensating different electron offsets. The resulting problems prevent the sequence from being applied to long-range distance measurements.

In analogy to TOCSY experiments in NMR, there should exist possible multi-pulse sequences that perform better than simple spin-locks. The problem is indeed very similar to broadband TOCSY, with the difference that the effective coupling Hamiltonian is a dipolar coupling instead of a *J*-coupling.

IF an effective Hamiltonian devoid of electron offsets can be generated with modulation periods short compared to the dipolar coupling, there might indeed be a possibility to measure distances where the upper range is limited by T_1, $T_{1\rho}$ or something similar in magnitude, instead of T_m. It is not very clear how the electron spins will relax under continuous multi-pulse sequences. Most likely, the "recoupling" of hyperfine interactions, as discussed in Chapter 5, should be avoided.

A technical problem that can be anticipated is the maximum gate length of the commonly used TWT amplifiers at X- and Q-bands, which are on the order of 10–50 µs. The observation of slow dipolar oscillations, corresponding to long distances, will need about an order of magnitude longer irradiation times. Solid-state power amplifiers might be promising in this regard.

For structural biology and supramolecular chemistry, longer distance restraints mean more information and better characterisation. These sequences are easiest to apply to trityl radicals, which can be rather bulky. Long-range measurements would partially alleviate this problem, because the size of the label matters less for longer distances.

Additionally, temperature-dependent relaxation measurements indicate that the rotating frame relaxation times of trityl are comparable at 50 K and 80 K. This means that such measurements could be conducted with liquid nitrogen cooling instead of liquid helium. Since the latter is currently truly a non-renewable resource on earth, this might become important sooner or later.

6.1.4 *DNP-ENDOR with multi-pulse rf-sequences and hyperfine decoupling*

Parts of this subsection were used in an SNF postdoc fellowship application.

The two most widely used pulse ENDOR sequences both generate states of the form $\hat{S}_z \hat{I}_z$. Davies ENDOR achieves this with a selective inversion pulse. This is inefficient for small couplings and is inherently insensitive, because the bandwidth of the inversion pulse determines the number of detected spins. Mims ENDOR uses a stimulated echo sequence. This can be implemented in a broadband fashion, but leads to blind-spots at $\frac{A\tau}{2} = n\pi$, where τ is the delay between the first two $\pi/2$ in the stimulated echo. The $\hat{S}_z \hat{I}_z$ operator is subject to electronic $T_{1,\mathrm{e}}$ relaxation and the polarisation grating in Mims ENDOR to spectral diffusion.

A "true" electron-nuclear polarisation transfer generates an $\hat{I}_z$ state. This is the aim of DNP. Interestingly, there seems to be no example of an EPR sequence where DNP is combined with reverse DNP, i. e. indirect excitation with indirect detection. This is standard in many NMR sequences. Even more surprising, there does not seem to be an example in the literature of "reverse" DNP at all, where nuclear polarisation is transferred back to the electrons.

The previously published Cross-Polarisation (CP)-ENDOR [166] does generate "true" nuclear polarisation by using the dressed-spin solid effect (DSSE) [156]. However, after rf-manipulation, a simple selective electron spin echo is used. It is not completely clear from the literature what state is

observed exactly, and if this is the most sensitive way of detecting the nuclear polarisation after the ENDOR sequence.

Figure 6.1 shows that DNP and reverse DNP is indeed possible, on the example of OX063 in deuterated water/glycerol (1:1 by volume) at $50\,\mathrm{K}$. The sequence is shown in (A). Both transfer steps used RA-NOVEL. Before the reverse transfer, the electron spins were saturated. This is necessary because DNP leads to a transfer of the *difference* in polarisation, and after a significant waiting time t, the electron polarisation is returning to equilibrium. Additionally, a $+/-$ phase cycle on the first $\pi/2$ pulse was used. Figure 6.1 (B) shows the echo intensity at the end of the sequence as a function of the length of the second transfer step. The first step was already optimised. As expected, no echo is observed for $t_{\mathrm{match}} = 0$. For longer transfers, an optimum of $10\,\%$ can be reached. Note that the intensity was normalised to a Hahn echo using the same $\pi/2$ and π pulse lengths. Even without rf-irradiation, some
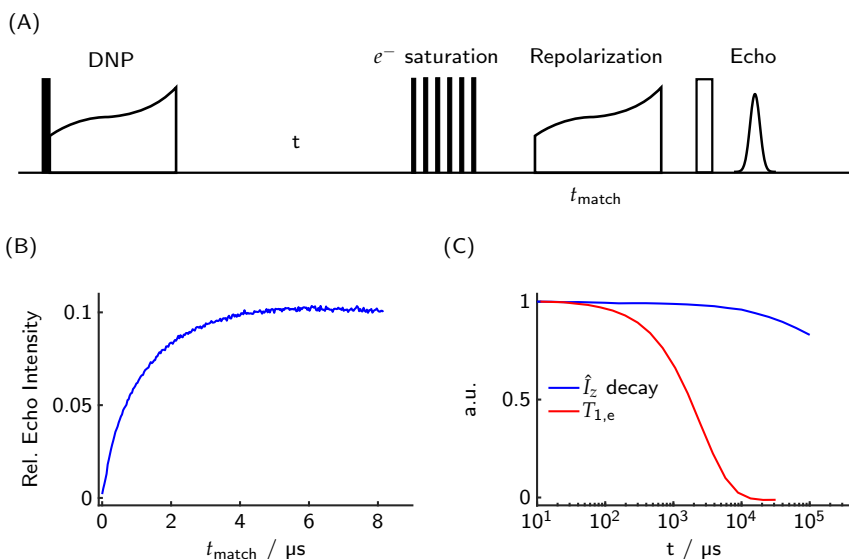

FIGURE 6.1: Preliminary results obtained with reverse DNP. (A) Sequence used for DNP, and indirect detection via reverse DNP. (B) Echo intensity as a function of the matching time of the reverse DNP step. (C) Decay of the indirectly detected nuclear polarisation (blue) compared to the longitudinal electron spin relaxation (red).

interesting phenomena can be observed. For example, Figure 6.1 (C) shows the decay of the echo intensity as a function of the waiting time t. Naively,

from looking at established ENDOR sequences, one could expect that the echo intensity should decay with the $T_{1,e}$, shown in red in Figure 6.1 (C) (red). However, the observed decay is about two orders of magnitude slower, i.e. an echo is still observed after more than $100 \cdot T_{1,e}$ after the initial DNP step. Note that in this case, the electron spin polarisation is fully relaxed after time t, but destroyed again due to the saturation train. The residual signal due to incomplete saturation is cancelled by the phase cycling.

An analysis of the matching profile of the DNP step reveals that the polarisation is indeed transferred to protons, as their NOVEL condition is fulfilled (data not shown). The decay of the nuclear polarisation must be due to "true" $T_{1,n}$ relaxation, but also due to spin diffusion, because only the nuclei close to the electron will be polarised by the DNP step. Which protons exactly are polarised remains to be determined. Note that the decay is faster in protonated solvent (data not shown).

The basic sequence shown above should be very interesting for ENDOR and DNP experiments. It gives a handle on the spin dynamics of the nuclei close to the electron spin, a range that is notoriously difficult to address and understand experimentally. It should also be possible to combine the sequence with established rf-parts of ENDOR sequences during the time t. In particular, I speculate that time-domain ENDOR with hyperfine decoupling during rf-excitation could lead to improved sensitivity. During hyperfine decoupling, the nuclear spectrum is much narrower, which should lead to the possibility of broadband excitation of the nuclear lines even with the limited rf-power.

6.2   EPR AS A FIELD

With many exceptions, chemists are afraid of unpaired electrons. Without having conducted a proper study, there seems to be a bias towards diamagnetic systems, especially in catalysis. Only in a few fields is it abundantly clear how powerful EPR is, notably in bio-inorganic chemistry, molecular magnetism, and photo-excited states. In other fields, EPR is largely unknown. This also hampers the development of advanced EPR methods, because of limited manpower and limited funding, and because the groups at the forefront of EPR development effectively act as user facilities, dedicating a lot of spectrometer and brain time. This is a hen and egg problem.

For a single group that does not use EPR as its primary tool, it is nearly impossible to acquire an EPR spectrometer, especially if pulsed capabilities are needed. Additionally, even the interpretation of "routine" CW spectra

can be very complicated, depending on the system. It thus seems absolutely necessary for the field as a whole that universities or consortia establish EPR user facilities with dedicated staff. Some centralisation is most likely necessary due to financial issues, but too much centralisation again leads to less people that actually learn about EPR. A sensible starting point might be NMR facilities. While the technical details are different, NMR spectroscopists are well prepared to quickly learn about EPR. The specialised EPR groups around the world should keep collaborating with chemists that are already aware of its potential and push for many of such facilities to be established.

Currently, it is even difficult for "EPR groups" to properly teach their students in depth. The international endeavour to teach advanced methods to students should be kept up and intensified. I was shocked to hear that an EPR professor at a famous UK university is not allowed to teach their students about EPR, *even in a lecture about magnetic resonance* (because apparently other Professors conduct the exams). This is of course absolutely detrimental for the field of EPR. We should teach as many people as possible about its usefulness, especially chemists that are not primarily spectroscopists.

EPR is already powerful, and it will become more powerful in the future. We should let the world know.

6.3 TWELVE POINTS FOR ACADEMIA

These points are general, they are not addressed at ETH Zurich in particular.

1. Research and teaching are work. A lot of work.

2. Doctoral students are heavily involved in research and teaching.

3. Workers should be employed and paid. With money, not with "experience".

4. There are more important things in life than research and academia. Researchers that tell anyone otherwise directly or indirectly obviously lack the ability for critical thinking and are unfit for leadership positions.

5. Research is conducted by humans.

6. Humans are political.

7. Humans make mistakes.

8. Because we make mistakes, there should be zero space for dishonesty. It undermines science itself and and its support by the public, i. e. the taxpayers.

9. Open communication about mistakes and the handling of problems is a prerequisite for a fair university. Institutional dishonesty breeds individual dishonesty.

10. Universities that brag about their ranking and argue directly or indirectly that they should be financed because of their ranking will inevitably pay the price for it sooner or later. Rankings are not "determined", they are made up. It is strategically unwise to rely on things that other people make up.

11. Scientists are not immune to propaganda or "fake news". They never have been. Nobel prices do not help[1].

12. Despite all these points, academia is still a great space for creativity.

---

1 https://en.wikipedia.org/wiki/Manifesto_of_the_Ninety-Three

BIBLIOGRAPHY

1. Schweiger, A. & Jeschke, G. *Principles of Pulse Electron Paramagnetic Resonance* (Oxford University Press, 2001).

2. *EPR Spectroscopy: Fundamentals and Methods* (eds Goldfarb, D. & Stoll, S.) (Wiley, 2018).

3. Abragam, A. & Pryce, M. H. L. P. Theory of the nuclear hyperfine structure of paramagnetic resonance spectra in crystals. *Proc. R. Soc. London. Ser. A. Math. Phys. Sci.* **205**, 135. doi:`10.1098/rspa.1951.0022` (1951).

4. Neese, F. Quantum chemistry and EPR parameters. *eMagRes* **6**, 1. doi:`10.1002/9780470034590.emrstm1505` (2017).

5. Gast, P. & Groenen, E. J. EPR interactions-g-anisotropy. *eMagRes* **5**, 1435. doi:`10.1002/9780470034590.emrstm1500` (2016).

6. Telser, J. EPR Interactions - Zero-Field Splittings. *eMagRes* **6**, 207. doi:`10.1002/9780470034590.emrstm1501` (2017).

7. Bennati, M. EPR interactions-hyperfne couplings. *eMagRes* **6**, 271. doi:`10.1002/9780470034590.emrstm1503` (2017).

8. Wili, N., Richert, S., Limburg, B., Clarke, S. J., Anderson, H. L., Timmel, C. R. & Jeschke, G. ELDOR-detected NMR beyond hyperfine couplings: a case study with Cu(ii)-porphyrin dimers. *Phys. Chem. Chem. Phys.* **21**, 11676. doi:`10.1039/C9CP01760G` (22 2019).

9. Stoll, S. & Goldfarb, D. EPR interactions - nuclear quadrupole couplings. *eMagRes* **6**, 495. doi:`10.1002/9780470034590.emrstm1504` (2017).

10. Bloch, F. Nuclear induction. *Phys. Rev.* **70**, 460. doi:`10.1103/PhysRev.70.460` (1946).

11. Sørensen, O., Eich, G., Levitt, M., Bodenhausen, G. & Ernst, R. Product operator formalism for the description of NMR pulse experiments. *Prog. Nucl. Magn. Reson. Spectrosc.* **16**, 163. doi:`10.1016/0079-6565(84)80005-9` (1984).

12. Canarie, E. R., Jahn, S. M. & Stoll, S. Quantitative Structure-Based Prediction of Electron Spin Decoherence in Organic Radicals. *J. Phys. Chem. Lett.* **11**, 3396. doi:`10.1021/acs.jpclett.0c00768` (2020).

13.   Tseitlin, M., Quine, R. W., Rinard, G. A., Eaton, S. S. & Eaton, G. R. Digital EPR with an arbitrary waveform generator and direct detection at the carrier frequency. *J. Magn. Reson.* **213**, 119. doi:10.1016/j.jmr.2011.09.024 (2011).

14.   Spindler, P. E., Zhang, Y., Endeward, B., Gershernzon, N., Skinner, T. E., Glaser, S. J. & Prisner, T. F. Shaped optimal control pulses for increased excitation bandwidth in EPR. *J. Magn. Reson.* **218**, 49. doi:10.1016/j.jmr.2012.02.013 (2012).

15.   Kaufmann, T., Keller, T. J., Franck, J. M., Barnes, R. P., Glaser, S. J., Martinis, J. M. & Han, S. DAC-board based X-band EPR spectrometer with arbitrary waveform control. *J. Magn. Reson.* **235**, 95. doi:10.1016/j.jmr.2013.07.015 (2013).

16.   Spindler, P. E., Schöps, P., Bowen, A. M., Endeward, B. & Prisner, T. F. Shaped Pulses in EPR. *eMagRes* **5**, 1477. doi:10.1002/9780470034590.emrstm1520 (2016).

17.   Doll, A., Pribitzer, S., Tschaggelar, R. & Jeschke, G. Adiabatic and fast passage ultra-wideband inversion in pulsed EPR. *Journal of Magnetic Resonance* **230**, 27. doi:10.1016/j.jmr.2013.01.002 (2013).

18.   Schöps, P., Spindler, P. E., Marko, A. & Prisner, T. F. Broadband spin echoes and broadband SIFTER in EPR. *J. Magn. Reson.* **250**, 55. doi:10.1016/j.jmr.2014.10.017 (2015).

19.   Doll, A. & Jeschke, G. Wideband frequency-swept excitation in pulsed EPR spectroscopy. *Journal of Magnetic Resonance* **280**, 46. doi:10.1016/j.jmr.2017.01.004 (2017).

20.   Breitgoff, F. D., Soetbeer, J., Doll, A., Jeschke, G. & Polyhach, Y. O. Artefact suppression in 5-pulse double electron electron resonance for distance distribution measurements. *Physical Chemistry Chemical Physics* **19**, 15766. doi:10.1039/C7CP01488K (2017).

21.   Tait, C. E. & Stoll, S. ENDOR with band-selective shaped inversion pulses. *J. Magn. Reson.* **277**, 36. doi:10.1016/j.jmr.2017.02.007 (2017).

22.   Wili, N. & Jeschke, G. Chirp echo Fourier transform EPR-detected NMR. *Journal of Magnetic Resonance* **289**, 26. doi:10.1016/j.jmr.2018.02.001 (2018).

23. Ashuiev, A., Allouche, F., Wili, N., Searles, K., Klose, D., Copéret, C. & Jeschke, G. Molecular and supported Ti(iii)-alkyls: efficient ethylene polymerization driven by the π-character of metal-carbon bonds and back donation from a singly occupied molecular orbital. *Chem. Sci.* **12**, 780. doi:`10.1039/d0sc04436a` (2021).

24. Schosseler, P., Wacker, T. & Schweiger, A. Pulsed ELDOR detected NMR. *Chemical Physics Letters* **224**, 319. doi:`10.1016/0009-2614(94) 00548-6` (1994).

25. Jeschke, G. & Spiess, H. W. NMR-correlated high-field electron paramagnetic resonance spectroscopy. *Chemical Physics Letters* **293**, 9. doi:`10.1016/S0009-2614(98)00765-9` (1998).

26. Cox, N., Nalepa, A., Lubitz, W. & Savitsky, A. ELDOR-detected NMR: A general and robust method for electron-nuclear hyperfine spectroscopy? *Journal of Magnetic Resonance* **280**, 63. doi:`10.1016/j. jmr.2017.04.006` (2017).

27. Cox, N., Nalepa, A., Pandelia, M.-E., Lubitz, W. & Savitsky, A. in *Methods in Enzymology* 1st ed., 211 (Elsevier Inc., 2015). doi:`10.1016/ bs.mie.2015.08.016`.

28. Goldfarb, D. ELDOR-Detected NMR. *eMagRes* **6**, 101. doi:`10.1002/ 9780470034590.emrstm1516` (2017).

29. Jeschke, G., Rakhmatullin, R. & Schweiger, A. Sensitivity Enhancement by Matched Microwave Pulses in One- and Two-Dimensional Electron Spin Echo Envelope Modulation Spectroscopy. *Journal of magnetic resonance* **131**, 261. doi:`10.1006/jmre.1998.1367` (1998).

30. Wacker, T. & Schweiger, A. Fourier transform EPR-detected NMR. *Chemical Physics Letters* **186**, 27. doi:`10.1016/0009-2614(91)80187- 3` (1991).

31. Willer, M. & Schweiger, A. Forbidden-transition-labelled EPR (FORTE). *Chemical Physics Letters* **230**, 67. doi:`10.1016/0009- 2614(94)01133-8` (1994).

32. Doll, A. & Jeschke, G. Fourier-transform electron spin resonance with bandwidth-compensated chirp pulses. *Journal of Magnetic Resonance* **246**, 18. doi:`10.1016/j.jmr.2014.06.016` (2014).

33. Segawa, T. F., Doll, A., Pribitzer, S. & Jeschke, G. Copper ESEEM and HYSCORE through ultra-wideband chirp EPR spectroscopy. *Journal of Chemical Physics* **143**. doi:`10.1063/1.4927088` (2015).

34. Pribitzer, S., Segawa, T. F., Doll, A. & Jeschke, G. Transverse inter-
     ference peaks in chirp FT-EPR correlated three-pulse ESEEM spectra.
     Journal of Magnetic Resonance **272**, 37. doi:10.1016/j.jmr.2016.08.
     010 (2016).

35. Kaminker, I., Wilson, T. D., Savelieff, M. G., Hovav, Y., Zimmermann,
     H., Lu, Y. & Goldfarb, D. Correlating nuclear frequencies by two-
     dimensional ELDOR-detected NMR spectroscopy. *Journal of Magnetic
     Resonance* **240**, 77. doi:10.1016/j.jmr.2013.12.016 (2014).

36. Potapov, A., Pecht, I. & Goldfarb, D. Resolving ligand hyperfine
     couplings of type 1 and 2 Cu(II) in ascorbate oxidase by high field pulse
     EPR correlation spectroscopy. *Physical chemistry chemical physics :
     PCCP* **12**, 62. doi:10.1039/b919069d (2010).

37. Soetbeer, J., Hülsmann, M., Godt, A., Polyhach, Y. & Jeschke, G.
     Dynamical decoupling of nitroxides in o-terphenyl: a study of tempera-
     ture, deuteration and concentration effects. *Phys. Chem. Chem. Phys.*
     20, 1615. doi:10.1039/C7CP07074H (2018).

38. Hetzke, T., Bowen, A. M. & Prisner, T. F. ELDOR-detected NMR at
     Q-Band. *Applied Magnetic Resonance* **48**, 1375. doi:10.1007/s00723-
     017-0927-4 (2017).

39. Doll, A. & Jeschke, G. Wideband frequency-swept excitation in pulsed
     EPR spectroscopy. *Journal of Magnetic Resonance* **280**, 46. doi:10.
     1016/j.jmr.2017.01.004 (2016).

40. Tschaggelar, R., Breitgoff, F. D., Oberhänsli, O., Qi, M., Godt, A.
     & Jeschke, G. High-Bandwidth Q-Band EPR Resonators. *Applied
     Magnetic Resonance*, 1. doi:10.1007/s00723-017-0956-z (2017).

41. Kunz, D. Use of frequency-modulated radiofrequency pulses in MR
     imaging experiments. *Magnetic Resonance in Medicine* **3**, 377. doi:10.
     1002/mrm.1910030303 (1986).

42. Böhlen, J.-M. & Bodenhausen, G. *Experimental Aspects of Chirp NMR
     Spectroscopy* 1993. doi:10.1006/jmra.1993.1107.

43. Rist, G. H. & Hyde, J. S. Ligand ENDOR of metal complexes in pow-
     ders. *Journal of Chemical Physics* **52**, 4633. doi:10.1063/1.1673696
     (1970).

44. Florent, M., Kaminker, I., Nagarajan, V. & Goldfarb, D. Determination
     of the 14N quadrupole coupling constant of nitroxide spin probes by
     W-band ELDOR-detected NMR. *Journal of Magnetic Resonance* **210**,
     192. doi:10.1016/j.jmr.2011.03.005 (2011).

45. Bahrenberg, T., Rosenski, Y., Carmieli, R., Zibzener, K., Qi, M., Frydman, V., Godt, A., Goldfarb, D. & Feintuch, A. Improved sensitivity for W-band Gd(III)-Gd(III) and nitroxide-nitroxide DEER measurements with shaped pulses. *Journal of Magnetic Resonance* **283**, 1. doi:10.1016/j.jmr.2017.08.003 (2017).

46. Liesum, L. & Schweiger, A. Multiple quantum coherence in HYSCORE spectra. *Journal of Chemical Physics* **114**, 9478. doi:10.1063/1.1368366 (2001).

47. Kasumaj, B. & Stoll, S. 5- and 6-pulse electron spin echo envelope modulation (ESEEM) of multi-nuclear spin systems. *Journal of Magnetic Resonance* **190**, 233. doi:10.1016/j.jmr.2007.11.001 (2008).

48. Cox, N., Lubitz, W. & Savitsky, A. W-band ELDOR-detected NMR (EDNMR) spectroscopy as a versatile technique for the characterisation of transition metal–ligand interactions. *Molecular Physics* **111**, 2788. doi:10.1080/00268976.2013.830783 (2013).

49. Rapatskiy, L., Cox, N., Savitsky, A., Ames, W. M., Sander, J., Nowaczyk, M. M., Rögner, M., Boussac, A., Neese, F., Messinger, J. & Lubitz, W. Detection of the water-binding sites of the oxygen-evolving complex of photosystem II using W-band17O electron-electron double resonance-detected NMR spectroscopy. *Journal of the American Chemical Society* **134**, 16619. doi:10.1021/ja3053267 (2012).

50. Collauto, A., Mishra, S., Litvinov, A., Mchaourab, H. S. & Goldfarb, D. Direct Spectroscopic Detection of ATP Turnover Reveals Mechanistic Divergence of ABC Exporters. *Structure* **25**, 1264. doi:10.1016/j.str.2017.06.014 (2017).

51. Bruch, E. M., Warner, M. T., Thomine, S., Tabares, L. C. & Un, S. Pulse Electron Double Resonance Detected Multinuclear NMR Spectra of Distant and Low Sensitivity Nuclei and Its Application to the Structure of Mn(II) Centers in Organisms. *The Journal of Physical Chemistry B* **119**, 13515. doi:10.1021/acs.jpcb.5b01624 (2015).

52. Flores, M., Agrawal, A. G., Van Gastel, M., Gärtner, W. & Lubitz, W. Electron-electron double resonance-detected NMR to measure metal hyperfine interactions:61Ni in the Ni-B state of the [NiFe] hydrogenase of Desulfovibrio vulgaris Miyazaki F. *Journal of the American Chemical Society* **130**, 2402. doi:10.1021/ja077976x (2008).

53. Aliabadi, A., Zaripov, R., Salikhov, K., Voronkova, V., Vavilova, E., Abdulmalic, M. A., Rüffer, T., Büchner, B. & Kataev, V. Electron Spin Density on the N-Donor Atoms of Cu(II)-(Bis)oxamidato Complexes As Probed by a Pulse ELDOR Detected NMR. *The Journal of Physical Chemistry B* **119**, 13762. doi:10.1021/acs.jpcb.5b03987 (2015).

54. Fan, C., Gorst, C. M., Ragsdale, S. W. & Hoffman, B. M. Characterization of the Ni-Fe-C Complex Formed by Reaction of Carbon Monoxide with the Carbon Monoxide Dehydrogenase from Clostridium thermoaceticum by Q-Band ENDOR. *Biochemistry* **30**, 431. doi:10.1021/bi00216a018 (1991).

55. Gurbiel, R. J., Fann, Y. C., Surerus, K. K., Werst, M. M., Musser, S. M., Doan, P. E., Chan, S. I., Fee, J. A. & Hoffman, B. M. Detection of two histidyl ligands to CuA of cytochrome oxidase by 35-GHz ENDOR. 14,15N and 63,65Cu ENDOR studies of the CuA site in bovine heart cytochrome aa3 and cytochromes caa3 and ba3 from Thermus thermophilus. *Journal of the American Chemical Society* **115**, 10888. doi:10.1021/ja00076a053 (1993).

56. Peloquin, J. M., Campbell, K. A. & Britt, R. D. 55Mn pulsed ENDOR demonstrates that the photosystem II 'split' EPR signal arises from a magnetically-coupled mangano-tyrosyl complex. *Journal of the American Chemical Society* **120**, 6840. doi:10.1021/ja981196u (1998).

57. Harmer, J., Finazzo, C., Piskorski, R., Bauer, G., Jaun, B., Duin, E. C., Goenrich, M., Thauer, R. K., Van Doorslaer, S. & Schweiger, A. Spin density and coenzyme M coordination geometry of the ox1 form of methyl-coenzyme M reductase: A pulse EPR study. *Journal of the American Chemical Society* **127**, 17744. doi:10.1021/ja053794w (2005).

58. Silakov, A., Reijerse, E. J., Albracht, S. P. J., Hatchikian, E. C. & Lubitz, W. The electronic structure of the H-cluster in the [FeFe]-hydrogenase from Desulfovibrio desulfuricans: A Q-band 57Fe-ENDOR and HYSCORE study. *Journal of the American Chemical Society* **129**, 11447. doi:10.1021/ja072592s (2007).

59. Kulik, L. V., Epel, B., Lubitz, W. & Messinger, J. Electronic structure of the Mn4OxCa cluster in the S0 and S2 states of the oxygen-evolving complex of photosystem II based on pulse 55Mn-ENDOR and EPR spectroscopy. *Journal of the American Chemical Society* **129**, 13421. doi:10.1021/ja071487f (2007).

60. Greer, S. M., McKay, J., Gramigna, K. M., Thomas, C. M., Stoian, S. A. & Hill, S. Probing Fe-V Bonding in a C3-Symmetric Heterobimetallic Complex. *Inorganic Chemistry* **57**, 5870. doi:`10.1021/acs.inorgchem.8b00280` (2018).

61. Potapov, A., Epel, B. & Goldfarb, D. A triple resonance hyperfine sublevel correlation experiment for assignment of electron-nuclear double resonance lines. *The Journal of Chemical Physics* **128**, 052320. doi:`10.1063/1.2833584` (2008).

62. Crossley, M. J. & Burn, P. L. An approach to porphyrin-based molecular wires: synthesis of a bis(porphyrin)tetraone and its conversion to a linearly conjugated tetrakisporphyrin system. *Journal of the Chemical Society, Chemical Communications* **8**, 1569. doi:`10.1039/c39910001569` (1991).

63. Anderson, H. L. Building molecular wires from the colours of life: conjugated porphyrin oligomers. *Chemical Communications*, 2323. doi:`10.1039/a904209a` (1999).

64. Kuang, G., Chen, S. Z., Wang, W., Lin, T., Chen, K., Shang, X., Liu, P. N. & Lin, N. Resonant Charge Transport in Conjugated Molecular Wires beyond 10 nm Range. *Journal of the American Chemical Society* **138**, 11140. doi:`10.1021/jacs.6b07416` (2016).

65. Li, Z., Park, T. H., Rawson, J., Therien, M. J. & Borguet, E. Quasi-ohmic single molecule charge transport through highly conjugated meso-to-meso ethyne-bridged porphyrin wires. *Nano Letters* **12**, 2722. doi:`10.1021/nl2043216` (2012).

66. Tanaka, T. & Osuka, A. Conjugated porphyrin arrays: Synthesis, properties and applications for functional materials. *Chemical Society Reviews* **44**, 943. doi:`10.1039/c3cs60443h` (2015).

67. Tsuda, A. & Osuka, A. Fully conjugated porphyrin tapes with electronic absorption bands that reach into infrared. *Science* **293**, 79. doi:`10.1126/science.1059552` (2001).

68. Tsuda, A., Furuta, H. & Osuka, A. Completely Fused Diporphyrins and Triporphyrin. *Angewandte Chemie International Edition* **39**, 2549. doi:`10.1002/1521-3773(20000717)39:14<2549::AID-ANIE2549>3.0.CO;2-A` (2000).

69. Tanaka, T. & Osuka, A. Triply Linked Porphyrinoids. *Chemistry - A European Journal*, 17188. doi:`10.1002/chem.201802810` (2018).

70.   Leary, E., Limburg, B., Alanazy, A., Sangtarash, S., Grace, I., Swada, K., Esdaile, L. J., Noori, M., González, M. T., Rubio-Bollinger, G., Sadeghi, H., Hodgson, A., Agraït, N., Higgins, S. J., Lambert, C. J., Anderson, H. L. & Nichols, R. J. Bias-Driven Conductance Increase with Length in Porphyrin Tapes. *Journal of the American Chemical Society* **140**, 12877. doi:10.1021/jacs.8b06338 (2018).

71.   Yoshida, N., Ishizuka, T., Osuka, A., Jeong, D. H., Cho, H. S., Kim, D., Matsuzaki, Y., Nogami, A. & Tanaka, K. Fine Tuning of Photophysical Properties of meso-meso-Linked ZnII–Diporphyrins by Dihedral Angle Control. *Chem. - A Eur. J.* **9**, 58. doi:10.1002/chem.200390004 (2003).

72.   Grozema, F. C., Houarner-Rassin, C., Prins, P., Siebbeles, L. D. A. & Anderson, H. L. Supramolecular control of charge transport in molecular wires. *Journal of the American Chemical Society* **129**, 13370. doi:10.1021/ja0751274 (2007).

73.   Rickhaus, M., Vargas Jentzsch, A., Tejerina, L., Grübner, I., Jirasek, M., Claridge, T. D. & Anderson, H. L. Single-Acetylene Linked Porphyrin Nanorings. *Journal of the American Chemical Society* **139**, 16502. doi:10.1021/jacs.7b10710 (2017).

74.   Ikeue, T., Furukawa, K., Hata, H., Aratani, N., Shinokubo, H., Kato, T. & Osuka, A. The importance of a β-β bond for long-range antiferromagnetic coupling in directly linked copper(II) and silver(II) diporphyrins. *Angewandte Chemie International Edition* **44**, 6899. doi:10.1002/anie.200501943 (2005).

75.   Khusnutdinova, D., Wadsworth, B. L., Flores, M., Beiler, A. M., Reyes Cruz, E. A., Zenkov, Y. & Moore, G. F. Electrocatalytic Properties of Binuclear Cu(II) Fused Porphyrins for Hydrogen Evolution. *ACS Catalysis* **8**, 9888. doi:10.1021/acscatal.8b01776 (2018).

76.   Leavesley, A., Shimon, D., Siaw, T. A., Feintuch, A., Goldfarb, D., Vega, S., Kaminker, I. & Han, S. Effect of electron spectral diffusion on static dynamic nuclear polarization at 7 Tesla. *Physical Chemistry Chemical Physics* **19**, 3596. doi:10.1039/C6CP06893F (2017).

77.   Haase, J., Conradi, M., Grey, C. & Vega, A. Population Transfers for NMR of Quadrupolar Spins in Solids. *Journal of Magnetic Resonance, Series A* **109**, 90. doi:10.1006/jmra.1994.1138 (1994).

78. Kaminker, I., Potapov, A., Feintuch, A., Vega, S. & Goldfarb, D. Population transfer for signal enhancement in pulsed EPR experiments on half integer high spin systems. *Physical Chemistry Chemical Physics* **11**, 6799. doi:10.1039/b906177k (2009).

79. Doll, A., Qi, M., Pribitzer, S., Wili, N., Yulikov, M., Godt, A. & Jeschke, G. Sensitivity enhancement by population transfer in Gd(iii) spin labels. *Physical Chemistry Chemical Physics* **17**, 7334. doi:10.1039/C4CP05893C (2015).

80. Ramirez Cohen, M., Mendelman, N., Radoul, M., Wilson, T. D., Saveli-eff, M. G., Zimmermann, H., Kaminker, I., Feintuch, A., Lu, Y. & Goldfarb, D. Thiolate Spin Population of Type I Copper in Azurin Derived from 33S Hyperfine Coupling. *Inorganic Chemistry* **56**, 6163. doi:10.1021/acs.inorgchem.7b00167 (2017).

81. Richert, S., Kuprov, I., Peeks, M. D., Suturina, E. A., Cremers, J., Anderson, H. L. & Timmel, C. R. Quantifying the exchange coupling in linear copper porphyrin oligomers. *Physical Chemistry Chemical Physics* **19**, 16057. doi:10.1039/c7cp01787a (2017).

82. Stoll, S. & Schweiger, A. EasySpin, a comprehensive software package for spectral simulation and analysis in EPR. *Journal of Magnetic Resonance* **178**, 42. doi:10.1016/j.jmr.2005.08.013 (2006).

83. McInnes, E. J. L. & Collison, D. EPR Interactions - Coupled Spins. *eMagRes* **5**, 1445. doi:10.1002/9780470034590.emrstm1502 (2016).

84. Belford, R. L. & Duan, D. C. Determination of Nuclear Quadrupole Coupling by Simulation of EPR spectra of frozen solutions. *Journal of Magnetic Resonance (1969)* **29**, 293. doi:10.1016/0022-2364(78)90154-3 (1978).

85. White, L. K. & Belford, R. Nuclear quadrupole coupling in $Cu(C_2O_4)_2$ dianion. *Chemical Physics Letters* **37**, 553. doi:10.1016/0009-2614(76)85036-1 (1976).

86. White, L. K. & Belford, R. L. Quadrupole Coupling Constants of Square-Planar Copper(II)-Sulfur Complexes from Single-Crystal Electron Paramagnetic Resonance Spectroscopy. *Journal of the American Chemical Society* **98**, 4428. doi:10.1021/ja00431a016 (1976).

87. Kita, S., Hashimoto, M. & Iwaizumi, M. Single crystal 63Cu and 65Cu ENDOR of bis(2,4-pentanedionato)copper(II). *Journal of Magnetic Resonance (1969)* **46**, 361. doi:10.1016/0022-2364(82)90090-7 (1982).

88. Eaton, S. S., More, K. M., Sawant, B. M. & Eaton, G. R. Use of the EPR Half-Field Transition To Determine the Interspin Distance and the Orientation of the Interspin Vector in Systems with Two Unpaired Electrons. *Journal of the American Chemical Society* **105**, 6560. doi:10.1021/ja00360a005 (1983).

89. Bleaney, B. & Bowers, K. D. Anomalous Paramagnetism of Copper Acetate. *Proceedings of the Royal Society A: Mathematical, Physical and Engineering Sciences* **214**, 451. doi:10.1098/rspa.1952.0181 (1952).

90. Cruickshank, P. A. S., Bolton, D. R., Robertson, D. A., Hunter, R. I., Wylde, R. J. & Smith, G. M. A kilowatt pulsed 94 GHz electron paramagnetic resonance spectrometer with high concentration sensitivity, high instantaneous bandwidth, and low dead time. *Review of Scientific Instruments* **80**, 103102. doi:10.1063/1.3239402 (2009).

91. Soetbeer, J., Gast, P., Walish, J. J., Zhao, Y., George, C., Yang, C., Swager, T. M., Griffin, R. G. & Mathies, G. Conformation of bis-nitroxide polarizing agents by multi-frequency EPR spectroscopy. *Physical Chemistry Chemical Physics* **20**, 25506. doi:10.1039/C8CP05236K (2018).

92. Wili, N., Hintz, H., Vanas, A., Godt, A. & Jeschke, G. Distance measurement between trityl radicals by pulse dressed electron paramagnetic resonance with phase modulation. *Magnetic Resonance* **1**, 75. doi:10.5194/mr-1-75-2020 (2020).

93. Jeschke, G. DEER Distance Measurements on Proteins. *Annual review of physical chemistry* **63**, 419. doi:10.1146/annurev-physchem-032511-143716 (2012).

94. Bordignon, E. & Bleicken, S. New limits of sensitivity of site-directed spin labeling electron paramagnetic resonance for membrane proteins. *Biochimica et Biophysica Acta - Biomembranes* **1860**, 841. doi:10.1016/j.bbamem.2017.12.009 (2018).

95. Duss, O., Yulikov, M., Jeschke, G. & Allain, F. H.-T. EPR-aided approach for solution structure determination of large RNAs or protein-RNA complexes. *Nature communications* **5**, 3669. doi:10.1038/ncomms4669 (2014).

96. Milov, A. D., Ponomarev, A. B. & Tsvetkov, Y. D. Electron-electron double resonance in electron spin echo: Model biradical systems and the sensitized photolysis of decalin. *Chemical Physics Letters* **110**, 67. doi:10.1016/0009-2614(84)80148-7 (1984).

97. Pannier, M., Veit, S., Godt, A., Jeschke, G. & Spiess, H. W. Dead-Time Free Measurement of Dipole-Dipole Interactions between Electron Spins. *Journal of Magnetic Resonance* **142**, 331. doi:`10.1006/jmre.1999.1944` (2000).

98. Borbat, P. P. & Freed, J. H. Multiple-quantum ESR and distance measurements. *Chemical Physics Letters* **313**, 145. doi:`10.1016/S0009-2614(99)00972-0` (1999).

99. Jeschke, G., Pannier, M., Godt, A. & Spiess, H. Dipolar spectroscopy and spin alignment in electron paramagnetic resonance. *Chemical Physics Letters* **331**, 243. doi:`10.1016/S0009-2614(00)01171-4` (2000).

100. Kulik, L. V., Dzuba, S. A., Grigoryev, I. A. & Tsvetkov, Y. D. Electron dipole-dipole interaction in ESEEM of nitroxide biradicals. *Chemical Physics Letters* **343**, 315. doi:`10.1016/S0009-2614(01)00721-7` (2001).

101. Milikisyants, S., Scarpelli, F., Finiguerra, M. G., Ubbink, M. & Huber, M. A pulsed EPR method to determine distances between paramagnetic centers with strong spectral anisotropy and radicals: The dead-time free RIDME sequence. *Journal of Magnetic Resonance* **201**, 48. doi:`10.1016/j.jmr.2009.08.008` (2009).

102. Georgieva, E. R., Ramlall, T. F., Borbat, P. P., Freed, J. H. & Eliezer, D. The Lipid-binding Domain of Wild Type and Mutant a-Synuclein. *Journal of Biological Chemistry* **285**, 28261. doi:`10.1074/jbc.m110.157214` (2010).

103. Ward, R., Bowman, A., Sozudogru, E., El-Mkami, H., Owen-Hughes, T. & Norman, D. G. EPR distance measurements in deuterated proteins. *Journal of Magnetic Resonance* **207**, 164. doi:`10.1016/j.jmr.2010.08.002` (2010).

104. Schmidt, T., Wälti, M. A., Baber, J. L., Hustedt, E. J. & Clore, G. M. Long Distance Measurements up to 160 Å in the GroEL Tetradecamer Using Q-Band DEER EPR Spectroscopy. *Angewandte Chemie - International Edition* **55**, 15905. doi:`10.1002/anie.201609617` (2016).

105. Borbat, P. P., Georgieva, E. R. & Freed, J. H. Improved sensitivity for long-distance measurements in biomolecules: Five-pulse double electron-electron resonance. *Journal of Physical Chemistry Letters* **4**, 170. doi:`10.1021/jz301788n` (2013).

106. Spindler, P. E., Waclawska, I., Endeward, B., Plackmeyer, J., Ziegler, C. & Prisner, T. F. Carr-Purcell Pulsed Electron Double Resonance with Shaped Inversion Pulses. *Journal of Physical Chemistry Letters* **6**, 4331. doi:10.1021/acs.jpclett.5b01933 (2015).

107. Blank, A. A new approach to distance measurements between two spin labels in the >10 nm range. *Physical Chemistry Chemical Physics* **19**, 5222. doi:10.1039/C6CP07597E (2017).

108. Jeschke, G. & Schweiger, A. Hyperfine decoupling in electron spin resonance. *Journal of Chemical Physics* **106**, 9979. doi:10.1063/1.474073 (1997).

109. Redfield, A. G. Nuclear magnetic resonance saturation and rotary saturation in solids. *Physical Review* **98**, 1787. doi:10.1103/PhysRev.98.1787 (1955).

110. Hoult, D. I. Rotating frame zeugmatography. *Journal of Magnetic Resonance (1969)* **33**, 183. doi:10.1016/0022-2364(79)90202-6 (1979).

111. Grzesiek, S. & Bax, A. Audio-Frequency NMR in a Nutating Frame. Application to the Assignment of Phenylalanine Residues in Isotopically Enriched Proteins. *Journal of the American Chemical Society* **117**, 6527. doi:10.1021/ja00129a016 (1995).

112. Jeschke, G. Coherent superposition of dressed spin states and pulse dressed electron spin resonance. *Chemical Physics Letters* **301**, 524. doi:10.1016/S0009-2614(99)00041-X (1999).

113. Cohen-Tannoudji, C., Dupont-Roc, J. & Grynberg, G. *Atom-Photon Interactions* (1992).

114. Saiko, A. P., Fedaruk, R. & Markevich, S. A. Suppression of electron spin decoherence in Rabi oscillations induced by an inhomogeneous microwave field. *Journal of Magnetic Resonance* **290**, 60. doi:10.1016/j.jmr.2018.02.003 (2018).

115. Laucht, A., Simmons, S., Kalra, R., Tosi, G., Dehollain, J. P., Muhonen, J. T., Freer, S., Hudson, F. E., Itoh, K. M., Jamieson, D. N., McCallum, J. C., Dzurak, A. S. & Morello, A. Breaking the rotating wave approximation for a strongly driven dressed single-electron spin. *Physical Review B* **94**, 1. doi:10.1103/PhysRevB.94.161302 (2016).

116.   Laucht, A., Kalra, R., Simmons, S., Dehollain, J. P., Muhonen, J. T., Mohiyaddin, F. A., Freer, S., Hudson, F. E., Itoh, K. M., Jamieson, D. N., McCallum, J. C., Dzurak, A. S. & Morello, A. A dressed spin qubit in silicon. *Nature Nanotechnology* **12**, 61. doi:`10.1038/nnano.2016.178` (2017).

117.   Cohen, I., Aharon, N. & Retzker, A. Continuous dynamical decoupling utilizing time-dependent detuning. *Fortschritte der Physik* **65**, 1. doi:`10.1002/prop.201600071` (2017).

118.   Chen, H.-Y. & Tycko, R. Slice Selection in Low-Temperature, DNP-Enhanced Magnetic Resonance Imaging by Lee-Goldburg Spin-Locking and Phase Modulation. *Journal of Magnetic Resonance*, 106715. doi:`10.1016/j.jmr.2020.106715` (2020).

119.   Godt, A., Schulte, M., Zimmermann, H. & Jeschke, G. How Flexible Are Poly(para-phenyleneethynylene)s? *Angewandte Chemie International Edition* **45**, 7560. doi:`10.1002/anie.200602807` (2006).

120.   Jeschke, G., Sajid, M., Schulte, M., Ramezanian, N., Volkov, A., Zimmermann, H. & Godt, A. Flexibility of shape-persistent molecular building blocks composed of p-phenylene and ethynylene units. *Journal of the American Chemical Society* **132**, 10107. doi:`10.1021/ja102983b` (2010).

121.   Hintz, H., Vanas, A., Klose, D., Jeschke, G. & Godt, A. Trityl Radicals with a Combination of the Orthogonal Functional Groups Ethyne and Carboxyl: Synthesis without a Statistical Step and EPR Characterization. *The Journal of Organic Chemistry* **84**. PMID: 30785294, 3304. doi:`10.1021/acs.joc.8b03234` (2019).

122.   Reginsson, G. W., Kunjir, N. C., Sigurdsson, S. T. & Schiemann, O. Trityl radicals: Spin labels for nanometer-distance measurements. *Chemistry - A European Journal* **18**, 13580. doi:`10.1002/chem.201203014` (2012).

123.   Rhim, W.-K., Pines, A. & Waugh, J. S. Violation of the Spin-Temperature Hypothesis. *Physical Review Letters* **25**, 218. doi:`10.1103/PhysRevLett.25.218` (1970).

124.   Klauder, J. R. & Anderson, P. W. Spectral Diffusion Decay in Spin Resonance Experiments. *Physical Review* **125**, 912. doi:`10.1103/PhysRev.125.912` (1962).

125. Ernst, M. Heteronuclear spin decoupling in solid-state NMR under magic-angle sample spinning. *J. Magn. Reson.* **162**, 1. doi:`10.1016/S1090-7807(03)00074-0` (2003).

126. Brown, I. M. in *Time Domain Electron Spin Resonance* (eds Kevan, L. & Schwartz, R.) 200 (John Wiley and Sons, Inc, New York, New York, 1979).

127. Meyer, A., Jassoy, J. J., Spicher, S., Berndhäuser, A. & Schiemann, O. Performance of PELDOR, RIDME, SIFTER, and DQC in measuring distances in trityl based bi- and triradicals: Exchange coupling, pseudosecular coupling and multi-spin effects. *Physical Chemistry Chemical Physics* **20**, 13858. doi:`10.1039/c8cp01276h` (2018).

128. Doll, A. *Frequency-Swept Microwave Pulses for Electron Spin Resonance* PhD thesis (ETH Zurich, 2016). doi:`10.3929/ethz-a-010670425`.

129. Shevelev, G. Y., Krumkacheva, O. A., Lomzov, A. A., Kuzhelev, A. A., Rogozhnikova, O. Y., Trukhin, D. V., Troitskaya, T. I., Tormyshev, V. M., Fedin, M. V., Pyshnyi, D. V. & Bagryanskaya, E. G. Physiological-temperature distance measurement in nucleic acid using triarylmethyl-based spin labels and pulsed dipolar EPR spectroscopy. *Journal of the American Chemical Society* **136**, 9874. doi:`10.1021/ja505122n` (2014).

130. Sahoo, D., Thiele, S., Schulte, M., Ramezanian, N. & Godt, A. Polar tagging in the synthesis of monodisperse oligo(p-phenyleneethynylene)s and an update on the synthesis of oligoPPEs. *Beilstein Journal of Organic Chemistry* **6**, 20. doi:`10.3762/bjoc.6.57` (2010).

131. Qi, M., Hülsmann, M. & Godt, A. Spacers for Geometrically Well-Defined Water-Soluble Molecular Rulers and Their Application. *Journal of Organic Chemistry* **81**, 2549. doi:`10.1021/acs.joc.6b00125` (2016).

132. Ritsch, I., Hintz, H., Jeschke, G., Godt, A. & Yulikov, M. Improving the Accuracy of Cu(II)-Nitroxide RIDME in the Presence of Orientation Correlation Evaluated with Water-soluble Cu(II)-Nitroxide Rulers. *Physical Chemistry Chemical Physics*. doi:`10.1039/C8CP06573J` (2019).

133. Michaeli, S., Sorce, D. J., Idiyatullin, D., Ugurbil, K. & Garwood, M. Transverse relaxation in the rotating frame induced by chemical exchange. *Journal of Magnetic Resonance* **169**, 293. doi:`https://doi.org/10.1016/j.jmr.2004.05.010` (2004).

134. Müller, L. & Ernst, R. Coherence transfer in the rotating frame. *Molecular Physics* **38**, 963. doi:`10.1080/00268977900102161` (1979).

135. Anders, J. & Lips, K. MR to go. *Journal of Magnetic Resonance* **306**, 118. doi:`10.1016/j.jmr.2019.07.007` (2019).

136. Sidabras, J. W., Duan, J., Winkler, M., Happe, T., Hussein, R., Zouni, A., Suter, D., Schnegg, A., Lubitz, W. & Reijerse, E. J. Extending electron paramagnetic resonance to nanoliter volume protein single crystals using a self-resonant microhelix. *Science Advances* **5**. doi:`10.1126/sciadv.aay1394` (2019).

137. Narkowicz, R., Suter, D. & Niemeyer, I. Scaling of sensitivity and efficiency in planar microresonators for electron spin resonance. *Review of Scientific Instruments* **79**. doi:`10.1063/1.2964926` (2008).

138. Blank, A., Twig, Y. & Ishay, Y. Recent trends in high spin sensitivity magnetic resonance. *Journal of Magnetic Resonance* **280**, 20. doi:`10.1016/j.jmr.2017.02.019` (2017).

139. Kundu, K., Mentink-Vigier, F., Feintuch, A. & Vega, S. *DNP Mechanisms* 295. doi:`10.1002/9780470034590.emrstm1550` (2019).

140. Ni, Q. Z., Daviso, E., Can, T. V., Markhasin, E., Jawla, S. K., Swager, T. M., Temkin, R. J., Herzfeld, J. & Griffin, R. G. High Frequency Dynamic Nuclear Polarization. *Accounts of Chemical Research* **46**. PMID: 23597038, 1933. doi:`10.1021/ar300348n` (2013).

141. Mentink-Vigier, F., Akbey, Ü., Oschkinat, H., Vega, S. & Feintuch, A. Theoretical aspects of Magic Angle Spinning - Dynamic Nuclear Polarization. *J. Magn. Reson.* **258**, 102. doi:`10.1016/j.jmr.2015.07.001` (2015).

142. Thurber, K. R. & Tycko, R. Theory for cross effect dynamic nuclear polarization under magic-angle spinning in solid state nuclear magnetic resonance: The importance of level crossings. *J. Chem. Phys.* **137**. doi:`10.1063/1.4747449` (2012).

143. Ardenkjaer-Larsen, J. H., Fridlund, B., Gram, A., Hansson, G., Hansson, L., Lerche, M. H., Servin, R., Thaning, M. & Golman, K. Increase in signal-to-noise ratio of > 10,000 times in liquid-state NMR. *Proc. Natl. Acad. Sci.* **100**, 10158. doi:`10.1073/pnas.1733835100` (2003).

144. Eichhorn, T. R., Niketic, N., Van Den Brandt, B., Filges, U., Panzner, T., Rantsiou, E., Wenckebach, W. T. & Hautle, P. Proton polarization above 70% by DNP using photo-excited triplet states, a first step towards a broadband neutron spin filter. *Nucl. Instruments Methods Phys. Res. Sect. A Accel. Spectrometers, Detect. Assoc. Equip.* **754**, 10. doi:10.1016/j.nima.2014.03.047 (2014).

145. Scheuer, J. & Naydenov, B. *Dynamic nuclear polarization (DNP) in diamond* 1st ed., 277. doi:10.1016/bs.semsem.2020.03.009 (Elsevier Inc., 2020).

146. Tan, K. O., Jawla, S., Temkin, R. J. & Griffin, R. G. Pulsed dynamic nuclear polarization. *eMagRes* **8**, 339. doi:10.1002/9780470034590.emrstm1551 (2019).

147. Henstra, A., Dirksen, P., Schmidt, J. & Wenckebach, W. T. Nuclear spin orientation via electron spin locking (NOVEL). *Journal of Magnetic Resonance (1969)* **77**, 389. doi:10.1016/0022-2364(88)90190-4 (1988).

148. Can, T. V., Walish, J. J., Swager, T. M. & Griffin, R. G. Time domain DNP with the NOVEL sequence. *J. Chem. Phys.* **143**. doi:10.1063/1.4927087 (2015).

149. Mathies, G., Jain, S., Reese, M. & Griffin, R. G. Pulsed Dynamic Nuclear Polarization with Trityl Radicals. *J. Phys. Chem. Lett.* **7**, 111. doi:10.1021/acs.jpclett.5b02720 (2016).

150. Can, T. V., Weber, R. T., Walish, J. J., Swager, T. M. & Griffin, R. G. Ramped-amplitude NOVEL. *J. Chem. Phys.* **146**. doi:10.1063/1.4980155 (2017).

151. Jain, S. K., Mathies, G. & Griffin, R. G. Off-resonance NOVEL. *J. Chem. Phys.* **147**, 164201. doi:10.1063/1.5000528 (2017).

152. Henstra, A., Dirksen, P. & Wenckebach, W. T. Enhanced dynamic nuclear polarization by the integrated solid effect. *Phys. Lett. A* **134**, 134. doi:10.1016/0375-9601(88)90950-4 (1988).

153. Can, T. V., Weber, R. T., Walish, J. J., Swager, T. M. & Griffin, R. G. Frequency-Swept Integrated Solid Effect. *Angew. Chemie - Int. Ed.* **56**, 6744. doi:10.1002/anie.201700032 (2017).

154. Tan, K. O., Weber, R. T., Can, T. V. & Griffin, R. G. Adiabatic Solid Effect. *J. Phys. Chem. Lett.* **11**, 3416. doi:10.1021/acs.jpclett.0c00654 (2020).

155. Wind, R. A., Li, L., Lock, H. & Maciel, G. E. Dynamic nuclear polarization in the nuclear rotating frame. *J. Magn. Reson.* **79**, 577. doi:`10.1016/0022-2364(88)90094-7` (1988).

156. Weis, V., Bennati, M., Rosay, M. & Griffin, R. G. Solid effect in the electron spin dressed state: a new approach for dynamic nuclear polarization. *J. Chem. Phys.* **113**, 6795. doi:`10.1063/1.1310599` (2000).

157. Tan, K. O., Yang, C., Weber, R. T., Mathies, G. & Griffin, R. G. Time-optimized pulsed dynamic nuclear polarization. *Science Advances* **5**. doi:`10.1126/sciadv.aav6909` (2019).

158. Schwartz, I., Scheuer, J., Tratzmiller, B., Müller, S., Chen, Q., Dhand, I., Wang, Z. Y., Müller, C., Naydenov, B., Jelezko, F. & Plenio, M. B. Robust optical polarization of nuclear spin baths using Hamiltonian engineering of nitrogen-vacancy center quantum dynamics. *Sci. Adv.* **4**, 1. doi:`10.1126/sciadv.aat8978` (2018).

159. Scholz, I., Van Beek, J. D. & Ernst, M. Operator-based Floquet theory in solid-state NMR. *Solid State Nucl. Magn. Reson.* **37**, 39. doi:`10.1016/j.ssnmr.2010.04.003` (2010).

160. Nielsen, A. B., Hansen, M. R., Andersen, J. E. & Vosegaard, T. Single-spin vector analysis of strongly coupled nuclei in TOCSY NMR experiments. *J. Chem. Phys.* **151**. doi:`10.1063/1.5123046` (2019).

161. Lilly Thankamony, A. S., Wittmann, J. J., Kaushik, M. & Corzilius, B. Dynamic nuclear polarization for sensitivity enhancement in modern solid-state NMR. *Prog. Nucl. Magn. Reson. Spectrosc.* **102-103**, 120. doi:`10.1016/j.pnmrs.2017.06.002` (2017).

162. Prisco, N. A., Pinon, A. C., Emsley, L. & Chmelka, B. F. Scaling analyses for hyperpolarization transfer across a spin-diffusion barrier and into bulk solid media. *Phys. Chem. Chem. Phys.* **23**, 1006. doi:`10.1039/d0cp03195j` (2021).

163. Baum, J., Tycko, R. & Pines, A. Broadband and adiabatic inversion of a two-level system by phase-modulated pulses. *Phys. Rev. A* **32**, 3435. doi:`10.1103/PhysRevA.32.3435` (1985).

164. Jeschke, G., Pribitzer, S. & Doll, A. Coherence Transfer by Passage Pulses in Electron Paramagnetic Resonance Spectroscopy. *J. Phys. Chem. B* **119**, 13570. doi:`10.1021/acs.jpcb.5b02964` (2015).

165.   Hogben, H. J., Krzystyniak, M., Charnock, G. T. P., Hore, P. J. &
        Kuprov, I. Spinach - A software library for simulation of spin dynamics
        in large spin systems. *J. Magn. Reson.* **208**, 179. doi:`10.1016/j.jmr.`
        `2010.11.008` (2011).

166.   Rizzato, R., Kaminker, I., Vega, S. & Bennati, M. Cross-polarisation
        edited ENDOR. *Mol. Phys.* **111**, 2809. doi:`10.1080/00268976.2013.`
        `816795` (2013).

ACKNOWLEDGEMENTS

Christophe Copéret, Thanks for all the nice discussions on EPR in catalysis, on science in general, and for your support regarding my postdoc application.

Thomas Wiegand, vielen Dank für die Zusammenarbeit auf dem DnaB Projekt. Insgesamt wurde daraus eine sehr schöne Publikation, obwohl ich hie und da eigentlich zu wenig Zeit investiert habe.

Laura Voelker, Danke für die Zeit und den Enthusiasmus, den Du in Deine Masterarbeit gesteckt hast. Entschuldige die vielen Hardware Schwierigkeiten. Für mich hat sich das alles am Ende ausbezahlt, ich hoffe, für die auch. Hoffentlich bleibst Du der Spindynamik weiterhin ein bisschen erhalten.

Lukas Schreder, Danke für Deine sehr selbstständige Arbeit bezüglich den dressed Spin Experimenten. Auch wenn die Semesterarbeit selbst nicht den gewünschenten "Erfolg" hatte, so hat sie doch sehr viel bewegt. Technisch und intelektuell.

Anton Ashuiev, Thanks for the collaboration on Ti(III). It was so nice, and I was so lucky that a new method could directly be used for something "real".

Agathe Vanas, vielen Dank für die Zusammenarbeit im VAC, und für die Hilfe mit all den Tritylsamples. z.B. die völlig entspannte Reaktion, als ich ein Röhrchen zerstört habe.

Laura Esteban Hofer, Danke für die vielen schönen Abende, die Kaffeepausen, und Deinen unermüdlichen Einsatz für die EPR Gruppe. Ein Danke in der Form hier trägt dem viel zu wenig Rechnung. Ich hoffe, mir fällt noch etwas Besseres ein. Und danke für Tips fürs Glyerol Pipettieren :D

Yevhen Polyhach, Zhenia, thanks for all the extended coffeebreaks, and all the discussions about coffee, with some peripheral EPR content here and there.

Jörg Fischer, Danke für den frischen Wind in der EPR Gruppe in einer Zeit, in der Soziales allgemein zu kurz kam.

Daniel Klose, Danke! Ohne dich könnte ich EPR-technisch *praktisch* fast nichts. ENDOR, W-band, Q-band HYSCORE, Probenvorbereitung, AWG Elektronik, Temperaturen, Lösungsmittel, ... Es scheint, als könntest Du alles. Und Du zeigst allen alles. Danke auch für all die Diskussionen im F231[1].

Maxim Yulikov, thanks for many stimulating discussions on spin diffusion and how it can be described in the context of EPR.

Luis Fábregas Ibáñez, merci hesch Du ändlech mau chli ornig I üsä code bracht, o we mr passiv widerstand hei gleischtet. Merci luägsch zur IT infrastruktur, und merci für dini Liäbi zu ässä und wii.

Frauke Breitgoff, vielen Dank für Deine Einführung ins Messen mit dem AWG Spektrometer und all das Troubleshooting in den ersten Monaten.

---

1 Ich muss meine Büronummer immer noch nachschauen...

Sergei Kuzin, thanks for all the dumplings :D

Mikhail Agrachev, Misha, thanks for bringing some Italo-Russian flair into the group, and props for all the cool band shirts.

Irina Ritsch, Danke für die Brettspielabende, die ganzen BBQs, und die vielen Gruppenevents, die Du organisiert hast.

René Tschaggelar, merci für au di Sachä wo dä gflickt oder putzt hesch, weni sä ha kabutt gmacht. Tuät mr leid wägem ENDOR Probächopf, woni gschlissä ha. U merci für die villä Diskussionä über Elektronik, wo für üs so wichtig isch, ig aber eich ke Ahnig drvo ha.

Janne Soetbeer, vielen Dank für die Zusammenarbeit im VAC, und für Deine geduldigen Diskussionen, jedesmal, wenn ich wieder was zu Relaxation gefragt und mich über die Literatur genervt habe.

Takuya Segawa, Merci für au di coolä gspräch über aui Formä vo Magnetresonanz.

Christoph Gmeiner, Danke für Deine Organisation unserer Labore, und für den vielen Wein, den wir geteilt haben.

Kathi Keller, Danke, dass Du mir gezeigt hast, wie man am W-band misst, und für Deine schier unendliche soziale Energie und die Organisation von all den Events.

Stephan Prbibitzer, Danke für Spidyan/Easyspin, und die kleinen Bugs, die Du für mich korrigiert hast.

Andrea Eggeling, Merci bisch id EPR Gruppä cho. Wott gseit hesch, Du wärsch cho d Semesterarbeit machä, wüu dä z Praktikum hesch cool gfungä, isch mir ds Härz ä chli ufgangä.

Valerie Mertens, Danke für die Zusammenarbeit am AWG, für die Kaffeepausen, und dass Du Sachen immer so lange hinterfragst.

Kristina Comiotto, Grazie! Merci, machsch Du d ETH chli mönschlecher. I ha immer zgfüäu gha, I chönnt mit jedem Problemli und Wehwehli zu Dir cho, und rächt oft hesch Dus o glöst.

Oli Oberhänsli, merci für au ds chlinä u grossä Züg wo mr geng bruchä. Das isch aubä sooo wichtig. U merci hesch mit mitgnoh zum curlä.

Seppi, Geilä Siäch.

Daniel Zindel, Hopp YB! (und merci für ganz vili synthese für di ganz Gruppä).

Und merci am ganzä Räscht vor *Wärchstatt* und *Elektronik* Crew. Dir sit extrem wichtig, immer hiufsbereit, o we öper vorä angärä Gruppä öppis fragt, und när ischs ersch no cool sit dr immer für nes biärli z ha.

Andrin Doll, Merci fürs AWG Spektrometer. Ohni di gäbs mini Doktorarbeit nid.

Now the problem with such a long acknowledgement section is, that it is even worse if I forgot someone who should totally be in it. I assure you, it's not that I did not think of you, it's just that the cognitive abilities are somewhat reduced after writing a thesis for such a long time. If you think I forgot you here, please get in touch, and I make it up to you!

CURRICULUM VITAE

PERSONAL DATA

Name	Nino Andrea Wili
Date of Birth	July 8, 1993
Place of Birth	Bern, Switzerland
Citizen of	Hitzkirch LU and Altwis LU, Switzerland, and of Germany

EDUCATION

05/2017–09/2021	ETH Zurich, Switzerland, PhD in the group of Prof. Gunnar Jeschke.
09/2014–02/2015	University of St Andrews, Scotland, UK, visiting scholar.
09/2011–10/2016	ETH Zurich, BSc and MSc Interdisciplinary Natural Sciences (Focus on Structural Biology and Physcial Chemistry).
08/2003–07/2011	Freies Gymnasium Bern, Switzerland, Matura.

SCIENTIFIC PROJECTS

Magnetic Resonance

05/2017–09/2021	PhD project with Prof. Gunnar Jeschke (ETH Zurich): *New electron spin resonance experiments with tailored waveform excitation*
04/2016–09/2016	Master Thesis with Prof. Matthias Ernst (ETH Zurich): *Pulse Transient Compensation in REDOR and Heteronuclear Decoupling under MAS.*

02/2016–04/2016	Research Project with Dr. René Verel (ETH Zurich): *Limitations of Cross Polarization for the Acquisition of 207Pb Solid State NMR Spectra.*
02/2014–06/2014	Bachelor thesis with Prof. Gunnar Jeschke (ETH Zurich): *Gd(III)-Gd(III)-DEER with Chirped Pump Pulses.*

Others

2016–2020	Several visits as a scientific assistant at University Hospital Balgrist (Zurich) as part of compulsory civil service (Zivildienst). One year in total: *Preparation and characterization of giant unilamellar vesicles (GUVs). Implementation of automatic image processing algorithms in MATLAB for a variety of biomechanical applications. Quantification of collagen and collagen crosslink content in mouse tendon.*
02/2015–06/2015	Research Project with Prof. Martin Pilhofer (ETH Zurich): *Cryo Electron Tomography of MAC Arrays.*
09/2014–02/2015	Research Project with Dr. Janet Lovett (University of St Andrews): *Spin labelling of Myosin RLC and Calmodulin.*

INTERNATIONAL ORAL PRESENTATIONS

04/2021	Dressing up electron spins to unlock their potential: Application to distance measurements between trityl radicals *RSC EPR* 2021 (online).
10/2020	Basics of EPR for NMR spectroscopists (tutorial): `https://www.youtube.com/watch?v=2qjbq-5olaM`
04/2019	ELDOR-detected NMR: The Curious Case of a Coupled Copper Complex. *RSC EPR* 2019 in Glasgow.

07/2018	The CHEESY Way to Hyperfine Spectroscopy. *EUROMAR* 2018 in Nantes.

SCHOLARSHIPS AND AWARDS

04/2021	JEOL Prize of the RSC ESR Group.
04/2019	Springer Poster Prize at the RSC EPR conference 2019 in Glasgow, UK.
04/2018	IES Poster Award at the RSC EPR conference 2018 in London, UK.
12/2016	„Willi Studer Prize" for the best master diploma in Interdisciplinary Natural Sciences at ETH Zurich in 2016.
02/2015–09/2016	Excellence Scholarship and Opportunity Programme (ETH).

TEACHING EXPERIENCE

09/2013-	Teaching assistant in Inorganic Chemistry (MO-theory), Informatics for chemists (C++ exercises), Physical Chemistry (Thermodynamics (2x), Quantum Mechanics, Magnetic Resonance (3x: basic physics, ssNMR, Relaxation theory), Statistical Thermodynamics) and lab courses (EPR spectroscopy (2x), flash light photolysis (2x)). Courses usually last one semester of 14 weeks with weekly exercise hours or biweekly lab days.
2018/2020	Supervision of two MSc research projects.
2015/2016	2x a week-long (about 20h) repetition course in magnetic resonance (NMR and EPR) for third year chemists.

OTHER ACTIVITIES

03/2020–	Founder and coordinator of the Virtual EPR meetings. Now with support from the International EPR/ESR society (IES). https://ieprs.org/on-line-activities/
11/2017–10/2019	President of the union of the assistants at the chemical labs of ETH Zurich, VAC.
12/2018–	Open Science Ambassador of the Swiss National Science Foundation.
10/2012–11/2013	Board member of the student association of chemists at ETHZ, VCS.
11/2012–11/2013	Founding Member of *Chemtogether*, an annual job fair for chemists at ETH.
2006–	Bass Player in various Jazz, Rock and Pop Projects. Hundreds of live concerts and several studio sessions. E.g. *Cachét, Ratskcors, Eskimo, Veronica Fusaro, Ta' Shan, Call me Ramsey, ...*

PUBLICATIONS

ORCID: `https://orcid.org/0000-0003-4890-3842`
*: As corresponding author

12. Malär, A. A., <u>Wili, Nino</u>, Völker, L. A., Kozlova, M. I., Cadalbert, R., Däpp, A., Weber, M. E., Zehnder, J., Jeschke, G., Eckert, H., Böckmann, A., Klose, D., Mulkidjanian, A. Y., Meier, B. H. & Wiegand, T. Spectroscopic glimpses of the transition state of ATP hydrolysis trapped in a bacterial DnaB helicase. *Nat. Commun.* **12**, 5293. doi:`10.1038/s41467-021-25599-z` (2021).

11. Ashuiev, A., Allouche, F., <u>Wili, Nino</u>, Searles, K., Klose, D., Copéret, C. & Jeschke, G. Molecular and supported Ti(iii)-alkyls: efficient ethylene polymerization driven by the π-character of metal-carbon bonds and back donation from a singly occupied molecular orbital. *Chem. Sci.* **12**, 780. doi:`10.1039/d0sc04436a` (2021).

10. Lacabanne, D., Wiegand, T., <u>Wili, Nino</u>, Kozlova, M. I., Cadalbert, R., Klose, D., Mulkidjanian, A. Y., Meier, B. H. & Böckmann, A. ATP Analogues for Structural Investigations: Case Studies of a DnaB Helicase and an ABC Transporter. *Molecules* **25**. doi:`10.3390/molecules25225268` (2020).

9. Aebischer, K., <u>Wili, Nino</u>, Tošner, Z. & Ernst, M. Using nutation-frequency-selective pulses to reduce radio-frequency field inhomogeneity in solid-state NMR. *Magn. Reson.* **1**, 187. doi:`10.5194/mr-1-187-2020` (2020).

8. <u>Wili, Nino</u>*, Hintz, H., Vanas, A., Godt, A. & Jeschke, G. Distance measurement between trityl radicals by pulse dressed electron paramagnetic resonance with phase modulation. *Magn. Reson.* **1**, 75. doi:`10.5194/mr-1-75-2020` (2020).

7. Parigoris, E., Dunkelmann, D. L., Murphy, A., <u>Wili, Nino</u>, Kaech, A., Dumrese, C., Jimenez-Rojo, N. & Silvan, U. Facile generation of giant unilamellar vesicles using polyacrylamide gels. *Sci. Rep.* **10**, 1. doi:`10.1038/s41598-020-61655-2` (2020).

6. Wili, Nino, Richert, S., Limburg, B., Clarke, S. J., Anderson, H. L., Timmel, C. R. & Jeschke, G. ELDOR-detected NMR beyond hyperfine couplings: A case study with Cu(ii)-porphyrin dimers. *Phys. Chem. Chem. Phys.* **21**, 11676. doi:`10.1039/c9cp01760g` (2019).

5. Holenstein, C. N., Lendi, C. R., Wili, Nino & Snedeker, J. G. Simulation and evaluation of 3D traction force microscopy. *Comput. Methods Biomech. Biomed. Engin.* **22**, 853. doi:`10.1080/10255842.2019.1599866` (2019).

4. Wili, Nino & Jeschke, G. Chirp echo Fourier transform EPR-detected NMR. *J. Magn. Reson.* **289**, 26. doi:`10.1016/j.jmr.2018.02.001` (2018).

3. Hellwagner, J., Wili, Nino, Ibáñez, L. F., Wittmann, J. J., Meier, B. H. & Ernst, M. Transient effects in π-pulse sequences in MAS solid-state NMR. *J. Magn. Reson.* **287**, 65. doi:`10.1016/j.jmr.2017.12.015` (2018).

2. Doll, A., Qi, M., Wili, Nino, Pribitzer, S., Godt, A. & Jeschke, G. Gd(III)-Gd(III) distance measurements with chirp pump pulses. *J. Magn. Reson.* **259**, 153. doi:`10.1016/j.jmr.2015.08.010` (2015).

1. Doll, A., Qi, M., Pribitzer, S., Wili, Nino, Yulikov, M., Godt, A. & Jeschke, G. Sensitivity enhancement by population transfer in Gd(III) spin labels. *Phys. Chem. Chem. Phys.* **17**, 7334. doi:`10.1039/C4CP05893C` (2015).

By Bill Waterson, published 8 July, 1993. printed with permission of Andrews McMeel licensing.